

# Sheffield Hallam University

*An investigation of aluminium intermetallic phases using  $^{57}\text{Fe}$  Mossbauer spectroscopy and complementary techniques.*

REEDER, Andrew J.

Available from the Sheffield Hallam University Research Archive (SHURA) at:

<http://shura.shu.ac.uk/20269/>

## A Sheffield Hallam University thesis

This thesis is protected by copyright which belongs to the author.

The content must not be changed in any way or sold commercially in any format or medium without the formal permission of the author.

When referring to this work, full bibliographic details including the author, title, awarding institution and date of the thesis must be given.

Please visit <http://shura.shu.ac.uk/20269/> and <http://shura.shu.ac.uk/information.html> for further details about copyright and re-use permissions.

LEARNING CENTRE  
CITY CAMPUS, POND STREET,  
SHEFFIELD, S1 1WB.

101 651 874 9



**REFERENCE**

ProQuest Number: 10700914

All rights reserved

INFORMATION TO ALL USERS

The quality of this reproduction is dependent upon the quality of the copy submitted.

In the unlikely event that the author did not send a complete manuscript and there are missing pages, these will be noted. Also, if material had to be removed, a note will indicate the deletion.



ProQuest 10700914

Published by ProQuest LLC (2017). Copyright of the Dissertation is held by the Author.

All rights reserved.

This work is protected against unauthorized copying under Title 17, United States Code  
Microform Edition © ProQuest LLC.

ProQuest LLC.  
789 East Eisenhower Parkway  
P.O. Box 1346  
Ann Arbor, MI 48106 – 1346

***An Investigation of Aluminium Intermetallic Phases using  $^{57}\text{Fe}$   
Mössbauer Spectroscopy and Complementary Techniques.***

Andrew J. Reeder

A thesis submitted in partial fulfilment of the requirements of Sheffield  
Hallam University for the degree of Doctor of Philosophy.

June 2000

Sponsored by the Materials Research Institute, Sheffield Hallam University,  
and Alcan International, Banbury.

## DEDICATION

This work is dedicated to my mum and dad.

Ann, who died suddenly on the 16th January 1999, and Lyle.

*“If you can dream - and not make dreams your master;  
If you can think - and not make thoughts your aim;  
If you can meet Triumph and Disaster  
And treat those two impostors just the same;”*

Rudyard Kipling.



## ACKNOWLEDGEMENTS

I would like to thank the following people for their contributions, whether intellectual, emotional or material, in the production of this work.

The first people I would like to thank are my supervisors. Dr. Sue Forder for being a constant thorn in my side (meant in the nicest possible way), and Prof. John Brooks who I could never pull the wool over his eyes. Also, everyone at Alcan International, especially Dr. Paul Evans and Dr. Havovy Cama, for providing the materials for this study, and guidance in the intricate world of solidification.

Next I would like to thank my colleagues. Dr. Julian Hamer and Dr. John Davidson, who were research students at the time I started this work, for introducing me to the Mössbauer Lab. Between the pair of them they armed me with enough knowledge about the Mössbauer world in room 820, so that I could take everything in my stride. The surface studies would not have been in this thesis without the help of Dr. Mike Rignall, the mountaineer.

That only leaves the technicians. I would like to thank them all for providing materials, and gossip within the School of Science and Maths at Sheffield Hallam University. Especially Charlie, for his perseverance with the Mössbauer Laboratory, Kevin Blake, the surface studies bloke from Doncaster. Last, but not least, Nick Lewus for lending me a PC, and also providing hours of endless sarcasm.

Thanks also to the variety of colourful characters I have met, while I was working as a doorman in a number of clubs in Sheffield. They provided me with an education that cannot be taught by any academic. In particular: Jeff Robinson, Roger Bell, Charlotte Akpınar, and Darren "Mucker" Bullimore. These people stood by me in quiet, and not so quiet, times.

I would like to mention Darren Wilson and his long time girl friend Alex O'Dea, for always dragging me away from my studies when I needed it. We shared some hectic, and relaxing, times in a variety of nightclubs and front rooms in Sheffield and Birmingham. To Darren - no pain no gain! Paul "Faz" Farrell and Richard "Dick" Walker should also receive some acknowledgement, for just being long time good friends who believed in me.

Finally I would like to thank my family, especially my mum and dad. These took the full force of my outbursts, without retaliating, before sitting me down and talking some sense back into me. Also my eldest sister and her husband, Gwen and Malcolm, who provided a great deal of emotional support, after the sudden death of my mum, during the critical writing stage. Without them I doubt this work would be here.

*An Investigation of Aluminium Intermetallic Phases using  $^{57}\text{Fe}$  Mössbauer Spectroscopy and Complementary Techniques*

A. J. Reeder

**A thesis submitted in partial fulfilment of the requirements of Sheffield Hallam University for the degree of Doctor of Philosophy.**

Pure intermetallic compounds  $\text{Al}_3\text{Fe}$ ,  $\text{Al}_m\text{Fe}$ ,  $\text{Al}_x\text{Fe}$ ,  $\alpha_c\text{-AlFeSi}$ , and  $\text{Al}_6(\text{Fe},\text{Mn})$  have been extracted from Bridgman grown model aluminium alloys by dissolving the aluminium matrix in butanol. The resultant transmission Mössbauer spectra for each intermetallic compound were interpreted according to their crystal structure. Variable temperature  $^{57}\text{Fe}$  Mössbauer studies have enabled the Debye temperature  $\theta_D$  of each compound to be determined.

The crystal structure of  $\text{Al}_3\text{Fe}$  contains five different Fe sites within the unit cell. Four of the iron, Fe(1)-Fe(4), sites are approximately identical and produced a  $\theta_D = 434 \pm 5$  K. The remaining Fe site, Fe(5), produced a  $\theta_D = 488 \pm 5$  K, and the combined spectral areas a  $\theta_D = 452 \pm 5$  K. There is only one individual site within the crystal structures of  $\text{Al}_m\text{Fe}$ ,  $\text{Al}_x\text{Fe}$ , and  $\text{Al}_6(\text{Fe},\text{Mn})$ , which produced a  $\theta_D$  of  $358 \pm 5$  K,  $360 \pm 5$  K, and  $352 \pm 5$  K respectively. The ternary intermetallic compound,  $\alpha_c\text{-AlFeSi}$ , has two different Fe sites within the unit cell. Fe(1) had a  $\theta_D = 297 \pm 5$  K, and Fe(2)  $\theta_D = 329 \pm 5$  K. The combined spectral areas of these two sites produced a  $\theta_D = 311 \pm 5$  K. The variation in the  $\theta_D$  values was attributed to changes in the Al-Fe shortest bond within the Fe centred Al polyhedra. The Fe centred Al polyhedra are a common feature of all the intermetallic compounds studied. The iron atom in all the intermetallic compounds may have existed in a  $\text{Fe}^{2+}$  oxidation state.

A Direct Chill-cast ingot was grown and two samples, *A* and *B*, were taken from regions within the ingot containing a mixture of two intermetallic compounds. Alloy sample *A* was found to contain the intermetallic compound combination  $\text{Al}_3\text{Fe} + \text{Al}_6\text{Fe}$ . The intermetallic combination  $\text{Al}_6\text{Fe} + \alpha_c\text{-AlFeSi}$  was found to exist in alloy sample *B*. Transmission Mössbauer spectroscopy was performed on the extracted phases and the insitu phases to determine the relative proportions of the intermetallic compounds within the two alloy samples. Alloy sample *A* had  $50:50 \pm 5$  %  $\text{Al}_3\text{Fe} + \text{Al}_6\text{Fe}$ , whereas alloy sample *B* had  $30:70 \pm 5$  %  $\text{Al}_6\text{Fe} + \alpha_c\text{-AlFeSi}$ .

The surface of alloy sample *B* was investigated using several surface techniques, CEMS, SAAES, and SAXPS, to determine whether the same relative proportions existed in the surface, and near surface, regions of the sample. A region of very fine amorphous iron super-paramagnetic grains were to dominate the near surface region of the sample, which was present due to selective oxidation of the  $\text{Al}_6\text{Fe}$  intermetallic compound. This was then removed when the surface of the alloy sample was KI electro-etched, which had the effect of leaving the intermetallic particles standing proud of the surface. The CEMS technique identified that the  $\text{Al}_6\text{Fe} + \alpha_c\text{-AlFeSi}$  existed in a  $80:20 \pm 5$  %. This change in phase ratio after the KI electro-etch process was attributed to the preferential etching of the  $\alpha_c\text{-AlFeSi}$  aluminium intermetallic compound.

## **CONTENTS**

1. INTRODUCTION	1
1.1 DEFINITION OF A LIGHT METAL	1
1.2 PRODUCTION OF ALUMINIUM AND ALUMINIUM ALLOYS	3
1.2.1 THE CASTING OF ALUMINIUM ALLOYS	6
1.2.1.1 FORMATION OF INTERMETALLIC COMPOUNDS DURING DC-CASTING	8
1.3 ALUMINIUM-IRON SYSTEM	17
1.3.1 Al <sub>3</sub> Fe	18
1.3.2 THE METASTABLE STATE	22
1.3.2.1 Al <sub>m</sub> Fe	27
1.3.2.2 Al <sub>6</sub> Fe	29
1.3.2.3 Al <sub>x</sub> Fe	30
1.4 ALUMINIUM-IRON-SILICON SYSTEM	32
1.4.1 α <sub>H</sub> -AlFeSi	34
1.4.2 α <sub>c</sub> -AlFeSi	39
1.5 MÖSSBAUER STUDIES AND INTERPRETATION	42
1.5.1 EARLY MÖSSBAUER STUDIES	42
1.5.2 Al <sub>3</sub> Fe	43
1.5.3 Al <sub>6</sub> Fe	46
1.5.3.1 THE PHASE TRANSITION Al <sub>6</sub> Fe → Al <sub>3</sub> Fe	48
1.5.4 Al <sub>m</sub> Fe	49
1.5.5 Al <sub>x</sub> Fe	50
1.5.6 α <sub>H</sub> -AlFeSi	51
1.5.7 α <sub>c</sub> -AlFeSi	54
1.5.7.1 TERNARY PHASE TRANSITIONS	55
REFERENCES	57

---

2. MÖSSBAUER SPECTROSCOPY	62
---------------------------	----

2.1 INTRODUCTION	62
2.2 THEORY OF THE MÖSSBAUER EFFECT	65
2.2.1 THEORETICAL LINEWIDTH OF THE EMITTED 14.4 keV $\gamma$ -RAY	69
2.2.2 RECOIL-FREE NUCLEAR RESONANCE ABSORPTION	71
2.3 EXPERIMENTAL	76
2.3.1 MÖSSBAUER $\gamma$ -RAY SOURCE	76
2.3.2 TRANSMISSION MÖSSBAUER ABSORBER PREPARATION	78
2.3.3 INSTRUMENTATION USED FOR MÖSSBAUER SPECTROSCOPY	80
2.3.3.1 TRANSMISSION MÖSSBAUER SPECTROSCOPY	82
2.3.3.2 TRANSMISSION MÖSSBAUER SPECTROMETER OPERATION	82
2.3.3.3 $\gamma$ - RAY DETECTION	84
2.3.3.4 THE CRYOGENICS SYSTEMS	87
2.3.3.4.1 THE HELIUM GAS ‘DISPLEX’ CRYOGENIC SYSTEM	87
2.3.3.4.2 THE LIQUID NITROGEN CRYOGENIC SYSTEM	90
2.3.3.5 BACKSCATTER MÖSSBAUER SPECTROSCOPY	91
2.3.3.5.1 CEMS MÖSSBAUER SPECTROMETER OPERATION	92
2.3.3.5.2 ELECTRON DETECTION	94
2.4 EXPERIMENTAL OBSERVATION OF THE MÖSSBAUER EFFECT	96
2.4.1 HYPERFINE INTERACTIONS	97
2.4.1.1 ISOMER SHIFT	98
2.4.1.2 NUCLEAR QUADRUPOLE INTERACTION	101
2.4.1.3 MAGNETIC HYPERFINE INTERACTION	106
2.5 MÖSSBAUER DATA ANALYSIS	110
2.5.1 SPECTROMETER CALIBRATION	110
2.5.2 COMPUTER FITTING	112
2.5.3 ANALYSIS OF VARIABLE TEMPERATURE DATA	113
2.5.3.1 TEMPERATURE DEPENDENCE OF THE ABSORPTION AREA, LNAT	114
2.5.3.2 TEMPERATURE DEPENDENCE OF THE ISOMER SHIFT, ISODS	117
2.6 OTHER TECHNIQUES	121
2.6.1 SCANNING ELECTRON MICROSCOPE	121
2.6.2 X-RAY DIFFRACTION	122

2.6.3 SURFACE ANALYSIS, SAAES AND SAXPS	122
REFERENCES	124
<hr/>	
3. THE PROJECT	126
3.1 BRIDGMAN FURNACE SAMPLES	126
3.2 DC-CAST SAMPLES	127
REFERENCES	128
<hr/>	
4 VARIABLE TEMPERATURE MÖSSBAUER SPECTROSCOPY	129
4.1 ALLOY PREPARATION	129
4.1.1 THE BRIDGMAN FURNACE	129
4.1.2 BUTANOL EXTRACTION	131
4.1.3 MÖSSBAUER ABSORBER PREPARATION	132
4.1.4 Al <sub>3</sub> Fe	133
4.1.4.1 THE Al <sub>3</sub> Fe SPECTRUM	138
4.1.4.1.1 DEBYE TEMPERATURE ANALYSIS	140
4.1.4.1.2 RESIDUAL ASYMMETRY WITHIN THE SPECTRUM	143
4.1.4.1.3 OXIDATION STATE	148
4.1.4.1.4 STUPEL CALCULATION	149
4.1.5 Al <sub>x</sub> Fe	151
4.1.5.1 THE Al <sub>x</sub> Fe SPECTRUM	155
4.1.5.1.1 OXIDATION STATE	157
4.1.5.1.2 ASYMMETRY WITHIN THE SPECTRUM	157
4.1.6 Al <sub>m</sub> Fe	158
4.1.6.1 THE Al <sub>m</sub> Fe SPECTRUM	162
4.1.6.1.1 OXIDATION STATE	163
4.1.7 α <sub>c</sub> -AlFeSi	164
4.1.7.1 THE α <sub>c</sub> -AlFeSi SPECTRUM	169

4.1.7.1.1 DEBYE TEMPERATURE ANALYSIS	171
4.1.7.1.2 STUPEL CALCULATION	172
4.1.7.1.3 OXIDATION STATE	174
4.1.8 Al <sub>6</sub> (Fe,Mn)	175
4.1.8.1 THE Al <sub>6</sub> (Fe,Mn) SPECTRUM	179
4.1.8.1.1 OXIDATION STATE	182
4.1.9 CONCLUSIONS	183
4.1.10 FUTURE WORK	187
REFERENCES	189

---

5 DC-CAST INGOT SAMPLES	192
5.1 ALLOY PREPARATION	192
5.1.1 PROCEDURE FOR THE DE-CONVOLUTION OF THE MÖSSBAUER SPECTRA FOR SAMPLE <i>A</i> AND <i>B</i>	192
5.1.2 SAMPLE <i>A</i>	193
5.1.3 SAMPLE <i>B</i>	199
5.1.4 RELATIVE PROPORTION OF THE INTERMETALLIC COMPOUNDS WITHIN SAMPLE <i>A</i> AND <i>B</i>	205
5.2 INITIAL SURFACE STUDIES APPLIED TO ALLOY SAMPLE <i>B</i> (CEMS, SEM, EDS)	209
5.2.1 THE APPLICATION OF CEMS TO THE Al-Fe SYSTEM	209
5.2.1.1 Fe/Al MULTI-LAYERS	209
5.2.1.2 ION IMPLANTATION STUDIES	210
5.2.2 CEMS STUDY OF ALLOY SAMPLE <i>B</i>	213
5.2.2.1 ANALYSIS OF THE CEMS SPECTRA OF ALLOY SAMPLE <i>B</i>	218
5.3 SAXPS AND SAAES	225
5.3.1 FUNDAMENTALS OF THE AUGER PROCESS	225
5.3.1.1 THE AUGER TRANSITIONS	226
5.3.1.1.1 j-j COUPLING	227
5.3.1.1.2 L-S COUPLING	228
5.3.1.1.3 INTERMEDIATE COUPLING	229

5.3.1.2 DEPTH RESOLUTION OF THE AES PROCESS	230
5.3.2 FUNDAMENTALS OF THE X-RAY PHOTOELECTRON SPECTROSCOPY	232
5.3.2.1 DEPTH RESOLUTION OF THE XPS PROCESS	233
5.3.3 SAAES AND SAXPS SPECTRA	235
5.3.3.1 INTERPRETATION OF THE SAAES AND SAXPS SPECTRA FROM THE UNETCHED SURFACE	239
5.3.3.2 INTERPRETATION OF THE SAAES AND SAXPS SPECTRA FROM THE KI ELECTRO-ETCHED SURFACE	241
5.4 CONCLUSIONS	243
5.5 FUTURE WORK	249
REFERENCES	250

---

6 GENERAL CONCLUSIONS	252
-----------------------	-----

---

7 POSTGRADUATE STUDY	258
7.1 COURSES AND CONFERENCES	258
7.2 PUBLICATIONS	259

---

LIST OF ABBREVIATIONS	vi
-----------------------	----

## CHAPTER 1

### INTRODUCTION

The introduction is divided into two parts. The first part is concerned with the general properties of aluminium, and its production from the ore bauxite to the DC casting of commercial alloys. The second part covers the main issues of this thesis, which are: where the common aluminium intermetallic compounds are formed within the aluminium matrix, their crystallographic structure, and finally the Mössbauer interpretation of known aluminium intermetallic compounds.

#### 1.1 DEFINITION OF A LIGHT METAL

Metals are often divided according to their specific weights into two main classes: the heavy metals and light metals. The dividing line between heavy and light metals is not laid down by any law, but is fixed arbitrarily. However, a specific weight of 3.8 constitutes a suitable dividing line between light and heavy metals, since the specific gravities of all commercial alloys, which can claim to be considered a light metal, lie below this limit.

The term light metal has been traditionally given to both aluminium and magnesium, because they are frequently used to reduce the weight of components and structures. On this basis titanium also qualifies and beryllium should be included, although it is little used in the construction of engineering components. These four metals have a specific gravity ranging from 1.7 to 4.5 which compares with 7.9 and 8.9 for the older structural metals, iron and copper, and 22.6 for osmium, the heaviest of all metals. The other elements in Table 1.1 are lighter than titanium but, with the exception of boron, in the form of strong fibres contained in a suitable matrix, none is used as a base material for engineering purposes. The reason being that all of the other elements are either alkali or alkaline metals, and are far too reactive to even be considered for any engineering purpose.

The property of lightness has led to the association of the light metals with the transportation and, more especially, with the aerospace industries which has provided a

great stimulus to the development of alloys during the last 50 years. Strength to weight ratios has thus been a dominant consideration, and these are particularly important in engineering design when parameters such as stiffness of resistance to buckling are involved. Concerns with the aspects of weight saving should not obscure the fact that light metals possess other properties of considerable technological importance. Typically the high corrosion resistance and high electrical and thermal conductivities of aluminium, the machinability of magnesium, and the extreme corrosion resistance of titanium [2].

Element	Atomic weight	Specific gravity in the solid state
Li	6.94	0.53
K	39.10	0.86
Na	23.00	0.97
Rb	85.48	1.52
Ca	40.08	1.55
Mg	24.32	1.75
Be	9.02	1.85
Cs	132.91	1.87
Sr	87.63	2.60
Al	26.97	2.70
Ti	47.88	4.51

Table 1.1 Compilation of the light metallic elements arranged in order of their specific gravities [1].

However, this study is concerned with aluminium as it is used in five major areas in most countries: building and construction, containers and packing, transportation, electrical conductors, machinery and equipment. The consumption pattern for aluminium varies widely from country to country, depending upon the level of industrialisation and economic growth. There is more attention being given to the recycling of materials and the incentive for this is particularly strong in the case of

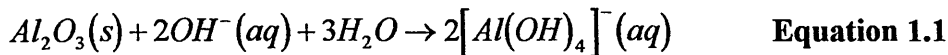
aluminium. This is due to the remitting of the scrap requires only 5% of the energy needed to produce the same weight of primary aluminium from the ore bauxite [3].

## 1.2 PRODUCTION OF ALUMINIUM AND ALUMINIUM ALLOYS

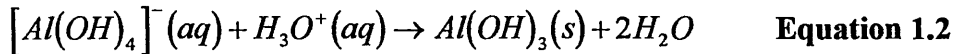
As is often the case, the potential military application of this new metal was seized upon by Napoleon the Third, as he foresaw its use in lightweight body armour for his guards. The first commercial preparation of aluminium occurred in France in 1855 when H. Sainte-Claire Deville reduced aluminium chloride with sodium. During the period 1855-59, the price of aluminium per kilogram fell from \$200 to \$30, and when the aluminium cap was placed upon the top of the Washington Monument in 1884 it was still classed a semiprecious metal. This all changed in 1886, as two independent discoveries by Charles Martin Hall in the United States and Paul Heroult in France led to the development of an economically feasible method for the production of aluminium by electrolysis.

Aluminium is obtained from bauxite, which is the collective name given to ores usually containing 40-60% hydrated alumina together with the main impurities  $\text{Fe}_2\text{O}_3$ ,  $\text{SiO}_2$ , and  $\text{TiO}_2$ . The name bauxite originates from the Les Baux, the district in Provence, France where the ore was first mined. Bauxite is formed by surface weathering of aluminium bearing rocks such as granite and basalt under tropical conditions, and the largest reserves are found in Australia, Guyana, and Brazil. However, immense amounts of aluminium are also present in clays, shales, and other minerals but it is difficult and uneconomic to extract the metal from these resources.

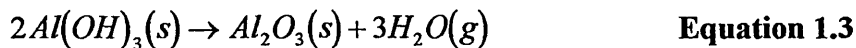
Production of aluminium from bauxite involves two distinct processes that are often operated at quite different locations. The first process is the extraction of alumina,  $\text{Al}_2\text{O}_3$ , from bauxite, which is almost exclusively achieved by the Bayer process [4]. This essentially involves the digesting of bauxite with strong caustic soda solution, see Equation 1.1. Most of the alumina is extracted leaving a residue known as ‘red mud’, consisting mainly of  $\text{Fe}_2\text{O}_3$ ,  $\text{SiO}_2$ , and  $\text{TiO}_2$ , which is removed by filtration.



The solution is then diluted with water, and alumina trihydrate is formed, see Equation 1.2:



The final process to form alumina involves the heating of alumina trihydrate at 240°C, see Equation 1.3:



Alumina has a high melting point, 2040°C [5], and is a poor conductor of electricity. The key to the successful production of aluminium lies in dissolving the alumina in molten cryolite,  $Na_2AlF_6$ , and a typical electrolyte contains 80-90% of this compound and 2-8% alumina together with additives such as aluminium and calcium fluorides. cryolite was first obtained from relatively inaccessible sources such as Greenland, but it is now made synthetically.

Figure 1.1 depicts a schematic cross section from a multi-anode aluminium production cell. The outer casing consists of a brick-lined, rectangular steel box which contains baked carbon, or graphite blocks, that serves both as the cathode and to collect the molten aluminium. The anodes are made from pre-baked carbon blocks that dip into the electrolyte, and they are gradually consumed in the reaction. The baths operate at temperatures around 950°C, and are arranged in series in so called "potlines". The current loading across these baths are typically 258 000 A, with a voltage drop of approximately 5 V across each cell. The aluminium produced is typically 99.6% to 99.8% pure and is extracted by tapping, or syphoning, from the base of the cell at regular intervals, and alumina is added as and when required.

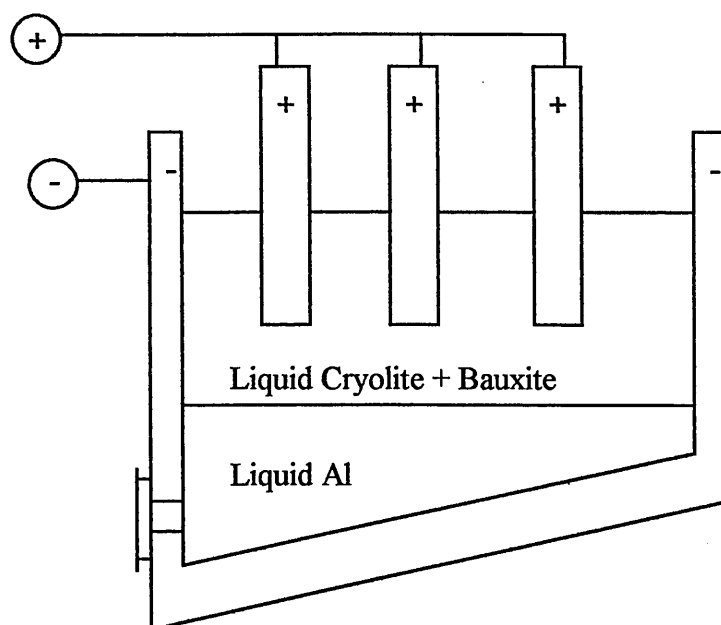
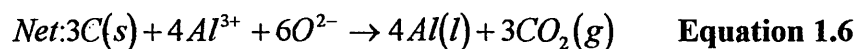
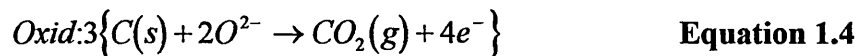


Figure 1.1 Schematic cross section from a multi-anode aluminium production cell.

The exact mechanism for the electrolyte reaction in the cell is uncertain, but it is probable that the current carrying ions are:  $\text{Na}^+$ ,  $\text{AlF}_4^-$ ,  $\text{AlF}_6^{3-}$ , and one or more complex ions such as  $\text{AlOF}_3^{2-}$ . At the cathode it is probable that the aluminium fluoride ions are discharged to produce aluminium metal and  $\text{F}^-$  ions while, at the anode, the complex ions dissociate to liberate oxygen which forms  $\text{CO}_2$ . The summary of the reactions that occur within the cell are shown below in Equation 1.4-1.6:



### 1.2.1 THE CASTING OF ALUMINIUM ALLOYS

The most common industrial method for producing aluminium ingots is the Direct Chill (DC) casting process, as it promotes a uniform ingot structure. Most commonly, the vertical process in which the molten alloy is poured into one or more fixed water cooled moulds having retractable bases casts ingots. The actual solidification process can be summarised as follows:

The outer skin solidifies in direct contact with the water cooled mould. Solidification shrinkage causes loss of thermal contact between the mould and the solidified material, with an accompanying decrease in solidification rate. Secondary cooling becomes effective a few millimetres below the mould, causing a rapid increase in solidification rate. Due to an increasing path length for heat transport, there is a gradual lowering of the solidification rate towards the ingot centre [6].

A problem with the with DC casing process is that the surfaces of the ingots tend to be rippled in contour, and this is due to "stick-slip" contact as they move past the sides of the mould when solidification occurs. Microstructure inhomogeneties, such as inverse segregation, tend to occur in the surface regions, and these may cause edge cracking during rolling. For both of these reasons, it is necessary to machine or scalp the surfaces of DC ingots prior to rolling, or extrusion, which adds cost to the overall operation.

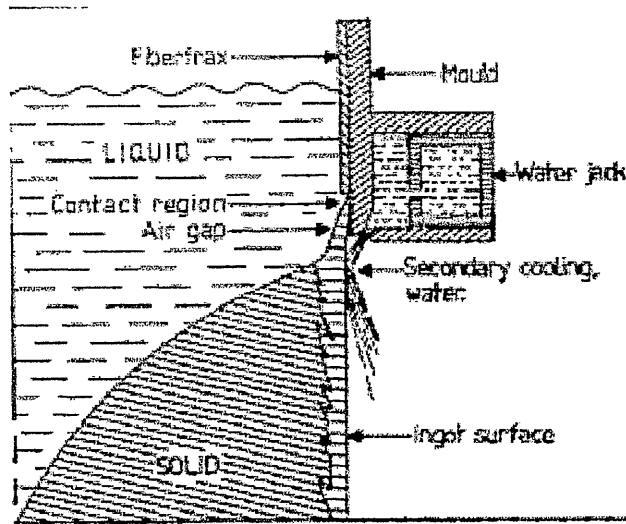


Fig 1.2 Cross section of a DC casting process

Note: The author apologises for the clarity of the image. This was due to the poor quality of the original image [6].

The aluminium and aluminium alloys that are produced are classified in the following manner:

Aluminium (99.0% min. and greater)		- 1xxx
Aluminium alloy groups (by major alloying element)	Cu	- 2xxx
	Mn	- 3xxx
	Si	- 4xxx
	Mg	- 5xxx
	Mg+Si	- 6xxx
	Zn	- 7xxx
	Other elements	- 8xxx
	Unused elements	- 9xxx

In the first group, aluminium containing more than 99.0% Al, the last two digits are the same as the two digits to the right of the decimal point in the “minimum % aluminium”,

when expressed to the nearest 0.01%. The second digit in the designation indicates modifications in impurity limits, or alloying elements. When the second digit is zero it indicates unalloyed aluminium having natural impurity limits. In the groups 2xxx to 8xxx the last two digits in the designation have no special significance, and are only used to identify different alloys in the group. The second digit indicates modifications to the alloy, and thus if the digit is zero it indicates the original alloy.

### 1.2.1.1 FORMATION OF INTERMETALLIC COMPOUNDS DURING DC-CASTING

Commercial purity Aluminium and aluminium based alloys usually contain a certain amount of Fe and Si. These elements are present either as unwanted impurities, or they are added deliberately to provide special material properties. The way that the Fe and Si is distributed in the as cast material depends strongly upon the solidification rate during casting. An extreme example is provided by splat quenching and related techniques, which allow solid solutions to be formed even when the Fe content is several wt. % [5].

Process	Solidification rate, °C s <sup>-1</sup>
Hunter engineering	200-700
Pressure die casting	20-80
DC casting	0.5-20
Book mould casting	≈0.1
Shell mould casting	≈0.01

Table 1.3 Solidification rates for several industrial processes [7].

However, the present commercial techniques produce materials where the major part of the Fe, and to a certain degree Si, are present as intermetallic compounds formed on

the grain boundaries and between the dendrite arms. Nevertheless, taking into consideration that the solidification rates in industrial casting processes varies by 5 to 6 orders of magnitude (Table 1.3), it is not unexpected that large microstructural differences are observed depending upon the casting method used.

When a pure metal solidifies crystal begins to form independently from a nucleus, or centre of crystallisation. The nucleus will be a simple unit of the appropriate crystal lattice, and from this the crystal will grow. The crystal develops by the addition of atoms according to the lattice pattern it will follow, and rapidly begins to assume in visible proportions, what is termed as a dendrite. These forms of crystal skeleton act like a backbone, and from which secondary and tertiary arms begin to sprout in a rigid geometrical pattern. There are several theoretical models that exist to predict the primary dendrite spacing in a steady state unidirectional solidified alloy [8-13], which can be defined by:

$$\lambda_1 G^{1/2} V^{1/4} = K_1 \quad \text{Equation 1.7}$$

where  $\lambda_1$  = is the primary dendrite spacing,  
 $K_1$  = is a function of a the alloy concentration,  
 $G$  = is the thermal gradient across the alloy,  
 $V$  = is the growth velocity of the alloy.

The dendrite arms continue to grow and thicken at the same time, until ultimately the space between them will become filled with solid. Meanwhile the outer arms begin to make contact with those of dendrites that have been developing independently at the same time. All these neighbouring crystals will be orientated differently, due to their independent formation. When contact has taken place between the outer arms of neighbouring crystals further growth outwards is impossible, and solidification will be complete when the remaining liquid is used up in thickening the existing dendrite arms.

If the metal is pure then no evidence of dendrite growth will be seen once solidification is complete, since all the atoms are identical. However, commercial purity Al and Al-based alloys contain Fe and Si as the main impurities, or they can be added deliberately to provide special material properties. These impurities are present in the final part of the liquid to solidify, due to their low solid solubility in aluminium, see Table 1.4.

Element	Solid Solubility	
	wt %	at %
Fe	0.052	0.025
Si	1.65	1.59
Mn	1.82	0.90
Cu	5.65	2.48
V	0.6	0.32
Cr	0.77	0.40

Table 1.4 Solid solubility of some elements in Al [14].

The rate at which a molten metal is cooling when it reaches its freezing point affects the size of the grains that form. A slow fall in temperature, which leads to a small degree of undercooling at the onset of solidification, promotes the formation of relatively few nucleation points, and the resultant grains will be large. Rapid cooling, on the other hand, leads to a high degree of undercooling being attained, and the onset of solidification results in a large number of smaller grains.

In a large industrially cast ingot the grain size may vary considerably from the outside surface to the centre. This is due to the variation that exists in the temperature gradient as the ingot solidifies. When the metal first makes contact with the mould the chilling effect results in the formation of small grains in the surface region. As the mould absorbs the heat and equilibrium is achieved, the chilling effect is reduced. That implies that the formation of nucleation points will be retarded as solidification proceeds, and

thus the grains towards the centre of the ingot will be larger [6a]. This variation of grain size, and thus the variation in secondary dendrite spacing, with the solidification rate across the ingot was investigated by Westengen [6], and an expression was evaluated for an alloy containing 0.30 wt% Fe and 0.11 wt% Si:

$$v = 3.57 \times 10^4 \cdot d^{-2.56} \quad \text{Equation 1.8}$$

where  $v$  = solidification rate

$d$  = secondary dendrite spacing

A further effect of the relatively rapid solidification rates observed in DC casting is a change in the types of intermetallic particles found. Some of these changes can be explained based upon the phase diagram. However, this method is limited by the fact that metastable phases can occur as a result of the high solidification rates [7,15]. The solidification rate varies substantially across the thickness of an industrially processed ingot, and thus the distribution of the different types of intermetallic phases will vary. In the early 1950s Altenpohl [16,17] observed some peculiar patterns on ingot cross sections, which were treated in a ferrous chloride etching reagent. The interior of the ingots showed different etching characteristics compared with the outer part. It was also noted that these zones reacted differently towards sulphuric acid anodising. The internal zone was termed “fir-tree”, due to its appearance. It has been suggested that the differences in etching characteristics are caused by different types of intermetallic compound [18].

In a study by Westengen [6] a commercial purity aluminium ingot was cast at 100 mm min.<sup>-1</sup>, with a chemical composition corresponding to a AA1050 alloy, Al-0.25 wt% Fe 0.13 wt % Si, by the level pour method [19], and was grain refined using AlTi5B1. Thin foils were prepared from the ingot using material taken from 15 and 50 mm from the surface, and these were representative for the structure outside and inside the “fir-tree” zone respectively. The foils were examined using selected area electron

diffraction and energy dispersive X-ray analysis. A summary of the observed phases is given in Table 1.5.

However, the distribution of the phases varied according to what region was examined. In the outer zone  $\alpha_T$  and  $Al_mFe$  dominates, with a trace level of  $\alpha_C$ , and in the inner zone  $Al_6Fe$  and  $Al_xFe$  dominates, with trace levels of Si,  $\beta_M$ , and  $Al_3Fe$ .

The following solidification sequence would be expected, which can be used to predict the formation of intermetallic compounds during rapid solidification. This sequence takes into account the alloys tendency for microsegregation [6]:

1. As the temperature of the liquid is lowered below the liquidus, Al with some Fe and Si in solid solutions forms, with an accompanying enrichment of the melt until the eutectic valley  $liq \rightarrow Al + Al_3Fe$  is reached.
2. The above reaction is suppressed by the rapid solidification and the liquid composition follows the eutectic valley until it reaches the peritectic point  $liq + Al_3Fe \rightarrow Al + \alpha_C$ .
3. At sufficiently high solidification rate the composition of the remaining liquid reaches a second  $liq + \alpha_C \rightarrow Al + \beta$ .
4. Eventually the ternary eutectic Al- $\beta$ -Si could be formed.

Phase	Structure	Lattice Parameters nm	Main Elements	Ref.
Al	fcc	a = 0.404	Al	[5]
$\alpha_C$	bcc	a = 1.256	Al,Fe,Si	[20]
$\alpha_H$	hexagonal	a = 1.23 c = 3.70	Al,Fe,Si	[21]
$\alpha_T$	tetragonal	a = 1.23 c = 3.70	Al,Fe,Si	[6]
$Al_3Fe$	monoclinic	a = 1.549 $\forall \beta = 107^\circ$ b = 0.808 c = 1.247	Al,Fe	[22]
$Al_6Fe$	orthorhombic, c-centred	a = 0.649 b = 0.744 c = 0.879	Al,Fe	[23]
$Al_mFe$	tetragonal, body centred	a = 0.884 c = 2.16	Al,Fe	[7]
$Al_xFe$	unknown	defect structure	Al,Fe	[6]
$\beta_M$	monoclinic	a = 0.89 $\forall \beta = 92^\circ$ b = 0.49 c = 4.16	Al,Fe,Si	[6]
Si	fcc	a = 0.542	Si	[5]

Table 1.5 Summary of observed phases by Westengen [6].

However, this pattern is not followed due to the introduction of metastable phases nucleated by rapid solidification. Various authors [7, 15, 24, 25] have studied this, and they reported that the various binary Al-Fe compounds form in the following solidification regimes:

The investigated samples from this study were taken from regions 15 mm from the surface with an estimated solidification rate of  $10^{\circ}\text{C s}^{-1}$ , and 50 mm from the surface, with a solidification rate approximately  $5^{\circ}\text{C s}^{-1}$ . That compared well with the phase distribution found within the foils, and the published information.

High temperature annealing of the foils for 5 hours at  $590^{\circ}\text{C}$  eliminated the presence of the “fir-tree” zones after caustic etching. The main change in the phase distribution was that the dominant metastable phase  $\text{Al}_m\text{Fe}$  in the outer region transformed to  $\text{Al}_3\text{Fe}$ , and the dominant metastable phase  $\text{Al}_6\text{Fe}$  also transformed to  $\text{Al}_3\text{Fe}$ . It implies that the different etching characteristics displayed across the ingot were attributed to the presence of  $\text{Al}_m\text{Fe}$  and  $\text{Al}_6\text{Fe}$ .

Intermetallic	Solidification rate, $^{\circ}\text{C s}^{-1}$	Ref.
$\text{Al}_m\text{Fe} / \text{Al}_9\text{Fe}_2$	$> 10$	[7, 15, 24, 25]
$\text{Al}_6\text{Fe}$	1 - 10	[7, 15, 24]
$\text{Al}_x\text{Fe}$	0.5 - 5	[25]
$\text{Al}_3\text{Fe}$	$< 1$	[7, 15, 24, 25]

Table 1.6 Solidification regimes to form different intermetallic compounds.

A separate study was performed by Per Skjerpe [26] on another commercial purity aluminium DC-cast ingot, having a chemical composition corresponding to an AA1050 alloy. This investigation involved taking sample foils from 10 mm, 50 mm, and 100 mm from the surface of the ingot, and selected area electron diffraction being performed. The phase distribution at 10 and 50 mm was nearly identical, and corresponded to a solidification rate of 6 to  $8^{\circ}\text{C s}^{-1}$ . The dominating phases in these regions were  $\alpha_{\text{C}}$  and  $\text{Al}_m\text{Fe}$ . The phase distributions at 100 mm from the ingot surface, which corresponded to a solidification rate of  $1^{\circ}\text{C s}^{-1}$ , the dominating phase was  $\text{Al}_3\text{Fe}$ . These results were consistent with those observed by Westengen [6].

Ping Liu *et al* [27] also performed an investigation on three DC-cast Al-Fe-Si alloys, with an emphasis being placed upon the role of solidification rate, iron content, and alloy purity (presence of trace elements) in determining which aluminium intermetallic phases appear in as-cast structures. Two alloys had an Fe content of  $\approx 0.25$  wt % and  $\approx 0.50$  wt %, and an Si content of  $\approx 0.125$  wt %, giving an Fe/Si weight ratios of 2 and 4, and they were prepared from commercially pure aluminium. The main trace elements present were Mn, V, Zn, Ca, and Cu. The third alloy was prepared from high purity aluminium 99.99 wt % Al, and 0.25 wt % Fe - 0.125 wt % Si were added to the melt. The alloys were cast, and sample foils were taken from positions within the ingot corresponding to a solidification rate of approximately  $10^\circ\text{C s}^{-1}$  and  $1^\circ\text{C s}^{-1}$ .

The usual aluminium intermetallics were found in the sample foils by selected area electron diffraction:  $\text{Al}_3\text{Fe}$ ,  $\alpha_{\text{C}}\text{-AlFeSi}$ ,  $\text{Al}_6\text{Fe}$  and  $\text{Al}_m\text{Fe}$ . These were consistent with the results by both Westengen [6] Per Skjerpe [26]. However, three additional phases were also discovered, and are summarised in Table 1.7.

The intermetallic phase observed in the alloy containing a Fe/Si ratio = 4, at the slower solidification rate, was  $\text{Al}_3\text{Fe}$ . At the higher solidification rate six different intermetallic phases were observed, but predominantly  $\text{Al}_3\text{Fe}$  and  $\text{Al}_p\text{Fe}$  were discovered on the grain boundaries. The remaining phases were only present as isolated precipitates, in small volume fractions. After annealing both the samples at  $600^\circ\text{C}$  for 24 hours the only remaining phase was  $\text{Al}_3\text{Fe}$ .

The only intermetallic phase present at the slower solidification rate for the alloy with a Fe/Si ratio = 2 was  $\text{Al}_3\text{Fe}$ . However, at the higher solidification rate the dominating intermetallic phases were  $\alpha_{\text{C}}\text{-AlFeSi}$  and  $q_1\text{-AlFeSi}$ . After annealing at  $600^\circ\text{C}$  for 24 hours the  $q_1\text{-AlFeSi}$  phase transformed into the  $q_2\text{-AlFeSi}$  phase, whereas the presence of the  $\alpha_{\text{C}}\text{-AlFeSi}$  remained unchanged.

Phase	Structure	Lattice Parameters nm	Main Elements
Al <sub>p</sub> Fe	bcc	a = 1.03	Al, Fe
q <sub>1</sub>	orthorhombic, c-centred	a = 1.27 b = 3.62 c = 1.27	A, Fe, Si
q <sub>2</sub>	monoclinic	a = 1.25 ∠β = 109° b = 1.23 c = 1.93	A, Fe, Si

Table 1.7 Summary of the additional phases discovered Ping Liu *et al* [27].

The high purity alloy, with a Fe/Si ratio = 2, contained only Al<sub>3</sub>Fe at the slower solidification rate, but at the higher solidification rate the dominant intermetallic phase was α<sub>C</sub>-AlFeSi, with low levels of Al<sub>3</sub>Fe and Al<sub>p</sub>Fe. However, after annealing, again at 600°C for 24 hours, the only intermetallic phases present were Al<sub>3</sub>Fe and α<sub>C</sub>-AlFeSi, at the slower and higher solidification rates respectively.

The three new intermetallic phases identified in this study have not been reported in any other work, and appear to be highly unstable intermediate metastable intermetallic phases as they transform readily to more stable variants after annealing. The Fe/Si appears to be an important factor in determining what intermetallic phase forms [7,15,28,29], but it has been suggested that the absolute Si content is far more significant [30]. Also the effect of trace elements have a role in determining what intermetallic phases form, and this could explain the discrepancies in the different types of intermetallic phases found by Westengen [6] and Per Skjerpe [26] compared to Ping Liu *et al* [27].

### 1.3 ALUMINIUM-IRON SYSTEM

It has already been stated that Fe is the dominant impurity in commercial grades of aluminium, as it is often unintentionally added through the use of steel tools for melting and casting. However, in some alloys of aluminium iron is often added intentionally, and amongst the most common is the Al-Cu-Ni group as it increases the high temperature strength. Fe is also added to the Al-Fe-Ni alloys, to increase the corrosion resistance of the material in steam at elevated temperatures, and the most common example of all is household foil, where 1-1.5% Fe is added to the aluminium to increase the strength of the material. These are just three examples where the addition of Fe is of benefit, where there are many.

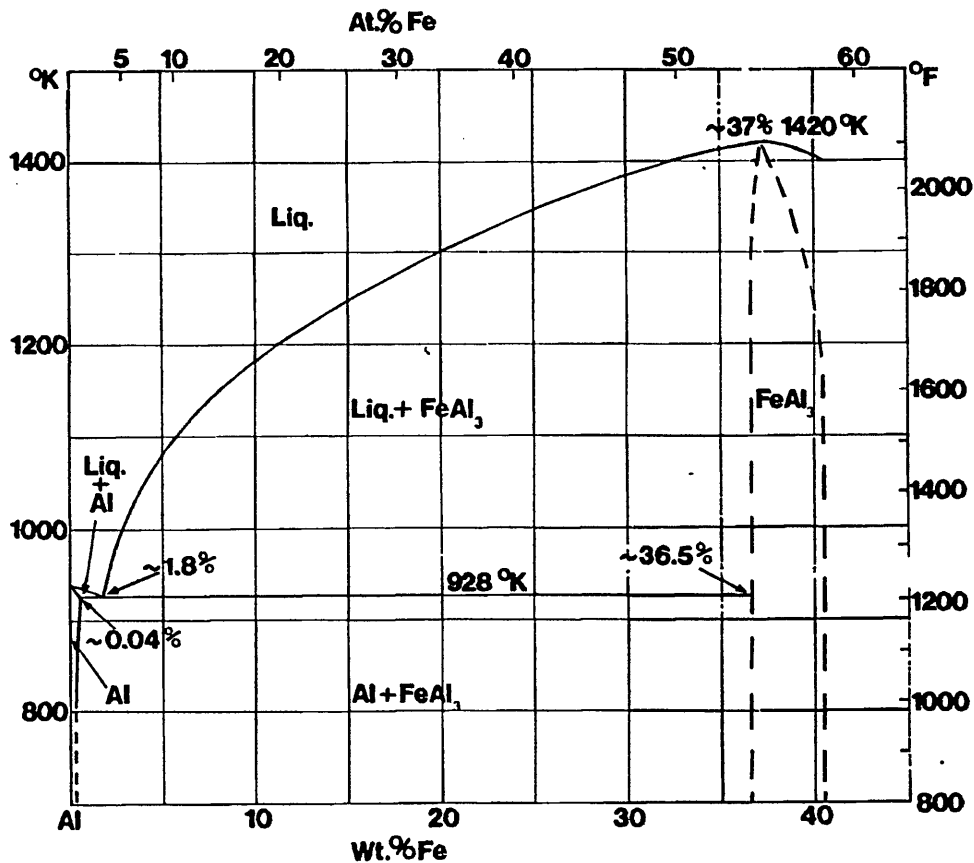


Fig. 1.3 The aluminium end of the aluminium-iron equilibrium phase diagram [5].

In the liquid state aluminium-iron alloys show clustering, which decreases from the melting point up to about 50 K above it. After that the atomic distribution becomes random [31]. There is a eutectic, Al-Al<sub>3</sub>Fe, which is found at the aluminium rich end of the equilibrium phase diagram, see Figure 1.3, at 928 K, with a probable composition within the range 1.7%-2.2% Fe [32]. The uncertainty of the eutectic position results from nucleation difficulties, which favour a divorced eutectic. The equilibrium solid solubility is in the order of 0.03%-0.05% at the eutectic temperature [33, 34, 35], and it decreases to values in the order of 0.00x at 700 K [36,37]. However, by rapidly quenching the liquid supersaturated solid solutions can be produced, containing up to approximately 8% Fe [38, 39], in which the iron atoms are not randomly distributed but clustered [40,41].

### 1.3.1 Al<sub>3</sub>Fe

The phase in equilibrium with aluminium is usually designated Al<sub>3</sub>Fe, or Al<sub>13</sub>Fe<sub>4</sub>, which forms directly from the liquid at 1420 K [42], and not by a reported peritectic reaction [32]. Black [43, 44] first proposed the correct structure of Al<sub>3</sub>Fe, and it was determined to have a monoclinic unit cell, space group C2/m, with 100 atoms per unit cell. The unit cell parameters were found to be:  $a = 15.849\text{\AA}$ ,  $b = 8.0831\text{\AA}$ ,  $c = 12.476\text{\AA}$ , and  $\beta = 107.74^\circ$ . However, previous studies [45, 46, 47], using single crystals, had reported that the unit cell was orthorhombic. This more symmetrical pseudo-symmetry can be attributed to the fact that the compound has a strong tendency to twinning [43].

The actual structure of Al<sub>3</sub>Fe can be described in terms of alternate puckered and flat layers of atoms perpendicular to the b-axis, see Figure 1.4. Both layers can be considered as periodic packing of pentagons. For the flat layer the pentagons have Fe atoms at their vertices, and there are either one (open packed region) or three (close packed region) Al atoms at the centre. Successive flat layers are arranged in such a fashion that the close packed regions of one lie on top the open region of another, with



central Fe atom. Fe site 5 has approximately the same mean distance as the Fe site 2, but it has two other Al neighbours at 3.3 Å and 3.4 Å, and if an allowance is made for the effects of these, it can be said that the mean Al-Fe distance for the 9 Al neighbours is shorter than for the ten Al neighbours.

Fe Site	No. of Al-Fe Bonds	Al-Fe Bond Length, Å
1	10	2.429 - 2.839
2	10	2.422 - 2.713
3	10	2.257 - 2.758
4	10	2.400 - 2.754
5	9	2.306 - 2.644

Table 1.8 Summary of the different types of Fe sites [44]. Site 3 has a Fe-Fe bond length of 2.906Å, and site 4 has a Fe-Fe bond length 3.005Å. The variations in the Al-Fe distances may be explained in terms of stacking effects.

An attempt to determine the electron configuration in Al-rich alloys containing transition metals was undertaken by Black [50]. The conclusion of this study on various alloys was that the geometry of the structures does suggest that there are localised and probably direct bonds between Al and transition metals. Also due to this similarity in Al-Transition Metal bonding there are several iso-structural compounds, for example  $\text{Al}_{13}\text{Co}_4$  [51].

Alternatively, the structure of  $\text{Al}_3\text{Fe}$  can be described as an arrangement of 9 and 10 co-ordinated Al polyhedra, with a Fe atom in the centre, perpendicular to the b axis. The two different types of Fe-centred polyhedra are summarised in Fig 1.5, along with the four different Al-centred polyhedra. The Al-centred polyhedra are not relevant to this study, and are only there for contrast.

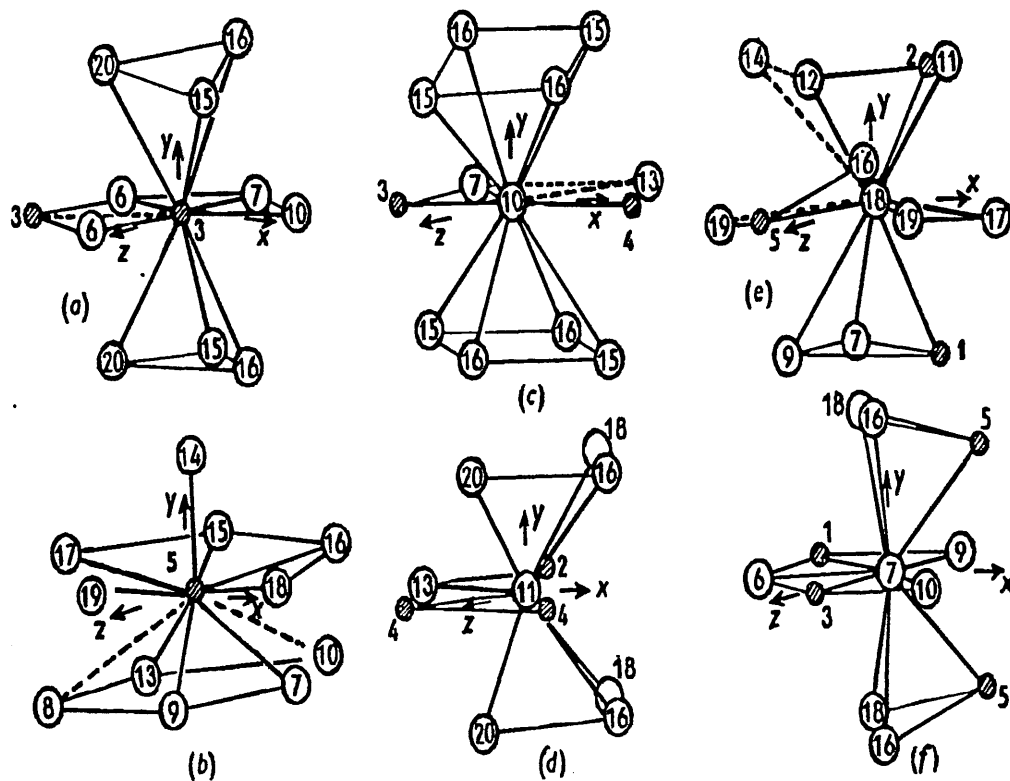


Fig 1.5 Polyhedra co-ordinations for the two different Fe site (a-b), and the Al sites (c-f). Contacts with central atoms are shown by full lines, neighbouring atoms that are not in direct contact are shown by broken lines. Fe atoms are shaded [43,44].

Also an interesting analogy between the atomic distribution in the decagonal Al-Fe quasicrystalline phase [52], and the crystalline  $\text{Al}_3\text{Fe}$  phase was derived by Kumar, see Fig 1.6, [48, 53] and Henley [49]. The stacking layers of the crystalline  $\text{Al}_3\text{Fe}$  phase have a striking similarity to those of a 2-D Penrose Lattice. Thus, the decagonal Al-Fe quasicrystalline phase can also be described as periodic packing of such 2-D Penrose Lattices.

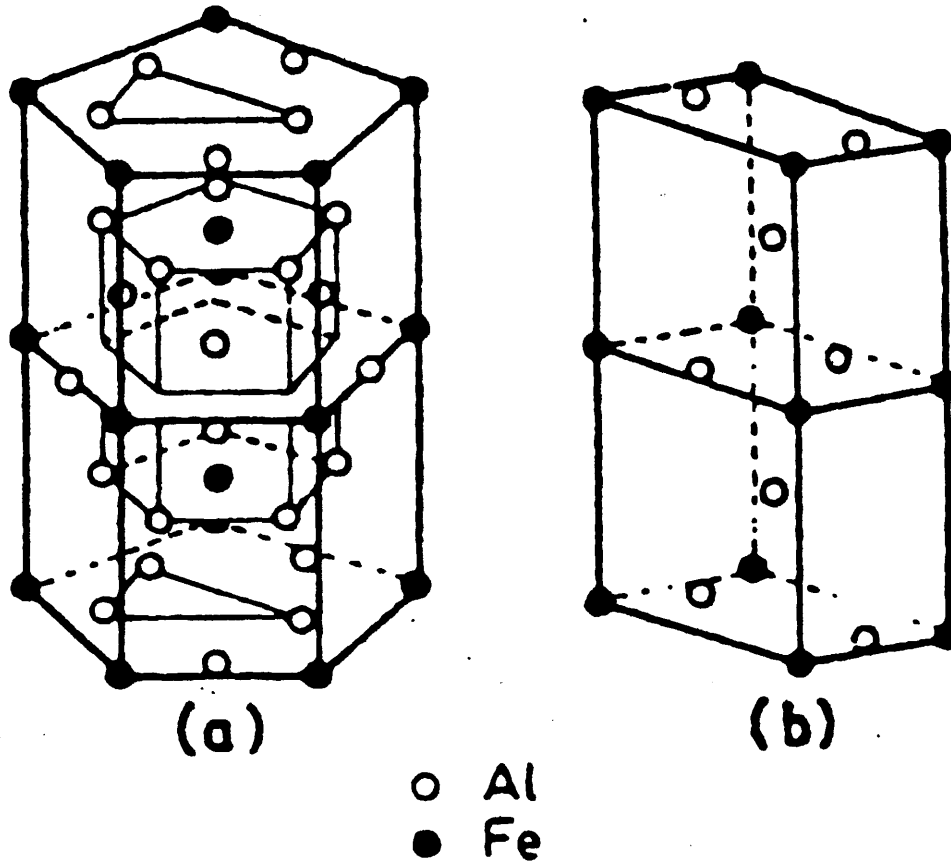


Fig. 1.6 The stacking of pentagonal bipyramids [48].

### 1.3.2 THE METASTABLE STATE

When a system undergoes a phase change the energy differences between the initial and final states can be calculated [54]. However, during the change the structure must go through intermediate stages, though obviously none of them are stable or they would be observable over a finite temperature range. It is important to appreciate that the only stable structures lie at the two end-points of the process. This implies that the structure goes through an activated phase, which has a higher energy than both the low temperature and the high temperature structures. Confirmation of this comes from the fact that in most phase changes the high temperature state can be super-cooled, it can

exist above the transition temperature, and the low temperature phase can similarly exist at temperatures slightly above the transition temperature [55].

This principal can be illustrated by plotting the potential energy of the structure against some convenient dimension  $z$  of the lattice, which increases monotonically during the transition. A hypothetical plot is shown in Fig. 1.7, where the values of  $z_A$  and  $z_B$  of the lattice are the equilibrium values in the initial and final states, at the absolute temperature.

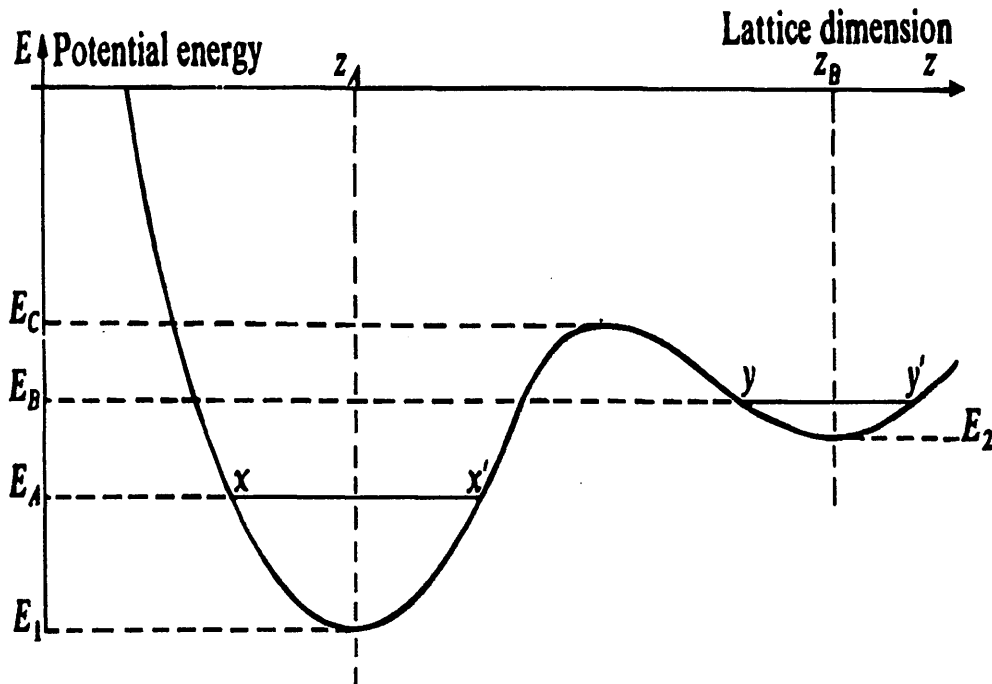


Fig 1.7 Condon-Morse curve illustrating a hypothetical plot of atomic energy against a lattice dimension for a solid undergoing a phase change [54,56].

Since the atoms have random thermal energies, their total energy is higher than  $E_1$  or  $E_2$ , and thus the mean total energy per atom is  $E_A$  in one phase and  $E_B$  in the other, when the temperature of both the phases is identical. The differences  $E_A - E_1$  and  $E_B - E_2$ , therefore, represent the average thermal energies of the atoms in either state. The

points  $x, x'$  and  $y, y'$  on the potential energy curves correspond to the turning points of the vibrating atoms, with the energies  $E_A$  and  $E_B$  respectively.

The phase change occurs since the energies  $E_A$  and  $E_B$  are mean values, and if the energy barrier  $E_C$  is not too high there may be atoms with enough energy to surmount it, and hence make the transition to the state B. Once there, the atoms may lose their energy by collision with neighbouring atoms, so they are then trapped in the potential well. The energy difference  $E_C - E_I$ , in this case, is referred to as the activation energy.

The net phase transition rate is the difference between the two flows of atoms in opposite directions, i.e. atoms changing from state A to state B, and atoms changing from state B to A. The former rate  $r_A$  may be defined as the number of atoms which make the A-B transition in unit time, and the number must be proportional to the following factors:

1. The number  $n_A$  of atoms in phase A with energies higher than  $E_C$ .
2. The frequency with which the atoms approach the barrier.
3. The relative thermodynamic probability of phase B compared to phase A.

The number  $n_A$  is given by the Boltzmann expression, see Equation 1.9, integrated over the energy range above  $E_C$ , see Equation 1.10, [56].

$$N(E) = C \cdot \exp\left(-\frac{E}{kT}\right) \quad \text{Equation 1.9}$$

$$n_A = \int_{E_c}^{\infty} C \cdot \exp\left(-\frac{E - E_I}{kT}\right) \cdot dE \quad \text{Equation 1.10}$$

$E_I$  appears because it is the energy at which atoms possess no kinetic energy in phase A. The factor  $C$  is assumed to be constant in this case, but it depends very weakly upon  $E$ . The result is as follows:

$$n_A = \frac{C}{kT} \exp\left(-\frac{E_c - E_1}{kT}\right) \quad \text{Equation 1.11}$$

The factor  $C$  can be evaluated by extending the range of the integration down to  $E_1$ , for then the number obtained is equal to the total number of atoms  $N_A$  in state A.

Therefore:

$$N_A = \frac{C}{kT} \quad \text{Equation 1.12}$$

hence,

$$n_A = N_A \exp\left(-\frac{E_c - E_1}{kT}\right) \quad \text{Equation 1.13}$$

The frequency of the atoms approaching the barrier may be taken to be the frequency of vibration  $\nu_A$  of the atoms in phase A. In most solids this is around  $10^{13}$  Hz. The final factor to be evaluated is the thermodynamic probability of phase B relative to phase A. It will be assumed that the thermodynamic probabilities  $W_A$  and  $W_B$  of the phases A and B can be defined, and that their ratio yields the required relative probability [56].

The rate,  $r_A$ , at which the phase change occurs is therefore, proportional to the products of all the factors discussed, and is expressed in Equation 1.14.

$$r_A = K \nu_A \frac{W_B}{W_A} N_A \exp\left(-\frac{E_c - E_1}{kT}\right) \quad \text{Equation 1.14}$$

$K$  is a constant that is only dependant on the geometry of the interface between the phases A and B. However, Equation 1.14 does not give the net phase transition rate since the reverse transition also occurs. The rate,  $r_B$ , can be defined in a similar fashion:

$$r_B = K v_B \frac{W_A}{W_B} N_B \exp\left(-\frac{E_C - E_2}{kT}\right) \quad \text{Equation 1.15}$$

Thus, the net phase transition rate is defined in Equation 1.16.

$$r = K v_A \frac{W_B}{W_A} N_A \exp\left(-\frac{E_C - E_1}{kT}\right) - K v_B \frac{W_A}{W_B} N_B \exp\left(-\frac{E_C - E_2}{kT}\right) \quad \text{Equation 1.16}$$

However, when the temperature of the solid at the transition temperature,  $T_t$ , the two phases exist at equilibrium, and the net phase transition rate is zero, Equation 1.17.

$$r = K v_A \frac{W_B}{W_A} N_A \exp\left(-\frac{E_C - E_1}{kT}\right) - K v_B \frac{W_A}{W_B} N_B \exp\left(-\frac{E_C - E_2}{kT}\right) = 0 \quad \text{Equation 1.17}$$

Consider an example of when the solid discussed in this case is cooled instantaneously from a temperature well above  $T_t$ , to a temperature well below  $T_t$ . Initially the number of atoms in phase A will be negligible, and the net phase transition rate is then equal to  $r_B$ , Equation 1.18.

$$r = r_B = K v_B \frac{W_A}{W_B} N_B \exp\left(-\frac{E_C - E_2}{kT}\right) \quad \text{Equation 1.18}$$

If the low temperature satisfies the criteria  $E_C - E_2 \gg kT$  then the phase transition rate can be regarded to be zero. Thus, by super-cooling the solid very rapidly to a low temperature before the phase transition can begin, it can effectively be halted. The number of atoms able to surmount the energy barrier is reduced to the extent that the high temperature phase appears to be stable. This is the simplified criterion for the formation of metastable phases [56].

The majority of the Al-Fe intermetallic phases present within a DC-cast ingot are metastable [6, 26], and therefore the formation of these phases cannot be predicted by referring to the Al-Fe equilibrium phase diagram. However, the crystal structure of the main Al-Fe metastable phases present within a DC-cast ingot have been investigated by many authors, and they are:  $\text{Al}_m\text{Fe}$ ,  $\text{Al}_x\text{Fe}$ , and  $\text{Al}_6\text{Fe}$ . Each of these phases will be discussed in detail for this study.

### 1.3.2.1 $\text{Al}_m\text{Fe}$

The metastable intermetallic phase  $\text{Al}_m\text{Fe}$  was first discovered by Mikki *et al* [7], as a solid precipitate within a DC-cast ingot, with a body centred tetragonal unit cell where  $a = 8.84 \text{ \AA}$  and  $c = 21.6 \text{ \AA}$ . The value of  $m$  has been measured by energy dispersive spectroscopy to be 4.4 [6], 4.2 [26], and 4.0 [58]. However, it was not until 1988 when Skjerpe [57] first proposed a comprehensive crystal structure model for this metastable phase.

The crystals obtained by Skjerpe were formed from a DC-cast Al-0.25 wt% Fe 0.13 wt % Si alloy of commercial purity. Ingot samples were taken from 25 mm, corresponding to a solidification rate of  $6 \text{ }^\circ\text{C s}^{-1}$ , and 100 mm, corresponding to a solidification rate of  $1 \text{ }^\circ\text{C s}^{-1}$ , from the surface of the ingot. The crystals were extracted from the aluminium matrix using butanol, using the method described by Simensen *et al* [59], and TEM and HREM studies were performed.

The possible structure model was determined, assuming the space group  $I4/mmm$ , and it predicted a single Fe site in layers along the (001), separated by two or three layers of Al atoms. The crystal density was not known for  $\text{Al}_m\text{Fe}$ , but an estimate was used by assuming a crystal density between  $\text{Al}_3\text{Fe}$  [43] and  $\text{Al}_6\text{Fe}$  [60], which have densities of  $3.77 \text{ g cm}^{-3}$  and  $3.45 \text{ g cm}^{-3}$  respectively, and since  $m = 4.0-4.4$  there are 20-22 Fe atoms and 110-120 atoms in total in the unit cell.

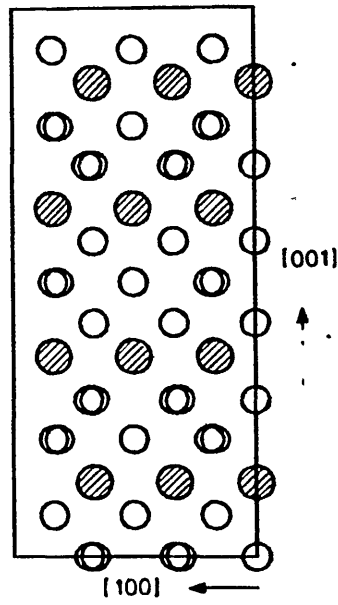


Fig 1.8 Possible structure of  $\text{Al}_m\text{Fe}$  viewed in the  $\langle 100 \rangle$  direction.  
Shaded areas represent Fe atoms [57].

A similar study was undertaken by Chandraseken *et al* [61] on a rapidly solidified super purity Al-Fe alloy. The unit cell determined was body centred tetragonal, with a lattice parameters of  $a = 8.89 \text{ \AA}$  and  $c = 21.5 \text{ \AA}$ , which was in good agreement with reported values [6, 26, 27]. There were no streaks, or super-reflections, observed in the analysis which indicates that the crystals were free from stacking faults and disorder, but these were observed in previous studies [6, 26, 27, 58]. However, the space group obtained was  $I4/m\bar{m}$ , and not  $I4/mmm$  as reported [6, 26, 27, 58], and the reason for this could be attributed to the absence of these stacking faults, and disorder, within the structure.

In all the studies performed upon  $\text{Al}_m\text{Fe}$  [6, 26, 27, 58, 61] Si is present within the particles, and the morphology is consistent with  $\text{Al}_m\text{Fe}$  being formed by a metastable eutectic reaction. Thus it is possible that the formation of this particular metastable

phase may only occur in conjunction with an impurity atom, which stabilises the formation of the phase. In this case Si fulfilled this stabilising role.

### 1.3.2.2 Al<sub>6</sub>Fe

The binary metastable phase Al<sub>6</sub>Fe was first reported by Hollingsworth *et al* [23], but a phase change of Al<sub>3</sub>Fe was reported by Bradley *et al* [63] but was never confirmed. A copper stabilised form of Al<sub>6</sub>Fe, however, has been investigated by Keller *et al* [64, 65, 66], and was confirmed by Phragmen [67]. Phragmen investigated the aluminium rich corner of the Al-Cu-Fe phase diagram, and assigned the formula (FeCu)(Al<sub>6</sub>Cu) to the  $\alpha$ -phase, and Phillips [68] also drew the same conclusions from his study. The structure of this phase was refined by Black *et al* [69] who found that the copper atoms were evenly distributed amongst the aluminium sites, and the structure was iso-structural with Al<sub>6</sub>Mn [70, 71].

Walford [60] refined the structure of Al<sub>6</sub>Fe by extracting a crystal, using electrolysis methods, from a 2 wt% Fe aluminium ingot. The density of the crystals was measured, using the flotation technique, and it was found to be  $3.45 \pm 0.05 \text{ g cm}^{-3}$ . This was in good agreement with the calculated density, which is obtained assuming that the unit cell contains a similar number of atoms, as in Al<sub>6</sub>Mn. However, the space group could not be defined accurately from three possibilities: Ccmm, Ccm2<sub>1</sub>, and Cc2m. The first being centro-symmetric, but the study by Walford indicated that the deviations from centro-symmetry were less than those in (FeCu)(Al<sub>6</sub>Cu) and Al<sub>6</sub>Mn. The unit cell, and cell parameters are shown in Table 1.9.

Author	Intermetallic Phase	Unit Cell	Parameters, Å
Nicol [70]	Al <sub>6</sub> Mn	Orthorhombic	a = 6.497 b = 7.552 c = 8.870
Black <i>et al</i> [69]	(FeCu)(Al <sub>6</sub> Cu)	Orthorhombic	a = 6.434 b = 7.460 c = 8.777
Hollingsworth <i>et al</i> [23]	Al <sub>6</sub> Fe	Orthorhombic	a = 6.492 b = 7.437 c = 8.788
Walford [60]	Al <sub>6</sub> Fe	Orthorhombic	a = 6.464 b = 7.440 c = 8.779

Table 1.9 Comparison of the literature values for Al<sub>6</sub>Fe, and its iso-structural compounds.

Within the orthorhombic unit cell there was only one Fe site determined, with 10 Al atoms surrounding, and having a mean Al-Fe bond length of  $2.511 \pm 0.056$  Å.

### 1.3.2.3 Al<sub>x</sub>Fe

The crystal structure of the metastable phase Al<sub>x</sub>Fe has not been unequivocally established [6, 26]. Westengen [6] partially failed to index the observed diffraction patterns, but suggested that the unit cell was orthorhombic, due to the structure containing stacking faults. Young *et al* [25] elaborates on this defective structure, and suggest that these stacking faults are incorporated within the unit cell and this effectively gives the appearance of a very large unit cell. Also the site occupancy of the

atoms is variable, which implies that the lattice parameters can vary over an appreciable range. However, the structure model Young *et al* [25] suggest for  $\text{Al}_x\text{Fe}$  ( $x = 4.5$ , monoclinic,  $a = 21.6 \text{ \AA}$ ,  $b = 9.3 \text{ \AA}$ ,  $c = 9.05 \text{ \AA}$ ,  $\beta = 94.0^\circ$ ) implies that the Fe environment is very similar to that of  $\text{Al}_6\text{Fe}$  [23, 60].

## 1.4 ALUMINIUM-IRON-SILICON SYSTEM

There are two main ternary equilibrium phases that form with aluminium, they are  $\alpha_H$ -AlFeSi and  $\beta_M$ -AlFeSi. However, another equilibrium phase,  $\delta_T$ -AlFeSi, is often present in high silicon alloys, and a fourth  $\gamma_M$ -AlFeSi forms in high iron and high silicon alloys [5]. The invariant reactions in the aluminium corner of the equilibrium phase diagram are shown in Table 1.10, and the liquidus curves are shown in Fig. 1.7a [5, 26], along with the probable phase distribution in the solid state Fig, 1.7b [5].

Reaction	Temperature, K.	Reaction Type
$\text{Liq.} \rightarrow \text{Al} + \text{Al}_3\text{Fe}$	928	Eutectic
$\text{Liq.} \rightarrow \text{Al} + \text{Si}$	850	Eutectic
$\text{Liq.} \rightarrow \text{Al} + \text{Si} + \beta_M$	849	Eutectic
$\text{Liq.} + \text{Al}_3\text{Fe} \rightarrow \alpha_H + \gamma_M$	983	Peritectic
$\text{Liq.} + \gamma_M \rightarrow \alpha_H + \beta_M$	948	Peritectic
$\text{Liq.} + \gamma_M \rightarrow \delta_T + \beta_M$	973	Peritectic
$\text{Liq.} + \text{Al}_3\text{Fe} \rightarrow \text{Al} + \alpha_H$	903	Peritectic
$\text{Liq.} + \alpha_H \rightarrow \text{Al} + \beta_M$	885	Peritectic
$\text{Liq.} + \delta_T \rightarrow \beta_M + \text{Si}$	869	Peritectic

Table 1.10 Invariant reactions at the aluminium end of the Al-Fe-Si system [5].

It has been shown that there are many different types of equilibrium, and metastable, Al-Fe-Si intermetallic phases that form during DC-casting [6, 26, 27], but the most common intermetallic phases are the equilibrium  $\alpha_H$ -AlFeSi phase, and the metastable  $\alpha_c$ -AlFeSi phase. Only these two phases will be discussed in detail.

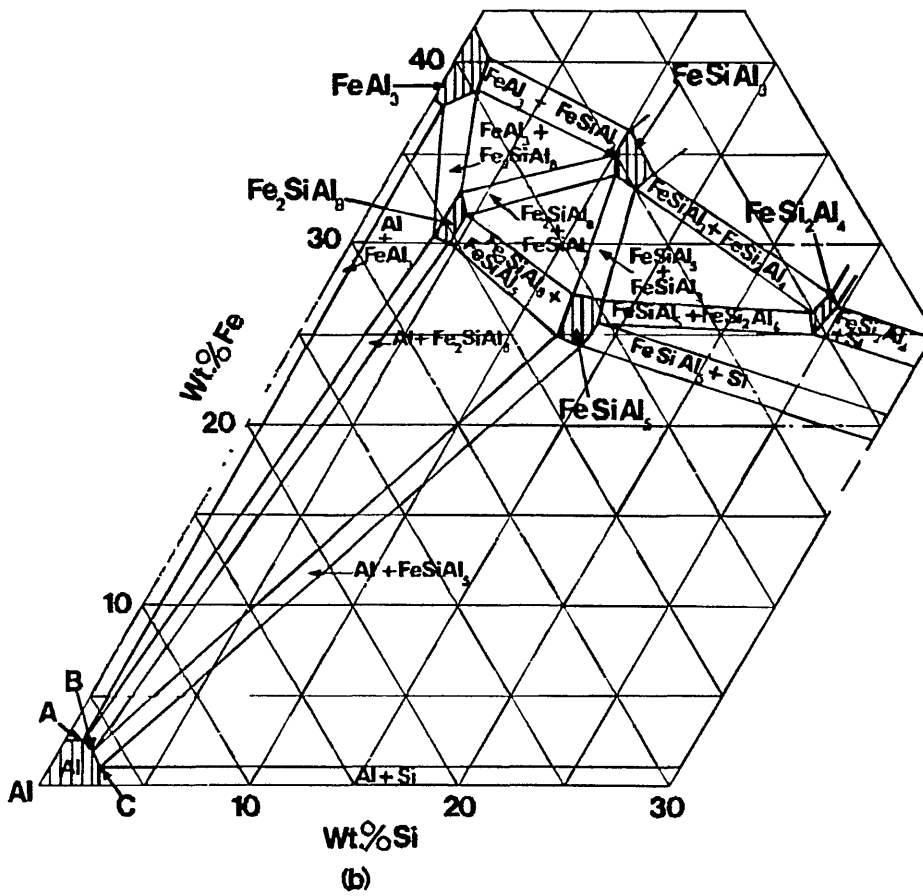
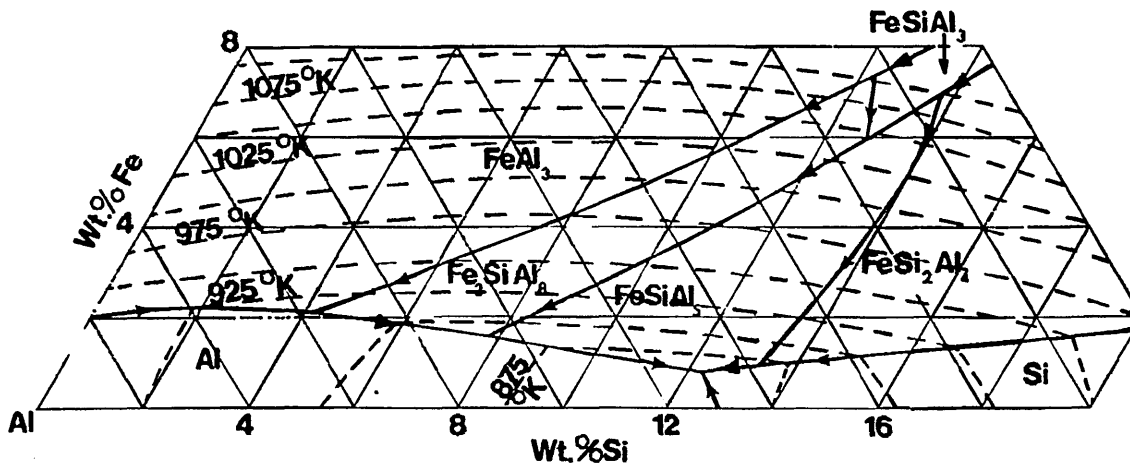


Fig 1.9 Aluminium corner of the Al-Fe-Si equilibrium phase diagram:  
 (a) liquidus [5, 26], (b) phase distribution in the solid [32].

### 1.4.1 $\alpha_{\text{H}}$ -AlFeSi

The crystal structure of the equilibrium phase  $\alpha_{\text{H}}$ -AlFeSi has been investigated by many authors [6, 21, 26, 72, 73, 74, 75], who concluded that it had a hexagonal unit cell,  $a = 12.3 \text{ \AA}$  and  $c = 26.3 \text{ \AA}$ , and a space group  $P6_3/mmc$ . However, the most comprehensive study regarding the crystal structure of  $\alpha_{\text{H}}$ -AlFeSi was performed by Corby *et al* [76], using the anomalous-dispersion methods. This technique was successfully applied to the determination of the crystal structure of  $\text{Al}_2\text{Fe}$  [77], which allowed the complete crystal structure to be resolved, and is described fully elsewhere [78].

The crystal structure that was determined by Corby *et al* [76] confirmed that the unit cell was hexagonal,  $a = 12.3 \text{ \AA}$  and  $c = 26.3 \text{ \AA}$ , and had a space group  $P6_3/mmc$ . On further analysis of the structure it was revealed that there were 5 independent Fe sites, and 26 independent Al sites. A summary of the Fe sites is given in Table 1.11.

Fe Site	No. of Al-Fe Bonds	Al-Fe Bond Length, $\text{\AA}$	Symmetry
1	9	2.35-2.72	12(k)
2	10	2.34-2.81	12(k)
3	10	2.29-2.62	12(k)
4	12	2.38-2.69	6(h)
5	12	2.45-2.93	4(f)

Table 1.11 Summary of the different types of Fe site [76].

There are three significant features of the structure of  $\alpha_{\text{H}}$ -AlFeSi that are directly visible when digesting the information reported by Corby *et al* [76]. The first feature is that all the atoms are in contact with at least eight neighbours. Secondly, no Fe atom is in direct contact with any other Fe atom, and nearly all the Al atoms, except Al(19),

are in direct contact with at least one Fe atom. Thirdly, the smallest Al-Fe bond length involves the Al atoms which themselves are bonded to the smallest number of Fe atoms. This is illustrated by considering Al(9) which has only one Fe neighbour, Fe(3), and the Al-Fe bond length is the smallest in the structure at 2.29 Å. Similarly, Al(15) also has only one Fe neighbour, Fe(3), and has the next smallest Al-Fe bond length at 2.34 Å. The overall mean Al-Fe bond lengths for those with two Fe neighbours is 2.47 Å, whilst those with three Fe neighbours the mean Al-Fe bond length is 2.59 Å. This is similar to features observed by Black [79] in other Al-Fe structures.

As no Fe atom is in contact with any other Fe atom, the structure can be described in terms of Al linkages between Fe-centred polyhedra [79]. The five such polyhedra are shown in Fig. 1.10, and those Al atoms masked by others are shown with an arrow indicating their position.

The polyhedra centred on Fe(1) and Fe(2) are shown together in Fig. 1.11. The Al(16) atoms provide the self-linkages between the Fe(1) polyhedra, and the Al(12) atoms play a similar role for the Fe(2) polyhedra. The two different types of polyhedra are linked together by Al(6) and Al(7) atoms into one continuous sheet (type sheet *A*), while Al(18) and Al(20) at a height  $\frac{1}{4}$  lie on this polyhedral sheet and link it to its mirror image *A'*.

The polyhedra centred on Fe(3) are shown in Fig 1.12, with Al(8) at height zero, and Al(10) and Al(13) providing the self linkages which form the continuous puckered type sheet *B*. The sheet contains the unit cell origin, and thus exhibits centro-symmetry unlike the type sheet *A*.

Their common atoms Al(6), Al(13), and Al(14) link the two types of sheet. The remaining Fe atoms serve to reinforce the joining of the sheets with Fe(4), lying in the mirror height  $\frac{1}{4}$ , joining *A* to *A'*, whilst Fe(5) joins *A* to *B*. The sheets finally stack in three dimensions as *A'BA (M) A'B'A*, where (*M*) indicates the height  $\frac{1}{4}$  mirror plane.

The main features of this structure are consistent with the features shown by  $\text{Al}_3\text{Fe}$  [43, 44],  $(\text{FeCu})(\text{Al}_6\text{Cu})$  [47], and  $\text{Al}_6\text{Fe}$  [60] as all of these structures show similar Fe-centred polyhedra. However, because of the difficulty of distinguishing Al atoms from Si atoms, it was not possible to determine the possible role of Si within this structure. It is possible to speculate that formation of  $\alpha_{\text{H}}\text{-AlFeSi}$  may be stabilised by a small amount of a third element, in this case Si, which plays no obvious role in the crystal structure. This is common with many Al-Fe containing intermetallic metastable phases [6, 26, 47, 57, 60].

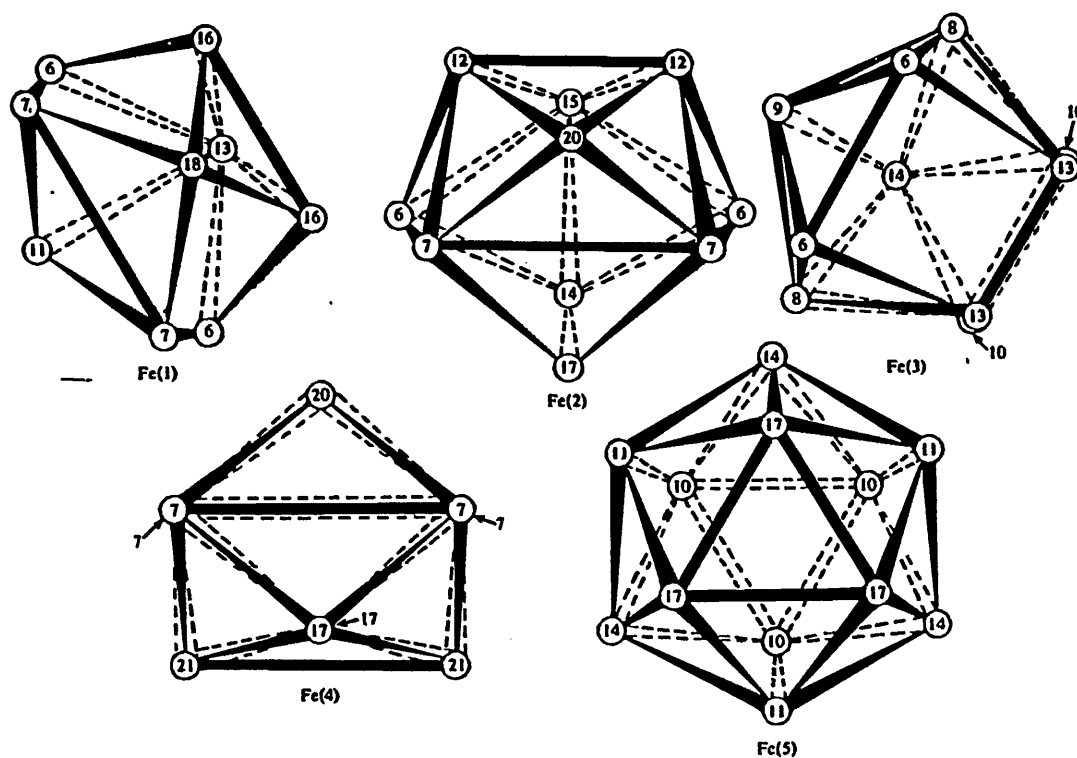


Fig. 1.10 The Fe-centred Al polyhedra. The lines connecting the Al atoms serve to aid in visualising the polyhedra, and do not necessarily represent bonds or atoms in contact [76].

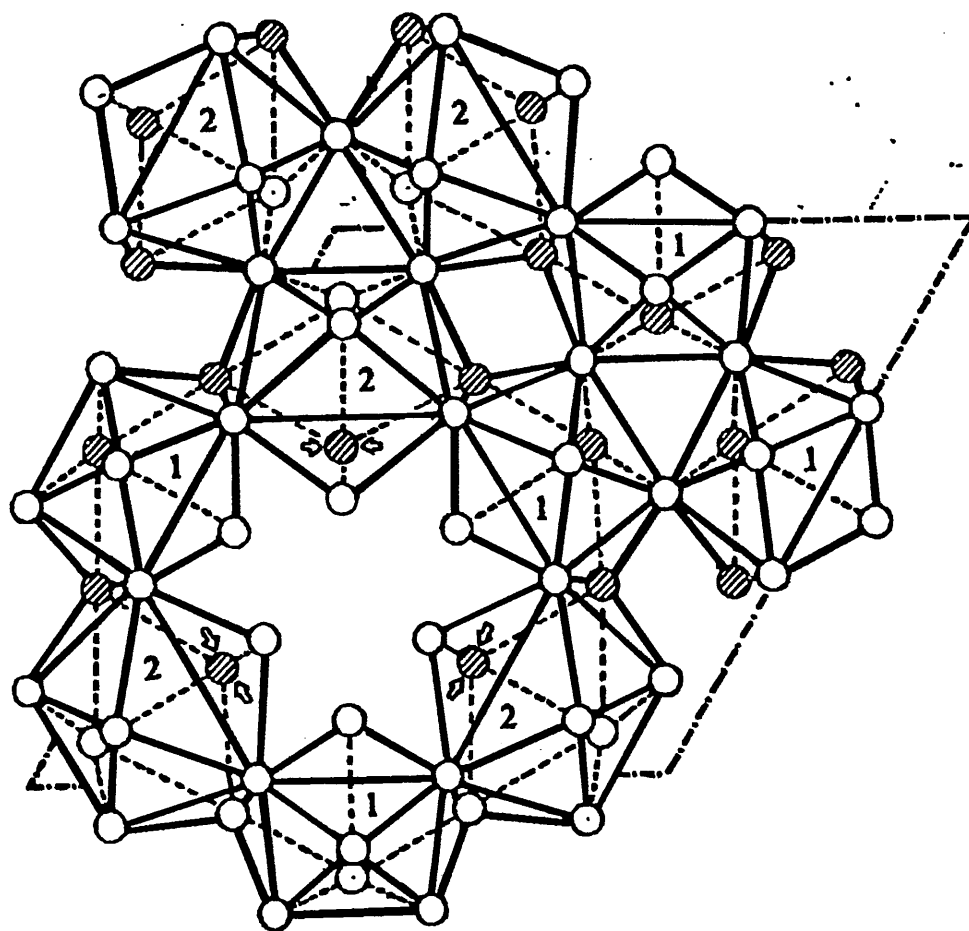


Fig 1.11 The type sheet *A* formed from Fe(1) and Fe(2)-centred polyhedra, and the numbers identify the polyhedra. The mean height of this sheet is 3.86 Å above the basal plane. The mirror plane at height  $\frac{1}{4}$  (6.56 Å above the basal plane) contains the Fe(4) atoms, with the positions shown by pairs of arrows, which serve to join the sheet to its mirror image *A'* at 9.26 Å above the basal plane. The apparent hole at  $(\frac{1}{3}, \frac{2}{3})$  is occupied by Fe(5) which serves to bind this sheet to the sheet type *B*. Shaded atoms are Al(6), Al(13), and Al(14) which are common to the type sheet *B* [76].

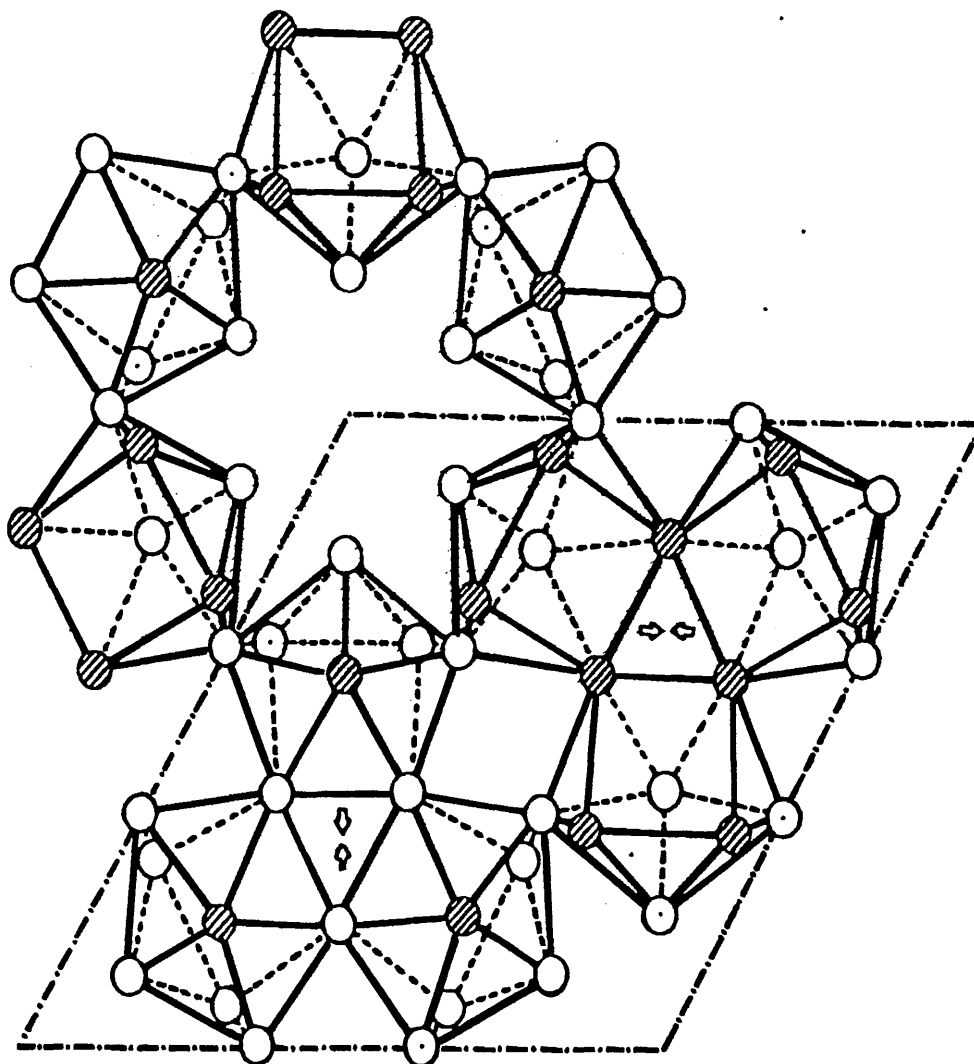


Fig 1.12 The type *B* sheet formed from the Fe(3)-centred polyhedra. The mean level of this sheet is in the basal plane. The Fe(5) atom at 2.63 Å above the basal plane, position shown by a vertical pair of arrows, serves to bind this sheet to the type *A* sheet above. The Fe(5) atom at 2.63 Å below the basal plane, position shown by the horizontal pair of arrows, serves to bind the sheet to the *A'* sheet below. The shaded atoms are those Al(6), Al(13), and Al(14) atoms that are common to the type *A* sheet [76].

### 1.4.2 $\alpha_c$ -AlFeSi

The crystal structure of the metastable phase  $\alpha_c$ -AlFeSi was determined by Cooper [80] in 1967. The actual investigation used single crystals, with a chemical composition defined by microprobe analysis of  $\text{Fe}_4\text{MnSi}_2\text{Al}_{19}$ . This was close to the chemical composition of  $\text{Fe}_5\text{Si}_2\text{Al}_{20}$  reported by Phragmen [47], and since the atomic radii of Fe and Mn are similar [4] it is assumed that the Mn directly substitutes for Fe.

The density of the crystals was determined by the flotation method to be  $3.59 \pm 0.06 \text{ g cm}^{-3}$ , which agrees with the calculated value of  $3.62 \text{ g cm}^{-3}$ , for an ideal unit cell consisting of 100 Al, 14 Si, and 24 Fe atoms [80]. The unit cell was obtained by diffraction techniques, and was found to be cubic with a cell size of 12.56 Å and space group Im3, which agreed with the structural information obtained by Phragmen [47]. However, the structure of  $\alpha_c$ -AlFeSi was not discussed in detail by Cooper [80], but it was discussed with reference to  $\alpha_c$ -AlMnSi [81]. This Mn ternary intermetallic compound is an isomorph of  $\alpha_c$ -AlFeSi, which can be explained in terms of the similar free electron to atom ratios, and the parameters are compared in Table 1.12.

The crystal structure of  $\alpha_c$ -AlMnSi was obtained, and refined, by Cooper *et al* [81], which was based upon the structure reported by Bergman of a unit cell containing 138 atoms [82]. Cooper *et al* [81] performed diffraction experiments on single crystals, and discovered that the unit cell was cubic,  $a = 12.68 \text{ Å}$  space group Pm3, with a density of  $3.62 \pm 0.06 \text{ g cm}^{-3}$ . This agreed with a calculated density of  $3.62 \text{ g cm}^{-3}$ , based upon a unit cell containing 100 Al, 14 Si, and 24 Mn atoms.

The intermetallic phase  $\alpha_c$ -AlMnSi is almost body centred. The main departure of this pattern is the aluminium atom Al(3), which has no body centred counterpart. This results in different co-ordination polyhedra centred on two types of manganese atoms Mn(1) and Mn(2), and nine different aluminium sites Al(1)-Al(9).

Author	Intermetallic Phase	Unit Cell	Space Group	Parameters
Cooper [80]	$\alpha_c$ -AlFeSi	Cubic	Im3	a = 12.56 Å
Cooper <i>et al</i> [81]	$\alpha_c$ -AlMnSi	Cubic	Pm3	a = 12.68 Å

Table 1.12 Comparison of  $\alpha_c$ -AlFeSi and  $\alpha_c$ -AlMnSi [80, 81]

Cooper *et al* [81] used a maximum contact distance of 2.84 Å for the manganese and aluminium atoms, and the co-ordination of the polyhedra is described as follows. The manganese atom Mn(1) has ten aluminium neighbours, at an average distance of 2.63 Å. This includes two short bonds to atoms Al(3), 2.46 Å, and Al(4), 2.43 Å. The manganese atom Mn(2) has nine aluminium neighbours, with only one short Al-Mn bond measuring 2.27 Å, Al(5). The bond to atom Al(5) is a direct complement to Al(4) in the Mn(1) environment, and is a feature of many Al-Transition Metal systems, as described earlier [50]. The difference in changing the co-ordination number of the Mn centred polyhedra from 10-fold to 9-fold only affects the number of coplanar bonds, and in this case the number of Al-Mn coplanar bonds reduces from 4 to 3.

The structure of the complete unit cell can be described as a complex three-dimensional network of polyhedra. However, it can alternatively be described in terms of layers of manganese atoms parallel to the (100) planes, and linked by aluminium atoms, but in the case of  $\alpha_c$ -AlMnSi this layering is not as marked as in other aluminium alloys of transition metals [25, 43, 44, 51, 60, 68, 70, 71, 76, 80].

The refinement of the crystal structure of  $\alpha_c$ -AlFeSi by Cooper [80] defined two iron 10-fold and 9-fold co-ordination polyhedra, Fe(1) and Fe(2), similar in atomic arrangement to those found in  $\alpha_c$ -AlMnSi, and twelve aluminium sites, Al(1)-Al(12). However, a consideration of the bond lengths showed that the crystal must be

composed of two types of unit cell. In one type of unit cell, sites Al(7), Al(9), and Al(11) are occupied, and in the other sites Al(8), Al(10), and Al(12) are occupied. This yields an average structure that belongs to the space group  $Im\bar{3}$ , although each type of unit cell, when considered separately, is primitive. The way that these two different types of unit cell interlock is not shown in the literature, or how the polyhedra are connected together, but the iron atoms are arranged parallel to the (100) plane, as in  $\alpha_c$ -AlMnSi. Table 1.13 shows a comparison of the iron and manganese polyhedra observed in  $\alpha_c$ -AlFeSi and  $\alpha_c$ -AlMnSi.

Intermetallic Phase	Site	No. of Al- Trans. Met. Bonds	Al-Trans. Met. Bond Length, Å
$\alpha_c$ -AlMnSi	Mn(1)	10	2.43 - 2.84
	Mn(2)	9	2.27 - 2.62
$\alpha_c$ -AlFeSi	Fe(1)	10	2.43 - 2.81
	Fe(2)	9	2.43 - 2.68

Table 1.13 Summary of the Transition Metal sites in  $\alpha_c$ -AlFeSi and  $\alpha_c$ -AlMnSi [80, 81].

Again, no attempt was made to distinguish between aluminium and silicon, in the crystal structure of  $\alpha_c$ -AlFeSi, or  $\alpha_c$ -AlMnSi, but silicon probably fulfils the same role as in  $\alpha_H$ -AlFeSi [76].

## 1.5 MÖSSBAUER STUDIES AND INTERPRETATION

It has already been stated that the main impurity element within aluminium is iron, and due to the very low solid solubility of iron in aluminium the iron forms intermetallic compounds in the final part of the solid that solidifies. Since iron is present in all the common intermetallic compounds, Mössbauer spectroscopy can be used to analyse them. The information that this produced using this technique gives a detailed insight into the iron environment, both structurally and dynamically, and the theory is clearly explained in Chapter 2.

The advantages of using this technique to analyse the aluminium intermetallics are summarised below:

1. Only a very small quantity of the sample is required, typically in the order of a few milligrams.
2. The samples can be in several forms: sheets, foils, single crystals and polycrystalline powders.
3. The technique is non-destructive.
4. Mössbauer spectroscopy can be used to study both bulk and surface properties.
5. Since each aluminium intermetallic phase has a unique crystal structure, therefore, they can be identified by their characteristic spectra.
6. Variable temperature Mössbauer spectroscopy can be used to study the lattice dynamics of the different phases.

### 1.5.1 EARLY MÖSSBAUER STUDIES

The earlier Mössbauer spectroscopy studies, performed in the 1960s, were mainly upon Al-Fe alloys containing very high amounts of iron, typically 20-50 wt% [83, 84, 85, 86, 87]. These investigations concerned the ordering and magnetic behaviour of Al-Fe alloys. These properties have no consequence in this study, due to the iron

content in industrially cast aluminium being typically less than 1 wt% [1], and are only mentioned in passing.

However, a more relevant study was performed by Bush *et al* [88], who used the Mössbauer effect to investigate precipitation in a dilute solution of iron in aluminium. The alloy used in this investigation contained 0.05 wt% Fe, and it was  $^{57}\text{Fe}$  enriched by 68%. Initially the Mössbauer spectrum for the alloy showed only a single Lorentzian,  $\delta = 0.77 \text{ mm s}^{-1}$ , which is a characteristic of iron dissolved in a paramagnetic matrix. After the alloy was annealed for 128 hours at  $320^\circ\text{C}$  a phase transition occurred, and the  $\text{Al}_3\text{Fe}$  intermetallic was formed. Mainly using X-ray diffraction techniques proved this, but Mössbauer spectroscopy was also used. The Mössbauer spectrum was deconvoluted into two Lorentzian lines,  $\delta = 0.43 \text{ mm s}^{-1}$  and  $\delta = 0.72 \text{ mm s}^{-1}$ , but no physical justification was given for this regarding the crystal structure of the alloy.

Since then there has been a considerable amount of work done in the area of dilute Al-Fe alloys, which utilises the very high resolution of the Mössbauer technique. This has enabled very fine, and detailed, structural information to be published in this area, including: monomers [89, 90, 91], dimers [92], vacancy [93, 94, 95, 96, 97, 98], interstitial [99, 100], grain boundary [101], cluster [92], AlFe solid solution [83, 86], and anti-domain boundary [83, 86],

However, this study only concerns the Al-Fe and Al-Fe-Si intermetallics, each of which shall be discussed in detail separately.

### 1.5.2 $\text{Al}_3\text{Fe}$

Initially Mössbauer studies detailed all the known intermetallics formed in the Al-Fe system [102, 103, 104, 105, 106]. The spectrum of the equilibrium intermetallic phase  $\text{Al}_3\text{Fe}$  is reported to consist of three Lorentzian components, whose origins were not justified [102, 103, 104, 105, 106, 111, 112]. That would imply that the crystal structure of this intermetallic would contain three symmetrical iron sites, with different

Al-Fe bond lengths. However, Black [43, 44] determined the crystal structure of  $\text{Al}_3\text{Fe}$ , and it was found to contain five different iron sites, so this de-convolution of the spectrum has no physical significance. However, Preston *et al* [102] and Stickels *et al* [103] described the crystal structure of this intermetallic in their studies, but attributed their three Lorentzian line interpretation procedure to computer ease.

Author	Lorentzian	Isomer Shift, $\text{mm s}^{-1}$	Width, $\text{mm s}^{-1}$
[102]	1	0.01	0.27
	2	0.20	0.27
	3	0.38	0.27
[103]	1	0.01	0.25
	2	0.21	0.29
	3	0.38	0.25
[104], [105]	1	0.01	0.27
	2	0.19	0.27
	3	0.38	0.27

Isomer shifts relative to  $\alpha$ -iron.

Table 1.14 A summary of the three Lorentzian line de-convolution approach for the Mössbauer spectrum of  $\text{Al}_3\text{Fe}$ .

The interpretation of the Mössbauer spectrum for  $\text{Al}_3\text{Fe}$ , according to the literature, seemed to evolve with time. Instead of the three Lorentzian line de-convolution approach, several authors [107, 108, 109] have suggested a two quadrupole de-convolution interpretation. These authors made no physical justification to the change in the interpretation of the Mössbauer spectrum for  $\text{Al}_3\text{Fe}$  in their studies. However, Chittaranjan *et al* [110] followed this same approach, and did fully justify it with regard to the crystal structure.

The crystal structure of  $\text{Al}_3\text{Fe}$  has been discussed in detail previously, see Chapter 1.3.1, and can be summarised as flat and puckered layers of atoms perpendicular to the  $b$  axis. In the flat layer there are four different types of iron sites, with some similarities in their local environment. In the iron sites 1, 3, and 4 there are 11 nearest neighbours, but one of the neighbouring atoms is more than  $2.8 \text{ \AA}$  away and, therefore, can be assumed to be too far away from Fe atom to pose any significant effect to the Mössbauer interaction [110]. The iron site 2 has only 10 nearest neighbours, but their mean nearest neighbour bond lengths is the shortest of the four sites. Aluminium atoms dominate the puckered layer, and in this layer the iron atoms have a single distinct position at the centre of a pentagon of aluminium atoms. Thus the five different types of iron sites can be distinguished into two classes:

1. Four different sites, but with a rather similar atomic environments in the flat layer.
2. One site with a unique atomic environment, in the puckered layer.

Both of the above classes are situated in a symmetry which is less than cubic, and so the spectrum of  $\text{Al}_3\text{Fe}$  can be expected to consist of two quadrupole interactions, with the observed experimental parameters for several authors shown in Table 1.15.

The quadrupole interaction arising from the puckered layer of atoms yields a doublet, with a very small splitting. This is due to the single iron site in this layer being in a near symmetrical environment with aluminium atoms as the nearest neighbours.

The other four iron sites in the flat layer of atoms produce a quadrupole interaction with a larger splitting, as they are in a more asymmetric environment. This larger splitting would arise from a larger electric field gradient across the iron atom, inherent in the more asymmetric environment. The line broadening observed by Chittaranjan *et al* [110] was attributed to the distributions of sites, but no attempt was made to distinguish between each of the four iron sites, as they are so closely related.

Author	Isomer Shift, mm s <sup>-1</sup>	Quadrupole Splitting, mm s <sup>-1</sup>
[107]	0.20	0.38
	0.20	0
[108]	0.197 ± 0.006	0.396 ± 0.006
	0.196 ± 0.006	< 0.06
[109]	0.20	0.40
	0.20	0
[110]	0.20 ± 0.23	0.42 ± 0.01
	0.20 ± 0.17	0.08 ± 0.05

Isomer shifts relative to  $\alpha$ -iron.

Table 1.15 A summary of the two quadrupole splitting de-convolution approach for the Mössbauer spectrum of Al<sub>3</sub>Fe.

### 1.5.3 Al<sub>6</sub>Fe

The crystal structure has been defined completely defined by Walford [60], and it was discovered that there was only one distinct iron site within the unit cell. The implications of that discovery, to the observed Mössbauer spectrum, were that only one quadrupole interaction component could be physically justified for the spectrum. This procedure was followed by a variety of different authors, who published Mössbauer parameters for this compound [104, 105, 107, 108, 109, 110, 111, 112], see Table 1.16 for a comparison of the literature values.

Chittaranjan *et al* [110] compared the local atomic environments of the iron sites residing in the flat layer of atoms in Al<sub>3</sub>Fe, and that of the local atomic environment of Al<sub>6</sub>Fe. Both systems are an arrangement of 10 co-ordination Al-Fe polyhedra with similar Al-Fe bond lengths. Accordingly, the electron charge density at the iron nucleus for the two systems was expected to be the same, and thus the isomer shifts. This can

be illustrated by comparing the literature values for the isomer shifts for  $\text{Al}_3\text{Fe}$ , see Table 1.15, and  $\text{Al}_6\text{Fe}$ , see Table 1.16. However, the corresponding quadrupole splittings were different, and this can be attributed to the different Al-Fe bond lengths, which would lead to a slightly different electric field gradients, across the Mössbauer atom, in the two intermetallic compounds.

Author	Isomer Shift, $\text{mm s}^{-1}$	Quadrupole Splitting, $\text{mm s}^{-1}$
[105]	0.22	0.32
[106]	0.22	0.32
[107]	0.22	0.26
[108]	$0.216 \pm 0.003$	$0.280 \pm 0.003$
[109]	$0.22 \pm 0.01$	$0.26 \pm 0.01$
[110]	0.22	0.32
[111]	0.22	0.32
[112]	0.22	0.32

Isomer shifts relative to  $\alpha$ -iron.

Table 1.16 Summary of the quadrupole splitting de-convolution approach for the Mössbauer spectrum of  $\text{Al}_6\text{Fe}$ .

### 1.5.3.1 THE PHASE TRANSITION $\text{Al}_6\text{Fe} \rightarrow \text{Al}_3\text{Fe}$

Several different authors [104, 105, 111, 112] have also published articles regarding the intermetallic phase transition from the metastable compound  $\text{Al}_6\text{Fe}$ , to the equilibrium compound  $\text{Al}_3\text{Fe}$ . This important transition occurs during the homogenising process of the aluminium ingot, which is an integral part of the industrial production process, as it alters the workability and chemical properties of the material.

Nagy *et al* [105] cast aluminium ingots using the DC casting method, containing 0.58 wt% Fe, and they were analysed using the Mössbauer technique. However, there was no indication where the samples were taken from within the ingot, but after analysis the as cast sample was found to contain predominantly a Mössbauer doublet attributed to  $\text{Al}_6\text{Fe}$  and with a small Mössbauer singlet attributed to AlFe solid solution. After annealing the sample at  $620^\circ\text{C}$  for 3000 minutes the  $\text{Al}_6\text{Fe}$  intermetallic transformed into  $\text{Al}_3\text{Fe}$ , but the area fraction of the Mössbauer singlet attributed to AlFe solid solution did not change. This can be explained as the iron was saturated in the aluminium, due to its limited solid solubility [14].

This transformation was corroborated by a study by Murgas *et al* [111], using an identical DC aluminium ingot, containing 0.58 wt% Fe, and the Mössbauer technique. However, the samples were taken from a region of the ingot that experienced a solidification rate of  $3^\circ\text{C s}^{-1}$ , and this was confirmed by applying dendrite spacing calculations [8,9,10,11,12,13]. The annealing procedure was performed at  $620^\circ\text{C}$  for 240 minutes, and the resultant Mössbauer spectrum was de-convoluted into predominately  $\text{Al}_3\text{Fe}$ , with small area fractions attributed to  $\text{Al}_6\text{Fe}$ , and AlFe in solid solution (which also remained constant throughout the annealing process). Murgas *et al* [111] did extrapolate area fraction vs. annealing time curves for the sample, and deduced that after approximately 3000 minutes the intermetallic  $\text{Al}_6\text{Fe}$  to  $\text{Al}_3\text{Fe}$  transition would be complete.

Other studies by Nagy *et al* [104] and Vertes *et al* [112] investigated the kinetics of the transition  $\text{Al}_6\text{Fe}$  to  $\text{Al}_3\text{Fe}$ , and tried to determine a simple model for the mechanism of the process. Both authors used a DC aluminium ingot, containing 0.58% wt Fe, and the Mössbauer technique was applied to follow the transition. Samples were taken from a region of the ingot which experienced a solidification rate of  $3^\circ\text{C s}^{-1}$ , and was confirmed by applying dendrite spacing calculations [8,9,10,11,12,13], as this solidification rate favours the precipitation of the  $\text{Al}_6\text{Fe}$  intermetallic metastable phase [7, 15, 24]. Several samples were annealed at different temperatures,  $580^\circ\text{C}$ - $635^\circ\text{C}$ , for 240 minutes, and the area fractions were analysed using the Arvami equation [113] combined with an Arrhenius plot. Nagy *et al* [104] determined the optimum activation energy of this process to be  $3.33 \pm 0.14$  eV, which agreed with the optimum value of  $3.33 \pm 0.47$  eV proposed by Vertes *et al* [112]. This activation energy is higher than the reported activation energy values, 1.9 eV-2.7 eV, for the volume diffusion of iron in aluminium [29, 114, 115, 116], which suggests that the transformation process is partly controlled by diffusion.

#### 1.5.4 $\text{Al}_m\text{Fe}$

The crystal structure of  $\text{Al}_m\text{Fe}$  has accurately been described Skjerpe [57], see Chapter 1.3.2.1, who determined that there was only one type of iron site within the body centred tetragonal unit cell. Therefore, the Mössbauer spectrum can only be deconvoluted into one quadrupole component, with any physical justification.

Kuzmann *et al* [117] rapidly quenched, and the solidification rate was typically in the order of  $10^5$   $^\circ\text{C s}^{-1}$ , two different aluminium alloys, containing 6.8 wt% Fe and 0.5 wt% Fe, in powder and ribbon form. The Mössbauer technique was applied to identify the intermetallic compounds that were created, and the intermetallic compound  $\text{Al}_m\text{Fe}$  was found to dominate in all cases (see Table 1.17 for the observed experimental Mössbauer parameters). This was not surprising, as the intermetallic compound  $\text{Al}_m\text{Fe}$  forms at high solidification rates  $10$ - $100$   $^\circ\text{C s}^{-1}$  [7, 15, 24, 25, 119], see Chapter 1.2.1.1. In this study  $m = 3.96$ , which was outside the reported range of  $4.0$  -  $4.4$  [6,

26, 58]. However, silicon was present in all the previous structural investigations [6, 26, 27, 58, 61], and not in the study by Kuzmann *et al* [117]. Therefore, the value of  $m$  appears to be only determined by the solidification rate, and not the presence of silicon.

Another Mössbauer investigation was performed by Schurer *et al* [118], upon various rapidly solidified Al-Fe alloys. The intermetallic compound  $\text{Al}_6\text{Fe}$  was found to be present, along with AlFe in solid solution, and the Mössbauer parameters for those agreed with earlier reported values [83, 86, 105, 106, 107, 108, 109, 110, 111, 112]. However, the parameters for  $\text{Al}_m\text{Fe}$  were reported, see Table 1.17, which compared to those of Kuzmann *et al* [117], within the limits of experimental error.

Author	Isomer Shift, $\text{mm s}^{-1}$	Quadrupole Splitting, $\text{mm s}^{-1}$
[117]	$0.16 \pm 0.01$	$0.32 \pm 0.02$
[118]	$0.19 \pm 0.02$	$0.32 \pm 0.02$

Isomer shifts relative to  $\alpha$ -iron.

Table 1.17 A summary of the quadrupole splitting de-convolution approach for the Mössbauer spectrum of  $\text{Al}_m\text{Fe}$ .

### 1.5.5 $\text{Al}_x\text{Fe}$

Reviewing the literature reveals a hole in the knowledge of the existing Mössbauer parameters of various Al-Fe and Al-Fe-Si intermetallic compounds, as there are no published articles regarding  $\text{Al}_x\text{Fe}$ . This could be due to variety of reasons, mainly:

1.  $\text{Al}_x\text{Fe}$  is a highly unstable metastable intermetallic compound [25] that readily transforms to other more stable varieties, typically  $\text{Al}_6\text{Fe}$  and  $\text{Al}_m\text{Fe}$ , within the aluminium matrix.

2. Only very small amounts of  $\text{Al}_x\text{Fe}$  are formed initially, within the aluminium matrix, and are found in conjunction with other metastable intermetallic compound [6]. Thus, accurate Mössbauer parameters for  $\text{Al}_x\text{Fe}$  are very difficult to isolate, when deconvoluting a Mössbauer spectrum obtained from an alloy specimen.

Young *et al* [25] suggest a structure model for  $\text{Al}_x\text{Fe}$  ( $x = 4.5$ , monoclinic,  $a = 21.6 \text{ \AA}$ ,  $b = 9.3 \text{ \AA}$ ,  $c = 9.05 \text{ \AA}$ ,  $\beta = 94.0^\circ$ ), which implies that the Fe environment is very similar to that of  $\text{Al}_6\text{Fe}$  [23, 60], see Chapter 1.3.2.3. The Mössbauer spectrum deconvolution for  $\text{Al}_6\text{Fe}$  has been reported by many authors [83, 86, 105, 106, 107, 108, 109, 110, 111, 112], and was defined as a single Mössbauer quadrupole interaction resulting in a well defined doublet. This was the procedure applied to the resultant Mössbauer spectrum for the extracted  $\text{Al}_x\text{Fe}$  sample, in this study.

#### 1.5.6 $\alpha_{\text{H}}\text{-AlFeSi}$

Suzuki *et al* [120] first attempted to determine the Mössbauer parameters for  $\alpha_{\text{H}}\text{-AlFeSi}$ , by preparing specific alloys from the equilibrium Al-Fe-Si phase diagram, see Fig 1.13. A ingot, containing 4% Fe and 5% Si, was rapidly cooled in water after being annealed for 90 minutes at 893 K, and the intermetallic compound was electrolytically extracted, using  $200 \text{ A m}^{-2}$  and 3.5% HCl. The reason that these specific conditions were chosen was due to the fact that  $\alpha_{\text{H}}\text{-AlFeSi} + \text{L}$  and  $\text{Al} + \alpha_{\text{H}}\text{-AlFeSi} + \text{L}$  coexist in the equilibrium phase diagram, see point A in Fig 1.13. Therefore, it was possible to obtain equilibrium phase  $\alpha_{\text{H}}\text{-AlFeSi}$  specifically, by rapid quenching from that specific point.

The crystal structure of the equilibrium intermetallic compound was determined by Corby *et al* [76], and confirmed that the unit cell was hexagonal,  $a = 12.3 \text{ \AA}$  and  $c = 26.3 \text{ \AA}$ , with a space group  $\text{P6}_3/\text{mmc}$ . On further analysis of the structure it was revealed that there were five Fe centred aluminium polyhedra, and 26 independent Al sites. A summary of the Fe sites is given in Table 1.11. However, Suzuki *et al* [120]

de-convoluted the Mössbauer spectrum into three Lorentzian lines, which had no physical justification when compared to the crystal structure.

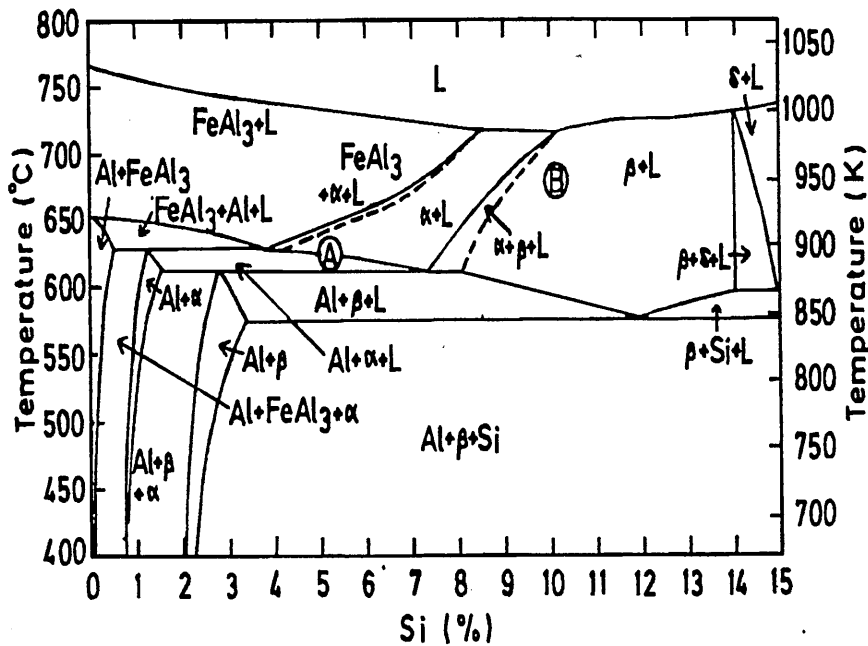


Fig 1.13 Vertical section of the ternary phase diagram of Al-Fe-Si at 4% Fe [120,121].

A later investigation by Nagy *et al* [122] attempted to de-convolute the Mössbauer spectrum for  $\alpha_H$ -AlFeSi, according to the crystal structure. The samples used in this study was a DC cast ingot, containing 32.5 m% Fe and 9.5 m% Si, which was annealed for 500 hrs at 600°C, as to promote the formation of the equilibrium phase. The individual existence of the equilibrium phase  $\alpha_H$ -AlFeSi, within the DC cast ingot, was confirmed by X-ray powder diffraction techniques.

Author	Lorentzian	Isomer Shift, mm s <sup>-1</sup>	Width, mm s <sup>-1</sup>
[120]	1	0.04	Not Given
	2	0.30	Not Given
	3	0.52	Not Given

Isomer shifts relative to  $\alpha$ -iron.

Table 1.18 Summary of the three Lorentzian line de-convolution approach for the Mössbauer spectrum for  $\alpha_{\text{H}}\text{-AlFeSi}$ , used by Suzuki *et al* [120].

The Mössbauer spectrum that was obtained by Nagy *et al* [122], was interpreted as consisting of two quadrupole doublets, see Table 1.19 for the obtained parameters. The quadrupole doublet 1 was attributed to represent sites Fe(1) and Fe(2), and the other component of the spectrum was assumed to consist of the other three iron sites. This approach was not fully justified and, therefore, should be used with some reservation.

Author	Doublet	Isomer Shift, mm s <sup>-1</sup>	Quadrupole Splitting, mm s <sup>-1</sup>	Width, mm s <sup>-1</sup>	Rel. Area, %
[122]	1	0.175	0.257	0.287	52.2 $\pm$ 0.07
	2	0.248	0.599	0.287	47.8 $\pm$ 0.07

Isomer shifts relative to  $\alpha$ -iron.

Table 1.19 A summary of the two quadrupole splitting de-convolution approaches for the Mössbauer spectrum of  $\alpha_{\text{H}}\text{-AlFeSi}$  [122].

When considering the iron sites, within the crystal structure of  $\alpha_{\text{H}}\text{-AlFeSi}$ , they can be split into three different categories:

1. Fe(1), with 9 Al-Fe bonds, and a total of 12 sites.
2. Fe(2) and Fe(3), with 10 Al-Fe bonds each, and a total of 24 sites .
3. Fe(4) and Fe(5), with 12 Al-Fe bonds each, and a total of 10 sites.

Thus, considering all aspects the Mössbauer spectrum for  $\alpha_{\text{H}}\text{-AlFeSi}$  should be de-convoluted into three quadrupole doublets, with the relative absorption areas linked to the total number of iron sites for each component . This compound was not studied in the current project, and, therefore, no further analysis is required.

### 1.5.7 $\alpha_{\text{c}}\text{-AlFeSi}$

In the same investigation by Nagy *et al* [122] the Mössbauer parameters for the metastable intermetallic compound  $\alpha_{\text{c}}\text{-AlFeSi}$  (cubic alpha) were obtained. An aluminium ingot was DC cast, containing 0.5 m% Fe and 0.2 m% Si, at a high solidification rate, typically in the order of  $2000\text{-}3000\text{ }^{\circ}\text{C min}^{-1}$ . However, no homogenising of the ingot took place, as it would have forced a phase change to occur within the ingot, and thus driving the metastable  $\alpha_{\text{c}}\text{-AlFeSi}$  phase to form one of the equilibrium Al-Fe-Si variants.

The Mössbauer spectrum was de-convoluted into two doublets, see Table 1.20 for the observed parameters, according to the crystal structure of  $\alpha_{\text{c}}\text{-AlFeSi}$ . The crystal structure of  $\alpha_{\text{c}}\text{-AlFeSi}$  was found to contain a single 10 co-ordinated iron centred Al-Fe polyhedra, and a single 9 co-ordinated iron centred Al-Fe polyhedra [80], see Chapter 1.4.2. Nagy *et al* [122] did not fully justify this approach, leaving the issue of which doublet was attributed to which iron site, but it will be addressed later in this project.

Author	Doublet	Isomer Shift, mm s <sup>-1</sup>	Quadrupole Splitting, mm s <sup>-1</sup>	Width, mm s <sup>-1</sup>	Rel. Area, %
[122]	1	0.30	0.20	0.29	34.6 ± 0.07
	2	0.18	0.30	0.29	65.4 ± 0.07

Isomer shifts relative to  $\alpha$ -iron.

Table 1.20 A summary of the two quadrupole splitting de-convolution approach for the Mössbauer spectrum of  $\alpha_c$ -AlFeSi [122].

#### 1.5.7.1 TERNARY PHASE TRANSITIONS

In a study by Nagy *et al* [105] the phase transition between Al<sub>3</sub>Fe and Al<sub>6</sub>Fe was investigated. The same author [122] also attempted to qualitatively analyse the phase transition that occurs when homogenising semi-continuously cast extrusion aluminium billets, containing 0.58 m% Fe and 0.21 m% Si, using the Mössbauer technique. In order to study the phase transformations in the ternary alloys heat treatments were performed at 450, 530, 590, and 620°C from 10 to 3000 minutes. The as-cast billet contained  $\alpha_c$ -AlFeSi predominately, with small levels of Al<sub>6</sub>Fe and Al<sub>3</sub>Fe being detected, and also a singlet attributed to AlFe was incorporated into the analysis. Annealing the billets at 450°C and 530°C, regardless of the time interval, did not significantly change the phase composition of the alloy. At 590°C there were no changes in the amounts of AlFe and Al<sub>6</sub>Fe, but  $\alpha_c$ -AlFeSi slowly decomposed forming Al<sub>3</sub>Fe + Si.

When the billet was annealed at 620°C three processes were witnessed to occur, in the first 90 minutes:

1.  $\alpha_c$ -AlFeSi rapidly decomposed to form  $\text{Al}_3\text{Fe}$  and Si.
2.  $\text{Al}_6\text{Fe}$  decomposed to form  $\text{Al}_3\text{Fe}$ .
3.  $\text{Al}_3\text{Fe}$  and Si combined to form  $\alpha_H$ -AlFeSi

After the annealing time passed 300 minutes no change was evident in the ratios of the remaining stable phases, namely  $\text{Al}_3\text{Fe}$ ,  $\alpha_H$ -AlFeSi, and AlFe. This analysis would seem to indicate that the metastable phase  $\text{Al}_6\text{Fe}$  is relatively more unstable when compared to  $\alpha_c$ -AlFeSi, but no attempt was made to quantify this, or the reaction kinetics.

## REFERENCES

- [1] A. V. Zeerleder, *“The Technology of Aluminum and its Light Alloys”*, (High Duty Alloys, 1938).
- [2] C. J. Smithells, *“Metals Reference Book”*, (Butterworths, London, 1976).
- [3] I. J. Polmear, *“Light Alloys - Metallurgy of the Light Metals”*, (Chapman and Hall, London, 1989).
- [4] R. Petrucci, *“General Chemistry”*, (Macmillan, London, 1985).
- [5] L. F. Mondolfo, *“Aluminum Alloys: Structure and Properties”*, (Butterworths, London, 1976).
- [6] H. Westengen, *Z. Metallkde.*, **73** (1982) 360.
- [6a] H. Matyja, B. C. Giessen, N. J. Grant, *J. Inst. Mets*, **96** (1968) 30.
- [7] I. Mikki, H. Kousage, K. Nagahama, *J. Inst. L. Met.*, **25** (1975) 1.
- [8] D. Laing, W. Jie, H. Jones, *J. Cryst. Growth*, **135** (1994) 561.
- [9] J. D. Hunt, *“Solidification and Casting of Metals”*, (Metals Society, London, 1979).
- [10] W. Kruz, D. J. Fisher, *Acta. Met.*, **29** (1981) 977.
- [11] R. Trivedi, *Met. Trans A*, **15A** (1984) 977.
- [12] A. Geying, L. Liwin, *J. Cryst. Growth*, **80** (1987) 383.
- [13] L. Makkonen, *Mater. Sci. Eng.*, **148A** (1991) 141.
- [14] K. R. Van Horn, *“Aluminum: Properties, Physical Metallurgy, and Phase diagrams”*, (Chapman and Hall, London, 1967).
- [15] H. Kosuge, I. Mizukami, *J. Inst. L. Met.*, **25** (1975) 48.
- [16] D. Altenpohl, *Z. Metallkde*, **44** (1953) 536.
- [17] D. Altenpohl, *Z. Metallkde*, **46** (1955) 535.
- [18] L. A. Morris, A. E. Hyde, *Technical note, Alcan International Ltd.*, (1971).
- [19] T. Saebo, *“Light Metals 1976”*, (American Institute of Mining, New York, 1976).
- [20] M. Cooper, *Acta. Cryst.*, **23** (1967) 1106.
- [21] K. Robinson, P. J. Black, *Phil Mag.*, **44** (1953) 1392.
- [22] P. J. Black, *Acta. Cryst.*, **8** (1955) 43.

- [23] E. H. Hollingsworth, G. R. Frank, R. E. Willet, *Trans. Met. Soc. AIME*, **224** (1962) 188.
- [24] A. Asami, T. Tanaka, A. Hidenno, *J. Inst. L. Met.*, **28** (1978) 321.
- [25] R. M. K. Young, T. W. Clyne, *Scripta Met.*, **15** (1981) 1211.
- [26] P. Skjerpe, *Met. Trans.*, **18A** (1987) 189.
- [27] P. Liu, T. Thorvaldsson, G. L. Dunlop, *Mat. Sci. Tech.*, **2** (1986) 1009.
- [28] H. Suzuki, M. Kanno, *J. Inst. L. Met.*, **28** (1978) 284.
- [29] H. Kosuge, T. Tanaka, *J. Inst. L. Met.*, **29** (1979) 64.
- [30] P. V. Evans, J. Worth, A. Bosland, S. C. Flood, “*Proc. 4<sup>th</sup> Decennial International Conf. on Solidification Processing*”, Sheffield (1997) 531.
- [31] P. J. Black, *Met. Abstracts*, **1** (1966-1967) 1172.
- [32] M. Hansen, K. Anderko, “*Constitution of Binary Alloys*”, (McGraw-Hill, New York, 1958).
- [33] A. Roth, *J. Inst. Mets.*, *Met. Abstracts*, **7** (1941) 8.
- [34] J. K. Edger, *J. Inst. Mets.*, *Met. Abstracts*, **16** (1950) 124.
- [35] J. K. Edger, *J. Inst. Mets.*, *Met. Abstracts*, **17** (1951) 799.
- [36] H. W. L. Phillips, *J. Inst. Mets.*, *Met. Abstracts*, **21** (1955) 517.
- [37] H. Zoller, *J. Inst. Mets.*, *Met. Abstracts*, **25** (1959) 130.
- [38] D. Laing, P. Gilgien, H. Jones, *Scripta Met.*, **32** (1995) 1513.
- [39] H. J. Seeman, *Metals Abstracts*, **5** (1973) 120149.
- [40] A. Fontaine, *Metals Abstracts*, **4** (1972) 140074.
- [41] A. Fontaine, *Metals Abstracts*, **4** (1972) 311417.
- [42] J. R. Lee, *J. Inst. Mets.*, *Met. Abstracts*, **28** (1962) 859.
- [43] P. J. Black, *Acta Cryst.*, **8** (1955) 43.
- [44] P. J. Black, *Acta Cryst.*, **8** (1955) 175.
- [45] A. Osawa, *Sci. Rep. Tohoku Univ.*, **22** (1933) 803.
- [46] A. Bachmetew, *Z. Krisallogr.*, **89** (1944) 575.
- [47] G. Phragmen, *J. Inst. Met.*, **77** (1950) 489.
- [48] V. Kumar, *Mat. Sci. Forum*, **22-24** (1987) 283.
- [49] C. L. Henley, *J. Non-Cryst. Sol.*, **75** (1985) 91.
- [50] P. J. Black, W. H. Taylor, *Rev. Mod. Phys.*, **30** (1958) 55.

- [51] R. C. Hudd, W. H. Taylor, *Acta Cryst.*, **15** (1962) 441
- [52] K. K. Fung, C. Y. Yang, Y. Q. Zhou, J. G. Zhou, W. S. Zhan, B. G. Shen, *Phys. Rev. Letts.*, **56** (1986) 191.
- [53] V. Kumar, D Sahoo, G. Athithan, *Phys. Rev.*, B34 (1986) 6924.
- [54] G. Rogers, Y. Mayhew, "*Engineering Thermodynamics*", (Longman Scientific and Technical, New York, 1989).
- [55] B. A. Mueller, J. H. Perepezko, *Met. Trans A*, **18A** (1987) 1143.
- [56] J. C. Anderson, K. D. Leaver, R. D. Rawlings, J. M. Alexander, "*Materials Science*", (Chapman and Hall, London, 1990).
- [57] P. Skjerpe, *Acta Cryst.*, **B44** (1988) 480.
- [58] D. A. Porter, H. Westengen, "*Quantitative Microanalysis with High Spatial Resolution*", (The Metals Society, London, 1981).
- [59] C. J. Simensen, P. Fartum, A. Andersen, *Fresenius Z. Anal. Chem.*, **319** (1984) 286.
- [60] K. L. Walford, *Acta Cryst.*, **18** (1965) 287.
- [61] M. Chandraseken, Y. P. Lin, R. Vincent, G. Staniek, *Scripta Met.*, **22** (1988) 797.
- [62] R. M. K. Young, T. W. Clyne, *Scripta Met.*, **15** (1981) 1211.
- [63] A. J. Bradley, A. Taylor, *Proc. Roy. Soc. London*, A166 (1938) 353.
- [64] F. Keller, G. W. Willcox, *Metal Progr.* **23(2)** (1933) 44.
- [65] F. Keller, G. W. Willcox, *Metal Progr.* **23(4)** (1933) 45.
- [66] F. Keller, G. W. Willcox, *Metal Progr.* **23(5)** (1933) 38.
- [67] G. Phragmen, *J. Inst. Met.*, **77** (1950) 489.
- [68] H. W. L. Phillips, *J. Inst. Met.*, **82** (1953-54) 197.
- [69] P. J. Black, O. S. Edwards, J. B. Forsyth, *Acta Cryst.*, **14** (1961) 993.
- [70] A. D. I. Nicols, *Acta Cryst.*, **6** (1953) 285.
- [71] J. B. Forsyth, M. Wells, *Acta Cryst.*, **12** (1959) 412.
- [72] V. G. Rivlin, G. V. Raynor, *J. Inst. Met. Rev.*, **3** (1981) 133.
- [73] J. N. Pratt, G. V. Raynor, *J. Inst. Met.*, **79** (1951) 211.
- [74] M. Armand, *J. Inst. Mets., Met. Abstracts*, **20** (1954) 621.
- [75] M. Armand, *J. Inst. Mets., Met. Abstracts*, **23** (1957) 626.
- [76] R. N. Corby, P. J. Black, *Acta Cryst.*, **B33** (1977) 3468.

- [77] R. N. Corby, P. J. Black, *Acta Cryst.*, **B29** (1973) 2669.
- [78] P. J. Black, R. N. Corby, "Anomalous Scattering", (Munksgaard, Copenhagen, 1975).
- [79] P. J. Black, *Acta Metall.*, **4** (1956) 172.
- [80] M. Cooper, *Acta Cryst.*, **23** (1967) 1106.
- [81] M. Cooper, K. Robinson, *Acta Cryst.*, **20** (1966) 614.
- [82] G. Bergamn, *Nature London*, 169 1057.
- [83] G. P. Huffamn, R. M. Fisher, *J. App. Phys.*, **38** (1967) 735.
- [84] L. Cser, J. Ostanevich, L. Pal, *Phys. Stat. Sol.*, **20** (1967) 581.
- [85] L. Cser, J. Ostanevich, L. Pal, *Phys. Stat. Sol.*, **20** (1967) 591.
- [86] G. K. Wertheim, J. H. Wernick, *Acta. Met.*, **15** (1967) 297.
- [87] V. V. Nemoshkalenko, O. N. Rasumov, V. V. Gorskii, *Phys. Stat. Sol.*, **29** (1968) 45.
- [88] R. H. Bush, C. A. Stickels, L. W. Hobbs, *Scripta Met.*, **1** (1967) 75.
- [89] S. Nasu, Y. Murakami, *Phys. Stat. Sol.*, **46** (1971) 711.
- [90] C. Janot, H. Gibert, *J. Phys F: Metal Phys.*, **7** (1977) 231.
- [91] R. S. Preston, R. Gerlach, *Phys. Rev. B*, **3** (1971) 1519.
- [92] S. Nasu, U. Gonser, P. H. Shingu, Y. Murakami, *J. Phys F: Metal Phys.*, **4** (1974) 124.
- [93] H. Ichinose, K. Sassa, Y. Ishida, M. Kato, *Phil. Mag.*, **39** (1977) 1367.
- [94] K. Sassa, H. Goto, Y. Ishida, M. Kato, *Scripta Met.*, **11** (1977) 1029.
- [95] R. S. Preston, S. Nasu, U. Gonser, *J. de Phys.*, **C2** (1979) 564.
- [96] G. Vogl, W. Mansel, G. Vogl, *J. Phys F: Metal Phys.*, **4** (1974) 2321.
- [97] S. Nasu, M. Kirtani, *Point Def. and Def. Int. Met.*, (1982) 461.
- [98] K. O. Sorensen, R. M. J. Cotterill, *Acta. Met.*, **22** (1974) 1331.
- [99] W. Mansel, G. Vogl, *J. Phys F: Metal Phys.*, **7** (1977) 253.
- [100] G. Vogl, W. Mansel, P. H. Dedrichs, *Phys. Rev. Lett.*, **36** (1976) 1497.
- [101] Z. Homonnay, A. Vertes, D. L. Beke, I. Godeny, *J. Radioanal. Nucl. Chem. Lett.*, **5** (1989) 371.
- [102] R. S. Preston, R. Gerlach, *Phys. Rev. B*, **3** (1971) 1519.
- [103] C. A. Stickels, R. H. Bush, *Met. Trans. A*, **2** (1971) 2031.

- [104] S. Nagy, L. Murgas, Z. Homonnay, A. Vertes, *Mat. Sci. Forum*, **13/14** (1987) 313.
- [105] S. Nagy, A. Vertes, Z. Homonnay, L. Murgas, *Acta Met.*, **35** (1987) 735.
- [106] R. S. Preston, *Met. Trans. A*, **3**(1972) 1831.
- [107] A. Vertes, S. Nagy, M. Zaki-Awad, J. Laker, E. Kovacs-Cselenyi, G. Groma, *Scripta Met.*, **16** (1982) 145.
- [108] S. Nasu, U. Gonser, “*Proceedings Mössbauer Conf.*”, Bratislava, 311.
- [109] S. Nasu, U. Gonser, R. S. Preston, *J. de Phys.*, **C1** (1980) 385.
- [110] C. M. Chittaranjan, V. Kumar, B. Viswanathan, K. P. Gopinathan, *Sol. Stat. Comm.*, **79** (1991) 69.
- [111] L. Murgas, Z. Homonnay, S. Nagy, A. Vertes, *Met Trans. A*, **19** (1988) 259.
- [112] A. Vertes, Cs. Szeles, S. Nagy, K. Suvegh, Z. Homonnay, L. Murgas, *Hyp. Int.*, **66** (1991) 191.
- [113] J. W. Christian, “*The Theory of Transformation in Metal and Metal Alloys*”, (Pergamon Press, London, 1975).
- [114] S. Mantl, W. Petry, K. Schroeder, G. Vogl, *Phys. Rev.*, **B27** (1983) 5313.
- [115] G. M. Hood, *Phil. Mag.*, **27** (1973) 305.
- [116] R. Tonejc, *Phil. Mag.*, **27** (1973) 753.
- [117] E. Kuzmann, A. Vertes, A. Griger, V. Stefaniay, *Hyp. Int.*, **92** (1994) 943.
- [118] P. J. Schurer, B. Koopmans, F. Van Der Woude, *Sol. Stat. Comm.*, **59** (1986) 619.
- [119] T. Turmezey, V. Stefaniay, A. Griger, *Key Eng. Mater.*, **39** (1989) 43.
- [120] T. Suzuki, K. Arai, M. Shiga, Y. Nakamura, *Met. Trans. A*, **16A** (1985) 1937.
- [121] H. W. L. Phillips, “*Annotated Equilibrium Diagram of Some Aluminum Alloy Systems*”, (The Institute of Metals, London, 1959).
- [122] S. Nagy, Z. Homonnay, A. Vertes, L. Murgas, *Acta Met.*, **35** (1987) 741.

## CHAPTER 2

# MÖSSBAUER SPECTROSCOPY

### 2.1 INTRODUCTION

The study of recoilless nuclear resonant absorption or fluorescence is more commonly known as Mössbauer spectroscopy. From its first origins in 1957, it has grown rapidly to become an important research method in solid-state physics and chemistry.

Resonant nuclear processes had been looked for without success for nearly thirty years before Rudolf L. Mössbauer made his first accidental observation of recoilless resonant absorption in  $^{191}\text{Ir}$  in 1957 [1]. He not only produced a theoretical explanation of the effect which now bears his name, but also devised an elegant experiment which today remains mostly unmodified as the primary technique of Mössbauer spectroscopy.

The Mössbauer effect is of fundamental importance, in that it provides a means of measuring the comparatively weak interactions between the nucleus and the surrounding electrons. Although the effect is only observed in the solid state, it is precisely in this area that some of the most exciting advances in chemistry and physics are being made. Because it is specific to a particular atomic nucleus, such problems as the electronic structure of impurity atoms in alloys, the after effects of nuclear decay, and the nature of the active centres in iron bearing proteins are just a few of the diverse and many applications.

Before delving into the details of the subject, it is worthwhile considering the historical perspective of what has come to be considered as a discovery of prime importance.

Atomic resonant fluorescence was predicted, and discovered, just after the turn of the century, and within a few years the underlying theory had been developed. From a simplified viewpoint, an atom in an excited electronic state can decay to its ground

state by the emission of a photon to carry off the excess energy. A second atom of the same kind can then absorb this photon by electronic excitation. Subsequent de-excitation re-emits the photon, but not necessarily in the initial direction so that scattering or resonant fluorescence occurs. Thus, if the monochromatic yellow light from a sodium lamp is collimated and passed through a glass vessel containing sodium vapour, one would expect to see a yellow glow as the incident beam is scattered by resonant fluorescence.

A close parallel can be drawn between atomic and nuclear resonant absorption. The primary decay of the majority of radioactive nuclides produces a daughter nucleus, which is in a highly excited state. The latter then de-excites by emitting a series of  $\gamma$ -ray photons until by one or more routes, depending on the complexity of the  $\gamma$ -cascade, it reaches a stable ground state. This is a clear analogue to electronic de-excitation, the main difference being in the much higher energies involved in nuclear transitions. It was recognised in the 1920s that it should be possible to use the  $\gamma$ -ray emitted during a transition to a nuclear ground state to excite a second stable nucleus of the same isotope, thus giving rise to nuclear resonance and fluorescence.

The first experiments to detect these resonant processes by Kuhn [2] in 1929 were a failure, although it was already recognised that certain effects were probably responsible. Continuing attempts to observe nuclear resonant absorption [3] were inspired by the realisation that the emitted  $\gamma$ -rays should be an unusually good source of monochromatic radiation.

Since then, over 50 isotopes have been shown to exhibit the Mössbauer effect and more than 20 isotopes can give useful information without any extreme experimental difficulty. However, the majority of Mössbauer spectroscopy applications have concentrated on the isotopes  $^{57}\text{Fe}$  and  $^{119}\text{Sn}$ . The Mössbauer effect, as a form of high-energy resolution spectroscopy, makes use of nuclear  $\gamma$ -rays with energies in the range of 10 -100 keV. The associated lifetimes of nuclear excited states producing such  $\gamma$ -

rays are typically  $10^{-10}$  s to  $10^{-6}$  s. This results in a typical natural linewidth of the order  $10^{-8}$  eV, which may be used to probe the hyperfine structure of nuclear energy levels. This represents a spectral energy resolution of  $1:10^{12}$ , and this is shown in Chapter 2.2.1. This is a much higher intrinsic spectral energy resolution than that of any other spectroscopy.

## 2.2 THEORY OF THE MÖSSBAUER EFFECT

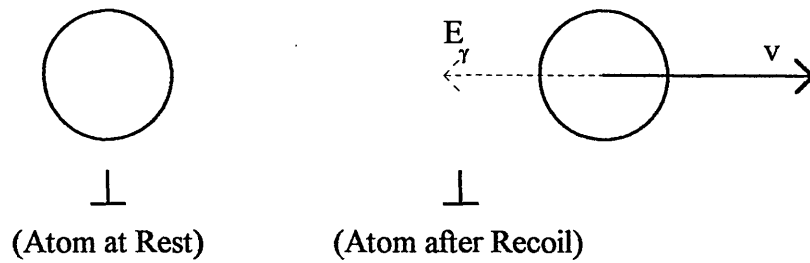
There are two factors to consider in order to observe the energy transitions associated with the Mössbauer effect. Firstly, Doppler broadening increases the effective linewidth, and secondly, the recoil of the emitting nucleus displaces the emission line from the absorption line. This makes the experimental observation of the resonance absorption interaction very difficult to measure. However, the discovery by Mössbauer was that when the emitting nucleus is within a solid matrix at low temperature, there is a high probability that the recoil momentum of the emitted  $\gamma$ -ray will be taken up by the crystal lattice as a whole, rather than by a single nucleus.

The mechanism may be described by considering an atom in the  $x$  plane, and assuming that it is in the excited state,  $E_{ex}$ . Its transition energy,  $E_t$ , between the ground state,  $E_g$ , and the excited state can be expressed as:

$$E_t = E_{ex} - E_g$$

**Equation 2.1**

The atom will also possess some thermal kinetic energy,  $\frac{1}{2}mV_x^2$ , and thus the total energy of the nucleus above the ground state before emission will be  $E + \frac{1}{2}mV^2$ . The atom then emits a  $\gamma$ -ray, and assuming there is no change in the mass of the atom, there is a change in the velocity of the atom. This is accordance with the law of conservation of energy, and the atom now has an energy  $\frac{1}{2}m(V_x + v)^2$ .



Velocity	$V_x$	$V_x + v$
Energy	$E_{ex} + \frac{1}{2}mV_x^2$	$E_\gamma + \frac{1}{2}m(V_x + v)^2$
Momentum	$mV_x$	$m(V_x + v) + E_\gamma/c$

$E_\gamma$  is the energy of the  $\gamma$ -ray. Also by the law of the conservation of energy [13]:

$$E_{ex} + \frac{1}{2}mV_x^2 = E_\gamma + \frac{1}{2}m(V_x + v)^2 \quad \text{Equation 2.2}$$

The transition energy of the atom between the excited and ground states  $\delta E$ , is the difference between  $E$  and  $E_\gamma$ . This can be written as:

$$\delta E = E_{ex} - E_\gamma = \frac{1}{2}mv^2 + mV_x v \quad \text{Equation 2.3}$$

$$\delta E = E_R + E_D \quad \text{Equation 2.4}$$

where  $E_R = \frac{1}{2}mv^2$

$$E_D = mV_x v$$

From the description of the simple mechanism, it can be seen that the  $\gamma$ -ray energy differs from the nuclear energy level separation by an amount that depends on the recoil kinetic energy,  $E_R$ , and is an inherent property of the atom. The other term is

proportional to the atom velocity before emission. This is known as the Doppler-effect energy term,  $E_D$ .

As the speeds involved are well below that of the speed of light, traditional mechanics can be used to determine the magnitude of Doppler broadening. The random thermal energy of a perfect gas is  $\frac{1}{2}kT$ , where  $k$  is the Boltzmann constant and  $T$  is the absolute temperature:

$$\frac{1}{2}mv_T^2 = \frac{1}{2}kT \quad \text{: mean kinetic energy (one dimensional case)}$$

$$\left(\frac{v_T^2}{2}\right)^{1/2} = \sqrt{\frac{kT}{m}}$$

From equations (2.3) and (2.4),  $E_D = mv_T v$

$$\therefore E_D = mv \left(\frac{v_T^2}{2}\right)^{1/2} = mv \sqrt{\frac{kT}{m}}$$

$$E_D = \sqrt{kTmv^2}$$

But  $E_R = \frac{1}{2}mv^2$

$$\therefore E_D = \sqrt{2kTE_R}$$

**Equation 2.5**

Therefore, it can be seen that the probability that resonance will occur depends on the magnitude of  $E_R$ . It can also be seen from (2.5) that for thermal broadening to be zero, and hence theoretical resolution achievable, recoil must be eliminated. This condition is achieved for some nuclear transitions due to the quantised nature of the lattice.

The same mechanisms described above can be applied to a nucleus absorbing a  $\gamma$ -ray. The atom will undergo recoil by the same amount, but in the opposite direction. Thus, there will be another distributions of energies broadened, and shifted by the relevant energy from  $E$  in the opposite direction. This is shown in Fig 2.2.

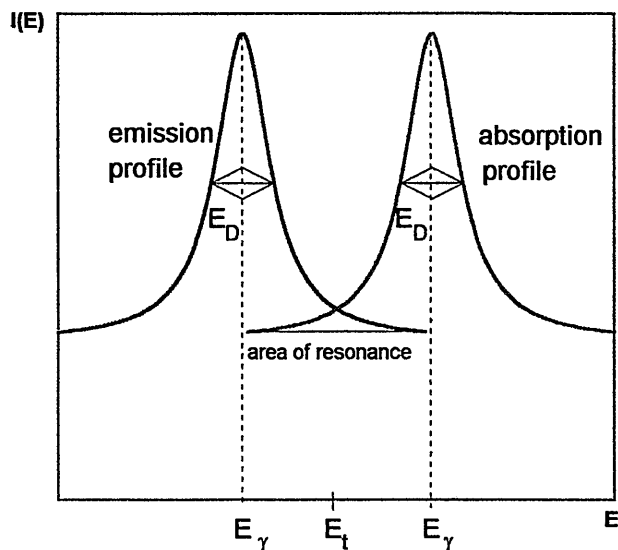


Fig. 2.2 Energy distribution profiles showing the effect of recoil and thermal Doppler broadening.

It can be seen that for an atom to absorb a  $\gamma$ -ray and then undergo the process of re-emission, there must be an overlap of the two energy distributions. That implies that the Doppler-effect energy must be of the same order of magnitude as  $2E_R$ . This was first achieved by Moon [4] in 1950, using an ultracentrifuge to accelerate the sample to over 1500 mph. Many other authors repeated the experiment using high temperatures, or nuclear reactions, to increase the Doppler broadening, and thus increasing the overlap of the two distributions. All these experiments are compensating for the recoil energy, and this remained the case until 1957.

In 1957 Mössbauer tried to increase the overlap by increasing the temperature. This implies that the molecules would have more energy and vibrate faster about their lattice positions, and thus broadening the energy distributions and providing increased

overlap. Actually what was observed was a decrease in overlap, and it was not the high-energy atoms that were causing the spectrum. This could only be reasoned if the whole lattice recoiled, and not the atom. Even in a powder, a crystallite contains around  $10^{15}$  atoms, and this reduces  $E_R$  by  $10^{15}$  making it negligible. The same argument can be applied to  $E_D$ .

The phenomenon of resonant absorption followed by recoil free emission was born, and attributed to Mössbauer which gained him the Nöbel prize.

### 2.2.1 THEORETICAL LINEWIDTH OF THE EMITTED 14.4 keV $\gamma$ -RAY

The radioactive isotope  $^{57}\text{Fe}$  is produced by the electron capture decay of  $^{57}\text{Co}$ , as shown in Fig. 2.3. The decay scheme of  $^{57}\text{Co}$  results in the emission of essentially three  $\gamma$ -rays of energies of 14.4, 122, and 136 keV.

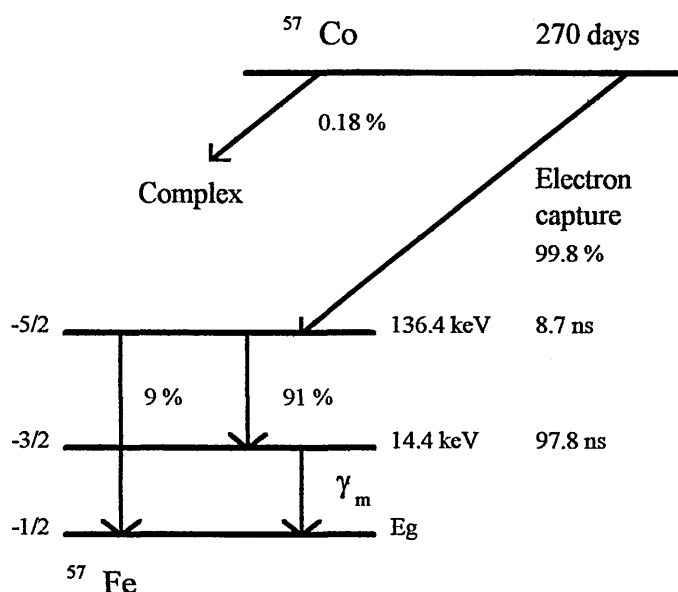


Fig 2.3 : Decay scheme for  $^{57}\text{Co}$ .

The emitted Mössbauer  $\gamma$ -ray,  $\gamma_m$  has a Lorentzian energy distribution centred on a mean energy,  $E_0$  and having a natural linewidth at half height,  $\Gamma$ , as shown in Fig. 2.4.

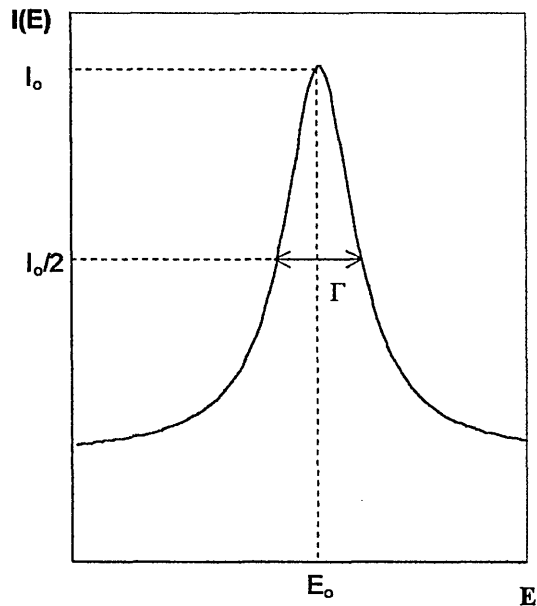


Fig. 2.4 The Lorentzian distribution of the emitted  $\gamma$ -ray.

The energy distribution of the  $\gamma$ -rays is defined by the Breit Wigner equation [5], as defined below:

$$I(E) = \text{const.} \left( \frac{\Gamma}{2\pi} \right) \frac{1}{(E - E_0)^2 + \left( \frac{\Gamma}{2} \right)^2} \quad \text{Equation 2.6}$$

The process of recoilless nuclear resonance fluorescence occurs by the superposition of the emission and absorption energy distributions associated with both the source, and the absorber.

Therefore, the theoretical Mössbauer natural linewidth,  $\Gamma_H = 2\Gamma$ , and is controlled by the Heisenberg uncertainty principle such that:

$$\Delta E \cdot \Delta t \geq \hbar \text{ or } \Gamma \cdot \tau = \hbar$$

where  $\hbar = h / 2\pi$  ( $h = \text{Planck's constant} = 6.626 \times 10^{-34} \text{ J s}$ )

and  $\tau$  is the mean lifetime, related to the half-life,  $t_{1/2}$  by the relationship:

$$\tau = \frac{t_{1/2}}{\ln 2}$$

Hence

$$\Gamma = \frac{\hbar \ln 2}{t_{1/2}} \quad \text{Equation 2.7}$$

The 14.4 keV excited state of the  $^{57}\text{Fe}$  nucleus has a half-life of 97.8 ns [6].

Substituting numerical values into Equation 2.7, the theoretical linewidth,  $\Gamma_H = 9.2 \times 10^{-9}$  eV. Therefore, this yields a theoretical resolution of:

$$\frac{\Gamma_H}{E} = \frac{9.2 \times 10^{-9}}{14.4 \times 10^3} \approx \frac{1}{10^{12}}$$

## 2.2.2. RECOIL-FREE NUCLEAR RESONANCE ABSORPTION.

The chemical binding and lattice energies in solids are of the order of 1-10eV, and are considerably greater than the free atom recoil energies. If the emitting atom is unable to recoil freely due to chemical binding, the recoiling mass can be considered to be the mass of the whole crystal.

However, this treatment is a gross over simplification. The nucleus in a solid is not bound rigidly in the crystal, but is free to vibrate. In these circumstances it is still true that the recoil energy is transferred to the crystal as a whole, since the mean displacement of the vibrating atom about its lattice position averages essentially to zero during the time of the nuclear decay. This recoil energy of a single nucleus can be taken up either by the whole crystal, or it can be transferred to the lattice by increasing the vibrational energy of the crystal.

The solid crystal lattice may be considered to be a single quantum mechanical system, and as such the vibrational energy levels are quantised. The form of this phonon quantisation will be extremely complex, and can be described using the Einstein model of solids [7]. This model assumes that a single lattice vibration frequency,  $\omega_E$ , will have allowed energy levels given by:

$$E_n = (n + \frac{1}{2})\hbar\omega_E \quad \text{Equation 2.8}$$

where  $n$  is any positive integer.

The minimum quantum of energy that the lattice will accept is thus:

$$E_E = \hbar\omega_E \quad \text{Equation 2.9}$$

where  $E_E$  is defined as the Einstein energy.

With the emission of high-energy  $\gamma$ -rays in excess of a few MeV, the associated nuclear recoil energy is comparable to typical atomic binding energies ( $\approx 10$  eV). Hence it may be possible to eject the atom from its lattice site. When  $\gamma$ -rays have energies between 0.1-1 MeV they are unlikely to cause lattice defects, but they will create large number of phonons due to the displacement of the nucleus from its mean position. The important  $\gamma$ -ray energy range, as regards to the Mössbauer effect, is that which has an

energy range of 10-100 keV. The associated recoil energy may now be less than the Einstein energy of the solid, and hence the recoil energy cannot be absorbed into the phonon spectrum. The recoil of the whole solid crystal lattice then absorbs the energy from this zero phonon transition. The emitted  $\gamma$ -ray then does not suffer any Doppler broadening effects.

A better approximation to the vibrational quantisation of a crystal lattice is given by the Debye model [6]. This model abandons the principle of a single vibration frequency, and embodies a continuum of oscillator frequencies ranging from zero up to a maximum,  $\omega_D$ .

This model is described by the following distribution formula:

$$N(\omega) = \text{const.} \times \omega^2 \qquad \text{Equation 2.10}$$

A characteristic temperature called the Debye temperature,  $\theta_D$ , is defined as:

$$\hbar\omega_D = k\theta_D \qquad \text{Equation 2.11}$$

The Debye temperature imposes a maximum number of modes of vibration in a solid. Values for  $\theta_D$  are often assigned to chemical compounds, but since the Debye model is grossly inadequate for many of the pure metals, the values used for compounds are merely an indication of the approximate lattice properties and should only be used quantitatively.

It has been shown qualitatively that the recoil-free fraction,  $f$ , or the probability of a zero phonon event will depend on three conditions:

- 1) the free atom recoil energy,
- 2) the properties of the solid crystal lattice,
- 3) the ambient temperature.

This implies that the  $f$  will be greater the smaller the probability of exciting lattice vibrations. From a quantitative perspective, the probability  $W$  of a zero-phonon  $\gamma$ -emission from a nucleus embedded in a solid lattice, which simultaneously changes its vibration state, can be calculated by using the dispersion theory [8].

For a zero-phonon emission to occur the lattice modes are unchanged, and hence the probability for this recoilless emission can be defined as:

$$f = \text{const.} \times \left| \langle L_f \rangle e^{ik \cdot x} \langle L_i \rangle \right|^2 \quad \text{Equation 2.12}$$

where  $L_f$  = final state of the atom

$L_i$  = initial state of the atom

$k$  = wave vector of the emitted photon

$x$  = co-ordinate vector of the centre of mass of the decaying nucleus

Since  $L$  is normalised the above equation can be written as:

$$f = \left[ e^{ik \cdot x} \right]^2$$

$$\therefore f = \exp\left[-k^2 \langle x^2 \rangle\right] = \exp[-2W] \quad \text{Equation 2.13}$$

The factor  $W$  is sometimes loosely called the Debye-Waller factor, though it should be called the Mössbauer-Lamb factor in this context. It was derived prior to the discovery of the Mössbauer effect as a part of the Bragg X-ray scattering theory.

Using the Debye model for a monoatomic cubic lattice  $f$  can be defined as [10,13]:

$$f = \exp \left[ -\frac{6E_R}{k\theta_D} \cdot \left\{ \frac{1}{4} + \left( \frac{T}{\theta_D} \right)^2 \int_0^{\theta_D/T} \frac{x}{e^x - 1} dx \right\} \right] \quad \text{Equation 2.14}$$

The Equation 2.14 describes the temperature dependence of the recoil-free fraction, and there are high and low temperature approximations that exists to Equation 2.14:

$$f = \exp \left[ -\frac{E_R}{k\theta_D} \left\{ \frac{3}{2} + \frac{\pi^2 T^2}{\theta_D^2} \right\} \right] \quad T \ll \theta_D \quad \text{Equation 2.15}$$

$$f = \exp \left[ -\frac{3E_R}{2k\theta_D} \right] \quad T = 0 \quad \text{Equation 2.16}$$

$$f = \exp \left[ -\frac{6E_R T}{k\theta_D^2} \right] \quad T > \frac{1}{2}\theta_D \quad \text{Equation 2.17}$$

At high temperatures it is often found that  $f$  is non-linear with respect to the temperature [11]. This indicates a departure from the Debye model, which assumes a harmonic potential for the vibrational modes [12].

## 2.3 EXPERIMENTAL

### 2.3.1 MÖSSBAUER $\gamma$ -RAY SOURCE

There are several requirements that must be fulfilled in selecting a Mössbauer  $\gamma$ -ray source before any Mössbauer resonance will be observed:

1. The energy of the  $\gamma$ -ray must be between 10 and 150 keV, preferably less than 50 keV. If the energy of the  $\gamma$ -ray is too small then the  $\gamma$ -ray will be simply absorbed by the surrounding matter. Too high an energy and the recoil free fraction falls to a very low value which could damage the surrounding matrix. This is because the recoil free fraction and the resonant cross-section both decrease with increasing  $\gamma$ -ray energy. This is the main reason why no Mössbauer resonances are known for lighter isotopes, as these  $\gamma$ -transitions are usually very energetic.
2. The half-life of the first excited state that determines  $\Gamma$  should be between 1 and 100 ns. If the half-life of the excited state is too long, then  $\Gamma$  is very narrow, which implies that it would be very difficult to record any resonance conditions due to mechanical vibrations within the spectrometer. Alternatively, if the half-life of the excited state is too short, then  $\Gamma$  is very broad, and thus a broad spectrum is obtained and obscures any useful hyperfine effects.
3. The internal conversion coefficient  $\alpha$  should be small (preferably  $<10$ ), so the production of  $\gamma$ -photons is more favourable than conversion electrons. This is achieved by ensuring that the absorption cross section is as large as possible ( $>0.06 \times 10^{-18} \text{ cm}^2$ ), as it maximises the production of  $\gamma$ -rays.

4. The non-resonant scattering of  $\gamma$ -rays should be kept at a minimum. For this reason the source isotope is usually embedded in a metal, or sometimes a metal oxide, host matrix which will have a high Debye temperature, and hence a high recoil-free fraction. The matrix, in the form of a thin foil, will usually contain the source isotope in a single, cubic, non-magnetic environment in order to prevent any quadrupole and magnetic interactions. Also the depth at which the radioactive source material is diffused into the host matrix is kept as small as possible, and this further reduces the production of non-resonant scattering of  $\gamma$ -rays.
5. The ground state isotope should be stable and have a high natural abundance, so that the inconvenience of enrichment of absorbers is unnecessary.

A  $^{57}\text{Co}$  source dispersed in an Rh metal matrix has been used in these studies. The  $^{57}\text{Co}$  nucleus undergoes electron capture with an efficiency of 99.84%, which results in a  $^{57}\text{Fe}_{26}$  excited state. The half-life of this decay process is approximately 270 days, and its initial activity was 28 mCi. The energy is then released in several ways so that the excited nucleus can reach the ground state. About 11% of the energy is lost as a 136.3 keV  $\gamma$ -ray, and 85% as a 121.9 keV  $\gamma$ -ray. The 121.9 keV  $\gamma$ -ray can then give rise to the 14.41 keV  $\gamma$ -ray, via the 3/2 to 1/2 transition, and this leaves the nucleus in the ground state. The 14.41 keV  $\gamma$ -ray is within the 10-100 keV range criteria, as discussed earlier, and it has an excited half-life of 99.3 ns. This is again in the 1-100 ns criteria, and gives rise to a minimum experimental line-width of  $0.192 \text{ mm s}^{-1}$ . The absorption cross section of  $^{57}\text{Fe}$  has an unusually large value of  $2.57 \times 10^{-18} \text{ cm}^2$ , and it again satisfies the relevant criteria. This is particularly useful as the internal conversion coefficient  $\alpha$  is fairly large ( $\alpha = 8.17$ ), which indicates that only 11% of the 3/2 to 1/2 transition emits a  $\gamma$ -ray [13]. The decay scheme is summarised in Figure 2.3.

The ground state isotope of  $^{57}\text{Fe}$  has natural abundance of approximately 2%. This is not large, but by considering the large absorption cross section of Fe, there is usually

no need for any artificial enrichment. However, the final, and main reason why this type of source was selected was all the aluminium intermetallic compounds studied contained Fe.

### 2.3.2 TRANSMISSION MÖSSBAUER ABSORBER PREPARATION

The preparation of a sample of material for Mössbauer analysis must take into account a number of different factors concerning its physical size and composition. The resulting absorber should contain enough of the resonant isotope to enable a spectrum to be recorded within a reasonable time period, but there exists an upper limit to the isotope concentration above which the resonance lines become broad due to self-absorption effect. If the material contains too much of the resonant isotope then it may prove necessary to dilute the absorber with graphite, or another inert dilutant. Too little resonant isotope may necessitate the artificial enrichment of the absorber, but this is a costly and delicate process.

The absorption may be defined in terms of the transmitted intensity at the resonant maximum,  $I_o$ , and the transmitted intensity at a large Doppler velocity where the absorption is zero,  $I_\infty$ , by [13]:

$$A = \frac{(I_\infty - I_o)}{I_\infty} \quad \text{Equation 2.18}$$

This has been evaluated, by Margulies *et al* [36], to be:

$$A = f \left[ 1 - e^{-\frac{t_a}{2}} J_0 \left( \frac{it_a}{2} \right) \right] \quad \text{Equation 2.19}$$

where  $f$  = recoil free fraction of the source,

$t_a$  = absorber thickness,

$J_0$  = zero order Bessel function.

The zero order Bessel function is defined as [23]:

$$J_0(ix) = 1 + \left(\frac{x}{2}\right)^2 + \left(\frac{\left(\frac{x}{2}\right)^4}{1^2 2^2}\right) + \left(\frac{\left(\frac{x}{2}\right)^6}{1^2 2^2 3^2}\right) + \dots \quad \text{Equation 2.20}$$

The value of  $A/f$  as a function of  $t_a$  is shown in fig 2.5, and this illustrates how the absorption shows a saturation behaviour with increasing thickness. It quickly becomes apparent that the optimum value for  $t_a$  is approximately  $10 \text{ mg cm}^{-2}$  of total iron, and this value was used as a basis for all experiments. The effects of non-resonant attenuation combined with more practical problems concerning background radiation levels make it advisable to use the smallest value of  $t_a$  which gives adequate absorption.

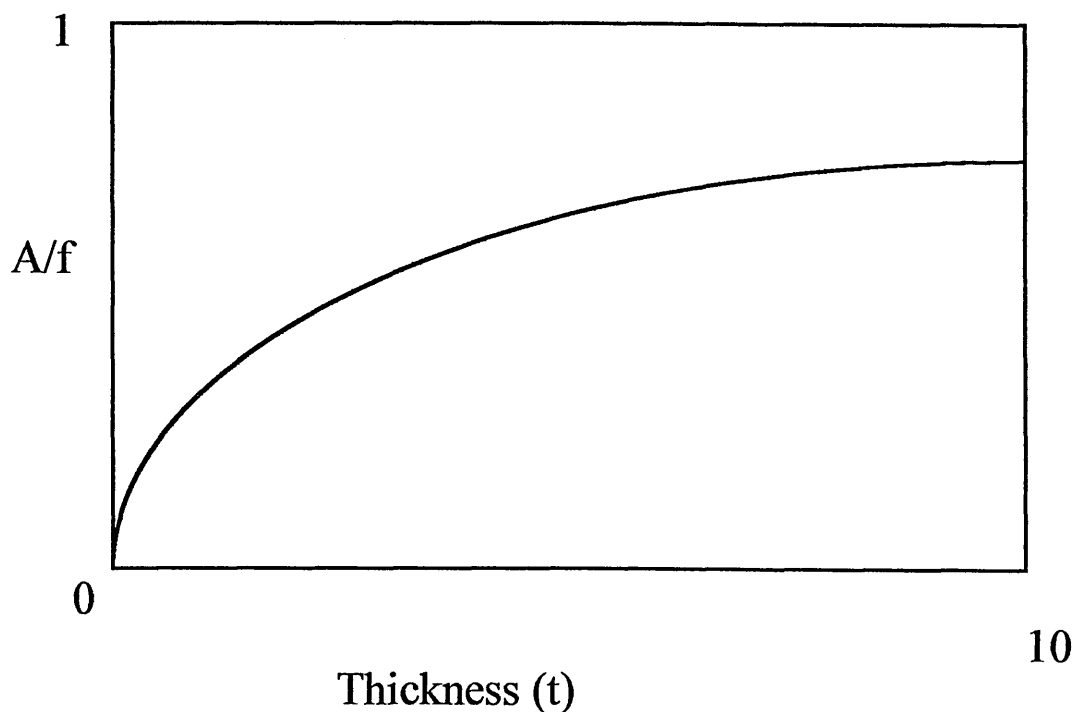


Fig 2.5 The schematic variation of  $A/f$  as function of  $t_a$  [13]

The effective Mössbauer thickness of an absorber  $t_a$  can be defined as:

$$t_a = \beta n f_a \sigma_o \quad \text{Equation 2.21}$$

Where  $\beta$  = multiplicity of the absorber spectrum,

$n$  = number of resonant nuclei per unit cross section area,

$f_a$  = recoil-free fraction of the absorber,

$\sigma_o$  = maximum absorber cross section.

For  $t_a \gg 1$  saturation effects will distort the absorption lines shapes, whilst for  $t_a \ll 1$  the line intensities are small. Optimum conditions are obtained when  $t_a \sim 0.1$ .

### 2.3.3. INSTRUMENTATION USED FOR MÖSSBAUER SPECTROSCOPY

A Mössbauer spectrum can be considered as a record of the rate of interactions occurring within a sample as a function of energy. The occurrence of the interactions can be detected by the absorption of  $\gamma$ -rays from the beam i.e. transmission Mössbauer spectroscopy, or by the detection of either conversion electrons or X-rays i.e. backscatter Mössbauer spectroscopy. The variation of  $\gamma$ -ray energy is obtained by introducing a relative motion,  $v$ , between the source and the sample by changing the energy according to the Doppler effect, given by:

$$\delta E_\gamma = E_\gamma v/c \quad \text{Equation 2.22}$$

Therefore a spectrum can be collected by recording the interaction rate for selected values of  $v$  in a “point by point” manner. This is referred as the constant velocity method. However, the need to almost constantly supervise these instruments in order to change the velocity settings proved the downfall of most of these experiments. A more convenient method, pioneered by de Beneditti [6], is to arrange a cyclic motion of either the source or sample, and to sweep through the range of velocities of interest.

By spending equal times in equal velocity increments, the motion must have constant acceleration, and this is referred to as the constant acceleration method. This is the method that most experiments are carried out today.

In this study, two Mössbauer spectrometers were used both in the constant acceleration mode. Early stages of the work used an experimental arrangement based around an Elsinct drive system. However for a major part of the work, experiments were performed using two, slightly different, modern WissEl function generator/driver systems. One was used in the transmission arrangement, and the other in the backscatter. The transmission arrangement will be discussed in detail first.

### 2.3.3.1 TRANSMISSION MÖSSBAUER SPECTROSCOPY

The transmission experimental arrangement used in this study is shown below:

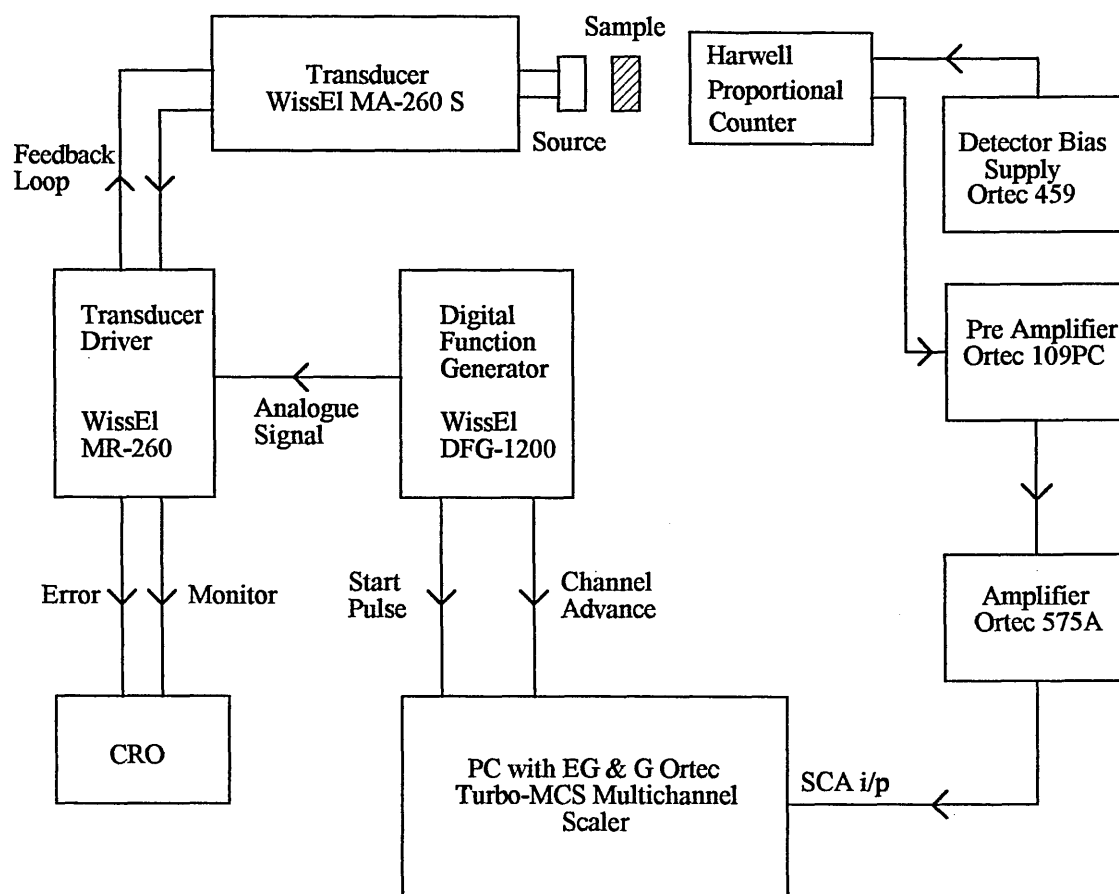


Fig. 2.6 The experimental arrangement used for transmission Mössbauer spectroscopy.

### 2.3.3.2 TRANSMISSION MÖSSBAUER SPECTROMETER OPERATION

The digital function generator DFG-1200 provides a triangular reference signal for the Mössbauer driving system 260. This reference signal is generated digitally to ensure that the source motion during the Mössbauer experiment is absolutely synchronous to the channel sweep of the Multichannel Scaler. The synchronisation is achieved by

sending a positive start pulse and a channel advance pulse when the analogue triangular reference waveform has reached its positive maximum.

The frequency of this analogue output is set at 20 Hz, which is divided in to 512 channels and hence provides the range for the velocities of interest. This analogue output is amplified by the driver unit 260 and provides the velocity transducer with precise motion of the Mössbauer source. To achieve this precise motion the driver unit and transducer form a feedback system, which minimises the deviation of the actual source motion from the ideal waveform.

The velocity transducer MA-260 S is based upon the principle of two mechanically coupled loudspeakers or coils. The first coil causes the motion of the transducer elements, and the second coil acts as a pickup to provide a signal proportional to the measured velocity back to the driver unit. This type of feedback set-up ensures an accuracy in the Mössbauer source motion to 0.15 % for a triangular waveform providing the source is rigidly mounted to the transducer and that the load is not greater than 400 g. This high accuracy of motion can be monitored by observing the CRO monitor, plus the error signals of the driver unit.

Operating bias for the counter is provided by the Ortec 459 supply unit , and was set throughout this study at -2.6 kV. The supply was fed directly into the Harwell gas filled proportional counter.

The gain of the amplifier is adjusted to give a sensible pulse height spectrum. The bipolar output pulses of the amplifier are then fed to the internal Single Channel Analyser (SCA) of the Turbo MCS Multichannel Scaler. The SCA generates an output pulse only for input voltages that rise above a lower level threshold, without exceeding an upper level threshold. These thresholds or discriminator levels are independently selectable, via the PC from 0 to +10V. However, for transmission Mössbauer spectroscopy, the discriminator levels are set,  $\pm 50$  channels, around the 14.41 keV  $\gamma$ -ray peak. This eliminates any contribution to the Mössbauer signal from

the 7.3 X-ray, and the amplifier. Thus, the SCA via a coincidence circuit allows for all pulses associated with the 14.41 keV peak to be recorded by the Multichannel Scaler (MCS).

The MCS records the number of counts over 512 channels synchronised by the digital function generator and by repetitive scanning, multiple scans are summed to diminish the statistical scatter in the recorded spectrum. Since a symmetrical waveform is used to drive the velocity transducer, a mirror image of the spectrum is obtained. This is useful as folding the data eliminates any curvature of the base line due to slightly different count rates detected at the extremes of the source motion. This symmetry also provides a useful check on the linearity of the system. Since any loss of linearity destroys the mirror symmetry.

### 2.3.3.3 $\gamma$ - RAY DETECTION

The photons generated from a  $^{57}\text{Co}$  source parent nuclide decay consist of 14.4 keV  $\gamma$ -rays (8.4 %), 122 keV  $\gamma$ -rays (85 %), 136 keV  $\gamma$ -rays (11 %) and 6.5 keV Fe K X-rays (52 %). A Mössbauer transmission  $\gamma$ -ray detector must therefore ensure high detection efficiency of the resonantly produced 14.4 keV  $\gamma$ -rays generated by the sample, whilst rejecting all the other non-resonantly produced radiations. These non-resonant radiations contribute only to the background signal.

There are three main types of detectors that can be used to identify and record Mössbauer  $\gamma$ -rays and these are scintillation counters, gas filled proportional counters, and Li drifted Ge/Si detectors.

The scintillation type of detector is frequently used for  $\gamma$ -rays with energies in the range of 50-100 keV. The resolution of this type of detector deteriorates with decreasing energy of the  $\gamma$ -photon, and these detectors can only be used for very soft  $\gamma$ -rays if the radiation background is low and there are no other X-ray or  $\gamma$ -ray lines with energies near that of the Mössbauer transition. However, the scintillation detector has

the advantage of a very high efficiency [6]. For the detection of low energy  $\gamma$ -rays, where  $E_\gamma < 40$  keV, a proportional counter offers a better resolution than the scintillation detector, but at the expense of a low efficiency and generally a lower reliability. There are a number of theories concerning the design of proportional counters, but the most successful work appears to have been achieved on an experimental and empirical basis. Li drifted Ge/Si detectors give a very highly resolved energy spectrum, but at the expense of low sensitivity, and some inconvenience in use. The resolution of this type of counter drops drastically with decreasing energy, and they are only of use at the higher end of the Mössbauer energy range [6].

This study used a gas filled proportional counter built at A.E.R.E. Harwell, containing a gas mixture of 95% Ar, and 5% CH<sub>4</sub> quench gas. The detector was used in end-on geometry, as this maximised the detection efficiency of the 14.4 keV  $\gamma$ -rays. The incident  $\gamma$ -rays pass through two 3 cm diameter aluminised mylar windows. These windows absorb the Fe K X-rays from the incident beam without significantly absorbing the higher energy 14.4 keV Mössbauer  $\gamma$ -rays. Also the counter has a 3 mm lead outer casing, and this suppresses further the generation of non-resonant radiation.

The 50  $\mu$ m diameter anode wire was operated at -2.6 kV, and the inner aluminium case was kept at 0 V. When the incident  $\gamma$ -rays pass into the counter they cause the gas mixture to ionise, and thus the charge flows to the inner aluminium case. This charge is recorded as voltage pulses, which are fed directly into the amplification section of the Mössbauer spectrometer. Fig 2.7 shows a cross section of the gas filled proportional counter.

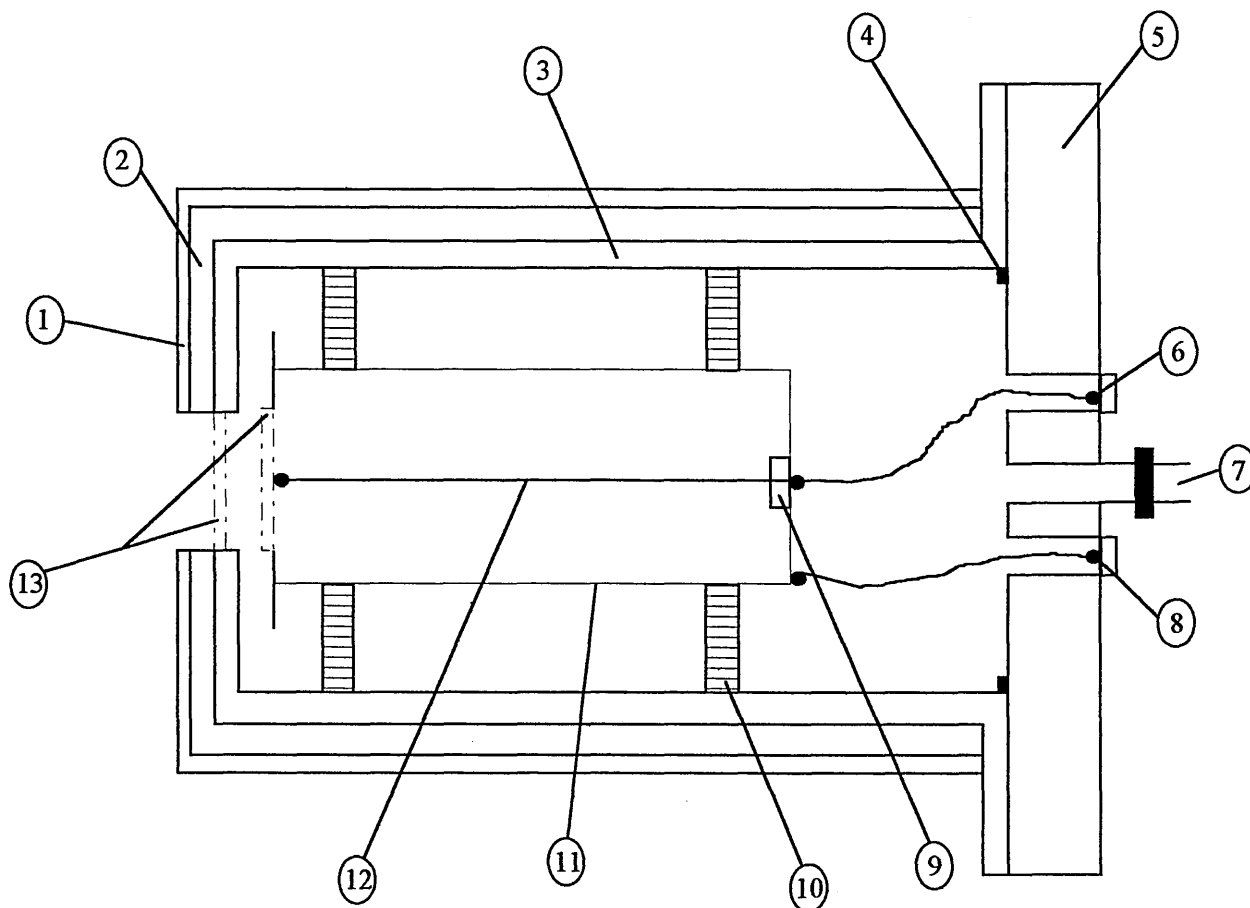


Fig. 2.7 Gas filled proportional counter. 1: outer brass casing, 2: 3 mm of lead, 3: inner brass casing, 4: O-ring seal, 5: steel end plate, 6: pre-amplifier connector, 7: gas charging valve, 8: HT connector, 9: anode wire clamp, 10: perspex insulators, 11: inner aluminium case, 12: anode wire, 13: aluminised mylar.

### 2.3.3.4 THE CRYOGENICS SYSTEMS

It may be desirable to record Mössbauer data at temperatures below room temperature. This maximises the number of zero phonon emissions from the sample. Also, variable temperature Mössbauer studies allow the detailed investigation of the hyperfine parameters of a material system to be studied. In certain circumstances the source is also cooled, but with the  $^{57}\text{Co}(\text{Rh})$  the activity is enough at room temperature that only the sample needs to be cooled. However, two considerations have to be taken into account when performing Mössbauer spectroscopy. The first of these, is the need for the path between the source, absorber, and detector to be transparent to the  $\gamma$ -rays. This is achieved by using either Be, or aluminised mylar in the relevant parts of the spectrometer. The second of these, is the absorber must not be subject to extraneous vibrations, as these would destroy any resonance conditions. This is achieved by isolating the absorber from any vibrations within the spectrometer.

For these studies the majority of the experiments were carried out using a closed-cycle He gas cryostat, which was used to achieve absorber temperatures between room temperature and 16 K. The other cryostat that was used was a liquid  $\text{N}_2$  system, and this achieved temperatures between room temperature and 77 K.

#### 2.3.3.4.1 THE HELIUM GAS 'DISPLEX' CRYOGENIC SYSTEM

The cryostat used in this study is based upon the 'Displex' system supplied by Air Products and Chemical Inc. It comprises a compressor (AP1RO2W); expansion module (AP DE202); mechanical interface (AP DMX20); temperature controller (AP DE3700) and a vacuum system, Fig 2.8. The cooling of the absorber is achieved by the expansion of He gas within a cold finger assembly, which is isolated from the absorber to negate any vibration effects.

High pressure He gas (280 Torr) from the water cooled compressor system enters the cryostat through a rotating valve. The gas then flows into the heat exchangers, and

through the slack cap. The heat exchangers, cooled during the previous cycle, cool the incoming gas. The He, as it flows through the slack cap, forces the slack cap up, and thus engaging and raising the displacer unit. This upward motion increases the available expansion volume at the two heat stations. The remaining gas above the slack cap is forced through a narrow passage into the surge volume. The rotating valve closes, and the resulting compression of the gas above the slack cap prevents the displacer unit from striking the inlet duct.

The rotating valve soon opens the exhaust port, and high pressure He within the heat exchangers is free to expand. This exhaust gas then returns to the compressor unit. This expansion of the He gas cools the two heat stations. The first heat station has a base temperature of 80 K, while the second heat station will reach a temperature of approximately 12 K. The sudden drop in pressure causes gas to bleed out of the surge volume, forcing the slack cap, and displacer unit, down. The residual gas within the displacer unit dampens this downward motion, and prevents the heat stations from colliding with the surrounding vacuum jacket. The rotating valve then closes with the displacer unit positioned for the next cycle.

For all applications of this system in this investigation it is sufficient to mount the sample at the base of the second stage heat station. However, for Mössbauer studies, vibration of the absorber due to motion of the displacer unit and valve motor is enough to destroy any resonance [15]. The vibration isolation in this system has been achieved by mounting the whole of the above assembly on a rigid platform, specifically by bolting it to one of the supporting concrete pillars of the building. The absorber and its associated heat exchangers are attached to a separate platform, which is bolted to the floor of the laboratory. The only couplings between the two components of the system are via a flexible rubber bellows, and the floor of the laboratory. The absorber disc is positioned within an In sealed sleeve at the base of the second stage heat exchanger unit.

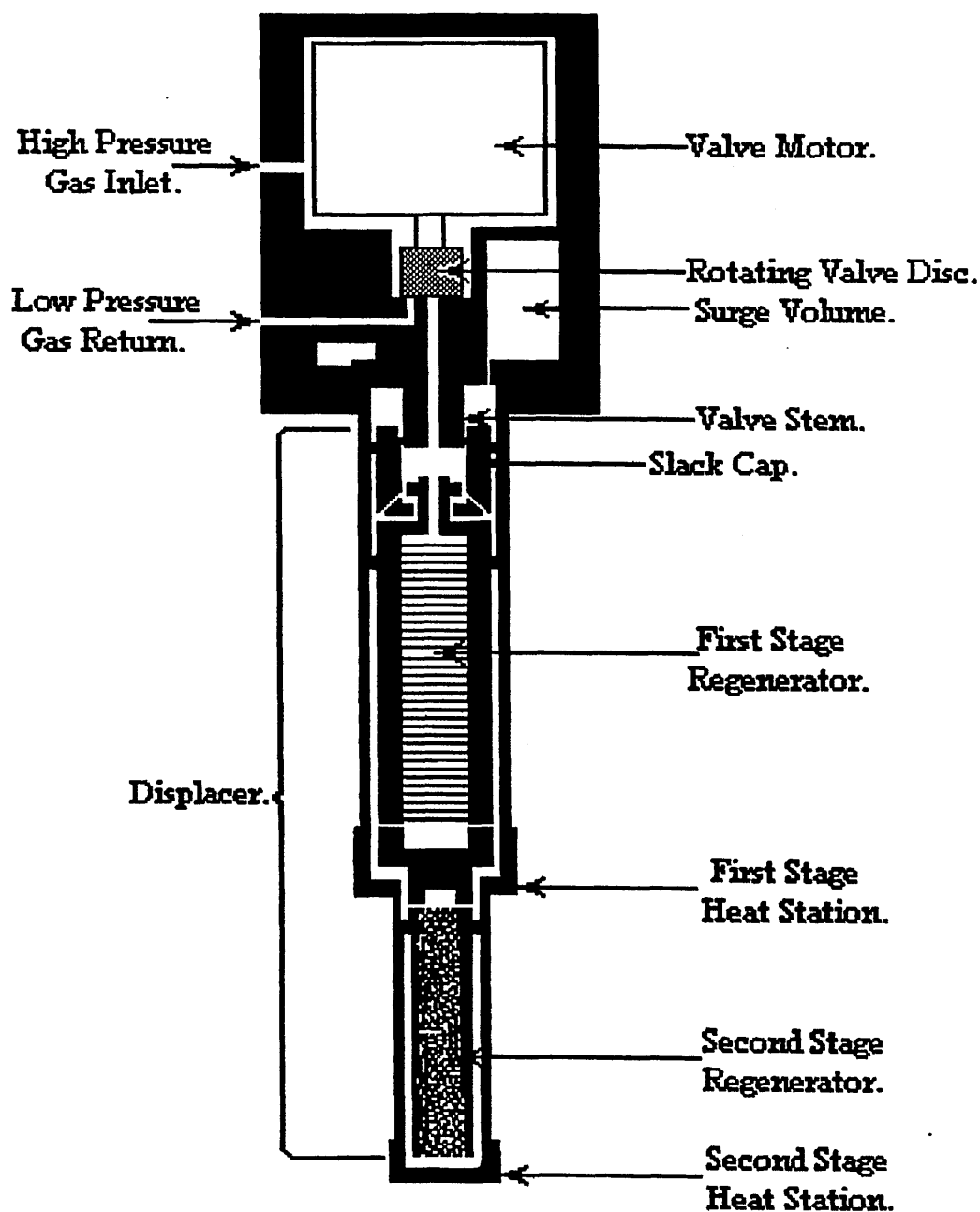


Figure 2.8 The Displex cryostat system.

An electric heater within the absorber heat exchanger allows the absorber to be maintained at any required temperature between approximately 12 K and room temperature. The heater, which has a maximum power output of 25 W, is stabilised by an electronic temperature controller which responds to a thermocouple embedded in the absorber heat exchanger.

A vacuum jacket encloses the whole arrangement, with the residual pressure maintained at  $10^{-6}$  Torr by a diffusion/rotary pump combination. Thin Be windows in this jacket enable the normal transmission Mössbauer spectroscopy to be observed.

#### 2.3.3.4.2 THE LIQUID NITROGEN CRYOGENIC SYSTEM

The sample is placed within a central chamber, and surrounded by the exchange gas. Tightly coiled around the bottom of the sample chamber is the heat exchanger. Nitrogen is drawn from the reservoir tank, and boils off cooling the chamber. The sample is then at 77 K, which is the boiling point of nitrogen. The study of the aluminium intermetallics above this temperature is achieved by a heating coil, which is wrapped around the heat exchanger. A platinum resistance probe, with an accuracy of  $\pm 2$  K, provides a signal that is fed to a temperature controller. This allows the power to the heater to be adjusted, thus keeping the sample at the required temperature. Since there are no moving parts within this system there are no vibrational problems to be addressed.

This system was used mainly for primary investigation experiments, before the aluminium intermetallics were placed within the Displex system. This enabled a comparison to be carried out on the Mössbauer parameters obtained between the two systems. As explained earlier the Displex system can experience vibrational problems.

## 2.3.3.5 BACKSCATTER MÖSSBAUER SPECTROSCOPY

The backscatter experimental arrangement used in this study is shown below:

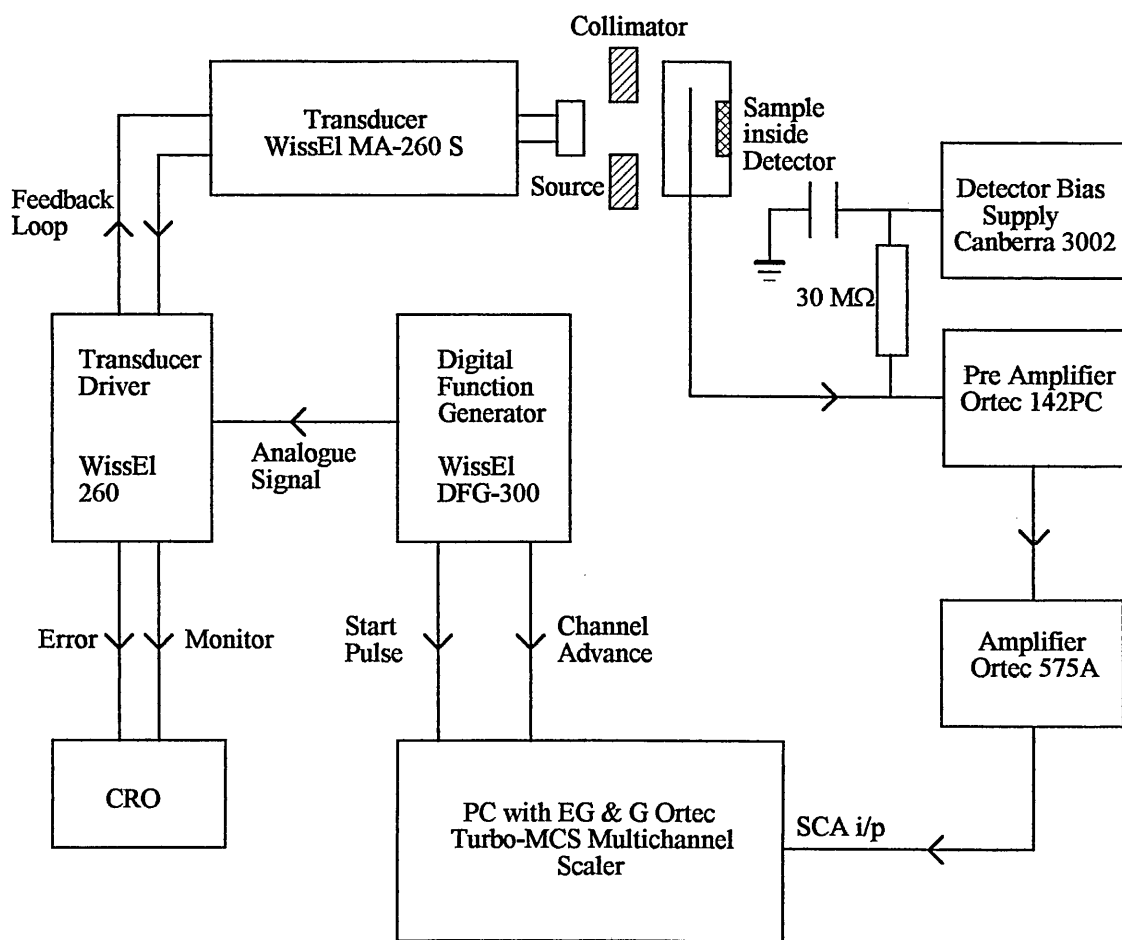


Fig. 2.9 The experimental arrangement used for backscatter Mössbauer spectroscopy.

### 2.3.3.5.1 CEMS MÖSSBAUER SPECTROMETER OPERATION

The digital function generator DFG-500 provides a triangular reference signal for the Mössbauer driving system 260. This reference signal is generated digitally to ensure that the source motion during the Mössbauer experiment is absolutely synchronous to the channel sweep of the Multichannel Scaler. The synchronisation is achieved by sending a positive start pulse and a channel advance pulse when the analogue triangular reference waveform has reached its positive maximum.

The frequency of this analogue output is set at 23 Hz that is divided in to 512 channels, and hence provides the range for the velocities of interest. This analogue output is amplified by the driver unit 260 and provides the velocity transducer with precise motion of the Mössbauer source. To achieve this precise motion the driver unit and transducer form a feedback system, which minimises the deviation of the actual source motion from the ideal waveform.

An identical velocity transducer, model MA-260 S, was used for the CEMS study, and has been described earlier in section 2.3.3.2.

Operating bias for the counter is provided through a filter and a large bias resistance of 30 M $\Omega$ . From there it is passed through the signal input cable to the counter as shown in Fig. 2.6. This input is via a short length of 93  $\Omega$  m<sup>-1</sup> impedance coaxial cable. This reduces the input capacitance to a minimum and decreasing ground loops and radio frequency pickup, both of which are sources of noise for the preamplifier. The preamplifier is powered from the 575A amplifier.

The creation of ion pairs within the counter generates a quantity of charge delivered as a narrow current pulse to the preamplifier 142PC. This preamplifier is a charge sensitive device and integrates the input charge on a feedback capacitor generating an output voltage proportional to the charge. The voltage is input to the 575A amplifier, which is powered by a NIM-standard bin unit providing  $\pm 6V$ ,  $\pm 12V$  and  $\pm 24V$ . The

amplifier provides Gaussian pulse shaping, and amplification to a suitable voltage level for further signal processing.

The gain of the amplifier is adjusted to give maximum output voltage pulses with a magnitude of 10V without saturation. The bipolar output pulses of the amplifier are then fed to the internal Single Channel Analyser (SCA) of the Turbo MCS Multichannel Scaler. The SCA generates an output pulse only for input voltages that rise above a lower level threshold without exceeding an upper level threshold. These thresholds, or discriminator, levels are independently selectable via the PC from 0 to +10V. However for CEMS, since the pulse height spectrum consists of a continual energy loss electron profile, it is only necessary to set an energy window, which eliminates the counts associated with the amplifier noise. To achieve this typical lower and upper level discriminator settings are 0.2V and 10V respectively. Thus the SCA via a coincidence circuit allows for all pulses, except for those associated with amplifier noise, to be recorded by the Multichannel Scaler (MCS).

The MCS records the number of counts over 512 channels synchronised by the digital function generator and by repetitive scanning, multiple scans are summed to diminish the statistical scatter in the recorded spectrum. Since a symmetrical waveform is used to drive the velocity transducer, a mirror image of the spectrum is obtained. This is useful as folding the data eliminates any curvature of the base line due to slightly different count rates detected at the extremes of the source motion. This symmetry also provides a useful check on the linearity of the system, since any loss of linearity destroys the mirror symmetry.

### 2.3.3.5.2 ELECTRON DETECTION

The photons generated from a  $^{57}\text{Co}$  source per parent nuclide decay consist of 14.4 keV  $\gamma$ -rays (8.4 %), 122 keV  $\gamma$ -rays (85 %), 136 keV  $\gamma$ -rays (11 %) and Fe K X-rays (52 %). A backscatter electron detector must, therefore, ensure high detection efficiency of both the resonantly produced conversion and Auger electrons generated by the 14.4 keV Mössbauer  $\gamma$ -rays, whilst rejecting the non-resonantly produced electrons associated with all incident radiations. These non-resonant electrons contribute only to the background signal and are generated by the photo-electric effect for interactions with high Z elements and Compton scattering for interactions with low Z elements.

In this study CEMS measurements were performed by mounting the sample in a gas flow proportional counter using He + 5 %  $\text{CH}_4$  as the gas mixture at a flow rate in the order of 10 ml per minute. The sample formed the cathode and the single wire formed the anode, and this was achieved by the application of a positive HT voltage to the wire. This enabled the detection of the 7.3 keV conversion and 5.6 keV Auger electrons. The counter was based upon the MBSC200 design produced by the Harwell Mössbauer group. The cylindrical chamber measured 55 mm in diameter and the anode used was 25  $\mu\text{m}$  diameter stainless steel wire. Collimation of the incident  $\gamma$ -rays was provided by a 3 mm thick lead plate having a 6 mm diameter hole. This ensured accurate beam alignment and restricted the incident  $\gamma$ -rays to the central region of the sample. Such collimation provides improved signal to noise ratio by reducing the production of non-resonant photo and Compton electrons generated by beam interactions with the counter walls. Fig. 2.9 shows a cross section of the gas flow proportional counter used.

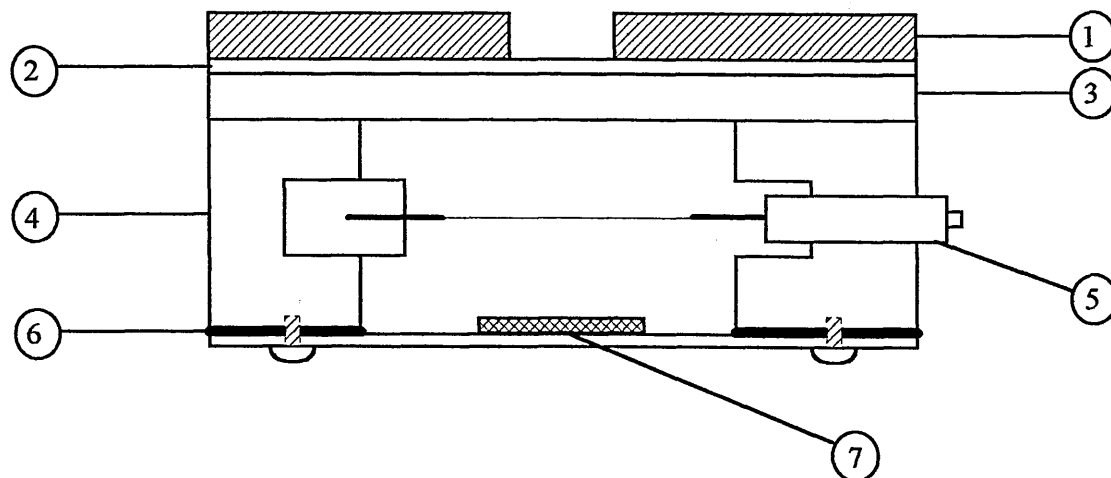


Fig. 2.10 Gas flow proportional counter; gas input and output pipes are not shown for clarity. 1: 3 mm of lead, 2: aluminised mylar, 3: perspex, 4: brass body, 5: HT connector, 6: vacuum seal and 7: sample [37].

From Fig. 2.10 it can be seen that between the collimator and the main body of the counter exists a thin aluminised mylar layer and a 4 mm thick perspex layer. These layers absorb the Fe K X-rays from the incident beam without significantly absorbing the higher energy 14.4 keV Mössbauer  $\gamma$ -rays, thereby further suppressing the creation of non-resonant electrons.

For CEMS measurements the counter is operated at a HT voltage of +1500 V that ensures the formation of ion pairs in the gas mixture and that no appreciable recombination of positive and negative ions occur. A major advantage of this counter is that by operating at a HT voltage of +1350 V, and using an Ar + 5% CH<sub>4</sub> gas mixture, the detection of the 6.3 keV fluorescent X-rays is made possible.

## 2.4 EXPERIMENTAL OBSERVATION OF THE MÖSSBAUER EFFECT

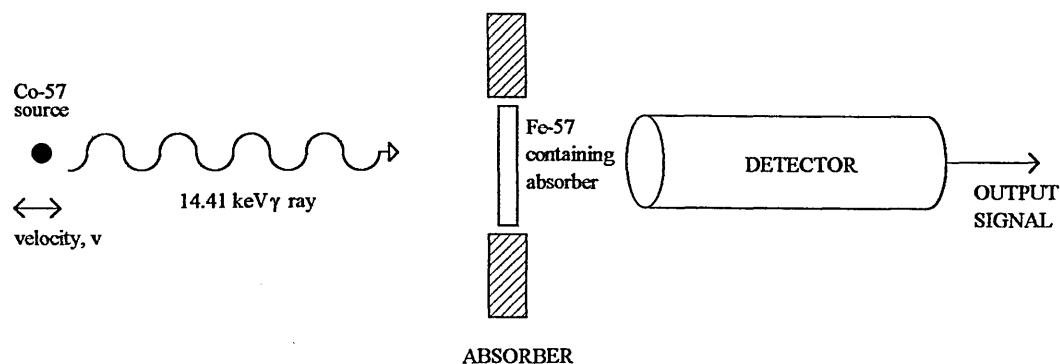


Fig. 2.11 Schematic representation of a Mössbauer experiment.

Fig. 2.11 considers the emission of the 14.41 keV Mössbauer  $\gamma$ -ray emitted by a  $^{57}\text{Co}$  source and an absorber containing  $^{57}\text{Fe}$  in an identical lattice. The detector is used to observe the intensity of the radiation that passes through the absorber. This intensity will be less than expected due to resonant absorption, and subsequent re-emission over a  $4\pi$  solid angle. In order to observe the resonance, a Doppler velocity,  $v$  is applied to the source with respect to the absorber thereby producing an energy shift of the source spectral line. The energy of the  $\gamma$ -ray,  $E_\gamma$  is modified by the Doppler relationship:

$$E_\gamma = E_o \pm \frac{E_o v}{c} \quad \text{Equation 2.23}$$

Therefore, by scanning a range of velocities, at a particular velocity and hence energy, when both the emission and absorption profiles are exactly coincident, resonance absorption will be observed. Thus a Mössbauer spectrum is a plot of absorption against a series of Doppler velocities between the source and absorber. Similarly, the modification of the emitted  $\gamma$ -ray energy by the Doppler effect can be used to achieve resonance when the transition energies of the source and absorber are different. Such differences in the nuclear energy levels are directly related to both the electronic and magnetic environment of the absorbing nuclei. Therefore, by utilising these differences

in the nuclear energy levels, Mössbauer spectroscopy is a powerful tool for investigating the chemical and physical environment of the nucleus.

#### 2.4.1 HYPERFINE INTERACTIONS

The most important consequence of the Mössbauer effect is that it makes possible the analysis of the hyperfine structure of the nuclear transitions. This is made possible by exploiting the precise energy resolution associated with the Mössbauer effect. The theoretical energy resolution provided by the Mössbauer effect for the  $^{57}\text{Fe}$  system has previously been shown to be approximately 1 part in  $10^{12}$ . The associated observed linewidths are comparable with or less than the interaction energies between the nuclei and the extra-nuclear electric and magnetic fields. These interactions between the nucleus and the surrounding environment are known as the “Hyperfine Interactions”.

The hyperfine interactions of an absorber containing a stable Mössbauer isotope are usually studied using a single line source. This radioactive source is mounted on a velocity transducer and the absorber is fixed in a suitable manner. Mössbauer absorption will take place within the absorber at a number of different Doppler energies due to the splitting of the nuclear energy levels by the hyperfine interactions. This is registered as a detected change in count rate when the Doppler velocity applied to the source brings the emitted  $\gamma$ -ray into coincidence with the absorption energy.

Three types of hyperfine interactions exist:

The isomer shift,  $\delta$ ,

The quadrupole splitting,  $\Delta E_Q$ ,

The magnetic Zeeman splitting,  $H$ .

Several review articles [6,14] describe the hyperfine interactions in detail. All the interactions can be expressed as a product of a nuclear term, which is a constant for any given Mössbauer  $\gamma$ -ray transition, and an electronic term that is related to the

absorber under study. A schematic representation of the hyperfine interactions is given in Table 2.1.

Solid State Factor	Magnetic Field	Electronic Field Gradient	Electron Density at Nuclear site
	↓	↓	↓
Interaction	$\Delta E = \mu H$	$+ Q \nabla E$	$+ \text{const} \langle R^2 \rangle \rho(0)$
	↑	↑	↑
Nuclear Interaction	Nuclear Magnetic Moment	Nuclear Quadrupole Moment	Mean Square Nuclear Charge Radius
	Magnetic Hyperfine interaction	Electric Quadrupole Interaction	Chemical Isomer Shift

Table 2.1 Schematic representation of the hyperfine interactions.

#### 2.4.1.1 ISOMER SHIFT

For many purposes, a simple description of the nucleus as a point charge that influences the extranuclear electrons, via the coulomb potential, is adequate.

However, since the nucleus has a finite volume, it is necessary to consider the nucleus-electron interaction more carefully for the purpose of understanding the nature of the isomer shift,  $\delta$ .

Essentially, the nucleus is surrounded and penetrated by electronic charge with which it interacts electrostatically. The term isomer shift refers to the difference in electrostatic interaction as a result of the difference in the nuclear radii of the ground and excited states. This change arises since the s-electron density wavefunction implies a non-zero electron charge density within the nuclear volume.

The resulting change in the coulomb interaction produces a shift in the nuclear energy levels, as shown in Fig 2.12.

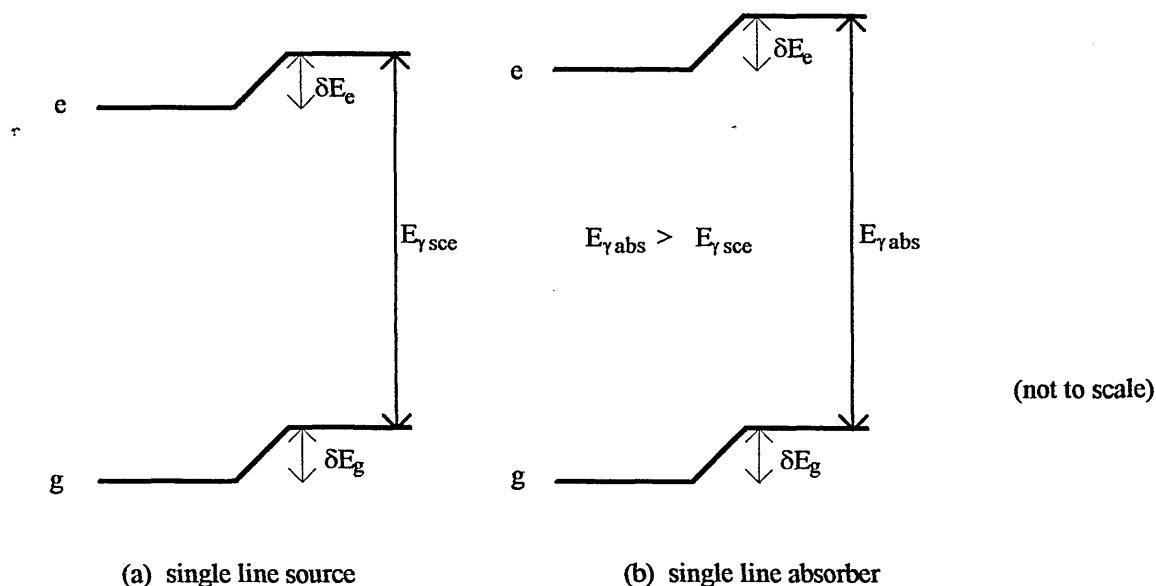


Fig 2.12 Isomer shift of the nuclear energy levels;  
(a) single line source and (b) single line absorber.

It is not possible to measure the change in the coulomb interaction directly since the change is only a small fraction of the total coulomb interaction. However it is possible to compare the change by means of a suitable reference i.e. the  $\gamma$ -ray emitted from the Mössbauer source. The observed chemical isomer shifts yields information regarding any change in the s-electron density, which may arise from a change in valence.

An expression for the isomer shift can be derived by considering the nucleus as a uniformly charged sphere of radius,  $R$  and possessing a constant s-electron density throughout the nucleus as  $|\Psi(0)|^2$ . By considering the difference between the electrostatic interaction of a point nucleus and of a nucleus having a radius,  $R$  the interaction energies can be estimated.

This energy difference,  $\delta E$  is given by:

$$\delta E = k|\Psi(0)|^2 R^2 \quad \text{Equation 2.24}$$

where  $k$  is a nuclear constant.

However, the nuclear radius,  $R$  is generally different for the ground and excited states,  $\delta E_g$  and  $\delta E_e$  respectively. Therefore equation 2.24 becomes:

$$\delta E_e - \delta E_g = k|\Psi(0)|^2 (R_e^2 - R_g^2) \quad \text{Equation 2.25}$$

The  $R$  values are nuclear constants, but  $|\Psi(0)|^2$  varies from compound to compound.

The energy difference is measurable in a Mössbauer experiment by comparing the source nuclear transition energy  $E_{\gamma_{sce}}$  with the absorber nuclear transition energy  $E_{\gamma_{abs}}$ .

This transition energy difference can be expressed as:

$$\delta = k(R_e^2 - R_g^2) \left\{ |\Psi(0)|_{abs}^2 - |\Psi(0)|_{sce}^2 \right\} \quad \text{Equation 2.26}$$

Since the change in the radius  $R_e - R_g$  is very small, the normalised radius difference,  $\delta R/R$  allows equation 2.26 to be re-written as:

$$\delta = 2kR^2 \frac{\delta R}{R} \left\{ |\Psi(0)|_{abs}^2 - c \right\} \quad \text{Equation 2.27}$$

where  $\delta R = R_e - R_g$  and  $c$  is a constant characteristic of the radioactive source used.

For a given nuclide both  $|\Psi(0)|_{sce}^2$  and  $\delta R/R$  are constant, and the isomer shift can be related to  $|\Psi(0)|_{abs}^2$  once the sign of  $\delta R/R$  is known. For the  $^{57}\text{Fe}$  system  $\delta R/R$  is less

than zero and the isomer shift decreases as  $|\Psi(0)|_{obs}^2$  increases. Hence an increase in the isomer shift implies a decrease in s-electron density.

Although changes in isomer shifts are due to s-electron density variation at the nucleus, differences in isomer shifts are observed on addition or removal of p-, d- and f-electrons. These electrons do not interact directly with the nuclear charge density but provide a screening effect, which effectively decreases the s-electron density at the nucleus. For example a  $3d^6 4s^1$  outer electronic configuration will have a higher s-electron density at the nucleus than a  $3d^7 4s^1$  electronic configuration. From this it can be clearly seen that observation of the isomer shift provides information relating to covalence and bond formation, i.e. the chemical bonding of the atom.

#### 2.4.1.2 NUCLEAR QUADRUPOLE INTERACTION

The excited spin state of a Mössbauer nucleus is invariably different to that of the ground state, due to certain nuclear selection rules. If the Mössbauer nucleus has a spin quantum number greater than  $I=1/2$  then a non-spherical charge distribution results. The effect of this is that either, or both, of the Mössbauer nucleus will possess a quadrupole moment.

This nuclear quadrupole moment will interact with the local electric field gradients surrounding the nucleus, and the magnitude of this deformation is described as the nuclear quadrupole moment,  $Q$ , and is defined as [13]:

$$eQ = \int \rho r^2 (3 \cos^2 \theta - 1) d\tau \quad \text{Equation 2.28}$$

where  $Q$  = nuclear quadrupole moment

$r$  = radius of the nucleus

$d\tau$  = volume element

$e$  = electronic charge

$\theta$  = angle to the nuclear spin quantisation axis.

The sign of the nuclear quadrupole moment depends entirely on the shape of the deformation. The implication of a negative nuclear quadrupole moment indicates that the nucleus is oblate shape, where a positive moment implies a prolate shape. The deviation of the nucleus from spherical symmetry is shown in Fig. 2.13.

When an atom is bonded chemically the charge distribution is rarely spherical, and so the electric field gradient is defined by the following tensor:

$$\nabla_{ij} E_{ij} = -V_{ij} = -\left( \frac{\delta^2 V}{\delta x_i \delta x_j} \right) \quad \text{Equation 2.29}$$

$(x_i x_j = x, y, z,)$

where  $V$  = electrostatic potential.

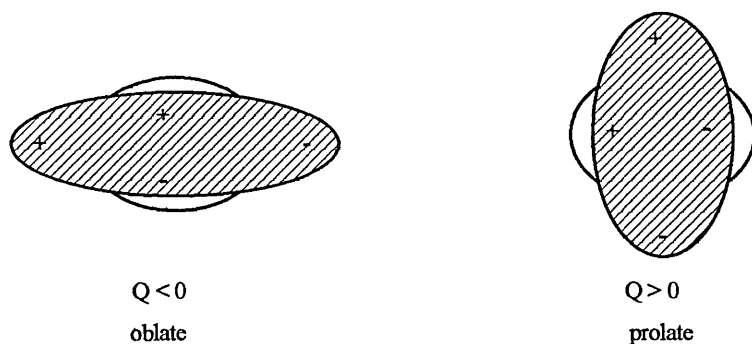


Fig. 2.13 Deviation of nucleus from spherical symmetry.

It is customary to define the axis of the resonant atom so that  $V_{zz} = eq$  is the maximum value of the electric field gradient.

The electric field gradient is usually expressed by three components  $V_{zz}$ ,  $V_{yy}$  and  $V_{xx}$ . These components do not exist independently and are related by the Laplace equation [16] to produce a co-ordinate system such that:

$$V_{xx} + V_{yy} + V_{zz} = 0 \quad \text{Equation 2.30}$$

and the asymmetry parameter defined as:

$$\eta = \frac{|V_{xx} - V_{yy}|}{V_{zz}} \quad \text{Equation 2.31}$$

Using the convention  $|V_{zz}| > |V_{yy}| > |V_{xx}|$  ensures that  $0 \leq \eta \leq 1$ . Evaluation of  $\eta$  from a Mössbauer spectrum is straightforward. However, relating  $\eta$  to the electronic structure of the compound under study is more difficult. This is due to the observed sign of  $e^2qQ$  being an important factor in deciding the origin of the electric field gradient. The simplest approach to overcome this problem is by considering a point

charge model of the electric field gradient for computing the relative magnitude of the electric field gradient [17,18].

The source of the electric field gradient is a combination from both the valence electrons of the atom and from the surrounding ions. The valence contribution,  $q_{\text{val}}$  arises from a total value of  $V_{zz} \neq 0$  due to the electron orbital population being non-spherical. The second source of the electric field gradient is termed the lattice contribution,  $q_{\text{lat}}$  resulting from the associated ligands. Both  $q_{\text{val}}$  and  $q_{\text{lat}}$  are not independent components due to shielding effects and by assuming an inverse cubic dependence on distance, the magnitude of  $q_{\text{val}}$  will be much greater than  $q_{\text{lat}}$ . Due to the two sources contributing to the electric field gradient, the observed quadrupole splitting of a Mössbauer spectrum is particularly useful for providing information regarding the spin state and the distribution geometry of the compound under study.

The quadrupole interaction results in an energy change,  $\Delta E_Q$  that is given by the following expression [3]:

$$\Delta E_Q = \frac{e^2 q Q}{4I(2I-1)} \left[ 3m_I^2 - I(I+1) \right] \left( 1 + \frac{\eta^2}{3} \right)^{1/2} \quad \text{Equation 2.32}$$

where  $Q$  = nuclear quadrupole moment

$\eta$  = asymmetry factor

$m_I$  = magnetic quantum number

$e$  = electronic charge

$eq$  = maximum value of the field gradient

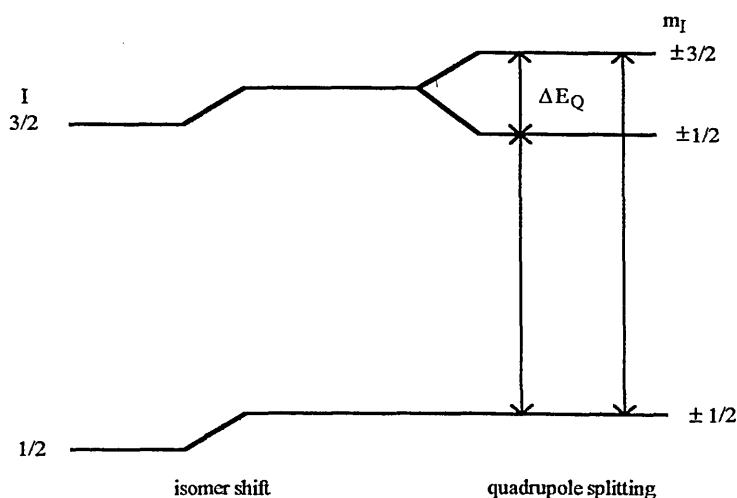
The magnitude of the quadrupole interaction is a product of two factors,  $eQ$  is a nuclear constant for a particular isotope and  $eq$  is a function of the chemical environment due to the nature of the electric field gradient.

The quadrupole interaction results in a splitting of the nuclear energy levels identified by the  $|I_z|$  quantum number. In general Mössbauer transitions occur between two nuclear levels, each of which may have a nuclear spin and quadrupole moment. This implies that the ground state and excited state levels may show a quadrupole interaction. A change in the  $I$  quantum number is allowed during the  $\gamma$ -ray transition, where:

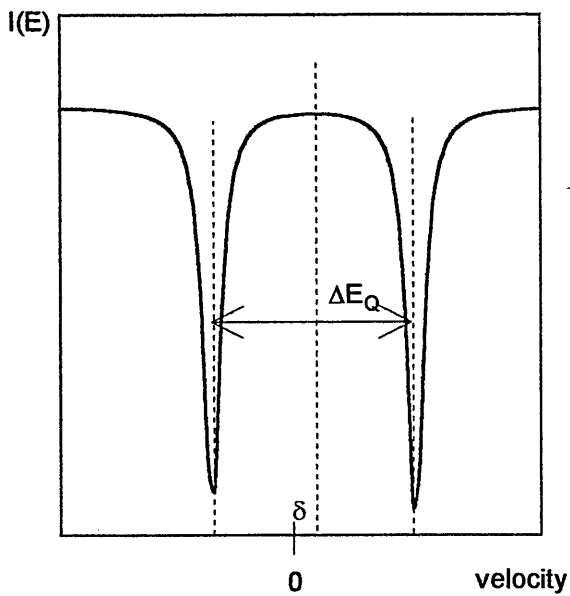
$$\left[ (I_z)_e - (I_z)_g \right] = m \quad \text{Equation 2.33}$$

$$m = 0 \pm 1$$

This means that for  $^{57}\text{Fe}$  system  $I_e = 3/2$  and  $I_g = 1/2$ , the  $I_e = 3/2$  level splits into two  $m_I = \pm 3/2$  and  $m_I = \pm 1/2$  levels. Both the possible transitions are allowed with equal probability, at temperatures above 1K, and a characteristic two line Mössbauer spectrum is observed. The separation of the two peaks is the quadrupole splitting,  $\Delta E_Q$ , and by convention is quoted in units of  $\text{mm s}^{-1}$ . Fig. 2.14 shows the quadrupole splitting of the nuclear energy levels combined with the isomer shift and the resulting Mössbauer spectrum.



(a) Energy level scheme (not to scale)



(b) Resultant Mössbauer spectrum

Fig. 2.14 Quadrupole splitting of the nuclear energy levels combined with the isomer shift for the  $^{57}\text{Fe}$  system; (a) energy level scheme and (b) resultant Mössbauer spectrum.

### 2.4.1.3 MAGNETIC HYPERFINE INTERACTION

As described in the earlier section, an electric field gradient at the nucleus leads to a partial loss of degeneracy of the nuclear energy levels, and gives rise to the nuclear quadrupole interaction. However, a magnetic field at the nucleus leads to a complete loss of degeneracy of the nuclear energy levels, and produces the nuclear Zeeman effect [19]. The magnetic field can be either within the atom, or crystal, or as a result of an externally applied magnetic field.

The magnetic hyperfine interaction,  $B$  arises from the interaction between the nuclear dipole moment,  $\mu$  with the hyperfine field,  $B$  existing at the nucleus. As a result of this interaction the energy levels are shifted by a quantity,  $E_m$ .

$$E_m = -\mu B \frac{m_I}{I} = \mu_N g_N B m_I \quad \text{Equation 2.34}$$

where  $I$  = nuclear spin

$g_N$  = nuclear g-factor ( $\mu/I\mu_N$ )

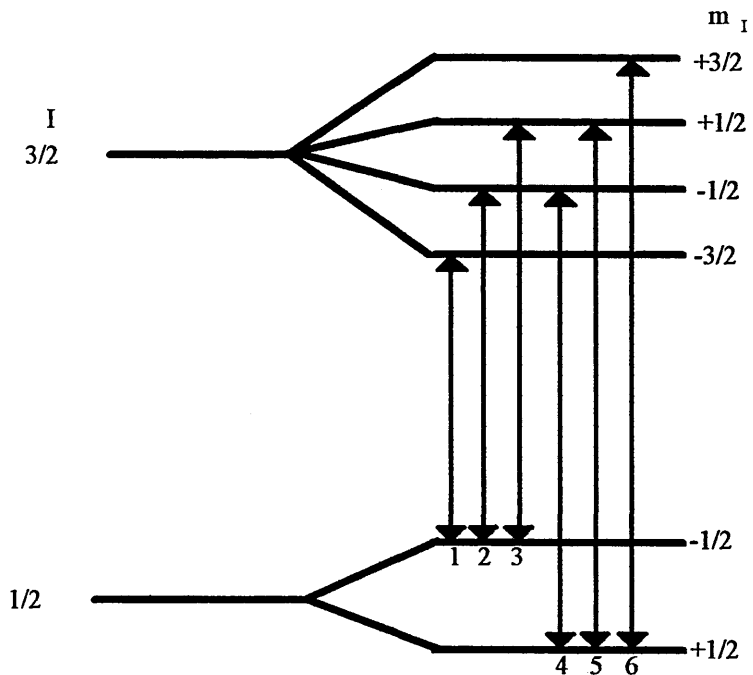
$\mu_N$  = nuclear Bohr magneton

The interaction completely removes the degeneracy of the nuclear spin,  $I$ , splitting each level into  $(2I+1)$  sub-levels. For the  $^{57}\text{Fe}$  system  $g_N$  differs in sign for the ground and excited states. The selection rule ( $\Delta m = 0$  or  $\pm 1$ ) describing the allowed Mössbauer transitions gives rise to a characteristic Mössbauer spectrum as shown in Fig. 2.15.

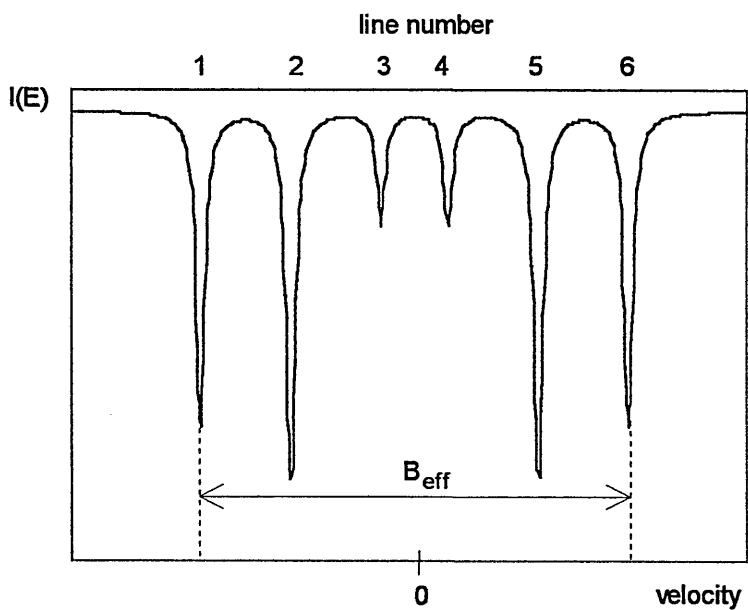
The magnetic hyperfine interaction is the product of a nuclear term, which is a constant for a given isotope and a magnetic field, which is dependent on the electronic structure of the compound under study. The observed magnetic field or effective field,  $B_{\text{eff}}$  (or  $H_{\text{eff}}$ ) may originate from the material itself or be due to an external source:

$$B_{\text{eff}} = B_{\text{internal}} + B_{\text{external}} \quad \text{Equation 2.35}$$

$B_{\text{internal}}$  originates from a number of factors arising from the motion of the electrons within the material [20]. These factors can produce field strengths at the nucleus of  $B_{\text{internal}} = 100\text{-}1000$  T.



(a) Nuclear energy scheme (not to scale)



(b) Resultant Mössbauer spectrum

Fig. 2.15 Magnetic splitting of the  $^{57}\text{Fe}$  system; (a) energy level scheme and (b) resultant Mössbauer spectrum.

Since the internal magnetic field of a magnetically ordered compound is usually proportional to the magnetisation, the temperature dependence of the magnetic splitting will follow a Brillouin function which approaches zero at the Curie or Néel temperature [3]. Observation of the magnetic splitting depends on the relaxation time of electronic spins compared with the Mössbauer event time. In Equation 2.35  $B$  is a vector product, which occurs over a time scale in the order of  $10^{-8}$  s. The electronic pairs, which generate  $B$ , undergo spin relaxation due to changes of direction. In paramagnetic compounds, this spin relaxation is rapid and results in  $B$  having a time average of zero and hence no magnetic splitting is observed. However, in ferromagnetic or antiferromagnetic compounds, the spin relaxation rate is slower and magnetic splitting is observed. Similarly, intermediate conditions regarding spin relaxation exist where the time scale is comparable with that of the Larmor frequency. Such systems include both ordered materials with unusually fast spin relaxation and also paramagnetic compounds with slow spin relaxation. These conditions result in the observation of complex Mössbauer spectra [19,21].

In compounds where two or more distinct magnetic lattices are present, the Mössbauer spectra will reveal the internal field at each individual site. Hence, observation of the magnetic splitting is particularly useful for confirming the presence of any magnetic ordering within the compound under study.

## 2.5 MÖSSBAUER DATA ANALYSIS

### 2.5.1 SPECTROMETER CALIBRATION

The spectrometer had to be calibrated, before any experiments were carried out on the system, to determine the velocity range associated with the helipot setting on the transducer drive unit. All the transmission experiments were recorded at  $\pm 2 \text{ mm s}^{-1}$ , and a suitable calibration standard used was sodium nitroprusside (SNP),  $[\text{Na}_2\text{Fe}(\text{CN})_5\text{NO} \cdot 2\text{H}_2\text{O}]$ . SNP has a single quadrupole splitting spectra, which shows a constant splitting under normal laboratory conditions of  $1.705 \text{ mm s}^{-1}$  [3].

After an inspection of the folded data set of a calibration experiment it yields initial estimates of the line positions. These are then used as starting parameters for a calibration program that fits Lorentzian lines to the data. The calibration constant,  $c$ , is then determined using the following expression:

$$c = \frac{\textit{splitting}}{2 \times \textit{Doppler velocity}} \text{ channels / mm s}^{-1} \quad \textbf{Equation 2.36}$$

A typical transmission spectrum calibration is shown in Fig. 2.16.

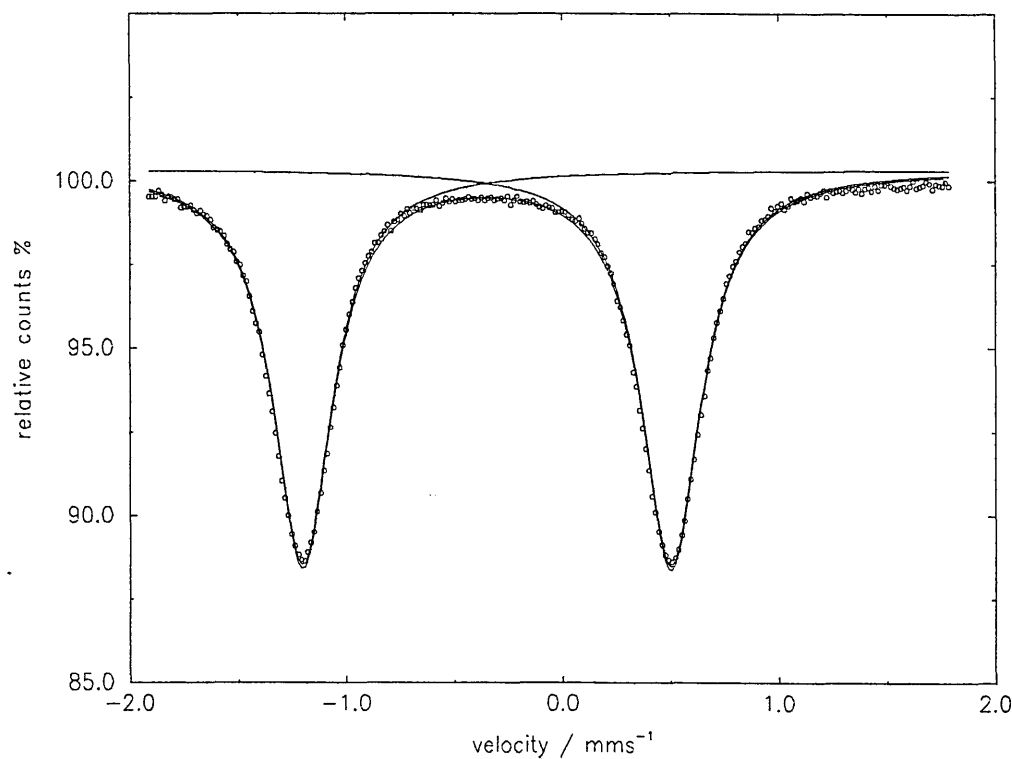


Fig 2.16 Typical transmission Mössbauer calibration from SNP.

The calibration CEMS spectrometer was performed using the magnetically split six line spectrum of a  $^{57}\text{Fe}$  enriched iron foil. The associated line positions are known to occur at the following Doppler velocities [22]:

$$\text{lines 1,6} = \pm 5.312 \text{ mm s}^{-1}$$

$$\text{lines 2,5} = \pm 3.076 \text{ mm s}^{-1}$$

$$\text{lines 3,4} = \pm 0.840 \text{ mm s}^{-1}$$

The same procedure for the determination of  $c$  is used as in SNP, but the final value for  $c$  is taken as an average of the three results obtained. However, in this study all the CEMS was obtained at  $\pm 2 \text{ mm s}^{-1}$ , therefore, only lines 3,4 were used. A typical CEMS spectrum calibration at  $\pm 8 \text{ mm s}^{-1}$  is shown in Fig. 2.17.

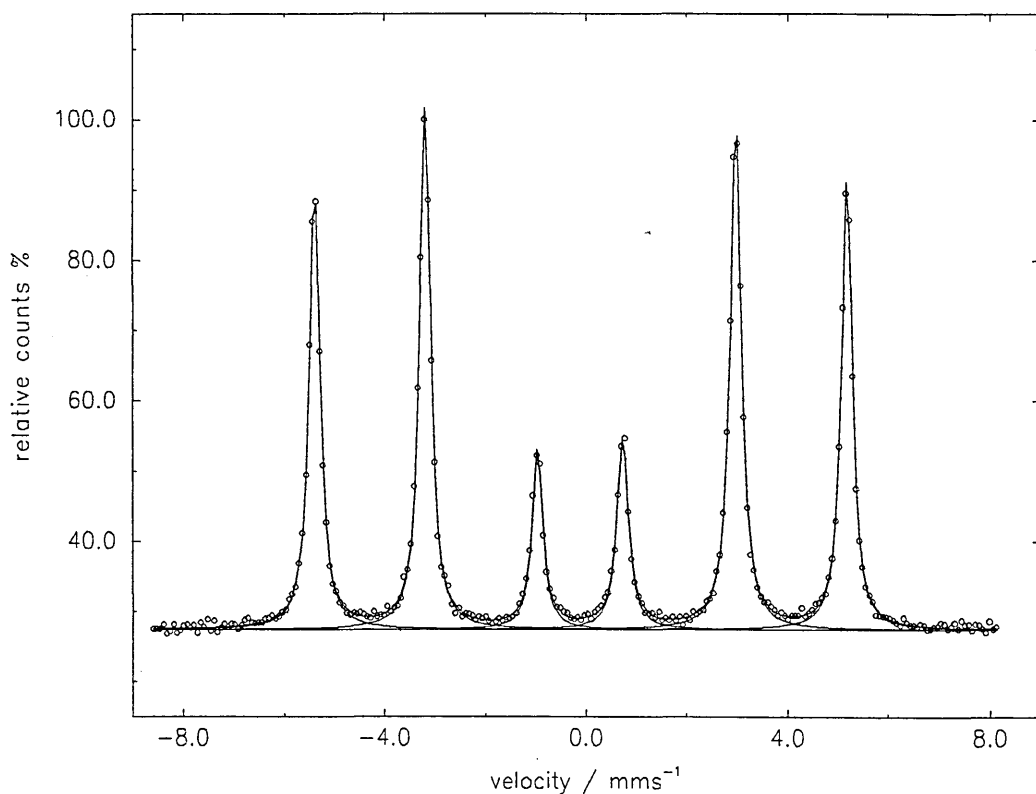


Fig. 2.17 Typical CEMS calibration from a  $^{57}\text{Fe}$  enriched iron foil.

It should be noted that any values for the isomer shift obtained during an experiment calibrated using this method, are quoted as relative to the source used. In this study a  $^{57}\text{Co}$  was used. In order to standardise these values, most publications quote the isomer shifts relative to natural iron. This then requires the addition of  $0.11 \text{ mm s}^{-1}$  to the isomer shift values.

### 2.5.2 COMPUTER FITTING

As in other spectroscopies the problem inherent in analysing Mössbauer spectra is to determine the parameters of the curve that best fits the data points comprising the spectrum. In its simplest form the Mössbauer spectrum comprises a single absorption line which has a Lorentzian shape, and therefore can be specified completely by four parameters: linewidth, line position, intensity of the absorption, and the baseline count

for zero absorption. These parameters may always be found by visual inspection, but more precise values, together with their standard deviations, are obtained by computing a least-squares fit to the data.

Marc Dominic DeLuca of Sheffield Hallam University wrote the programs used to fit the spectra in this study. These fitting programs were based upon a program written at UKAEA Harwell, by G. Longworth and T. Cranshaw [19]. The fitting values are allowed to vary as determined by the user, and then the program utilises a hybrid non-linear least squares regression algorithm routine to produce a minimisation surface. This least squares regression algorithm uses aspects from a Newton-Raphson steepest descent, and Levenberg-Marquardt methods [23]. The curve with the steepest descent determines the best fit, then the parameters are varied again within the routine from that point, until a requisite number of attempts have been made. It is then up to the user to either accept or change the parameters, and the process is repeated until a reasonable fit is obtained.

However, one word of caution must be given. A good fit to experimental data is not unambiguous proof that the theoretical function is a correct one. In a complicated spectrum it is quite feasible to fit a function which has no physical significance. The final data analysis must be compatible with other scientific evidences, and inevitably there will be instances where it is not possible to distinguish between alternative hypotheses.

### 2.5.3 ANALYSIS OF VARIABLE TEMPERATURE DATA

Most Mössbauer experiments are concerned with the identification of the hyperfine interactions that a nucleus may exhibit. In addition, it is possible to examine the vibrational properties of the Mössbauer atom by recording a series of variable temperature spectra. From these spectra there are two independent methods for determining the Debye temperature,  $\theta_D$ , and hence temperature dependence of the recoil free fraction,  $f_a(T)$ , of the absorber. The first method involves the accurate

measurement of the change in absorption line area with temperature. The second method makes use of the second order Doppler shift of the resonance line, which produces a small, but measurable, temperature dependent component to the chemical isomer shift. Both methods assume that the vibrational properties of the absorber can be represented by the Debye model. This is not strictly true, which means that the results can only be treated qualitatively, or on a comparative basis. (see Chapter 2.2.2).

### 2.5.3.1 TEMPERATURE DEPENDENCE OF THE ABSORPTION AREA, LNAT.

The probability of a recoil free emission of a  $\gamma$ -ray has been defined as:

$$f = \exp[-k^2 \langle x^2 \rangle] = \exp[-2W] \quad \text{Equation 2.13}$$

Using the Debye model for a monoatomic cubic lattice  $f$  can be defined as [10]:

$$f = \exp \left[ -\frac{6E_R}{k\theta_D} \cdot \left\{ \frac{1}{4} + \left( \frac{T}{\theta_D} \right)^2 \cdot \int_0^{\theta_D/T} \frac{x}{e^x - 1} \cdot dx \right\} \right] \quad \text{Equation 2.14}$$

The equation 2.17 describes the temperature dependence of the recoil-free fraction, and there are high and low temperature approximations to Equation 2.17, as there is no exact solution to the Debye integral. The value of the Debye integral has been tabulated for  $\theta_D/T = 0.1$  to  $\theta_D/T = 20$  using a Simpson's rule integration [24]. An approximation of the integral has been derived by fitting an arbitrary function to the tabulated data and employing a least squares minimisation routine to determine the best values for the constant [25]. The resulting approximation to the Debye integral is given by:

$$\int_0^{\theta_D/T} \frac{x}{e^x - 1} \cdot dx = 1.6449 \left( 1 - \exp \left( -0.64486 \frac{\theta_D}{T} \right) \right) \quad \text{Equation 2.37}$$

This approximation to the Debye integral gives a maximum 6% error, which can be reduced to 2% by the addition of a second arbitrary function. A second numerical method has been developed which evaluates the Debye integral in terms of an infinite series [26]. The two formulae that were derived yield less than 0.1% error within the specified ranges of  $\theta_D/T$ .

High temperature formula:

$$\int_0^{\theta_D/T} \frac{x}{e^x - 1} dx = \frac{\theta_D}{T} \left[ 1 - \frac{\theta_D/T}{4} + \frac{(\theta_D/T)^2}{36} - \frac{(\theta_D/T)^4}{3600} \right] \quad 0 \leq \theta_D/T \leq 2.2$$

**Equation 2.38**

Low temperature formula:

$$\int_0^{\theta_D/T} \frac{x}{e^x - 1} dx = \frac{\pi^2}{6} + \frac{\theta_D}{T} \log(1 - y) - y - \frac{y^2}{4} \quad 1.7 \leq \theta_D/T \leq \infty$$

**Equation 2.39**

$$\text{where } y = \exp\left(-\frac{\theta_D}{T}\right)$$

The approximations to Equation 2.17 are:

$$f = \exp\left[-\frac{E_R}{k\theta_D} \left\{ \frac{3}{2} + \frac{\pi^2 T^2}{\theta_D^2} \right\}\right] \quad T \ll \theta_D \quad \text{Equation 2.15}$$

$$f = \exp\left[-\frac{3E_R}{2k\theta_D}\right] \quad T = 0 \quad \text{Equation 2.16}$$

$$f = \exp\left[-\frac{6E_R T}{k\theta_D^2}\right] \quad T > \frac{1}{2}\theta_D \quad \text{Equation 2.17}$$

For a thin Mössbauer absorber the thickness has been defined as (see Chapter 2.3.2):

$$t_a = \beta n f_a \sigma_o \quad \text{Equation 2.21}$$

However, if  $t \leq 1$  then the absorption area is proportional to the absorber thickness, and Equation 2.24 becomes:

$$A = K(\beta n f_a \sigma_o) \quad \text{Equation 2.40}$$

$K$  is a constant. Therefore, the temperature approximations for the recoil free fraction can now be defined as [13,38]:

$$\ln(A(T)) = \ln(K\beta n \sigma_o) \left[ -\frac{3E_R}{2k\theta_D} \right] \quad T = 0$$

$$\text{Equation 2.41}$$

$$\ln(A(T)) = \ln(K\beta n \sigma_o) \left[ -\frac{3E_R}{k\theta_D} \right] + \ln(K\beta n \sigma_o) \left[ -\frac{3E_R}{k\theta_D} \right] \cdot T \quad T > \frac{1}{2}\theta_D$$

$$\text{Equation 2.42}$$

If  $\ln(A)$  is plotted against  $T$  the line produced will be flat at the y-axis, and slowly bend to give a straight line of a gradient  $(-3E_R/k\theta_D)$ . However, in practice the line will bend again at the high temperature limit due to anharmonicity in the crystal lattice. This fitting is done within the laboratory using a program written by Gavin Williams of Sheffield Hallam University, and is based on the Levenberg-Marquant algorithm. This program requires the normalised absorption areas, and the respective temperatures, to

be inputted into the program, and it evaluates the Debye integral. A least squares minimisation routine then combines the theoretical and experimental values to give a goodness of fit approximation. The output of the program yields the Debye temperature,  $\theta_D$ , and the recoil free fraction at 291K,  $f_{291}$ .

### 2.5.3.2 TEMPERATURE DEPENDENCE OF THE ISOMER SHIFT, ISODS.

The observed line shift is not entirely caused by the chemical isomer shift, as described in Chapter 2.4.1.1. There are two minor factors to be considered, temperature and pressure. Since all the experiments carried out in this study were done at constant atmospheric pressure, only the temperature effect will be discussed in detail. This generally smaller contribution termed the second order Doppler shift, was first observed by Pound and Rebka in 1960 [27]. The emitting or absorbing nucleus is not stationary, but is vibrating on its lattice site at a rate of approximately  $10^{12}$  per second. However, the lifetime of the excited state of a Mössbauer nucleus is in the order of  $10^{-7}$  seconds. That implies that the average displacement and velocity are effectively zero, but the mean squared values of the velocity,  $\langle v^2 \rangle$ , are finite.

The relativistic equation for the Doppler effect on the apparent frequency,  $\nu$ , of the emitted photon, as recorded at the absorbing nucleus, is defined as [28]:

$$\nu_{obs} = \nu_o \left[ 1 - \frac{v}{c} \cos \alpha \right] \left[ 1 - \frac{v^2}{c^2} \right]^{-1/2} \quad \text{Equation 2.43}$$

where  $\nu_{obs}$  = observed frequency of  $\gamma$ -ray

$\nu_o$  = frequency a stationary nucleus,

$v$  = apparent relative velocity of the emitting nucleus, along a direction making an angle  $\alpha$  with the  $\gamma$ -ray direction.

Applying a series expansion for  $v^2/c^2 \ll 1$  then Equation 2.43 can be defined as:

$$\nu_{obs} = \nu_o \left[ 1 - \frac{v}{c} \right] \left[ 1 + \frac{v^2}{2c^2} + \dots \right] \quad \text{Equation 2.44}$$

But  $\langle v \rangle = 0$ , therefore:

$$\nu_{obs} = \nu_o \left[ 1 + \frac{\langle v^2 \rangle}{2c^2} \right] \quad \text{Equation 2.45}$$

The mean value  $\langle v \rangle$  is non zero, and hence there is a frequency shift in the emitted  $\gamma$ -ray. Also the change in the energy  $\delta E$  due to the thermal motion of the nucleus is given by:

$$\delta E = h\nu_o - h\nu_{obs} = h\nu_o - h\nu_o \left[ 1 + \frac{\langle v^2 \rangle}{2c^2} \right] \quad \text{Equation 2.46}$$

Thus the fractional energy change is given by:

$$\frac{\delta E}{E_\gamma} = -\frac{\langle v^2 \rangle}{2c^2} \quad \text{Equation 2.47}$$

This is also the definition of the second order Doppler shift:

$$\frac{\delta E}{E} = \frac{\delta_{SODS}}{c} \quad \text{Equation 2.48}$$

Therefore:

$$\delta_{SODS} = -\frac{\langle v^2 \rangle}{2c} \quad \text{Equation 2.49}$$

This small shift in the  $\gamma$ -ray line position is dependent upon the mean thermal energy of the nucleus,  $\frac{1}{2}m\langle v^2 \rangle$ , and can be related to the total energy of the lattice per unit mass,  $\frac{1}{2}mU$ , [29]:

$$\frac{1}{2}m\langle v^2 \rangle = \frac{1}{2}mU \quad \text{Equation 2.50}$$

$$\therefore U = \langle v^2 \rangle \quad \text{Equation 2.51}$$

It can be seen that by substituting Equation 2.49 into Equation 2.51:

$$\delta_{\text{SODS}} = -\frac{U}{2c} \quad \text{Equation 2.52}$$

Assuming that the Debye model can describe the density of the vibrational states of the nucleus, an expression can be derived for  $U$  [30]:

$$U = \frac{9k_B\theta_D}{8M} + \frac{9k_B T}{M} \left[ \frac{T}{\theta_D} \right]^3 \int_0^{\theta_D/T} \frac{x^3}{e^x - 1} dx \quad \text{Equation 2.53}$$

where  $M$  = mass of the nucleus.

$$\therefore \delta = -\frac{9k_B\theta_D}{16Mc} - \frac{9k_B T}{2Mc} \left[ \frac{T}{\theta_D} \right]^3 \int_0^{\theta_D/T} \frac{x^3}{e^x - 1} dx \cdot \left[ \frac{\theta_D}{T} \right] \quad \text{Equation 2.54}$$

The integrals in the above two equations are another form of the Debye integral, and as stated earlier it has no exact analytical solution. However, there are high and low temperature approximation [26] which give a less than 0.1% error within the specified ranges of  $\theta_D/T$ .

High temperature formula:

$$\int_0^{\theta_D/T} \frac{x^3}{e^x - 1} dx = \frac{[\theta_D]^3}{T} \left[ 1 - \frac{3\left(\frac{\theta_D}{T}\right)}{8} + \frac{\left(\frac{\theta_D}{T}\right)^2}{20} - \frac{\left(\frac{\theta_D}{T}\right)^4}{1680} + \frac{\left(\frac{\theta_D}{T}\right)^6}{90720} \right]$$

$$0 \leq \theta_D/T \leq 2.5$$

**Equation 2.55**

Low temperature formula:

$$\int_0^{\theta_D/T} \frac{x^3}{e^x - 1} dx = \frac{\pi^4}{15} + \left[ \frac{\theta_D}{T} \right]^3 \log(1 - y) - 3 \sum_{n=1}^{\infty} \frac{y^n}{n^4} - \left[ n^2 \left[ \frac{\theta_D}{T} \right]^2 + 2n \left[ \frac{\theta_D}{T} \right] + 2 \right]$$

$$2.5 \leq \theta_D/T \leq \infty$$

**Equation 2.56**

where  $y = \exp\left(-\frac{\theta_D}{T}\right)$

Using a program written by E. Vanderberge [31] the experimental isomer shifts and temperatures are fitted, using a least squares minimisation routine to the theoretical values. The program produces a value for  $\theta_D$ , and the intrinsic isomer shift for the compound under study. However, with the recoiling mass, and the complex vibrational modes, of the compound difficult to predict there are inaccuracies in the absolute value of  $\theta_D$  produced. Again, the values can only be used in comparative studies.

## 2.6 OTHER TECHNIQUES

### 2.6.1 SCANNING ELECTRON MICROSCOPE

Scanning Electron Microscopy (SEM) depends on the interaction of an electron beam with a sample, and the details of the theory are available from standard texts [32, 33]. However, a general summary of the principle is useful in understanding what information this technique produces.

At the surface of the sample a number of phenomena occur in the region of electron impact. Most importantly, these include the emission of secondary electrons with energies a few tens of eV and the re-emission or reflection of higher energy backscattered electrons from the primary beam. The intensity of emission of both secondary and backscattered electrons is sensitive to the angle at which the primary beam strikes the surface of the sample and hence provides topographical information. In addition to secondary and backscattered electrons, the interaction of the primary beam with the sample produces characteristic X-rays. This occurs since during electron emission by the inelastic collision with the primary beam, the resultant ion undergoes relaxation from the excited state by dropping an outer shell electron into the vacancy in the inner shell. Subsequently, energy is emitted during this transition in the form of an X-ray photon, characteristic of the element from which it came. Therefore, this phenomenon can be utilised for elemental compositional spectrometry, with either a Wavelength Dispersive or Energy Dispersive detector for the purpose of EDS or WDS respectively.

This study used a Philips XL40 ASEM equipped with EDS, and the ingot samples were either polished, using standard process, or they were placed directly into the sample chamber, without any surface polishing after chemical etching.

## 2.6.2 X-RAY DIFFRACTION

All X-ray diffraction [34] measurements were performed at Alcan International Research Laboratories, by the research team resident there. Although of limited use in this study, X-ray diffraction was a useful tool when comparing the intermetallic compounds, extracted from the aluminium matrix, with the Mössbauer Spectroscopy results.

The limitations of this technique was that X-ray diffraction could only be performed on the extracted intermetallics, and not on phases within the aluminium matrix.

## 2.6.3 SURFACE ANALYSIS, SAAES AND SAXPS

The theory describing the process of Auger Electron Spectroscopy, AES, and X-Ray Photoelectron Spectroscopy, XPS, is described elsewhere [35].

In this study a Kratos Axis 165 spectrometer was used fitted with two un-monochromatic X-ray sources, Mg ( $K_{\alpha}$  12.56 eV) and Al ( $K_{\alpha}$  1.486 eV), but only the Al X-ray source was used, as it gave the highest energy resolution, typically 0.9 eV. Also a standard electron gun, which operated at 10-15 keV, was fitted to the instrument, along with a standard Oxford Instruments EDS system, which was adapted to operate in a UHV environment.

The instrument allowed the accurate placement, and fixing, of the electron beam on a particular region, which enabled point EDS measurements to be carried out. The same surface area of the sample could then be analysed using XPS and AES, with the X-ray beam being focused, by arrangement magnetic lenses, to approximately 60  $\mu\text{m}$  in diameter. This enabled accurate Small Area Auger Electron Spectroscopy, SAAES, and Small Area X-ray Photoelectron Spectroscopy, SAXPS, measurements to be accumulated.

Some surface cleaning of the samples was required, and this was performed insitu within the spectrometer, using a standard Ar<sup>+</sup> gun operating at 5 keV.

## REFERENCES

- [1] R. L. Mössbauer, *Z Physik* **151** (1958) 24.
- [2] W. Kuhn, *Phil. Mag.* **8** (1929) 625.
- [3] F. R. Metzger, *Progr. Nuclear Phys.* **7** (1959) 54.
- [4] P. B. Moon, *Proc Phys Soc*, **A64** (1951) 76.
- [5] G. Briet, E. Wigner, *Phys Rev* **49** (1936) 519.
- [6] N. N. Greenwood, T. C. Gibb, "*Mössbauer Spectroscopy*", (Chapman and Hall, London, 1971).
- [7] P. Wilkes, "*Solid State Theory in Metallurgy*", (Cambridge University Press, London, 1973).
- [8] H. J. Lipkin, *Ann. Phys* **9** (1960) 332.
- [9] W. E. Lamb, *Phys Rev* **55** (1939) 190.
- [10] A. J. F. Boyle, H. E. Hall, *Repts Progr in Phys* **25** (1962) 441.
- [11] S. Bharati, R. Parthasarathy, K. J. Rao, C. N. R. Rao, *Sol Stat Comm* **46** (1983) 457.
- [12] A. J. F. Boyle, D. P. Burbury, C. Edwards, H. E. Hall, *Pro Phys Soc* **77** (1960) 129.
- [13] T. C. Gibb, "*Principles of Mössbauer Spectroscopy*", (Chapman and Hall, London, 1976).
- [14] A. Vertes, L. Korecz, K. Burger, "*Mössbauer Spectroscopy*", (Elsevier, London, 1979).
- [15] S. C. Thorpe, "*Surface Corrosion Studies by Mössbauer Spectroscopy*". Ph.D. Thesis, Sheffield City Polytechnic, 1987.
- [16] K. A. Stroud, "*Engineering Mathematics*", (Macmillan, London, 1990).
- [17] R. L. Collins, J. C. Travis, "*Mössbauer Effect Methodology*", (Plenum Press, New York, 1967).
- [18] R. V. Parish, R. H. Platt, *Inorg. Chim. Acta.* **4** (1970) 65.
- [19] G. L. Long, "*Mössbauer Spectroscopy Applied to Inorganic Chemistry*", (Plenum Press, New York, 1984).

- [20] V. I. Goldanskii, R. H. Heber in *"Chemical Applications of Mössbauer Spectroscopy"*, (Academic Press, 1968).
- [21] S. S. Hana, J. Heberle, G. J. Perlow, R. S. Preston, D. H. Vincent, *Phys Rev Letts* **4** (1960) 513.
- [22] *Mössbauer Effect Reference Data Journal*, **3**, (1980), 99.
- [23] ] K. A. Stroud, *"Further Engineering Mathematics"*, (Macmillan, London, 1990).
- [24] A. H. Muir. *"Tables and Graphs for Computing Debye-Waller Factors in Mössbauer Effect Studies"*, (Atomics International, 1962.).
- [25] K. A. Hardy, F. T. Parker, J. C. Walker, *Nucl. Inst. Meths.*, **86** (1970) 171.
- [26] J. Herble, *Mössbauer Effect Meth.*, **7** (1970) 299.
- [27] R. V. Pound, G. A. Rebka, *Phys. Rev. Lett.* **3** (1960) 554.
- [28] W. Rosser, *"An Introduction to the Theory of Relativity"*, (Butterworth, 1964).
- [29] B. D. Joesphson, *Phys. Rev. Lett.* **4** (1960) 341
- [30] A. Decker, *"Solid State Physics"*, (Macmillan, London, 1958).
- [31] Program source code.
- [32] D. K. Bowen and C. R. Hall, *"Microscopy of Materials"*, (Macmillan, London, 1975).
- [33] I. M. Watt, *"The Principles and Practice of Electron Microscopy"*, (Cambridge University Press, Cambridge, 1989).
- [34] F. C. Ladd, R. A. Palmer, *"Structure Determination By X-Ray Crystallography"*, (Plenum Press, London, 1977).
- [35] D. Brigg, M. P. Seah, *"Practical Surface Analysis Volume 1: X-Ray Photoelectron Spectroscopy"*, (Wiley, London, 1983).
- [36] S. Marguiles, J. R. Ehrman, *Nucl. Inst. Meths.*, **12** (1961) 131.
- [37] J. L. Davidson *"<sup>57</sup>Fe Mössbauer Studies of Surface Interactions in a PVD Process"*, Ph.D, Sheffield Hallam University, 1997.
- [38] J. C. E. Harmer, *"Organo-Iron Compounds on Clays and Pillared Clays"*, PhD Thesis, Sheffield Hallam University, 1998.

## CHAPTER 3

### THE PROJECT

This study focuses on expanding the present Mössbauer understanding of the Al-Fe intermetallic compounds that form during DC-casting. The first section of this study concentrates on isolating the individual intermetallic compounds from the aluminium host matrix. This is achieved by growing an aluminium alloy using a Bridgman furnace, and extracting the aluminium intermetallic compounds by using the butanol dissolution technique. The Mössbauer information that is produced will be used to quantify the amounts of aluminium intermetallic compounds present within DC-cast aluminium alloys. This work will then be extended to the surface regions of a sample taken from the bulk of a DC-cast alloy.

#### 3.1 BRIDGMAN FURNACE SAMPLES

In a previous Mössbauer investigation on the intermetallic phases that form in Al-Fe alloys, Forder *et al* [1] had published the Mössbauer parameters and Debye temperatures for  $\text{Al}_3\text{Fe}$  and  $\text{Al}_6\text{Fe}$ . The Mössbauer spectra were de-convoluted according to Murgas *et al* [2]. The Debye temperatures were 419 K for  $\text{Al}_3\text{Fe}$ , using a combined area spectral analysis approach, and 327 K for  $\text{Al}_6\text{Fe}$ .

The alloys used in this study were prepared from super-purity based, Al-0.5 wt% Fe, Bridgman grown model Al-Fe binary alloys, and the intermetallic phases of interest were extracted from the aluminium matrix. The Bridgman furnace arrangement was designed to permit the alloys to be grown at specific velocities, and hence solidification rates. This enabled individual, or a required combination of, intermetallic compounds to be grown. Forder *et al* [1] applied this property of the Bridgman furnace to grow an alloy with a mixture of  $\text{Al}_3\text{Fe}$  and  $\text{Al}_6\text{Fe}$  intermetallic compounds. The Mössbauer technique enabled the determination of the relative proportions of these phases, both in the extracted and insitu form.

The initial part of the work reported in this thesis, Chapter 4, expands the number of metastable intermetallic phases studied by the Mössbauer technique, namely the binary Al-Fe phases  $\text{Al}_m\text{Fe}$  and  $\text{Al}_x\text{Fe}$ , as they are some of the most common intermetallic compounds that form during DC-casting of commercial alloys. The Mössbauer spectra for these compounds were de-convoluted according to their crystal structure, and further variable temperature analysis would enable the Debye temperature for each phase to be calculated. Also, the common ternary metastable intermetallic phase,  $\alpha_c$ -AlFeSi, was investigated using the Mössbauer technique, and examined in the same detailed meticulous manner as the binary phases, to determine the lattice dynamics of the Mössbauer nucleus.

As Mn is also a common impurity within commercial cast aluminium, the effect of substitution has been addressed in this project. The metastable intermetallic phase  $\text{Al}_6(\text{Fe},\text{Mn})$  has been cast in the Bridgman furnace, and the resultant effect on the Mössbauer parameters, and Debye temperature, will be discussed in reference to  $\text{Al}_6\text{Fe}$ .

There was a minor aberration in the de-convolution procedure of the Mössbauer spectrum of  $\text{Al}_3\text{Fe}$  used by Forder *et al* [1]. The procedure used had no physical justification, and therefore the published value of the Debye temperature should be treated with caution. This project will endeavour to rectify this small discrepancy, and de-convolute the Mössbauer spectrum according to its crystal structure. A more detailed, and representative, Debye temperature for this equilibrium phase will be reported.

### 3.2 DC-CAST SAMPLES

Since each intermetallic phase has a distinct Mössbauer spectrum, Forder *et al* [1] used this property to analyse a Bridgman grown alloy containing a mixture of known phases. In Chapter 5 this procedure has been extended, using alloy samples taken from

regions within a DC-cast ingot. The mixture of intermetallic phases were unknown, and the Mössbauer technique was used not only to identify which phases were present, insitu, but also in what relative proportions. The findings of this part of the study were confirmed by XRD studies performed on the same butanol extracted samples at Alcan International. This will hopefully prove that Mössbauer spectroscopy can be used to identify the intermetallic phase composition of any iron containing aluminium alloy insitu within the aluminium matrix.

The final part of Chapter 5 involved a surface investigation of the same DC-cast alloy samples, without any  $^{57}\text{Fe}$  enrichment, used in the phase identification process. This part of the project utilised a range of techniques: conversion electron Mössbauer spectroscopy, Auger electron spectroscopy, X-Ray photoelectron spectroscopy, energy dispersive spectroscopy, and finally scanning electron spectroscopy. This has been used to produce an accurate picture of the intermetallic phase distribution within the surface, and near surface, regions of the sample. This is of critical importance as these intermetallics comprise typically 1% of the microstructure, and they affect the final gauge properties of the commercially produced ingot. To the authors knowledge this type of analysis has not been previously attempted, and it provides a detailed scientific information regarding a common system that is of value.

## REFERENCES

- [1] S. D. Forder, J. S. Brooks, P. V. Evans, *Atca Met.*, **35** (1996) 1167.
- [2] L. Murgas, Z. Homonnay, S. Nagy, A. Vertes, *Met Trans. A*, **19** (1988) 259.

## CHAPTER 4

### VARIABLE TEMPERATURE MÖSSBAUER SPECTROSCOPY

#### 4.1 ALLOY PREPARATION

A model binary Al-Fe alloy was prepared from 99.5 wt% Al and 0.5 wt% Fe. The aluminium used was 99.999 wt% pure. The alloys were cast at different velocities using a Bridgman Furnace, depending on which individual intermetallic phase was required. This enabled a single phase to be grown, which was then extracted from the aluminium matrix using the butanol extraction technique described by Simensen *et al* [1]. The intermetallics phases that were prepared using this method were  $\text{Al}_3\text{Fe}$  and  $\text{Al}_x\text{Fe}$ .

A model ternary Al-Fe-Si alloy was also prepared from a 99.4 wt% Al, 0.5 wt% Fe, and 0.1 wt% Si. The aluminium used was 99.999 wt% pure. This alloy was cast, and extracted, in the same manner as the model binary alloy, and enabled the production of the intermetallic phases  $\text{Al}_m\text{Fe}$  and  $\alpha_c\text{-AlFeSi}$ .

##### 4.1.1 THE BRIDGMAN FURNACE

The Bridgman process was a technique designed to achieve unidirectional solidification, under conditions of steady state growth. The Bridgman furnace, see Figure 4.1, used in this study consisted of a cylindrical, double walled, water-cooled tank, inserted in the base of a vertical tube furnace. A drive rod, co-axial with the furnace and water tank, could be raised or lowered manually, at a constant velocity via a screw drive and a computer controlled stepper motor. Water was retained in the tank by a rolling “O” ring seal at the exit point of the drive rod, and excessive evaporation from the surface was prevented by a thermal shield. Depending on the operating conditions (furnace temperature, water level, presence/absence of the thermal shield), the thermal gradient could be selected in the range of 5-15 K  $\text{mm}^{-1}$ . All samples in this

study were grown under high thermal gradient conditions, at velocities in the range of 5-12 mm min<sup>-1</sup>. The model alloys were initially cast in permanent moulds, as rods of 10 mm diameter, and were then subsequently swaged and wire drawn to a final diameter of ~2 mm. For the Bridgman furnace ~15 cm of the chosen alloy was inserted into a 20 cm long, thin walled alumina tube (external diameter ~3 mm, internal diameter ~2 mm), leaving sufficient length for expansion on heating and melting. The sample was then attached to the drive rod, and raised into the furnace. The start position was chosen so that the bottom 20-30mm of the sample always remained solid, providing a seed for subsequent growth. After thermally equilibrating, for ~5min, the sample was solidified by withdrawal from the furnace at the desired constant velocity. Samples were taken from the central portion of the resolidified alloy, and were cut for intermetallic extraction.

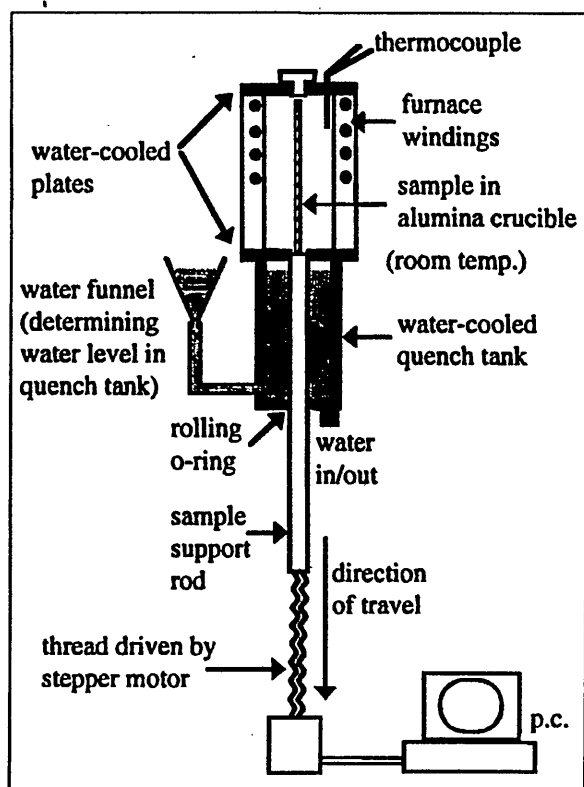
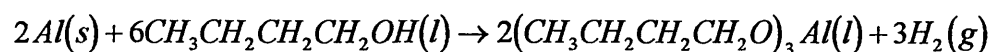


Fig 4.1 Schematic representation of the Bridgman apparatus

## 4.1.2 BUTANOL EXTRACTION

This work employed the "SIBUT" intermetallic extraction method, as described by Simensen *et al* [1]. A section, typically less than 1g, of the grown sample was placed in an autoclave with anhydrous 1-butanol. On heating the aluminium solid solution was dissolved by the following reaction:



Equation 4.1

The insoluble intermetallic particles in suspension were filtered, using a PTFE paper, from the soluble aluminium butoxide and remaining 1-butanol. The typical yield from a 0.4 g sample of a commercial purity alloy was ~5 mg.

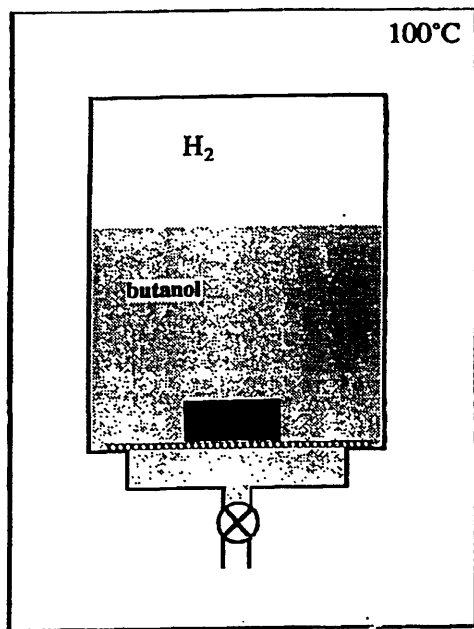


Fig 4.2 Schematic representation of the "SIBUT" apparatus

## 4.1.3 MÖSSBAUER ABSORBER PREPARATION

The intermetallic particles, which were extracted from the aluminium matrix, were ground and mixed with graphite. They were then packed within a perspex absorber disc, 15 mm in diameter, and placed into a cryogenic system chosen to suit the experiments to be performed.

The mass of intermetallic phase used was determined by the effective Mössbauer thickness equation [2], see Chapter 2.3.2, so that  $t_a$  was  $< 1$ . For  $t_a \gg 1$  saturation effects will distort the shapes of the absorption lines, whilst for  $t_a \ll 1$  the line intensities are too small, i.e. the signal to noise ratio is poor. Optimum conditions are obtained when  $t_a \sim 0.1$ . The actual values for  $t_a$  that were calculated for this study are shown in Table 4.1

Intermetallic	R.M.M.	Total Mass allowed, $t_a = 1$ , mg	Actual Mass used, mg	Actual $t_a$ Value
$\text{Al}_m\text{Fe}$ ( $m = 4$ )	164.00	20.70	6.50	0.31
$\text{Al}_x\text{Fe}$ ( $x = 4.5$ )	177.50	22.40	6.30	0.28
$\alpha_c\text{-Al}_{20}\text{Fe}_5\text{Si}_2$	876.00	44.23	8.20	0.19
$\text{Al}_6(\text{Fe},\text{Mn})$	218.00	3.89	2.40	0.62

Table 4.1 Calculated effective Mössbauer thickness for the intermetallic phases studied.

#### 4.1.4 Al<sub>3</sub>Fe

The Mössbauer spectrum of Al<sub>3</sub>Fe, see Fig 4.3, consisted of two quadrupole interactions ( $\Delta = 0.42 \pm 0.02 \text{ mm s}^{-1}$  and  $0.12 \pm 0.02 \text{ mm s}^{-1}$ ), which remained constant between 20 and 295 K, see Table 4.2 and Fig 4.4. The isomer shift of the two doublets exhibited a standard second order Doppler shift effect, with values of  $0.31 \pm 0.02 \text{ mm s}^{-1}$  and  $0.31 \pm 0.02 \text{ mm s}^{-1}$  at 20 K decreasing to  $0.21 \pm 0.02 \text{ mm s}^{-1}$  and  $0.19 \pm 0.02 \text{ mm s}^{-1}$  at 295 K.

Analysis of the normalised spectral areas led to a Debye temperature,  $\theta_D$ , of  $434 \pm 5 \text{ K}$ , and a recoil free fraction at 291 K,  $f_{291}$ , of  $0.80 \pm 0.02$  for the larger quadrupole interaction (Fe(1)-Fe(4)), see Fig 4.5. The smaller quadrupole doublet (Fe(5)) produced a  $\theta_D$  of  $488 \pm 5 \text{ K}$ , and a  $f_{291}$  of  $0.84 \pm 0.02$ , when the spectral areas were investigated, see Fig 4.6. Also, the combined normalised spectral areas, for Fe sites Fe(1)-Fe(5), led to a  $\theta_D$  of  $452 \pm 5 \text{ K}$ , and a  $f_{291}$  of  $0.81 \pm 0.02$ , see Fig 4.7.

The analysis of the variation of the isomer shift with temperature for the Fe sites Fe(1)-Fe(4), produced a  $\theta_D$  of  $480 \pm 5 \text{ K}$ , and an intrinsic isomer shift of  $0.32 \pm 0.02 \text{ mm s}^{-1}$ , see Fig 4.8. The same analysis led to a  $\theta_D$  of  $504 \pm 5 \text{ K}$ , and an intrinsic isomer shift of  $0.33 \pm 0.02 \text{ mm s}^{-1}$ , see Fig 4.9, for Fe site Fe(5).

The half-widths of both the quadrupole doublets remained constant between 20 K and 295 K. This can be attributed to the high  $\theta_D$  values, as this indicates that the iron atom is tightly held within the crystal structure.

These values of the Mössbauer parameters, at room temperature, for Al<sub>3</sub>Fe agreed with other published work [3, 4, 5, 6]. However, a complete comparison was not possible due to the lack of other published low temperature work.

File	Temp. K	$\delta$ , mm s <sup>-1</sup>	$\Delta/2$ , mm s <sup>-1</sup>	(l) $\Gamma/2$ , mm s <sup>-1</sup>	(r) $\Gamma/2$ , mm s <sup>-1</sup>	Rel. Area, %	Norm. Area	$\chi^2$
sf191	20	0.31	0.21	0.15	0.14	66.49	1.74498	0.566
		0.31	0.04	0.14	0.14	33.51	0.87926	
sf193	50	0.31	0.21	0.15	0.14	63.15	1.60378	0.557
		0.30	0.04	0.15	0.14	36.85	0.93600	
sf198	60	0.30	0.22	0.16	0.17	63.56	1.58934	1.257
		0.30	0.06	0.14	0.14	36.44	0.91111	
sf194	100	0.29	0.21	0.15	0.14	62.45	1.58367	0.619
		0.29	0.05	0.15	0.15	37.55	0.95214	
sf199	120	0.28	0.22	0.16	0.16	65.22	1.58001	0.906
		0.29	0.05	0.14	0.15	34.78	0.84248	
sf195	151	0.27	0.21	0.15	0.15	62.97	1.58557	0.715
		0.28	0.06	0.15	0.15	37.03	0.93235	
sf196	200	0.25	0.21	0.15	0.15	63.07	1.590937	0.546
		0.26	0.06	0.13	0.16	36.93	0.88387	
sf197	251	0.22	0.20	0.16	0.14	64.29	1.49448	0.627
		0.22	0.06	0.14	0.14	35.71	0.82086	
sf192	295	0.21	0.20	0.16	0.14	63.39	1.41783	0.639
		0.19	0.07	0.14	0.12	36.61	0.81883	

Errors:  $T = \pm 2$  K,  $\delta = \pm 0.02$  mm s<sup>-1</sup>,  $\Delta/2 = \pm 0.02$  mm s<sup>-1</sup>,  $\Gamma/2 = \pm 0.02$  mm s<sup>-1</sup>,

$\theta_D = \pm 5$  K,  $f_{291} = \pm 0.02$ .

Isomer shifts relative to  $\alpha$ -iron.

Table 4.2 Fitting parameters for Al<sub>3</sub>Fe.

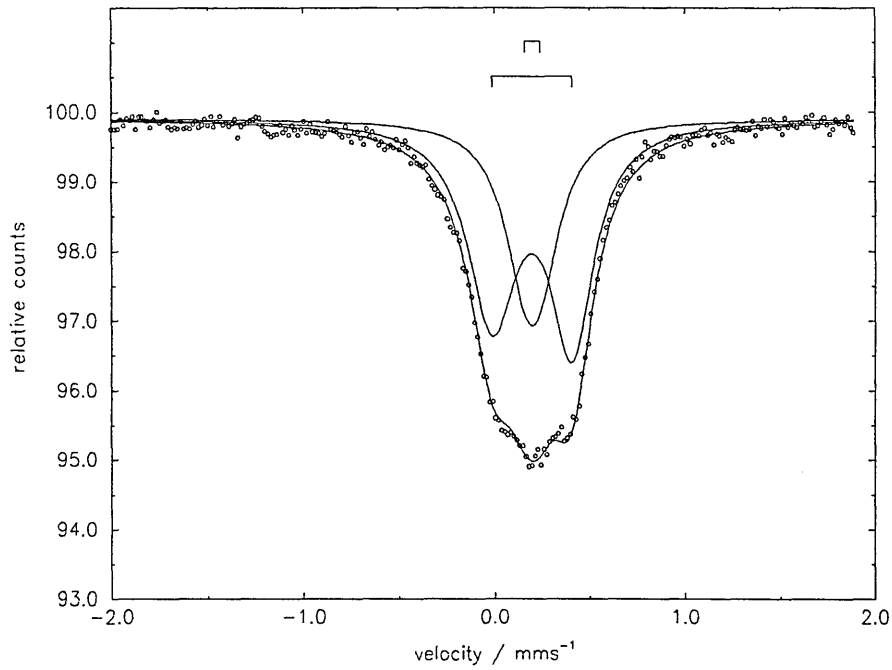


Fig 4.3 Typical Mössbauer spectrum for  $\text{Al}_3\text{Fe}$

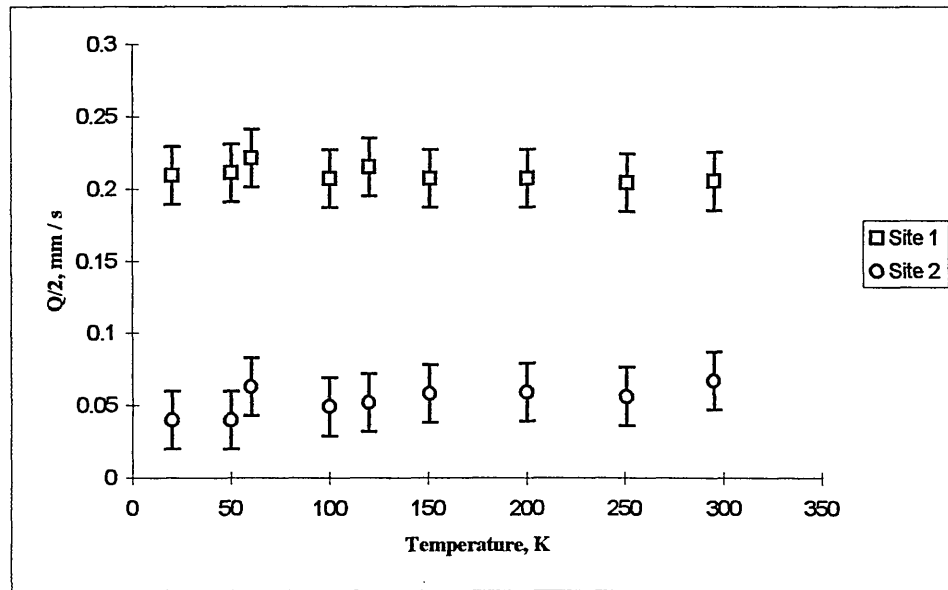


Fig 4.4 Variation of the quadrupole splitting with temperature for  $\text{Al}_3\text{Fe}$

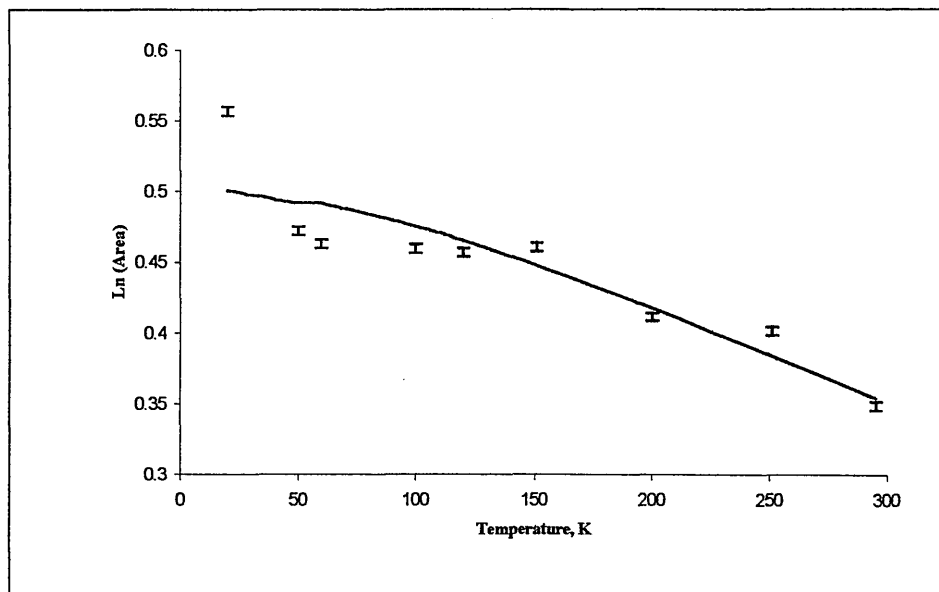


Fig 4.5 Variation of the Mössbauer spectral areas for Fe site Fe(1)-Fe(4)

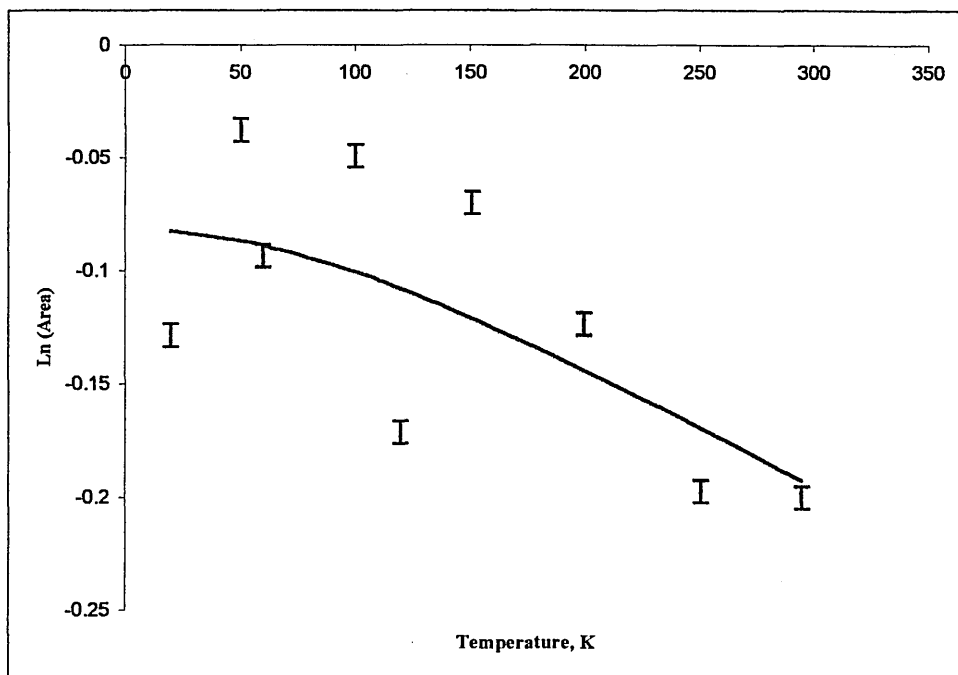


Fig 4.6 Variation of the Mössbauer spectral areas for Fe site Fe(5)

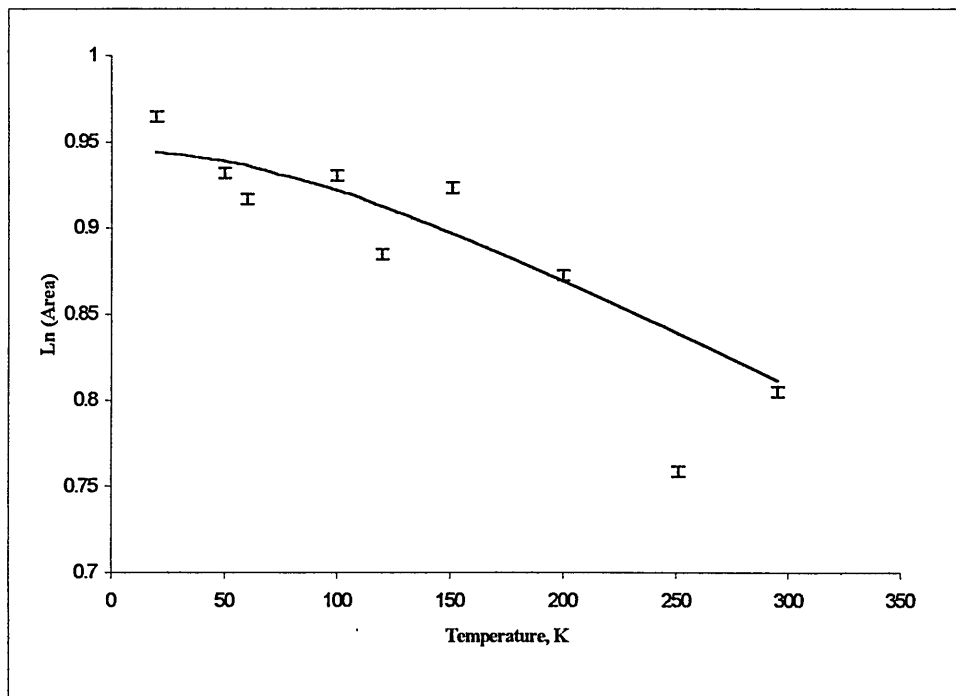


Fig 4.7 Variation of the Mössbauer combined spectral areas for Fe sites Fe(1)-Fe(5)

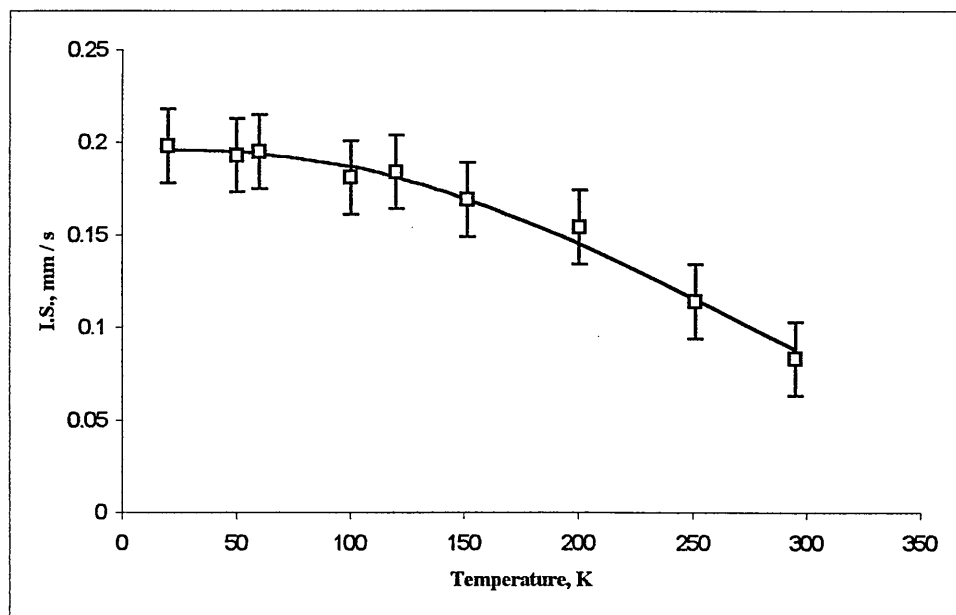


Fig 4.8 Variation of the isomer shift for  $\text{Al}_3\text{Fe}$  for Fe site Fe(1)-Fe(4)

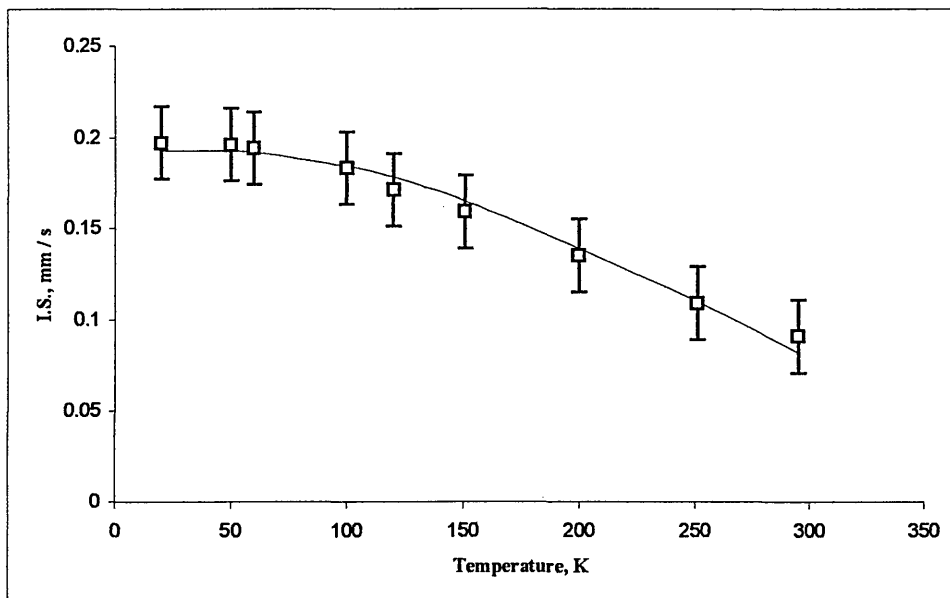


Fig 4.9 Variation of the isomer shift for  $\text{Al}_3\text{Fe}$  Fe site Fe(5)

#### 4.1.4.1 THE $\text{Al}_3\text{Fe}$ SPECTRUM

The crystal structure of  $\text{Al}_3\text{Fe}$  has been fully described by Black [7, 8], see Chapter 1.3.1. The crystal has a monoclinic unit cell, with a space group  $C2/m$ , and contains 100 atoms per unit cell. There are five different Fe sites within the unit cell, but they can be arranged into approximately two different atomic environments.

The first type atomic environment to be considered will be Fe sites Fe(1)-Fe(4). The Fe atom resides in the centre of Al 10 co-ordination polyhedra. When viewing the polyhedra along the y-axis it can be seen that the Al atoms are arranged, such that four Al atoms, in a non-symmetrical alignment, are in the same plane as the Fe atoms. Above, and below, the Fe atom are three Al atoms, in the next atomic plane. This creates a 3-4-3 atomic arrangement around the central Fe site.

The similar atomic environments of the Fe sites Fe(1)-Fe(4) can be illustrated fully by referring to Table 4.3. Each of the central Fe atoms have three Al atoms above the basal plane, which is then reflected in the same arrangement below the basal plane.

Also the Al-Fe bond lengths in this section of the polyhedral are similar, and further illustrated by referring to Table 4.3. However, the Al atoms that lie in the basal plane with the Fe central atoms are positioned so that three of the Al atoms are weighted to one side of the Fe atom. This is the justification of the less than symmetrical environment of the Fe sites Fe(1)-Fe(4), which produces the larger quadrupole interaction.

	Fe(1)	Al-Fe Bond Length, Å	Fe(2)	Al-Fe Bond Length, Å	Fe(3)	Al-Fe Bond Length, Å	Fe(4)	Al-Fe Bond Length, Å	Mean Al-Fe Bond Length, Å	Error, Å
Above Plane	Al(17)	2.429	Al(18)	2.455	Al(15)	2.502	Al(16)	2.4	2.45	0.04
	Al(18)	2.616	Al(19)	2.493	Al(20)	2.528	Al(20)	2.48	2.53	0.06
	Al(19)	2.771	Al(17)	2.713	Al(16)	2.758	Al(15)	2.754	2.75	0.03
In Plane	Al(6)	2.538	Al(8)	2.453	Al(6)	2.45	Al(11)	2.495	2.48	0.04
	Al(8)	2.523	Al(11)	2.422	Al(6)	2.556	Al(11)	2.629	2.53	0.08
	Al(9)	2.513	Al(12)	2.48	Al(7)	2.576	Al(10)	2.565	2.53	0.05
	Al(9)	2.759	Al(13)	2.621	Al(10)	2.257	Al(13)	2.633	2.6	0.20
Below Plane	Al(17)	2.429	Al(18)	2.455	Al(15)	2.502	Al(16)	2.4	2.44	0.04
	Al(18)	2.616	Al(19)	2.493	Al(20)	2.528	Al(20)	2.48	2.53	0.06
	Al(19)	2.771	Al(17)	2.713	Al(16)	2.758	Al(15)	2.754	2.75	0.03

Table 4.3 Al-Fe bond lengths for Fe sites Fe(1)-Fe(4) [7, 8]

The final Fe site, Fe(5), is a completely different scenario. The Fe(5) has only one Al atom lying directly above, only two Al atoms in the basal plane, and three Al atoms beneath. However, there are three Al atoms that are positioned at  $+1/2$  above the plane. This has the effect of placing the central Fe atom in a near symmetrical environment, and thus has the effect of producing the smaller quadrupole interaction. The bond lengths for this particular atomic arrangement are shown in Table 4.4.

	Fe(5)	Al-Fe Bond Length, Å
Above Plane	Al(14)	2.306
+½ Above Plane	Al(15)	2.476
	Al(17)	2.575
	Al(16)	2.580
In Plane	Al(19)	2.463
	Al(18)	2.644
Below Plane	Al(7)	2.514
	Al(13)	2.574
	Al(9)	2.615

Table 4.4 Al-Fe bond lengths for Fe site Fe(5) [7, 8]

This assumption is the basis for de-convoluting the Mössbauer spectrum with two quadrupole components, which was followed by several different authors [3, 4, 5, 6]. The larger quadrupole interaction, as a result of an asymmetrical Fe environment, being attributed to the Fe sites Fe(1)-Fe(4), and the smaller quadrupole interaction is representative of the remaining Fe site Fe(5).

#### 4.1.4.1.1 DEBYE TEMPERATURE ANALYSIS

In the previous section the five Fe centred nine and ten co-ordinated Al polyhedra were discussed in detail, with reference to the de-convoluting procedure used when attempting to interpret the resultant Mössbauer spectrum for Al<sub>3</sub>Fe. The findings being that the five Fe sites could be approximately de-convoluted to two quadrupole interactions, the larger quadrupole interaction attributed to the ten co-ordinated Al-Fe polyhedra, Fe sites Fe(1)-Fe(4), and the remaining Fe site Fe(5) having the smaller quadrupole interaction. The variation of the Al-Fe bond lengths, and the average bond lengths are shown in Table 4.5.

Fe Site	No. of Al-Fe Bonds	Al-Fe Bond Length	Mean Al-Fe Bond Length
1	10	2.429 - 2.839 Å	2.6 ± 0.1 Å
2	10	2.422 - 2.713 Å	2.5 ± 0.1 Å
3	10	2.257 - 2.758 Å	2.5 ± 0.2 Å
4	10	2.400 - 2.754 Å	2.6 ± 0.1 Å
5	9	2.306 - 2.644 Å	2.5 ± 0.1 Å

Table 4.5 The variation in the Al-Fe bond lengths within the Fe sites Fe(1)-Fe(5)

The first step when calculating the Debye temperature for each component within the Mössbauer spectrum is normalising the spectrum area. This is achieved by dividing the total area counts by the background area counts, obtained by averaging the first and last five data points of the spectrum, for each temperature. This information is then applied within the LNAT area analysis program, see Chapter 2.5.3.1. The program used an effective recoiling mass of 57 amu that yields the Debye temperature,  $\theta_D$ , and the recoil free fraction at 291 K,  $f_{291}$ .

The larger quadrupole interaction doublet, Fe(1)-Fe(4), produced a  $\theta_D$  of  $434 \pm 5$  K and a  $f_{291}$  of  $0.80 \pm 0.02$ . However, when applying the same process the smaller quadrupole interaction, Fe(5), the resultant  $\theta_D$  was discovered to be  $488 \pm 5$  K, and the  $f_{291}$  value was  $0.84 \pm 0.02$ . The difference in the  $\theta_D$  between the two quadrupole interactions can be explained due to the different Al-Fe bond lengths. The ten co-ordinate Fe centred polyhedra, sites Fe(1)-Fe(4), have an average Al-Fe bond length of 2.5621 Å compared to the Fe centred nine co-ordinated polyhedra, which was an average Al-Fe bond length of 2.5274 Å, Fe(5). This implies that the Fe(5) site is more tightly bonded within the nine co-ordinated polyhedra than the ten co-ordinated Fe(1)-

Fe(4) polyhedra, and thus would have less vibrational freedom. This was brought out by the  $54 \pm 5$  K difference in the  $\theta_D$  value for the two quadrupole interactions.

On closer investigation the factor that dictates the  $\theta_D$  value to a greater extent, is the shortest Al-Fe bond length within the respective polyhedra. Chittaranjan *et al* [9] drew the comparison between the Fe atomic environments in  $\text{Al}_6\text{Fe}$ , and the Fe sites Fe(1)-Fe(4) in  $\text{Al}_3\text{Fe}$ , as they are both 10 co-ordinated Fe centred aluminium polyhedra with a similar atomic arrangement. However, the reported  $\theta_D$  value for  $\text{Al}_6\text{Fe}$  is 327 K [10], which is dramatically lower than the calculated value for Fe(1)-Fe(4). The reason being is that the average Al-Fe bond lengths are slightly longer, 2.5621 Å for Fe(1)-Fe(4) and 2.511 for  $\text{Al}_6\text{Fe}$ , but more significantly the shortest Al-Fe bond length within the  $\text{Al}_6\text{Fe}$  polyhedra is 2.445 Å compared to 2.377 Å for Fe(1)-Fe(4). That implies that not only the average Al-Fe bond length, but also the shortest Al-Fe bond length contribute to the overall bonding within aluminium cage. This reasoning is re-enforced when considering Fe(5), as the average Al-Fe bond length in this case is 2.5274 Å, which is very similar to that of both  $\text{Al}_6\text{Fe}$  and Fe(1)-Fe(4), but the shortest Al-Fe bond length is only 2.306 Å. This is the smallest Al-Fe bond length in all the aluminium intermetallic phases studied, and thus produces the highest  $\theta_D$  value,  $488 \pm 5$  K, so far.

The combined normalised spectral areas, for Fe site Fe(1)-Fe(5), produced a  $\theta_D$  value of  $452 \pm 5$  K, and a  $f_{291}$  of  $0.81 \pm 0.02$ . This value is an average, and is quoted for the intermetallic compound as a whole.

The analysis of the variation of the isomer shift with temperature, using the program ISODS, Fe(1)-Fe(4), produced a  $\theta_D$  of  $480 \pm 5$  K, and the same procedure led to a  $\theta_D$  value of  $504 \pm 5$  K for Fe site Fe(5). These values are significantly higher than those determined by the interpretation of the absorption spectral area data, and this is a direct consequence of the methods by which the  $\theta_D$  values are calculated. The mean square vibrational amplitude of the Mössbauer nucleus,  $\langle x^2 \rangle$ , is weighted towards the lower frequencies, whilst the mean square thermal velocity,  $\langle v^2 \rangle$ , is weighted towards

the higher frequencies [11]. Therefore, a higher characteristic temperature is derived from the ISODS data. However, the information produced by this technique follows the same trend as the results obtained by using the spectral areas, and can also be used as a qualitative tool.

The Debye temperature produced by the spectral area analysis method will be used throughout this study for comparative analysis.

#### 4.1.4.1.2 RESIDUAL ASYMMETRY WITHIN THE SPECTRUM

Previous authors [3, 4, 5, 6] have reported that a small degree of asymmetry was observed for the larger quadrupole interaction, Fe(1)-Fe(4). They attributed the asymmetry to the presence of AlFe solid solution within the samples, as the Mössbauer spectra were recorded with the aluminium intermetallic phase within the aluminium matrix. The Mössbauer spectrum for AlFe consists of a singlet with an isomer shift of  $0.42 \text{ mm s}^{-1}$ , relative to  $\alpha$ -iron, [12, 13]. The author speculates that the effect of the introducing the Mössbauer component attributed to AlFe would be very small, but never the less physically correct, due to the very low solid solubility of iron in aluminium [14] and would not account fully for this observed asymmetry. Therefore, the asymmetry within these Mössbauer spectra must have another physical source. This can be re-enforced by the similar asymmetry that was observed within the Mössbauer spectrum for  $\text{Al}_3\text{Fe}$  in this study, and since the aluminium intermetallic phase was extracted from the aluminium matrix the presence of any AlFe would have been removed.

Another possibility for the observed asymmetry within the larger quadrupole interaction of the  $\text{Al}_3\text{Fe}$  spectrum could be the Goldanskii-Karyagin effect [15, 16].

The intensity of a particular hyperfine transition between quantized sub-levels is determined by the coupling of the two nuclear momentum states [17]. This can be expressed as the product of two terms, with one being angular-dependent and the

other angular-independent. However, the former averages to unity when all orientations are equally probable, for example in a randomly oriented polycrystalline powder sample, and it is convenient to consider the angular-independent term first.

The intensity in this instance is given by the square of the appropriate Clebsch-Gordan coefficient [18]:

$$\text{Intensity} \propto \langle I_1 J - m_1 m | I_2 m_2 \rangle^2 \quad \text{Equation 4.2}$$

Where the two nuclear spin states  $I_1$  and  $I_2$  have  $I_z$  values of  $m_1$  and  $m_2$ , and their coupling obeys the vector sums:

$$J = I_1 + I_2 \quad \text{Equation 4.3}$$

$$m = m_1 - m_2 \quad \text{Equation 4.4}$$

Most of the Mössbauer transitions take place without a change in parity, so that the radiation is classified as a magnetic dipole (M1) or electric quadrupole (E2) transition. The selection rule for an M1 or E2 transition can be expressed as:

$$\Delta m_z = 0, \pm 1 \quad \text{Equation 4.5}$$

$$\Delta m_z = 0, \pm 1, \pm 2 \quad \text{Equation 4.6}$$

The most frequently used coefficients are those for the  $1/2 \rightarrow 3/2$  M1 transition, and are shown elsewhere [18] along with other spin states [19]. The  $I_1$  transition may be either the ground or excited spin state. Although there are nominally eight possible transitions the  $+3/2 \rightarrow -1/2$  and  $-3/2 \rightarrow +1/2$  transitions have a zero probability, and are commonly referred to as forbidden. The remaining six finite coefficients, which express the angular-independent intensity, have a total probability of unit intensity and give directly the 3:2:1:1:2:3 intensity ratios for a magnetic hyperfine splitting. The corresponding

terms for a quadrupole spectrum are obtained by summation, and give an intensity ratio of 1:1.

The angular-dependent terms,  $\Theta(J,m)$ , are expressed as the radiation probability in a direction at an angle  $\theta$  to the quantization axis. It can be shown that the angular dependence of the  $\pm 3/2 \rightarrow \pm 1/2$  line in a single crystal is defined as [18]:

$$I + \cos^2 \theta \quad \text{Equation 4.7}$$

The  $\pm 1/2 \rightarrow \pm 1/2$  transition has a similar angular dependence, which is also defined as [18]:

$$\frac{2}{3} + \sin^2 \theta \quad \text{Equation 4.8}$$

The average values for a random polycrystalline samples are then given by integrating over all orientations, and the relative line intensities become:

$$\frac{I_{3/2}}{I_{1/2}} = \frac{\int_0^\pi (1 + \cos^2 \theta) \sin \theta d\theta}{\int_0^\pi \left(\frac{2}{3} \sin^2 \theta\right) \sin \theta d\theta} = 1 \quad \text{Equation 4.9}$$

The above argument is only rigorous if the recoilless absorption (or emission) is the same in all directions. If it is isotropic then the intensity of the absorption will be weighted in favour of a particular orientation of the crystallites. Writing the recoilless fraction,  $f$ , as a function of the angle between the direction of observation and the principal z-axis of the electric field gradient for a thin absorber Equation 4.9 becomes:

$$\frac{I_{3/2}}{I_{1/2}} = \frac{\int_0^\pi (1 + \cos^2 \theta) f(\theta) \sin \theta d\theta}{\int_0^\pi \left(\frac{2}{3} \sin^2 \theta\right) f(\theta) \sin \theta d\theta} \neq 1 \quad \text{Equation 4.10}$$

This anisotropic recoilless fraction should result in an asymmetry in the intensities of the quadrupole doublet, which is independent of the sample, and is referred to as the Goldanskii-Karyagin effect [15,16].

The anisotropy of the recoilless fraction also increases with temperature, and therefore the observed asymmetry within the quadrupole doublet should increase. This was not observed in this study, as the observed asymmetry within the Al<sub>3</sub>Fe spectrum was constant with temperature. This implies that the factor responsible for this phenomenon could only be the influence of residual texture within the absorber, which was not removed by grinding the crystalline absorber powder before placing within the absorber disc.

Texture effects within a sample arise if the compacted polycrystalline absorber has a tendency towards partial orientation, with respect to the angle between the observation and the principal z-axis of the electric field gradient. This implies that the values of  $\Theta(J,m)$  for a particular transition does not average to unity, i.e.:

$$\sum_{m_1 m_2} \frac{1}{4} |I_1 J - m_1 m_2| I_2 m_2 \langle \Theta(J,m) \rangle \neq 1 \quad \text{Equation 4.11}$$

The effect on the Mössbauer spectrum is such that there is some residual asymmetry observed in the quadrupole interaction, which is angular dependent. This phenomenon can be quite large, and exceedingly difficult to eliminate in fibrous and platelike materials. The extracted intermetallic phase Al<sub>3</sub>Fe has been shown to exist as such platelike strands [10, 20,21].

The anisotropic mechanical stress field arising in the intermetallic phase during solidification could lead to an effect very similar to texture. This Bridgman process promotes the formation of these mechanical stress fields, as it forms the solid by directional solidification [23]. Janot *et al* [22] investigated the influence of mechanical stress fields on the Mössbauer spectrum of a unidirectionally solidified Al-Al<sub>3</sub>Fe composite material. The direction of the applied elongation stress coincided with that of the crystal growth, and the [001] axis of the Al<sub>3</sub>Fe crystallites. The spectrum of Al<sub>3</sub>Fe was evaluated as consisting of two quadrupole interactions, the larger interaction containing a certain degree of asymmetry. Therefore, it is impossible to determine whether the residual observed asymmetry could be attributed to solely particle texture or mechanical field stress, but it is more likely to be a mixture of the two components.

Nagy *et al* [23] investigated the effect on the Mössbauer spectrum of Al<sub>6</sub>Fe, prepared by semicontinuous casting, in relation to the growth direction. Alloy samples were prepared parallel and perpendicular to the growth direction, and these were then compared to the Mössbauer spectrum obtained from an alloy containing randomly orientated Al<sub>6</sub>Fe particles. The asymmetry of the quadrupole doublet was very pronounced, and shifted by 90° depending on the growth direction. A similar asymmetry was also observed by Forder *et al* [10, 24], based upon investigations using Bridgman grown super-purity alloys. This information may appear to be initially irrelevant. However, Chittarajan *et al* [9] compared that local atomic environments of the iron sites residing in the flat layer of atoms in Al<sub>3</sub>Fe, attributed to the larger quadrupole interaction, and that of the local atomic environment of Al<sub>6</sub>Fe. Both systems are an arrangement of 10 co-ordination Al-Fe polyhedra with similar Al-Fe bond lengths, and atomic co-ordinates.

## 4.1.4.1.3 OXIDATION STATE

To the first approximation, the oxidation state of a compound can be readily correlated to its isomer shift. In section 2.4.1.1 it was shown that the isomer shift depends on the s-electron density at the nucleus. Atomic bonding has very little effect on the inner s-electrons, and therefore has little effect on the isomer shift. However, the outermost s-electrons are very sensitive to the shielding effects of the valance p-, d-, and f-electrons, and so the isomer shift. In Chapter 2.4.1.1 it was shown that the isomer shift could be expressed as:

$$\delta = k(R_e^2 - R_g^2) \left\{ |\Psi(0)|_{abs}^2 - |\Psi(0)|_{scs}^2 \right\} \quad \text{Equation 2.26}$$

For  $^{57}\text{Fe}$   $k(R_e^2 - R_g^2)$  has a negative value. That implies that any factors leading to a reduction in the s-electron density at the nucleus will lead to a more positive isomer shift relative to the source. For instance, the oxidation of  $\text{Fe}^{2+}$  to  $\text{Fe}^{3+}$  leads to a reduction in the d-electron density. This decreased shielding experienced by the nucleus leads to an increase in the s-electron density, and therefore a less positive isomer shift is observed.

The observed experimental isomer shifts for the two quadrupole interactions, attributed to the Mössbauer spectrum of  $\text{Al}_3\text{Fe}$ , are  $0.21 \pm 0.02 \text{ mm s}^{-1}$  and  $0.19 \pm 0.02 \text{ mm s}^{-1}$  at room temperature relative to  $\alpha$ -iron. These isomer shift values are inconclusive, regarding whether the oxidation state of the  $^{57}\text{Fe}$  nucleus is (II) or (III).

However, since the magnitude of the quadrupole interaction, in both cases, is constant with respect to temperature, it implies that the spin state of the  $^{57}\text{Fe}$  nucleus is either low-spin Fe(II) or high-spin Fe(III) [25]. This is due to the spherical symmetry of the electrons, within the 3d orbital. Therefore, there is no inherent electric field gradient across the  $^{57}\text{Fe}$  Mössbauer nucleus, and the observed quadrupole interaction of both Fe sites is attributed to the external Al atoms. The variation of the quadrupole interaction

with temperature for high-spin Fe(II), and low-spin Fe(III) has been examined elsewhere with regard to crystal field theory [26, 27] and valence contributions [28]. This type of investigation has been applied to various systems, including phosphate glasses [29].

Therefore, taking all aspects into account, a speculative assumption can be made as to the oxidation state both of the  $^{57}\text{Fe}$  Mössbauer nuclei, within the aluminium intermetallic compound. The  $^{57}\text{Fe}$  Mössbauer nuclei may exist within these aluminium polyhedra in the low-spin Fe(II) state [18, 25].

#### 4.1.4.1.4 STUPEL CALCULATIONS

Stupel *et al* [30] used Mössbauer spectroscopy to identify various intermetallic phases that form within the titanium rich Ti-Fe system. The room temperature Mössbauer parameters were reported for a variety of phases, including:  $\alpha_m$ ,  $\alpha$ ,  $\theta$ ,  $\omega$ ,  $\beta$ , and TiFe. However, some difficulty was experienced when trying to discern the Mössbauer parameters for TiFe.

The intermetallic compound TiFe precipitates mainly from the supersaturated  $\alpha$ , and the metastable  $\beta$  in a very slow reaction, and therefore there was some residual  $\alpha$  phase present. Stupel used the Equation 4.12 to analyse the room temperature Mössbauer spectrum to determine the relative spectral areas of the  $\alpha$  and TiFe phase,  $A_\alpha$  and  $A_{\text{TiFe}}$  respectively.

$$R = \left( \frac{A_\alpha}{A_{\text{TiFe}}} \right) = \left( \frac{C_{\text{Fe}}^\alpha}{C_{\text{Fe}}^{\text{TiFe}}} \right) \left( \frac{X_\alpha}{X_{\text{TiFe}}} \right) \left( \frac{f_\alpha}{f_{\text{TiFe}}} \right) \quad \text{Equation 4.12}$$

where  $C_{\text{Fe}}^\alpha$  and  $C_{\text{Fe}}^{\text{TiFe}}$  = concentrations of iron in the  $\alpha$  and TiFe phase

$X_\alpha$  and  $X_{\text{TiFe}}$  = weight fractions of the  $\alpha$  and TiFe phase

$f_\alpha$  and  $f_{\text{TiFe}}$  = Mössbauer  $f$  factors of the  $\alpha$  and TiFe phase

This equation can be applied to the aluminium intermetallic phase  $\text{Al}_3\text{Fe}$  to determine the iron concentrations within the two quadrupole interactions that are attributed to the Mössbauer spectrum, see Equation 4.13. The results that were obtained when applied to the variable temperature Mössbauer data are shown in Table 4.6.

$$\left( \frac{C_{Fe}^{Fe(5)site}}{C_{Fe}^{Fe(1)-Fe(4)site}} \right) = \left( \frac{A_{Fe(5)site}}{A_{Fe(1)-Fe(4)site}} \right) \left( \frac{X_{Fe(5)site}}{X_{Fe(1)-Fe(4)site}} \right) \left( \frac{f_{Fe(5)site}}{f_{Fe(1)-Fe(4)site}} \right) \quad \text{Equation 4.13}$$

The average value obtained for the ratio of iron concentration between the two different Fe environments,  $C_{Fe}^{Fe(5)site} / C_{Fe}^{Fe(1)-Fe(4)site}$ , was  $2.4 \pm 0.1$ . This is very similar to the value reported by Chittaranjan [6], which was 2.23. However, when considering the crystal structure of  $\text{Al}_3\text{Fe}$  the expected ratio should be 2 [7, 8]. Chittaranjan attributed the difference between the observed and expected values to small defects within the unit cell, which would produce small errors in the final fitting parameters of the spectrum.

Temp. K	Rel. Area, %	<i>f</i> factor	<i>R</i> value	$X_{Fe(5)} / X_{Fe(1)-Fe(4)}$	$f_{Fe(5)} / f_{Fe(1)-Fe(4)}$	$C_{Fe}^{Fe(5)} / C_{Fe}^{Fe(1)-Fe(4)}$																																																																			
20	66.49	0.9235	0.504	0.229	1.009	2.178																																																																			
	33.51	0.9319					50	63.15	0.9183	0.584	0.229	1.011	2.518	36.85	0.9282	60	63.56	0.9155	0.573	0.229	1.012	2.472	36.44	0.9262	100	62.45	0.9007	0.601	0.229	1.016	2.580	37.55	0.9154	120	65.22	0.8915	0.533	0.229	1.019	2.282	34.78	0.9085	151	62.97	0.8761	0.588	0.229	1.025	2.503	37.03	0.8967	200	63.07	0.8499	0.586	0.229	1.031	2.477	36.93	0.8763	251	64.29	0.8220	0.555	0.229	1.039	2.332	35.71	0.8540	295	63.39	0.7979	0.578
50	63.15	0.9183	0.584	0.229	1.011	2.518																																																																			
	36.85	0.9282					60	63.56	0.9155	0.573	0.229	1.012	2.472	36.44	0.9262	100	62.45	0.9007	0.601	0.229	1.016	2.580	37.55	0.9154	120	65.22	0.8915	0.533	0.229	1.019	2.282	34.78	0.9085	151	62.97	0.8761	0.588	0.229	1.025	2.503	37.03	0.8967	200	63.07	0.8499	0.586	0.229	1.031	2.477	36.93	0.8763	251	64.29	0.8220	0.555	0.229	1.039	2.332	35.71	0.8540	295	63.39	0.7979	0.578	0.229	1.046	2.408	36.61	0.8345				
60	63.56	0.9155	0.573	0.229	1.012	2.472																																																																			
	36.44	0.9262					100	62.45	0.9007	0.601	0.229	1.016	2.580	37.55	0.9154	120	65.22	0.8915	0.533	0.229	1.019	2.282	34.78	0.9085	151	62.97	0.8761	0.588	0.229	1.025	2.503	37.03	0.8967	200	63.07	0.8499	0.586	0.229	1.031	2.477	36.93	0.8763	251	64.29	0.8220	0.555	0.229	1.039	2.332	35.71	0.8540	295	63.39	0.7979	0.578	0.229	1.046	2.408	36.61	0.8345													
100	62.45	0.9007	0.601	0.229	1.016	2.580																																																																			
	37.55	0.9154					120	65.22	0.8915	0.533	0.229	1.019	2.282	34.78	0.9085	151	62.97	0.8761	0.588	0.229	1.025	2.503	37.03	0.8967	200	63.07	0.8499	0.586	0.229	1.031	2.477	36.93	0.8763	251	64.29	0.8220	0.555	0.229	1.039	2.332	35.71	0.8540	295	63.39	0.7979	0.578	0.229	1.046	2.408	36.61	0.8345																						
120	65.22	0.8915	0.533	0.229	1.019	2.282																																																																			
	34.78	0.9085					151	62.97	0.8761	0.588	0.229	1.025	2.503	37.03	0.8967	200	63.07	0.8499	0.586	0.229	1.031	2.477	36.93	0.8763	251	64.29	0.8220	0.555	0.229	1.039	2.332	35.71	0.8540	295	63.39	0.7979	0.578	0.229	1.046	2.408	36.61	0.8345																															
151	62.97	0.8761	0.588	0.229	1.025	2.503																																																																			
	37.03	0.8967					200	63.07	0.8499	0.586	0.229	1.031	2.477	36.93	0.8763	251	64.29	0.8220	0.555	0.229	1.039	2.332	35.71	0.8540	295	63.39	0.7979	0.578	0.229	1.046	2.408	36.61	0.8345																																								
200	63.07	0.8499	0.586	0.229	1.031	2.477																																																																			
	36.93	0.8763					251	64.29	0.8220	0.555	0.229	1.039	2.332	35.71	0.8540	295	63.39	0.7979	0.578	0.229	1.046	2.408	36.61	0.8345																																																	
251	64.29	0.8220	0.555	0.229	1.039	2.332																																																																			
	35.71	0.8540					295	63.39	0.7979	0.578	0.229	1.046	2.408	36.61	0.8345																																																										
295	63.39	0.7979	0.578	0.229	1.046	2.408																																																																			
	36.61	0.8345																																																																							

Table 4.6 Stupel calculation applied to Al<sub>3</sub>Fe4.1.5 Al<sub>x</sub>Fe

The Mössbauer spectrum of Al<sub>x</sub>Fe, see Fig 4.10, consisted of a single asymmetrical quadrupole interaction ( $\Delta = 0.32 \pm 0.02 \text{ mm s}^{-1}$ ), which remained constant between 20 and 300 K, see Table 4.7 and Fig 4.11. The isomer shift of the doublet exhibited a standard second order Doppler shift effect, with a value of  $0.26 \pm 0.02 \text{ mm s}^{-1}$  at 20 K decreasing to  $0.18 \pm 0.02 \text{ mm s}^{-1}$  at 300 K.

Analysis of the normalised spectral areas led to a Debye temperature,  $\theta_D$ , of  $360 \pm 5$  K, and a recoil free fraction at 291 K,  $f_{291}$ , of  $0.73 \pm 0.02$ , see Fig 4.12. However, the analysis of the variation of the isomer shift with temperature produced a  $\theta_D$  of  $648 \pm 5$  K, and an intrinsic isomer shift of  $0.34 \pm 0.02$  mm s<sup>-1</sup>, see Fig 4.13.

The half-widths of the quadrupole doublet remained constant between 20 K and 300 K. This can also be attributed to the high  $\theta_D$  values, as this indicates that the iron atom is tightly held within the crystal structure.

No comparison of the Al<sub>x</sub>Fe Mössbauer parameters could be made, due to the lack of published work in this area.

File	Temp. K	$\delta$ , mm s <sup>-1</sup>	$\Delta/2$ , mm s <sup>-1</sup>	(l) $\Gamma/2$ , mm s <sup>-1</sup>	(r) $\Gamma/2$ , mm s <sup>-1</sup>	Rel. Area, %	Norm. Area	$\chi^2$
ar054	20	0.26	0.15	0.21	0.17	100.00	1.93100	0.687
ar055	60	0.28	0.16	0.19	0.16	100.00	1.97679	0.647
ar052	80	0.28	0.16	0.19	0.17	100.00	1.97793	0.699
ar056	100	0.27	0.16	0.19	0.17	100.00	1.87991	0.617
ar057	150	0.24	0.15	0.20	0.17	100.00	1.82939	0.572
ar058	200	0.23	0.16	0.21	0.17	100.00	1.68600	0.551
ar059	250	0.21	0.16	0.22	0.19	100.00	1.69908	0.650
ar053	300	0.18	0.16	0.23	0.19	100.00	1.55344	0.532

Errors: T =  $\pm 2$  K,  $\delta = \pm 0.02$  mm s<sup>-1</sup>,  $\Delta/2 = \pm 0.02$  mm s<sup>-1</sup>,  $\Gamma/2 = \pm 0.02$  mm s<sup>-1</sup>,

$\theta_D = \pm 5$  K,  $f_{291} = \pm 0.02$ .

Isomer shifts relative to  $\alpha$ -iron.

Table 4.7 Fitting parameters for Al<sub>x</sub>Fe.

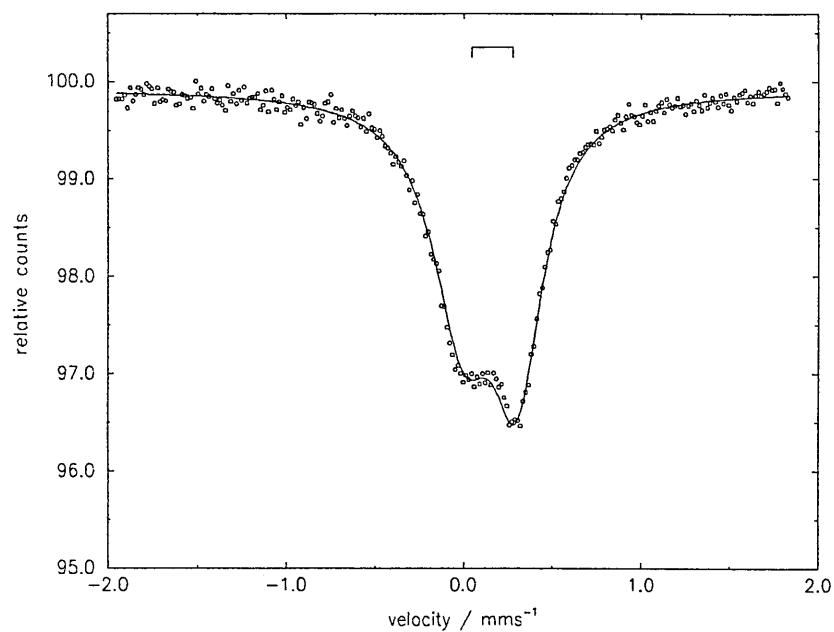


Fig 4.10 Typical Mössbauer spectrum for  $\text{Al}_x\text{Fe}$

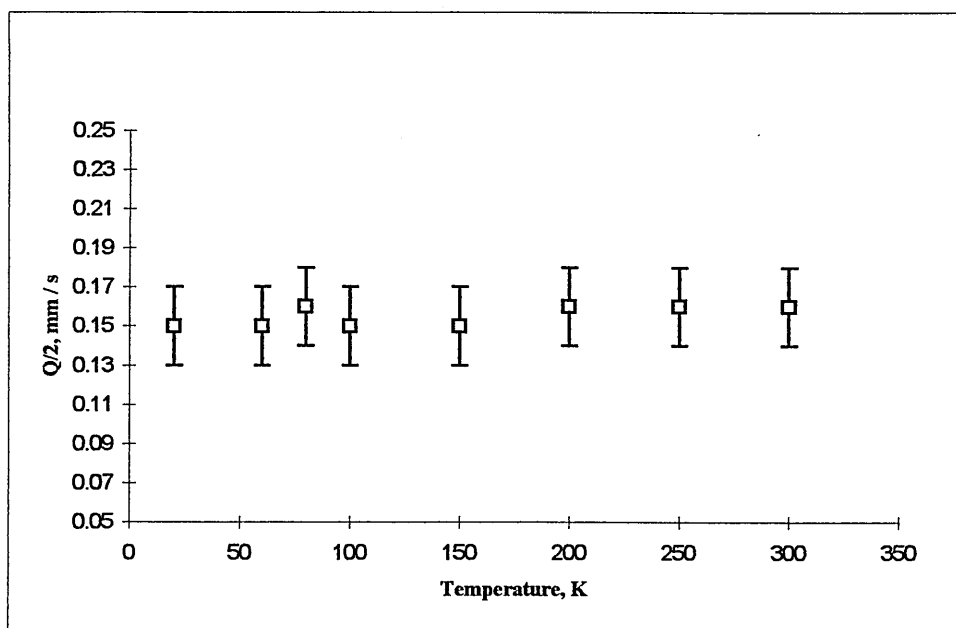


Fig 4.11 Variation of the quadrupole splitting with temperature for  $\text{Al}_x\text{Fe}$

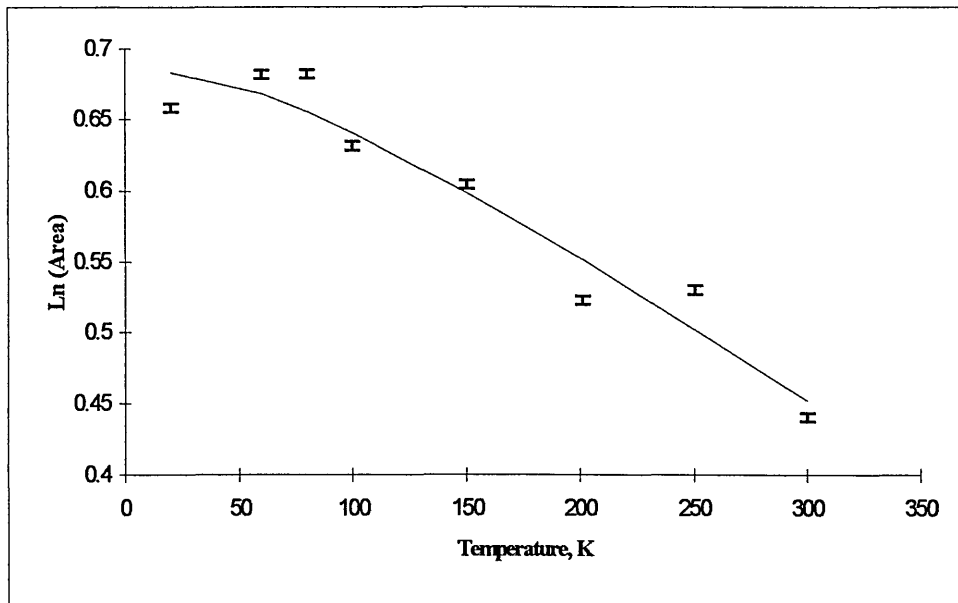


Fig 4.12 Variation of the Mössbauer spectral areas for  $Al_xFe$

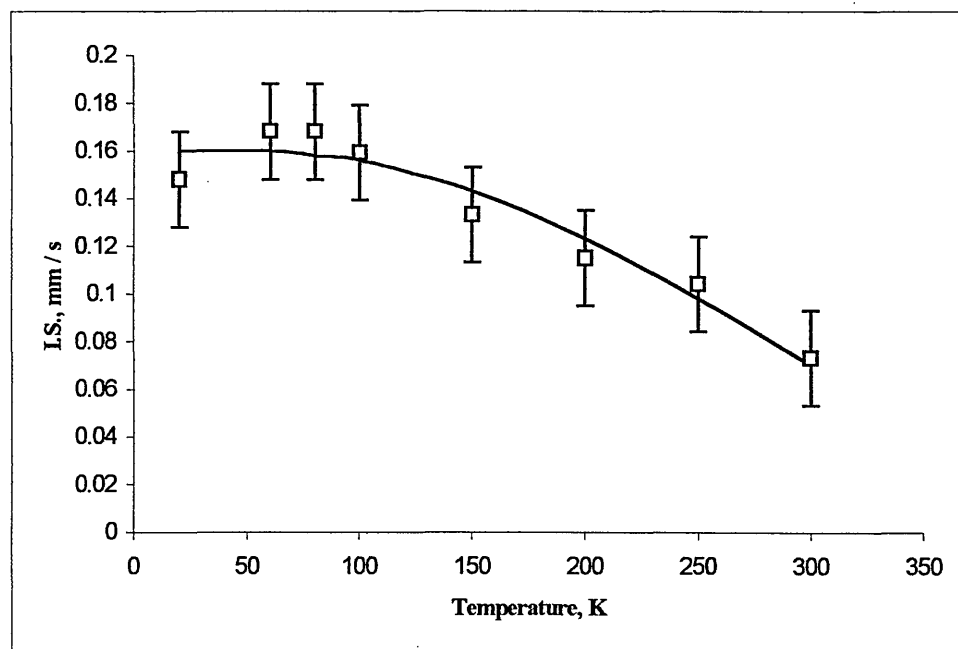


Fig 4.13 Variation of the isomer shift for  $Al_xFe$

#### 4.1.5.1 THE $\text{Al}_x\text{Fe}$ SPECTRUM

Young *et al* [31] established a structure model for  $\text{Al}_x\text{Fe}$  ( $x = 4.5$ , monoclinic,  $a = 21.6$  Å,  $b = 9.3$  Å,  $c = 9.05$  Å,  $\beta = 94.0^\circ$ ), which implied that the Fe environment is very similar to that of  $\text{Al}_6\text{Fe}$  [32, 33]. However, it was also shown that this structure is inherently highly defective, and that stacking faults are incorporated within the unit cell. This effectively gives the appearance of a very large unit cell. Also the lattice parameters can vary over an appreciable range, and this is due to the variable site occupancy of the atoms within the unit cell [31].

A detailed analysis of the crystal structure was not possible, due to the lack of published information regarding the atomic co-ordinates of this system. Therefore, the obtained Mössbauer spectrum for the intermetallic metastable phase  $\text{Al}_x\text{Fe}$  was de-convoluted to consist of a single quadrupole interaction. This was consistent with the de-convolution of the Mössbauer spectrum of  $\text{Al}_6\text{Fe}$ , which was used in a previous study [10].

When comparing the Mössbauer parameters of  $\text{Al}_x\text{Fe}$  and  $\text{Al}_6\text{Fe}$  some similarities are evident, see Table 4.8. The quadrupole interactions of the Fe environments in the two phases are identical, within experimental error, and this indicates that the electric field gradient the Fe atom experiences, in both cases, are nearly identical. This implies that the Fe atom, within  $\text{Al}_x\text{Fe}$ , must reside inside similar Al polyhedra, and thus having a similar atomic arrangement. However, the exact atomic positions within the  $\text{Al}_x\text{Fe}$  unit cell are unknown and thus it is impossible to speculate further on this matter.

However, when comparing the isomer shifts of  $\text{Al}_x\text{Fe}$  and  $\text{Al}_6\text{Fe}$  there is a  $0.05 \text{ mm s}^{-1}$  discrepancy.  $\text{Al}_x\text{Fe}$  has the lower isomer shift value, and this indicates that the Fe atom within this crystal structure may experience a higher covalence contribution than that in  $\text{Al}_6\text{Fe}$ . This increased covalence contribution causes an effective decrease in the 3d-electron shielding, due to the nephelauxetic ("cloud-expanding") effect. This implies that the s-electron density at the Fe nucleus is increased, and therefore the isomer shift

is decreased. This increased covalence experienced by the Fe atom within  $\text{Al}_x\text{Fe}$  could also explain the difference in the  $\theta_D$  values for the two intermetallic compounds.

The  $\theta_D$  value obtained, using the spectral area analysis method, for  $\text{Al}_x\text{Fe}$  is significantly higher than that of  $\text{Al}_6\text{Fe}$ . Since the Fe atom within  $\text{Al}_x\text{Fe}$  experiences a greater degree of covalence, and it would imply that the Fe atom is held more rigidly within the crystal structure than that of  $\text{Al}_6\text{Fe}$ .

There are significant differences in the line-widths between the two systems. The Mössbauer spectrum of  $\text{Al}_6\text{Fe}$  was de-convoluted into a single symmetrical quadrupole interaction, with narrow line-widths [10]. However, the Mössbauer spectrum of  $\text{Al}_x\text{Fe}$  was de-convoluted into a single asymmetrical quadrupole interaction, with comparably very broad line-widths. The possible reasons for this line broadening, and asymmetry, will be discussed in the next section, see Chapter 4.1.5.1.2.

	$\delta$ , mm s <sup>-1</sup>	$\Delta/2$ , mm s <sup>-1</sup>	(l) $\Gamma/2$ , mm s <sup>-1</sup>	(r) $\Gamma/2$ , mm s <sup>-1</sup>	$\theta_D$
$\text{Al}_6\text{Fe}$	0.23	0.15	0.15	0.15	327
$\text{Al}_x\text{Fe}$	0.18	0.16	0.23	0.19	360

Errors:  $\delta = \pm 0.02$  mm s<sup>-1</sup>,  $\Delta/2 = \pm 0.02$  mm s<sup>-1</sup>,  $\Gamma/2 = \pm 0.02$  mm s<sup>-1</sup>,

$\theta_D = \pm 5$  K.

Isomer shifts relative to  $\alpha$ -iron.

Table 4.8 Comparison of the room temperature Mössbauer parameters for  $\text{Al}_6\text{Fe}$  and  $\text{Al}_x\text{Fe}$ .

#### 4.1.5.1.1 OXIDATION STATE

The variation of the quadrupole interaction of the metastable intermetallic compounds  $\text{Al}_x\text{Fe}$  is independent of temperature. This indicates that the oxidation state could either be low-spin Fe(II) or high-spin Fe(III) [25], but when taking the isomer shift into account the Fe atom may exist in a low-spin Fe(II) state. This is identical to that of  $\text{Al}_3\text{Fe}$ , see Chapter 4.1.4.1.3.

#### 4.1.5.1.2 ASYMMETRY WITHIN THE SPECTRUM

It has already been stated that the temperature independent asymmetry observed within the spectra of  $\text{Al}_6\text{Fe}$  and  $\text{Al}_3\text{Fe}$  can be attributed to a possible combination of two different factors: particle texture and internal mechanical stress fields, which are due to the production process, see Chapter 4.1.4.1.2.

The metastable intermetallic phase  $\text{Al}_x\text{Fe}$  exists as rod-like particles within the aluminium matrix [34], which are very similar in shape to the particles of  $\text{Al}_6\text{Fe}$  [20]. This information, coupled with the proposed similarities between the two Fe environments within  $\text{Al}_x\text{Fe}$  and  $\text{Al}_6\text{Fe}$  suggests that particle texture plays a role in the observed temperature independent asymmetry. Also the internal mechanical stress fields, which are produced by the Bridgman process, are a contributing factor as well.

However, there is another possible factor, which has to be considered. The presence of a larger number of similar Fe sites can lead to an asymmetric spectrum, and with many of the lines following a Gaussian distribution. The main principles of this physical characteristic upon the resultant Mössbauer spectrum is that it actually consists of many overlapping spectra, with very small differences in the hyperfine parameters. The fitting of these spectra is inherently difficult, as the precise positioning of the overlapping spectra is often ambiguous. When attempting to de-convolute the spectrum to take into account the Fe site distribution the fitting procedures may assume that the parameters are identical, and merely de-convolute the spectrum with

negative areas, which is compensated by excessively positive areas attributed to the remaining components. However, treating the resultant Mössbauer spectrum as a single hyperfine interaction the presence of a larger number of similar Fe sites lead to broad Lorentzian line-widths being observed.

The crystal structure of  $\text{Al}_x\text{Fe}$  is highly defective, and there are stacking faults incorporated within the unit cell [31]. It is also known that there is variable site occupancy of all the atoms within the unit cell. The observed Mössbauer spectrum, see Fig 4.10, exhibits asymmetry and line broadening, which is independent of temperature, and indicates that there exists a possible Fe site distribution within the unit cell.

Therefore, it is a combination of physical characteristics, which are responsible for the observed asymmetry within the Mössbauer spectrum of  $\text{Al}_x\text{Fe}$ : particle texture, internal mechanical stress fields, and the presence of a distribution of Fe sites. It is impossible to speculate as to what physical characteristic is the predominant, but the asymmetry observed within the Mössbauer spectra of  $\text{Al}_6\text{Fe}$  and  $\text{Al}_3\text{Fe}$  is considerably less than that observed for  $\text{Al}_x\text{Fe}$ . It seems that the distribution of Fe sites could possibly be the dominant phenomenon.

#### 4.1.6 $\text{Al}_m\text{Fe}$

The Mössbauer spectrum of  $\text{Al}_m\text{Fe}$ , see Fig 4.14, consisted of a single symmetrical quadrupole interaction ( $\Delta = 0.32 \pm 0.02 \text{ mm s}^{-1}$ ), which remained constant between 21 and 308 K, see Table 4.9 and Fig 4.15. The isomer shift of the quadrupole interaction exhibited a standard second order Doppler shift effect, with a value of  $0.25 \pm 0.02 \text{ mm s}^{-1}$  at 21 K decreasing to  $0.18 \pm 0.02 \text{ mm s}^{-1}$  at 308 K.

Analysis of the normalised spectral areas led to a Debye temperature,  $\theta_D$ , of  $358 \pm 5 \text{ K}$ , and a recoil free fraction at 291 K,  $f_{291}$ , of  $0.72 \pm 0.02$ , see Fig 4.16. However, the

analysis of the variation of the isomer shift with temperature produced a  $\theta_D$  of  $755 \pm 5$  K, and a intrinsic isomer shift of  $0.35 \pm 0.02$  mm s<sup>-1</sup>, see Fig 4.17.

The half-widths of the quadrupole doublet remained constant between 21 K and 308 K. This can also be attributed to the high  $\theta_D$  values, as this indicates that the iron atom is tightly held within the crystal structure.

File	Temp. K	$\delta$ , mm s <sup>-1</sup>	$\Delta/2$ , mm s <sup>-1</sup>	(l) $\Gamma/2$ , mm s <sup>-1</sup>	(r) $\Gamma/2$ , mm s <sup>-1</sup>	Rel. Area, %	Norm. Area	$\chi^2$
ar038	21	0.25	0.16	0.21	0.21	100.00	2.67767	0.771
ar033	42	0.26	0.17	0.20	0.20	100.00	2.73842	0.734
ar018	50	0.26	0.16	0.21	0.21	100.00	2.63949	0.838
ar027	60	0.26	0.16	0.21	0.21	100.00	2.78409	0.836
ar019	100	0.24	0.16	0.21	0.21	100.00	2.51519	0.771
ar035	100	0.25	0.16	0.21	0.21	100.00	2.56902	0.878
ar020	150	0.23	0.16	0.22	0.22	100.00	2.41320	0.803
ar024	200	0.22	0.16	0.23	0.23	100.00	2.39150	0.757
ar034	225	0.21	0.16	0.21	0.22	100.00	2.29420	0.759
ar025	250	0.20	0.16	0.22	0.22	100.00	2.30529	0.663
ar016	300	0.18	0.16	0.23	0.23	100.00	2.13807	0.748
ar036	308	0.18	0.17	0.23	0.23	100.00	2.08504	1.078

Errors:  $T = \pm 2$  K,  $\delta = \pm 0.02$  mm s<sup>-1</sup>,  $\Delta/2 = \pm 0.02$  mm s<sup>-1</sup>,  $\Gamma/2 = \pm 0.02$  mm s<sup>-1</sup>,

$\theta_D = \pm 5$  K,  $f_{291} = \pm 0.02$ .

Isomer shifts relative to  $\alpha$ -iron.

Table 4.9 Fitting parameters for Al<sub>m</sub>Fe.

These values of the Mössbauer parameters, at room temperature, for Al<sub>m</sub>Fe agreed with other published work [36, 37]. However, a complete comparison was not possible due to the lack of other published low temperature work.

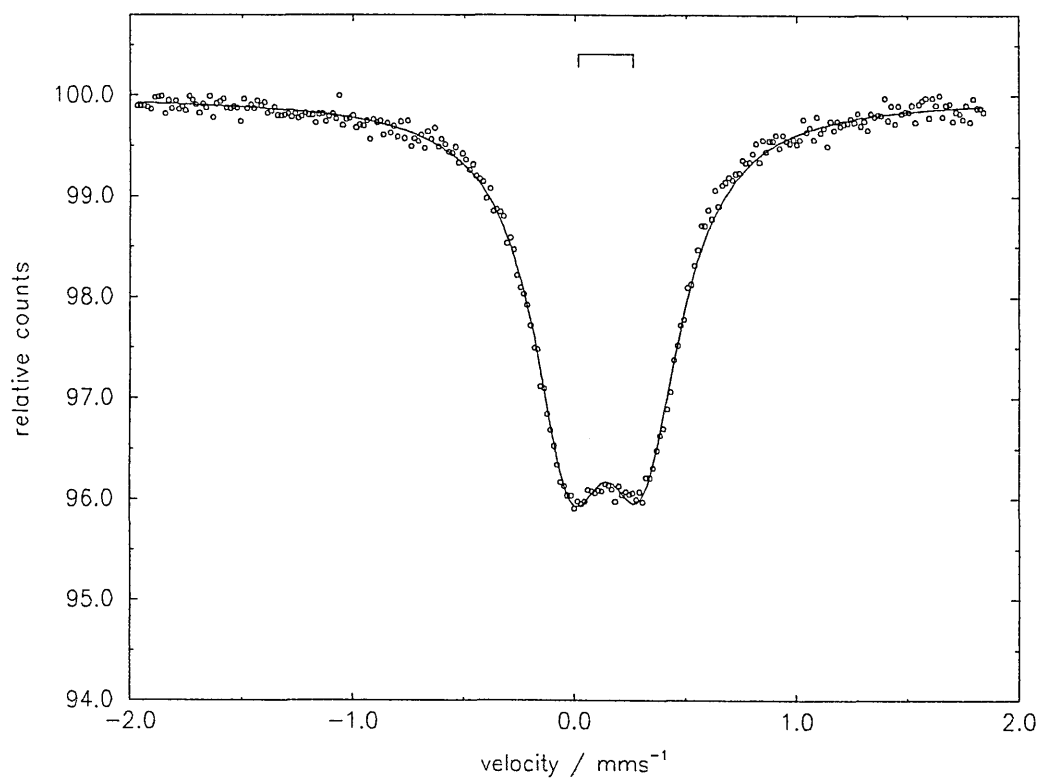


Fig 4.14 Typical Mössbauer spectrum for  $\text{Al}_m\text{Fe}$

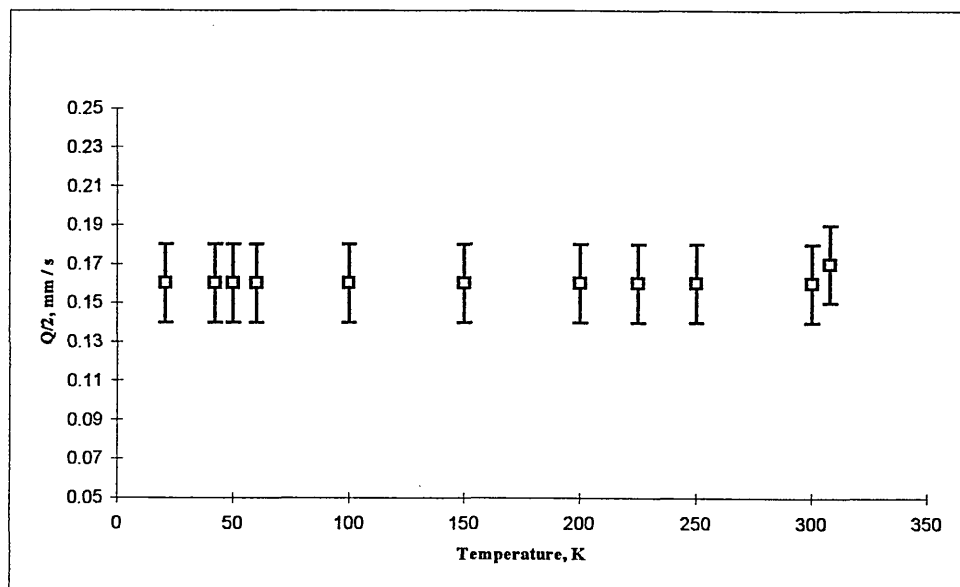


Fig 4.15 Variation of the quadrupole splitting with temperature for  $\text{Al}_m\text{Fe}$

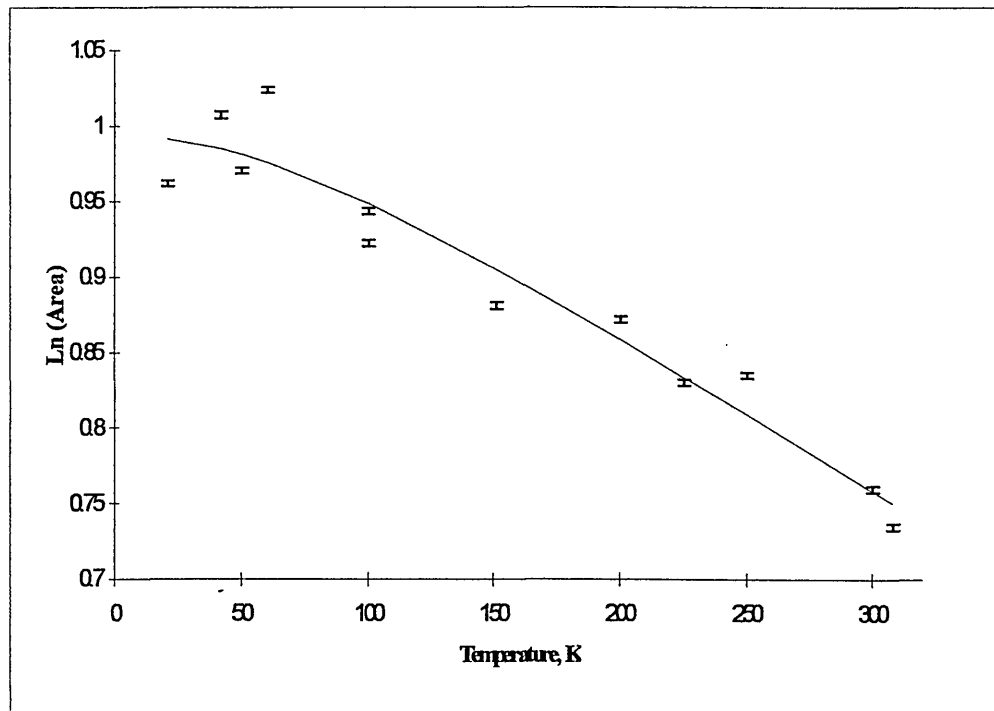


Fig 4.16 Variation of the Mössbauer spectral areas for  $Al_mFe$

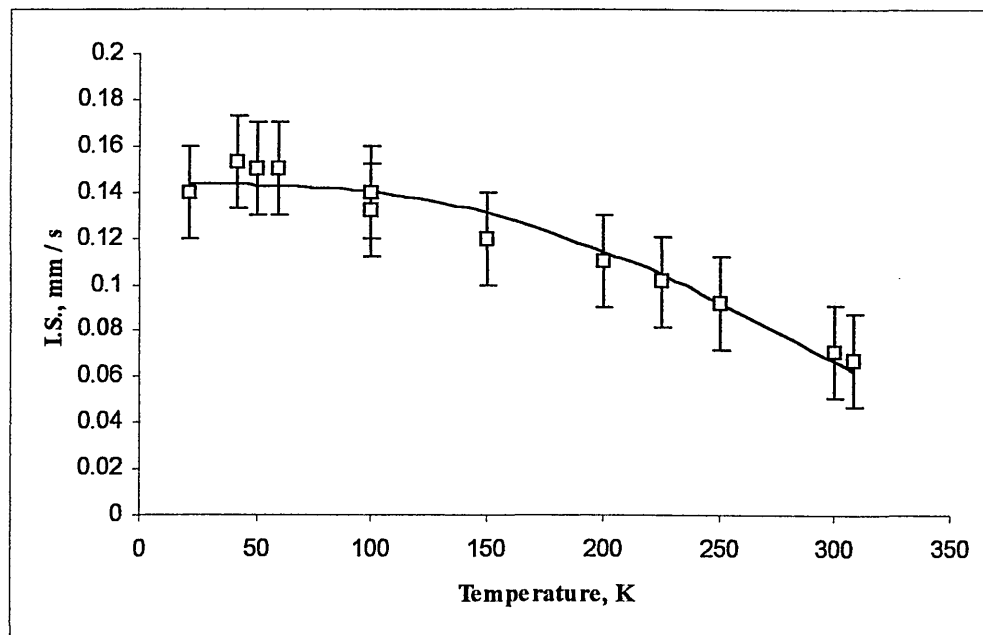


Fig 4.17 Variation of the isomer shift for  $Al_mFe$

#### 4.1.6.1 THE $\text{Al}_m\text{Fe}$ SPECTRUM

The metastable intermetallic phase  $\text{Al}_m\text{Fe}$  was first discovered by Mikki *et al* [38], as a solid precipitate within a DC-cast ingot, with a body centred tetragonal unit cell where  $a = 8.84 \text{ \AA}$  and  $c = 21.6 \text{ \AA}$ . However, Skjerpe [39] first proposed a comprehensive crystal structure model for this metastable phase, which was based upon the space group  $I4/mmm$ . This predicted a single Fe site in layers along the (001), separated by two or three layers of Al atoms. Since  $m$  lies in the range of 4.0-4.4 it implies that there are 20-22 Fe atoms, and 110-120 atoms in total within the unit cell.

The de-convoluting procedure used for this particular metastable intermetallic compound was based upon the crystal model proposed by Skjerpe [39], which consisted of attributing a single quadrupole interaction to the spectrum. However, a detailed analysis of the Fe environment was not possible, due to the lack of published information regarding the atomic co-ordinates of this system.

The comparison between the similar observed Mössbauer hyperfine parameters, and thus the Fe environments, of the two metastable intermetallic compounds  $\text{Al}_x\text{Fe}$  and  $\text{Al}_6\text{Fe}$  has been made in Chapter 4.1.5.1. However, an even closer comparison was evident between the observed Mössbauer hyperfine parameters of  $\text{Al}_x\text{Fe}$  and  $\text{Al}_m\text{Fe}$ , see Table 4.10. The isomer shift, the magnitude of quadrupole interaction, and the  $\theta_D$  are indistinguishable, within experimental error, between the two metastable intermetallic compounds, which indicates that the Fe environments are very closely related.

The only difference observed was the lack of any asymmetry in the  $\text{Al}_m\text{Fe}$  Mössbauer spectrum, compared to the prominent asymmetry within the  $\text{Al}_x\text{Fe}$  Mössbauer spectrum. However,  $\text{Al}_m\text{Fe}$  had the same broad Lorentzian line-widths as  $\text{Al}_x\text{Fe}$ , thus indicating that a number of very similar Fe environments existed within the unit cell.

	$\delta$ , mm s <sup>-1</sup>	$\Delta/2$ , mm s <sup>-1</sup>	(l) $\Gamma/2$ , mm s <sup>-1</sup>	(r) $\Gamma/2$ , mm s <sup>-1</sup>	$\theta_D$
Al <sub>6</sub> Fe	0.23	0.15	0.15	0.15	327
Al <sub>x</sub> Fe	0.18	0.16	0.23	0.19	360
Al <sub>m</sub> Fe	0.18	0.17	0.23	0.23	358

Errors:  $\delta = \pm 0.02$  mm s<sup>-1</sup>,  $\Delta/2 = \pm 0.02$  mm s<sup>-1</sup>,  $\Gamma/2 = \pm 0.02$  mm s<sup>-1</sup>,  
 $\theta_D = \pm 5$  K.

Isomer shifts relative to  $\alpha$ -iron.

Table 4.10 Comparison of the room temperature Mössbauer parameters for Al<sub>6</sub>Fe, Al<sub>x</sub>Fe, and Al<sub>m</sub>Fe.

Therefore, the resultant Mössbauer spectrum consisted of a number of very similar quadrupole interactions, and any slight residual asymmetry, attributed to particle texture and internal mechanical stress fields, would possibly be lost in the computer fitting process.

#### 4.1.6.1.1 OXIDATION STATE

The variation of the quadrupole interaction of the metastable intermetallic compound Al<sub>m</sub>Fe is independent of temperature. This indicates that the oxidation state could either be low-spin Fe(II) or high-spin Fe(III) [25], but when taking the isomer shift into account the Fe atom may exist in a low-spin Fe(II) state. This is identical to that of Al<sub>3</sub>Fe, see Chapter 4.1.4.1.3, and Al<sub>x</sub>Fe, see Chapter 4.1.5.1.1.

#### 4.1.7 $\alpha_c$ -AlFeSi

The Mössbauer spectrum of  $\alpha_c$ -AlFeSi, see Fig 4.17, consisted of two quadrupole interactions ( $\Delta = 0.22 \pm 0.02 \text{ mm s}^{-1}$  and  $0.36 \pm 0.02 \text{ mm s}^{-1}$ ), which remained constant between 20 and 300 K, see Table 4.11 and Fig 4.18. The isomer shift of the two quadrupole interactions exhibited a standard second order Doppler shift effect, with values of  $0.38 \pm 0.02 \text{ mm s}^{-1}$  and  $0.30 \pm 0.02 \text{ mm s}^{-1}$  at 20 K decreasing to  $0.28 \pm 0.02 \text{ mm s}^{-1}$  and  $0.18 \pm 0.02 \text{ mm s}^{-1}$  at 300 K.

Analysis of the normalised spectral areas led to a Debye temperature,  $\theta_D$ , of  $297 \pm 5 \text{ K}$ , and a recoil free fraction at 291 K,  $f_{291}$ , of  $0.63 \pm 0.02$  for the smaller quadrupole interaction, Fe(1), see Fig 4.19. The larger quadrupole interaction, Fe(2), produced a  $\theta_D$  of  $329 \pm 5 \text{ K}$ , and a  $f_{291}$  of  $0.68 \pm 0.02$ , when the spectral areas were investigated, see Fig 4.20. Also the combined normalised spectral areas, Fe(1)-Fe(2), led to a  $\theta_D$  of  $311 \pm 5 \text{ K}$ , and a  $f_{291}$  of  $0.66 \pm 0.02$ , see Fig 4.21.

The analysis of the variation of the isomer shift with temperature for Fe(1) produced a  $\theta_D$  of  $606 \pm 5 \text{ K}$ , and an intrinsic isomer shift of  $0.43 \pm 0.02 \text{ mm s}^{-1}$ , see Fig 4.22. The same analysis led to a  $\theta_D$  of  $585 \pm 5 \text{ K}$ , and an intrinsic isomer shift of  $0.34 \pm 0.02 \text{ mm s}^{-1}$ , see Fig 4.23, for Fe(2).

The half-widths of both the quadrupole interactions remained constant between 20 K and 300 K. This can be attributed to the high  $\theta_D$  values, as this indicates that the iron atom is tightly held within the crystal structure.

These values of the Mössbauer parameters, at room temperature, for  $\alpha_c$ -AlFeSi agreed with other published work [40]. However, a complete comparison was not possible due to the lack of published low temperature work.

File	Temp. K	$\delta$ , mm s <sup>-1</sup>	$\Delta/2$ , mm s <sup>-1</sup>	(l) $\Gamma/2$ , mm s <sup>-1</sup>	(r) $\Gamma/2$ , mm s <sup>-1</sup>	Rel. Area, %	Norm. Area	$\chi^2$
ar101	20	0.38	0.11	0.20	0.20	51.97	1.26958	0.762
		0.30	0.19	0.20	0.20	48.03	1.17335	
ar090	50	0.38	0.11	0.17	0.17	49.26	0.95242	0.967
		0.29	0.18	0.17	0.17	50.74	0.98100	
ar105	75	0.37	0.11	0.17	0.17	48.65	1.11103	0.815
		0.28	0.18	0.17	0.17	51.35	1.17273	
ar091	100	0.36	0.11	0.18	0.18	49.15	0.98276	0.954
		0.28	0.19	0.18	0.18	50.85	1.01676	
ar104	150	0.34	0.11	0.18	0.18	49.94	1.04627	0.764
		0.26	0.19	0.18	0.18	50.06	1.04864	
ar092	150	0.34	0.11	0.18	0.18	50.14	0.88392	0.895
		0.26	0.19	0.18	0.18	49.86	0.87984	
ar093	200	0.32	0.11	0.18	0.18	49.40	0.81774	0.969
		0.24	0.19	0.18	0.18	50.60	0.83773	
ar103	225	0.32	0.11	0.18	0.18	49.85	0.93996	0.684
		0.23	0.19	0.18	0.18	50.15	0.94547	
ar094	250	0.31	0.11	0.19	0.19	47.12	0.75122	0.800
		0.22	0.19	0.19	0.19	52.88	0.84292	
ar098	300	0.28	0.10	0.19	0.19	49.36	0.67935	0.769
		0.18	0.19	0.19	0.19	50.64	0.78164	

Errors:  $T = \pm 2$  K,  $\delta = \pm 0.02$  mm s<sup>-1</sup>,  $\Delta/2 = \pm 0.02$  mm s<sup>-1</sup>,  $\Gamma/2 = \pm 0.02$  mm s<sup>-1</sup>,

$\theta_D = \pm 5$  K,  $f_{291} = \pm 0.02$ .

Isomer shifts relative to  $\alpha$ -iron.

Table 4.11 Fitting parameters for  $\alpha_c$ -AlFeSi

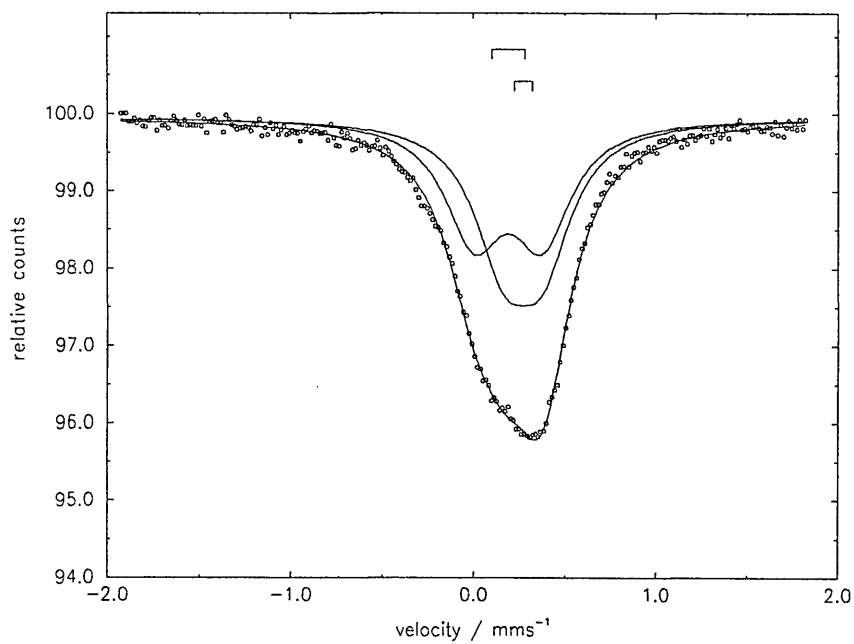


Fig 4.17 Typical Mössbauer spectrum for  $\alpha_c$ -AlFeSi

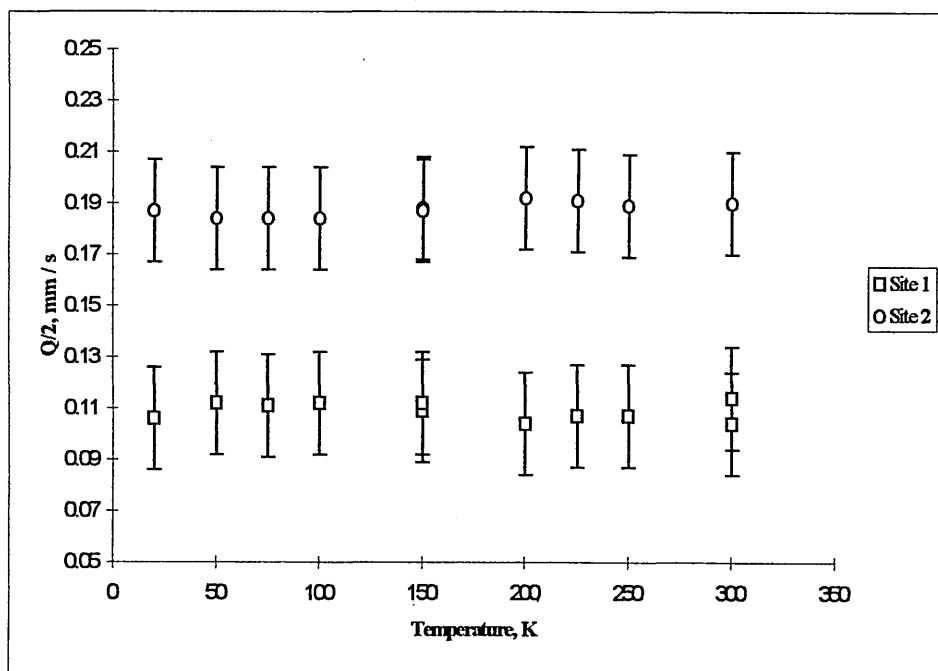


Fig 4.18 Variation of the quadrupole interaction with temperature for  $\alpha_c$ -AlFeSi

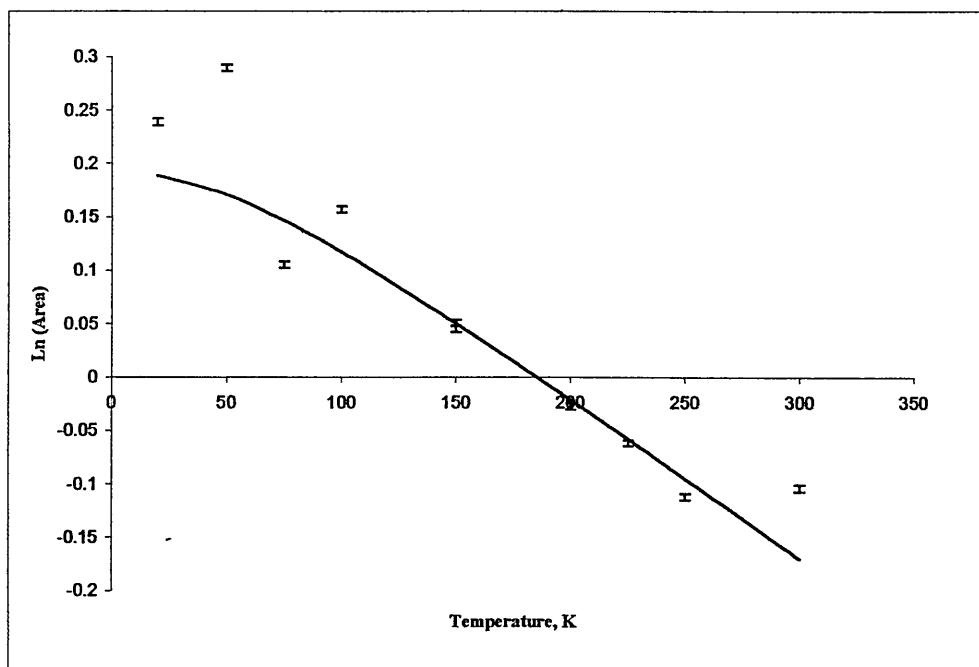


Fig 4.19 Variation of the Mössbauer spectral areas for Fe(1)

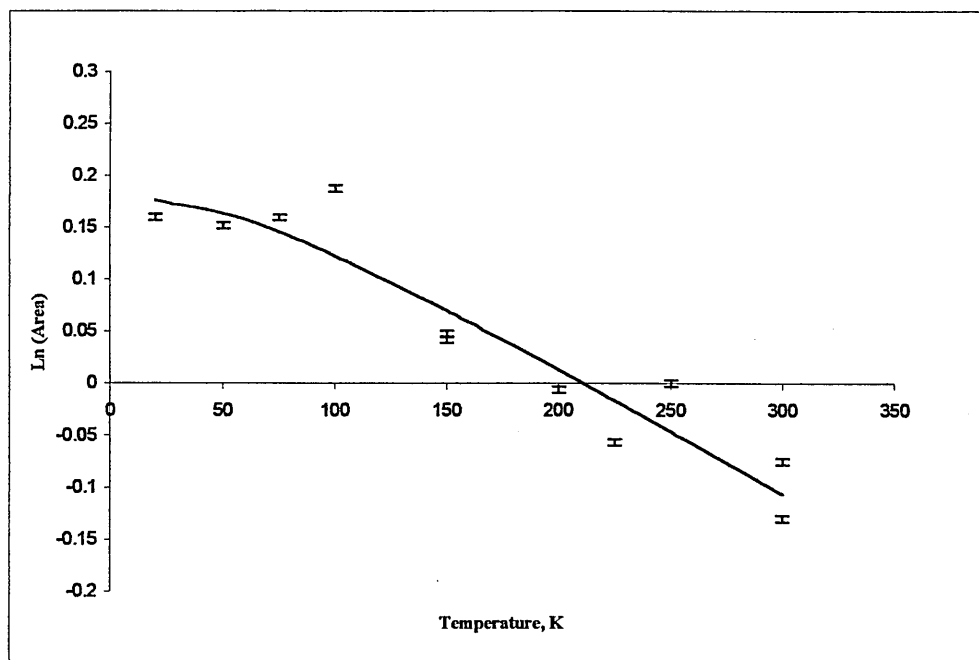


Fig 4.20 Variation of the Mössbauer spectral areas for Fe(2)

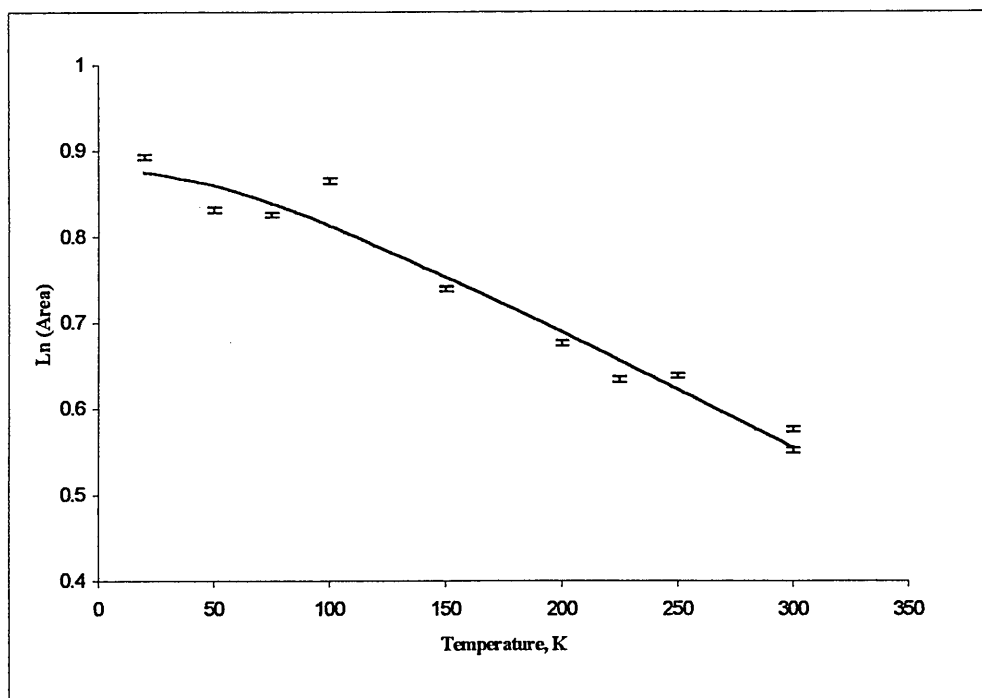


Fig 4.21 Variation of the Mössbauer combined spectral areas for  $\alpha_c$ -AlFeSi, Fe(1)-Fe(2)

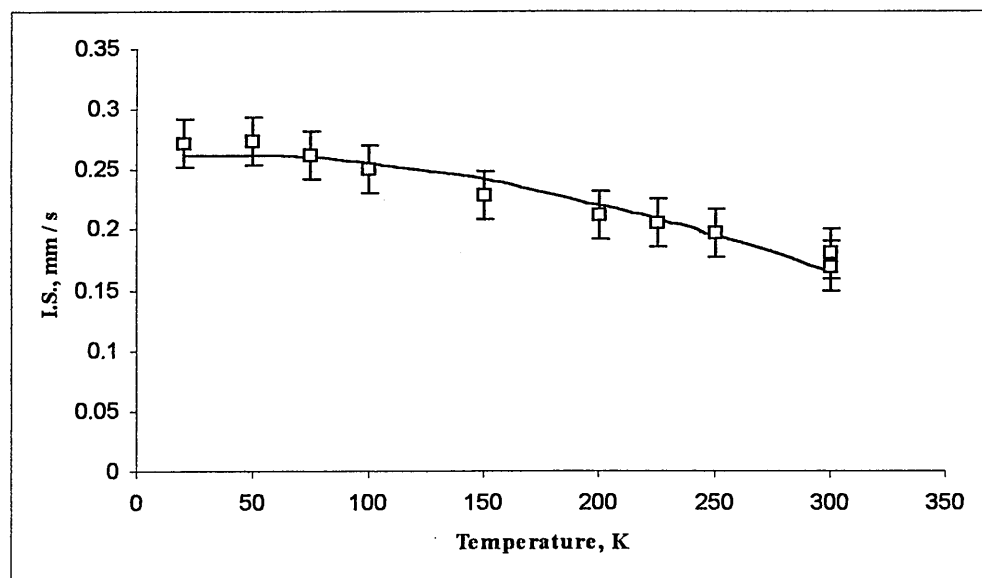


Fig 4.22 Variation of the isomer shift for  $\alpha_c$ -AlFeSi Fe(1)

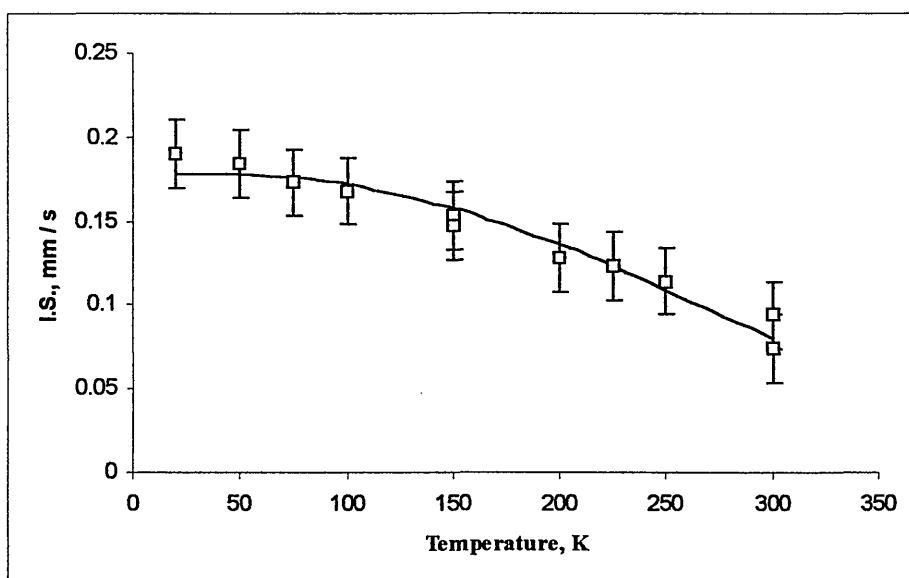


Fig 4.23 Variation of the isomer shift for  $\alpha_c$ -AlFeSi Fe(2)

#### 4.1.7.1 THE $\alpha_c$ -AlFeSi SPECTRUM

The crystal structure of the metastable phase  $\alpha_c$ -AlFeSi has been fully described earlier, see Chapter 1.4.2. The unit cell is cubic, with a cell size of 2.56 Å and space group Im3 [41], and there is an isomorph within the Al-Mn-Si system,  $\alpha_c$ -AlMnSi [42]. Within the unit cell there are two Fe environments, one Fe site, Fe(1), is an Fe centred 10 co-ordinated Al polyhedra and the other Fe environment, Fe(2), is an Fe centred 9 co-ordinated Al polyhedra, see Table 4.12.

The atomic arrangement of the two different Fe centred Al polyhedra are identical to those found within the equilibrium hexagonal compound,  $\alpha_H$ -AlFeSi [43], and the only discrepancies are in slight changes in certain Al-Fe bond lengths. The Fe(1) site has 10 Al nearest neighbours arrange in a 3-4-3 system, which are distributed in a near symmetrical fashion around the central Fe atom. This implies that the component within the resultant Mössbauer spectrum with the smaller quadrupole interaction can be attributed to the Fe(1) environment. The remaining Fe site, Fe(2), has 9 Al nearest neighbours distributed in a 3-3-3 arrangement, around the central Fe atom, and the

three Al atoms within the same basal plane as the Fe atom are distributed so that two Al atoms are weighted to one side of the Fe atom. This has the effect of increasing the electric field gradient across the Fe atom, and thus increasing the magnitude of the quadrupole interaction. Therefore, when the resultant Mössbauer spectrum was de-convoluted the component with the larger quadrupole interaction was attributed to the Fe(2) site.

Intermetallic Phase	Site	No. of Al- Trans. Met. Bonds	Al-Trans. Met. Bond Length
$\alpha_c$ -AlMnSi	Mn(1)	10	2.43 - 2.84 Å
	Mn(2)	9	2.27 - 2.62 Å
$\alpha_c$ -AlFeSi	Fe(1)	10	2.43 - 2.81 Å
	Fe(2)	9	2.43 - 2.68 Å

Table 4.12 Summary of the Transition Metal sites in  $\alpha_c$ -AlFeSi and  $\alpha_c$ -AlMnSi [41,42].

This de-convoluting procedure of the Mössbauer spectrum of this metastable intermetallic compound was identical to that of the one employed by Nagy *et al* [40], but it was not fully justified within that particular publication. This issue has now been addressed, but it will be re-enforced when considering the next section.

The line-widths of the two symmetrical quadrupole interactions are broad, but not as broad when compared to  $Al_mFe$ , see Chapter 4.1.6.1, and that of  $Al_xFe$ , see Chapter 4.1.5.1.2. This would indicate that there is present a certain degree of Fe site distribution within Fe(1) and Fe(2). This is not surprising when considering the crystal structure, as there are two primitive unit cells that are linked together to yield an average unit cell with a space group of  $Im\bar{3}$ . In one primitive unit cell sites Al(7), Al(9), and Al(11) are occupied and in the other sites Al(8), Al(10), and Al(12) are

occupied. However, the occupation of the different Fe environments was not unequivocally established, but they appear to be well established [41]. This would lead to a slight disorder within the average unit cell, which would be responsible for the broad Mössbauer line-widths observed.

#### 4.1.7.1.1 DEBYE TEMPERATURE ANALYSIS

In the previous section the Mössbauer spectrum of  $\alpha_c$ -AlFeSi was de-convoluted with two quadrupole interactions, with different magnitudes. The quadrupole interaction with the smaller splitting was attributed to Fe(1), and the remaining quadrupole interaction was attributed to the Fe(2) site.

When the spectral areas were analysed the smaller quadrupole interaction produced a  $\theta_D$  of  $297 \pm 5$  K, and a recoil free fraction at 291 K,  $f_{291}$ , of  $0.63 \pm 0.02$ , and for the larger quadrupole interaction produced a  $\theta_D$  of  $329 \pm 5$  K, and a  $f_{291}$  of  $0.68 \pm 0.02$ . The difference in the  $\theta_D$  between the two quadrupole components can be explained due to the different Al-Fe bond lengths. The ten co-ordinated Fe centred polyhedra, Fe(1), has a Al-Fe bond range of 2.43 - 2.81 Å, compared to the nine co-ordinated Fe centred polyhedra, Fe(2), which has an Al-Fe bond range of 2.43 - 2.68 Å. This implies that the Fe(2) atom is more tightly held within the aluminium cage than Fe(1), and would thus have less vibrational freedom. This is illustrated by the  $49 \pm 5$  K difference in the  $\theta_D$  value for the two quadrupole interactions.

The issue of the shortest Al-Fe bond length does not play the significant role as in  $\text{Al}_3\text{Fe}$ . This is due to the two different polyhedra having the same shortest Al-Fe bond, which is 2.43 Å in length. Therefore, only the bond distribution is the only significant contribution to the  $\theta_D$ . It was not possible to quote an average Al-Fe bond length, due to the lack of published information.

The combined normalised spectral areas for Fe sites, Fe(1) and Fe(2), produced a  $\theta_D$  value of  $312 \pm 5$  K, and a  $f_{291}$  of  $0.66 \pm 0.02$ . This value is an average, and is quoted for the intermetallic compound as a whole.

#### 4.1.7.1.2 STUPEL CALCULATIONS

The Stupel equation [30] was applied to the  $\text{Al}_3\text{Fe}$  equilibrium compound, see Chapter 4.1.4.1.4, to determine the relative Fe ratios, within the flat and puckered layers of atoms, that are present within the unit cell, Equation 4.13.

$$\left( \frac{C_{Fe}^{Fe(5)site}}{C_{Fe}^{Fe(1)-Fe(4)site}} \right) = \left( \frac{A_{Fe(5)site}}{A_{Fe(1)-Fe(4)site}} \right) \Bigg/ \left( \frac{X_{Fe(5)site}}{X_{Fe(1)-Fe(4)site}} \right) \left( \frac{f_{Fe(5)site}}{f_{Fe(1)-Fe(4)site}} \right) \quad \text{Equation 4.13}$$

A very similar type of equation can also be applied to the  $\alpha_c\text{-AlFeSi}$  compound to determine the relative Fe concentrations of the Fe centred 10 co-ordinated Al polyhedra compared to the Fe centred 9 co-ordinated Al polyhedra, see Equation 4.14.

$$\left( \frac{C_{Fe}^{Fe(1)}}{C_{Fe}^{Fe(2)e}} \right) = \left( \frac{A_{Fe(1)}}{A_{Fe(2)}} \right) \Bigg/ \left( \frac{X_{Fe(1)}}{X_{Fe(2)}} \right) \left( \frac{f_{Fe(1)}}{f_{Fe(2)}} \right) \quad \text{Equation 4.14}$$

where  $C_{Fe}^{Fe(1)}$  and  $C_{Fe}^{Fe(2)}$  = concentrations of iron in the Fe(1) site and Fe(2) site

$X_{Fe(1)}$  and  $X_{Fe(2)}$  = weight fractions of the Fe(1) and Fe(2) site

$f_{Fe(1)}$  and  $f_{Fe(2)}$  = Mössbauer f factors of the Fe(1) and Fe(2) site

$A_{Fe(1)}$  and  $A_{Fe(2)}$  = Absorption spectral areas of the Fe(1) and Fe(2) site

The  $R$  value is determined by the absorption spectral areas, and is given by Equation 4.15.

$$R = \left( \frac{A_{Fe(1)}}{A_{Fe(2)}} \right) \quad \text{Equation 4.15}$$

The results that were obtained when applied to the variable temperature Mössbauer data are shown in Table 4.13. The average iron concentration ratio that was calculated,  $C_{Fe}^{Fe(1)} / C_{Fe}^{Fe(2)}$ , was  $1.128 \pm 0.081$ . This is in good experimental agreement with the expected iron concentration, which should be 1 when investigating the crystal structure [41]. However, the small discrepancy could be explained by the slight disorder within the unit cell, which would produce small errors in the final parameters.

Temp. K	Rel. Area, %	<i>f</i> factor	<i>R</i> value	$X_{Fe(1)}/X_{Fe(2)}$	$f_{Fe(1)}/f_{Fe(2)}$	$C_{Fe}^{Fe(1)}/C_{Fe}^{Fe(2)}$
20	57.97	0.88846	1.207	0.917	0.986	1.332
	48.03	0.899542				
50	49.26	0.872788	0.971	0.917	0.983	1.077
	50.74	0.887874				
75	48.65	0.851862	0.947	0.917	0.977	1.057
	51.35	0.871827				
100	49.15	0.827119	0.967	0.917	0.970	1.086
	50.85	0.852278				
150	50.14	0.772723	1.006	0.917	0.956	1.147
	49.86	0.808692				
150	49.94	0.772723	0.998	0.917	0.957	1.137
	50.06	0.808692				
200	49.40	0.720192	0.976	0.917	0.943	1.129
	50.60	0.763862				
225	49.85	0.694214	0.994	0.917	0.936	1.158
	50.15	0.741716				
250	47.12	0.668921	0.891	0.917	0.929	1.046
	52.88	0.719949				
300	48.26	0.61765	0.933	0.917	0.914	1.113
	51.74	0.676036				

Table 4.13 Stupel calculation applied to  $\alpha_c$ -AlFeSi

## 4.1.7.1.3 OXIDATION STATE

The variation of both of the quadrupole interactions, within the resultant Mössbauer spectrum, of the metastable intermetallic compound  $\alpha_c$ -AlFeSi is independent of temperature. This indicates that the oxidation state could either be low-spin Fe(II) or high-spin Fe(III) [25], but when taking the isomer shift into account the Fe atoms may exist in a low-spin Fe(II) state. This is identical to that of Al<sub>3</sub>Fe, see Chapter 4.1.4.1.3,

$\text{Al}_x\text{Fe}$ , see Chapter 4.1.5.1.1, and  $\text{Al}_m\text{Fe}$ , see Chapter 4.1.6.1.1. This appears to be indicative of all Al-Fe, and Al-Fe-Si intermetallic compounds.

#### 4.1.8 $\text{Al}_6(\text{Fe},\text{Mn})$

A model ternary Al-Fe-Mn alloy was also prepared from a 99.999 wt% Al, 0.5 wt% Fe, and 0.1 wt% Mn. This alloy was cast, and extracted, in the same manner as the model Al-Fe binary, and ternary Al-Fe-Si, alloys, which enabled the production of the equilibrium intermetallic compound  $\text{Al}_6(\text{Fe},\text{Mn})$  to be produced.

The Mössbauer spectrum of  $\text{Al}_6(\text{Fe},\text{Mn})$ , see Fig 4.24, consisted of a single symmetrical quadrupole doublet ( $\Delta = 0.30 \pm 0.02 \text{ mm s}^{-1}$ ), which remained constant between 20 and 300 K, see Table 4.14 and Fig 4.25. The isomer shift of the doublet exhibited a standard second order Doppler shift effect, with a value of  $0.31 \pm 0.02 \text{ mm s}^{-1}$  at 20 K decreasing to  $0.24 \pm 0.02 \text{ mm s}^{-1}$  at 300 K.

Analysis of the normalised spectral areas led to a Debye temperature,  $\theta_D$ , of  $352 \pm 5 \text{ K}$ , and a recoil free fraction at 291 K,  $f_{291}$ , of  $0.71 \pm 0.02$ , see Fig 4.26. However, the analysis of the variation of the isomer shift with temperature produced a  $\theta_D$  of  $842 \pm 5 \text{ K}$ , and an intrinsic isomer shift of  $0.42 \pm 0.02 \text{ mm s}^{-1}$ , see Fig 4.27.

The half-widths of the quadrupole doublet remained constant between 20 K and 300 K. this can be attributed to the high  $\theta_D$  values, as this indicates that the iron atom is tightly held within the crystal structure.

No comparison of the  $\text{Al}_6(\text{Fe},\text{Mn})$  Mössbauer parameters could be made, due to the lack of published work in this area.

File	Temp. K	$\delta$ , mm s <sup>-1</sup>	$\Delta/2$ , mm s <sup>-1</sup>	(l) $\Gamma/2$ , mm s <sup>-1</sup>	(r) $\Gamma/2$ , mm s <sup>-1</sup>	Rel. Area, %	Norm. Area	$\chi^2$
ar243	14	0.31	0.16	0.15	0.14	100.00	2.25187	0.689
ar244	50	0.31	0.16	0.16	0.15	100.00	2.21878	0.719
ar256	50	0.31	0.16	0.14	0.14	100.00	2.18874	0.623
ar255	100	0.30	0.15	0.15	0.15	100.00	2.0942	0.638
ar247	150	0.28	0.15	0.15	0.14	100.00	2.03219	0.652
ar260	150	0.29	0.15	0.16	0.16	100.00	2.08757	0.627
ar250	200	0.27	0.15	0.16	0.16	100.00	1.9995	0.725
ar261d	200	0.28	0.15	0.16	0.16	100.00	1.98222	0.713
ar258	250	0.25	0.15	0.15	0.14	100.00	1.80000	0.591
ar262	250	0.26	0.15	0.16	0.16	100.00	1.85023	0.652
ar253	300	0.24	0.15	0.17	0.18	100.00	1.85709	0.776
ar257b	300	0.24	0.15	0.16	0.15	100.00	1.62577	0.610
ar263	300	0.24	0.15	0.15	0.14	100.00	1.76511	0.593

Errors:  $T = \pm 2$  K,  $\delta = \pm 0.02$  mm s<sup>-1</sup>,  $\Delta/2 = \pm 0.02$  mm s<sup>-1</sup>,  $\Gamma/2 = \pm 0.02$  mm s<sup>-1</sup>,

$\theta_D = \pm 5$  K,  $f_{291} = \pm 0.02$ .

Isomer shifts relative to  $\alpha$ -iron.

Table 4.14 Fitting parameters for Al<sub>6</sub>(Fe,Mn)

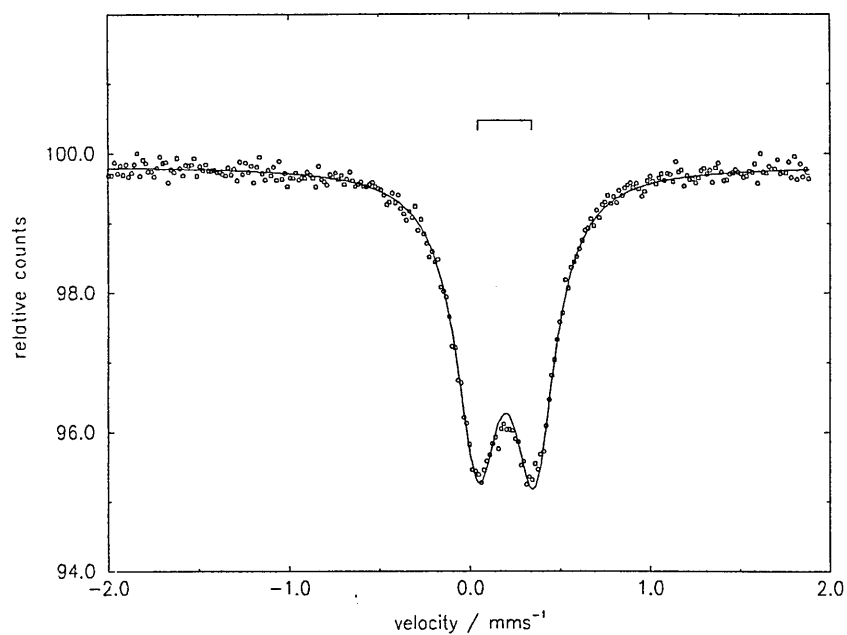


Fig 4.24 Typical Mössbauer spectrum for  $\text{Al}_6(\text{Fe},\text{Mn})$

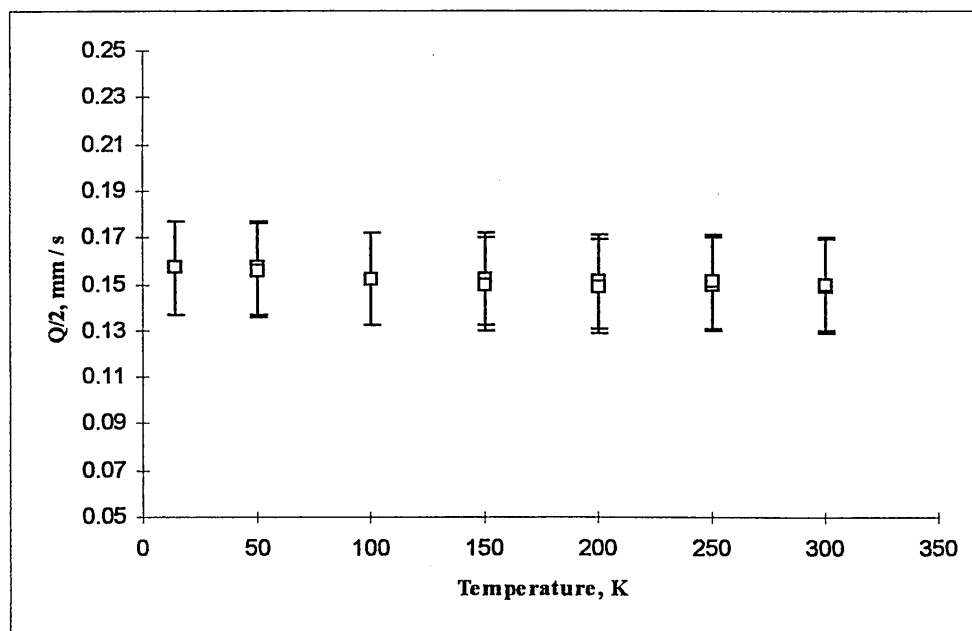


Fig 4.25 Variation of the quadrupole splitting with temperature for  $\text{Al}_6(\text{Fe},\text{Mn})$

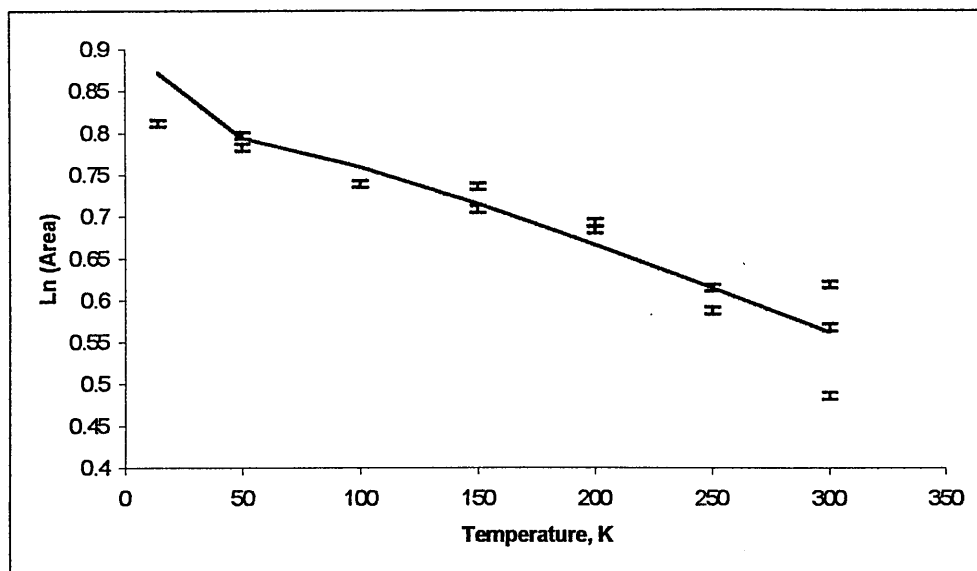


Fig 4.26 Variation of the Mössbauer spectral areas for  $\text{Al}_6(\text{Fe},\text{Mn})$

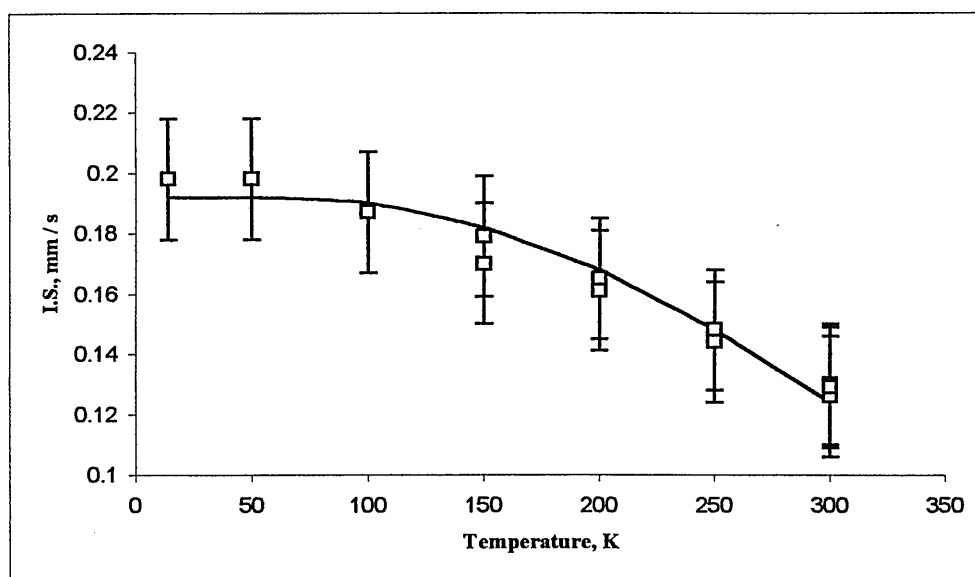


Fig 4.27 Variation of the isomer shift for  $\text{Al}_6(\text{Fe},\text{Mn})$

4.1.8.1 THE  $\text{Al}_6(\text{Fe,Mn})$  SPECTRUM

When considering the aluminium corner of the Al-Fe-Mn system it can be seen that only binary intermetallic compounds are formed: Al,  $\text{Al}_3\text{Fe}$ ,  $\text{Al}_6\text{Mn}$ , and  $\text{Al}_4\text{Mn}$  [45]. However, the Mn atoms within  $\text{Al}_6\text{Mn}$  can be substituted by Fe, up to the composition of  $\text{Al}_{12}\text{FeMn}$  (13.0% Fe, 14% Mn) and is usually given the designation of  $\text{Al}_6(\text{Fe,Mn})$  [46]. This is not surprising when considering the atomic radii of the two atoms only differ by approximately 1 pm [47], and it would also imply that the substitution would take place with only minor distortion being experienced by the unit cell. The equilibrium intermetallic compound  $\text{Al}_6(\text{Fe,Mn})$  could also be considered as the  $\text{Al}_6\text{Fe}$  metastable compound that is stabilised by Mn, and is completely miscible with  $\text{Al}_6\text{Mn}$ , which forms readily within the 3xxx series of commercial alloys [48,49].

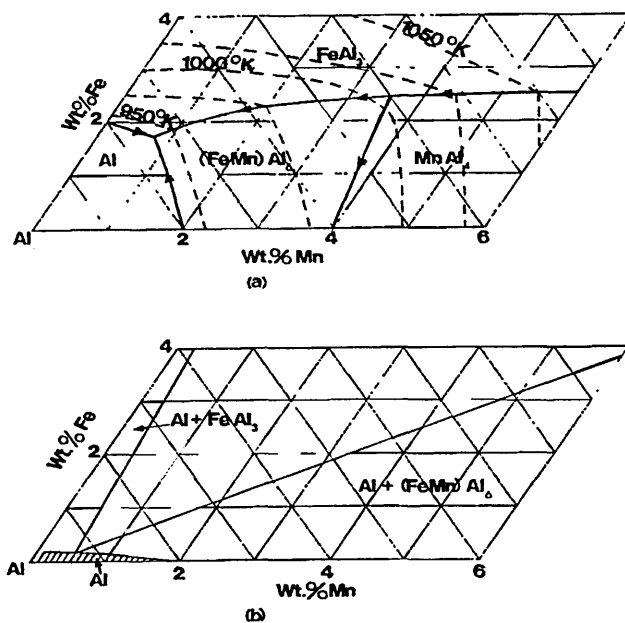


Fig 4.28 The aluminium corner of the Al-Fe-Mn equilibrium phase diagram: (a) liquidus; (b) phase distribution at 900 K [45]

The equilibrium intermetallic compound  $\text{Al}_6(\text{Fe,Mn})$  is iso-structural to the equilibrium compound  $\text{Al}_6\text{Mn}$  and the metastable compound  $\text{Al}_6\text{Fe}$ , see Table 4.15 for a

comparison of the unit cell parameters. There is only one Fe site within the unit cell of all three compounds, which exists in the centre of a 10 co-ordinated Al polyhedron. This site is very similar in atomic arrangement to that of the Fe(1)-Fe(4) sites within the equilibrium  $\text{Al}_3\text{Fe}$  compound [7,8], and is illustrated in Fig 4.29 with reference to the Mn site in  $\text{Al}_6\text{Mn}$ .

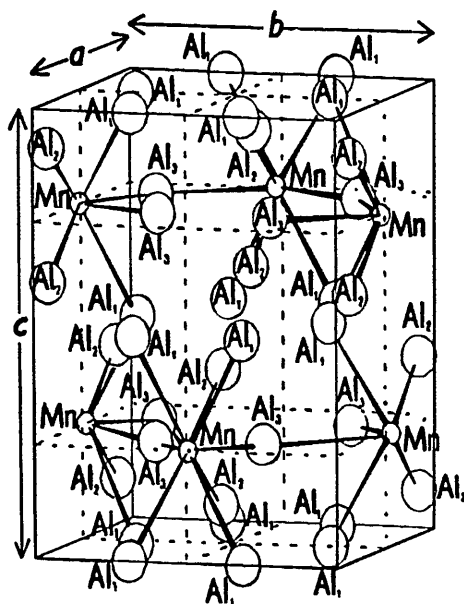


Fig 4.29 The Mn site within  $\text{Al}_6\text{Mn}$  [44]

The small differences in the unit cell parameters of the three intermetallic compounds can be explained by the increase in average Al-TM bond length (average Al-Fe bond length in  $\text{Al}_6\text{Fe} = 2.511 \pm 0.056 \text{ \AA}$  [33] and the average Al-Mn bond length in  $\text{Al}_6\text{Mn} = 2.563 \pm 0.075 \text{ \AA}$  [44]), and the increase in preferred TM-TM spacing (Fe-Fe spacing =  $3.9 \text{ \AA}$  and Mn-Mn spacing =  $4.7 \text{ \AA}$ ) [50].

Compound	a, Å	b, Å	c, Å	No. Atoms / Unit Cell	Space Group	Ref.
Al <sub>6</sub> Mn	6.498	7.552	8.870	28	<i>Ccmm</i>	[44]
Al <sub>6</sub> (Fe,Mn)	6.495	7.498	8.837	28	<i>Ccmm</i>	[45]
Al <sub>6</sub> Fe	6.464	7.440	8.779	28	<i>Ccmm</i>	[33]

Table 4.15 Comparison of the unit cell parameters for the intermetallic compounds Al<sub>6</sub>Mn, Al<sub>6</sub>(Fe,Mn), and Al<sub>6</sub>Fe

	$\delta$ , mm s <sup>-1</sup>	$\Delta/2$ , mm s <sup>-1</sup>	(l) $\Gamma/2$ , mm s <sup>-1</sup>	(r) $\Gamma/2$ , mm s <sup>-1</sup>	$\theta_D$	Ref.
Al <sub>6</sub> Fe	0.23	0.15	0.15	0.15	327	[10]
Al <sub>6</sub> (Fe,Mn)	0.22	0.15	0.15	0.15	N / A	[4]
Al <sub>6</sub> (Fe,Mn)	0.24	0.15	0.16	0.16	352	

Errors:  $\delta = \pm 0.02$  mm s<sup>-1</sup>,  $\Delta/2 = \pm 0.02$  mm s<sup>-1</sup>,  $\Gamma/2 = \pm 0.02$  mm s<sup>-1</sup>,

$\theta_D = \pm 5$  K.

Isomer shifts relative to  $\alpha$ -iron.

Table 4.16 Comparison of the room temperature Mössbauer parameters for Al<sub>6</sub>Fe and Al<sub>6</sub>(Fe,Mn)

The Mössbauer spectrum of Al<sub>6</sub>(Fe,Mn) was de-convoluted into a single symmetrical quadrupole interaction, which was identical to the approach used for Al<sub>6</sub>Fe used by several different authors [4,10, 51, 52, 53, 54, 55, 56, 57]. When comparing the Mössbauer parameters of Al<sub>6</sub>(Fe,Mn) and Al<sub>6</sub>Fe, see Table 4.16, it can be seen that they are identical, within experimental error. This would indicate that the atomic environments of the two Fe sites are identical.

However, when comparing the calculated  $\theta_D$  values, obtained by the normalised spectral method, there was a  $25 \pm 5$  K discrepancy. This could be explained as the  $\text{Al}_6\text{Mn}$  compound has two short Al-Mn bonds each 2.44 Å in length, compared to the two Al-Fe short bonds in  $\text{Al}_6\text{Fe}$  each 2.45 Å in length. It is assumed that the Fe atom directly substitutes for the Mn atom, and due to the slight increase in atomic radii of the Fe atom, these short bonds would be slightly smaller in length. This would have the effect of slightly decreasing the motion of the Fe atom, and therefore increasing the observed  $\theta_D$  value by a similar relative amount.

It has already been shown that these short bonds play a considerable role in determining the  $\theta_D$  value of the intermetallic compound under study, see Chapter 4.1.4.1.1 and Chapter 4.1.7.1.1.

#### 4.1.8.1.1 OXIDATION STATE

The variation of both of the quadrupole interactions, within the resultant Mössbauer spectrum, of the equilibrium intermetallic compound  $\text{Al}_6(\text{Fe},\text{Mn})$  is independent of temperature. This indicates that the oxidation state could either be low-spin Fe(II) or high-spin Fe(III) [25], but when taking the isomer shift into account the Fe atom may exist in a low-spin Fe(II) state. This is identical to that of  $\text{Al}_3\text{Fe}$ , see Chapter 4.1.4.1.3,  $\text{Al}_x\text{Fe}$ , see Chapter 4.1.5.1.1, and  $\text{Al}_m\text{Fe}$ , see Chapter 4.1.6.1.1.

## 4.2 CONCLUSIONS

The most common aluminium intermetallic compounds that form during commercial DC casting of the 1xxx series alloys have been investigated using  $^{57}\text{Fe}$  variable temperature Mössbauer spectroscopy. They were the equilibrium Al-Fe compound,  $\text{Al}_3\text{Fe}$ , the metastable Al-Fe compounds,  $\text{Al}_m\text{Fe}$ ,  $\text{Al}_x\text{Fe}$ , and the metastable Al-Fe-Si compound,  $\alpha_c\text{-AlFeSi}$ . Also the equilibrium intermetallic compound  $\text{Al}_6(\text{Fe},\text{Mn})$  has been analysed using the same techniques, which can be considered as being a Fe substituted form of the equilibrium Al-Mn intermetallic compound,  $\text{Al}_6\text{Mn}$ .

Model alloys were prepared using a Bridgman furnace, which enabled the solidification rate of the alloy to be accurately determined, and the growth velocity could be tuned to promote the formation of an individual intermetallic compound between the dendrite arms of the host alloy matrix. The intermetallic compounds were then extracted from the aluminium matrix using the butanol extraction method, pioneered by Simensen *et al* [1]. The XRD traces of the individual intermetallic compounds were compared to a database prepared in-house at Alcan International [58], as a check to prove that only a single aluminium intermetallic compound was formed.

The Mössbauer spectra for each of the aluminium intermetallic compounds studied were de-convoluted according to their crystallographic structure. When studying the crystallographic structure of each of the aluminium intermetallics it was found that the Fe site resided in the centre of a polyhedron with aluminium atoms at the vertices. The only changes in the different types of polyhedra were the co-ordination number, from 9-10 in some cases, and slight variations in the Al-Fe bond lengths. This analysis was possible due to the detailed crystallographic information published on the intermetallic compounds  $\text{Al}_3\text{Fe}$  [7, 8],  $\alpha_c\text{-AlFeSi}$  [41, 42], and  $\text{Al}_6(\text{Fe},\text{Mn})$  [33, 44]. However, the atomic co-ordinates for the intermetallic compounds  $\text{Al}_m\text{Fe}$  [36] and  $\text{Al}_x\text{Fe}$  [31] have not been published, due to these compounds having a high degree of inherent defects within their unit cells, but their Mössbauer parameters are very similar to those of

$\text{Al}_6\text{Fe}$  [10]. Therefore, the Fe environments in these two compounds must be very similar to the Fe environment within the unit cell of  $\text{Al}_6\text{Fe}$  [33].

The  $\theta_D$  values, when calculated by the normalised spectral area method, produce a variety of different values for the intermetallic compounds studied, see Table 4.17.

Intermetallic	Calculated $\theta_D$ , K	Calculated $f_{291}$
$\text{Al}_3\text{Fe}$	452 Fe(1)-Fe(5)	0.81 Fe(1)-Fe(5)
	434 Fe(1)-Fe(4)	0.80 Fe(1)-Fe(4)
	488 Fe(5)	0.84 Fe(5)
$\text{Al}_x\text{Fe}$	360	0.73
$\text{Al}_m\text{Fe}$	358	0.72
$\alpha_c\text{-AlFeSi}$	311 Fe(1)-Fe(2)	0.66 Fe(1)-Fe(2)
	297 Fe(1)	0.63 Fe(1)
	329 Fe(2)	0.68 Fe(2)
$\text{Al}_6(\text{Fe},\text{Mn})$	352	0.71

Errors:  $\theta_D = \pm 5$  K,  $f_{291} = \pm 0.02$ .

Table 4.17 Comparison of the calculated  $\theta_D$  and  $f_{291}$  for the various aluminium intermetallic compounds studied

On closer investigation it appears that the factor that determines the  $\theta_D$  value was the Al-Fe shortest bond, which was a common feature of all the known Fe centred Al polyhedra, see Fig 4.30, and appears to follow grossly a linear relationship. The shorter the Al-Fe bond would imply that the Fe atom would be held more tightly within the aluminium cage, and this is reflected in the calculated  $\theta_D$ .

However, it appears that as the shortest Al-Fe bond length increases the Al-Fe bonds of the remaining atoms play a more significant role in determining the  $\theta_D$  value, and this would account for the scattering of the values at lower  $\theta_D$  values.

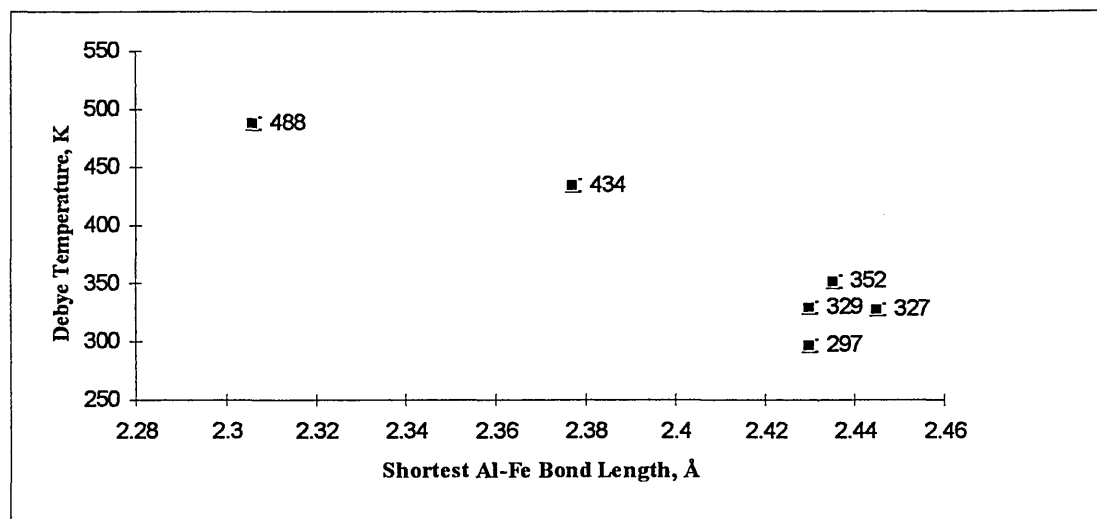


Fig 4.30 The variation of the  $\theta_D$  with shortest Al-Fe bond length for the known Fe centred polyhedra of  $\text{Al}_3\text{Fe}$ ,  $\alpha\text{-AlFeSi}$ ,  $\text{Al}_6(\text{Fe},\text{Mn})$  and  $\text{Al}_6\text{Fe}$ . The value of the Al-Fe shortest bond length quoted for  $\text{Al}_3\text{Fe}$  Fe(1)-Fe(4) is an average.

The quadrupole interaction does not vary with temperature for all the aluminium intermetallic compounds studied. This indicates that the oxidation state of the iron nucleus could either be low spin Fe(II) or high spin Fe(III), but by taking the value of the isomer shift into account a speculative assessment can be made regarding the oxidation state. The oxidation state may be being low spin Fe(II).

Asymmetry was observed within the spectra of  $\text{Al}_x\text{Fe}$ , and to a lesser degree,  $\text{Al}_3\text{Fe}$ . This was attributed to a combination of physical characteristics: preferred growth directions, and the presence of internal mechanical stress fields. However, it was not possible to speculate which was the major contributing factor, but due to the unidirectional solidification mechanism of the Bridgman furnace it would appear that preferred growth direction would be the most probable cause.

Observed line broadening was present within all the Mössbauer spectra of the aluminium intermetallic compounds studied . This would indicate that a distribution of Fe environments exist within the different unit cells. The different aluminium intermetallic compounds have internal defects, which would contribute to the observed line broadening, and thus the distribution of Fe sites.

### 4.3 FUTURE WORK

1. The different Fe atomic environments with  $\text{Al}_3\text{Fe}$  and  $\alpha\text{-AlFeSi}$  have accurately been determined, and thus they have been used in the interpretation of the relevant Mössbauer spectra. However, further studies should be considered necessary to determine the Fe atomic environments within  $\text{Al}_x\text{Fe}$  and  $\text{Al}_m\text{Fe}$ , possibly using detailed XRD methods or EXAFS. This would confirm the structure approximations used in this study, and the Mössbauer interpretation used.
2. It has been shown that a number a very similar Fe environments exist within all the aluminium intermetallic compounds studied, which resulted in broad Lorentzian line-widths being observed. In order to estimate the magnitude of the site distribution, a Poly-Quadrupole/Hyperfine (PQH) fitting routine could be applied to the spectra. This routine assumes a linear relationship between the isomer shift and the quadrupole splitting, by the following relationship [35]:

$$\delta = csq + \varepsilon \cdot \Delta \qquad \text{Equation 4.16}$$

where  $\delta$  = overall isomer shift

$csq$  = centre of the isomer shifts of the range of quadrupoles

$\varepsilon$  = correlation coefficient for the range of quadrupoles

$\Delta$  = the observed quadrupole splitting

Philips, Twomey, and Morup [59] developed the fitting routine, which works on the principal of dividing the spectrum equally into a distribution of quadrupole interactions between a maximum and minimum value defined by the user. The minimisation routine then calculates the relative area each quadrupole interaction contributes to the overall spectrum. The results are then presented as a series of probability values, which is an indication of the Fe site existing in a particular environment.

Although this is an extremely useful tool, the fitting technique has its limits. In practice, a very careful selection of the fitting parameters has to be chosen, including the number of quadrupole interactions within the distribution per observed quadrupole interaction. Failure to do so causes the fitting routine to exceed the error threshold and fail almost immediately.

3. This type of detailed structural study could be extended to other common aluminium intermetallic compounds, including  $\alpha_{\text{H}}\text{-AlFeSi}$ ,  $\alpha_{\text{c}}\text{-Al(Fe,Mn)Si}$  and  $\text{Al}_3(\text{Fe,Mn})$ , that are found within DC cast alloys.
  
4. The Mössbauer experiments could be repeated with the intermetallic compounds being placed within an external magnetic field. This would have the result of determining accurately the oxidation state of the Fe atom. If the Fe atom exists in the high spin Fe(III) state, the full removal of the degeneracy of the excited states would be observed, a six line spectrum would be obtained. However, if the Fe atom exists in the low spin Fe(II) state the spectrum would remain unchanged.

## REFERENCES

- [1] C. J. Simensen, P. Fartum, A. Andersen, *Fresenius Z. Anal. Chem.*, **319** (1984) 286.
- [2] J. M. Williams, J. S. Brooks, *Nucl. Inst. Meths.*, **128** (1975) 363.
- [3] A. Vertes, S. Nagy, M. Zaki-Awad, J. Laker, E. Kovacs-Cselenyi, G. Groma, *Scripta Met.*, **16** (1982) 145.
- [4] S. Nasu, U. Gonser, "Proceedings Mössbauer Conf.", Bratislava, 311.
- [5] S. Nasu, U. Gonser, R. S. Preston, *J. de Phys.*, **C1** (1980) 385.
- [6] C. M. Chittaranjan, V. Kumar, B. Viswanathan, K. P. Gopinathan, *Sol. Stat. Comm.*, **79** (1991) 69.
- [7] P. J. Black, *Acta Cryst.*, **8** (1955) 43.
- [8] P. J. Black, *Acta Cryst.*, **8** (1955) 175.
- [9] C. M. Chittaranjan, V. Kumar, B. Viswanathan, K. P. Gopinathan, *Sol. Stat. Comm.*, **79** (1991) 69.
- [10] S. D. Forder, J. S. Brooks, P. V. Evans, *Acta Met.*, **35** (1996) 1167.
- [11] L. D. Lafleur, C. Goodman, *Phys. Rev.*, **B4(9)** (1971) 2915.
- [12] G. P. Huffamn, R. M. Fisher, *J. App. Phys.*, **38** (1967) 735.
- [13] G. K. Wertheim, J. H. Wernick, *Acta. Met.*, **15** (1967) 297.
- [14] K. R. Van Horn, "Aluminum: Properties, Physical Metallurgy, and Phase diagrams", (Chapman and Hall, London, 1967).
- [15] V. I. Goldanskii, G. M. Goldanskii, S. V. Karyagin, L. A. Korytko, L. M. Krizhanskii, E. F. Makarov, I. P. Suzdalev, V. V. Khrapov, *Proc. Acad. Sci. USSR Phys. Chem. Sect.*, **147** (1963) 766.
- [16] S. V. Karyagin, *Proc. Acad. Sci. USSR Phys. Chem. Soc.*, **148** (1964) 110.
- [17] M. E. Rose, "Multipole Fields", (Chapman and Hall, London, 1955).
- [18] T. C. Gibb, "Principles of Mössbauer Spectroscopy", (Chapman and Hall, London, 1976).
- [19] N. N. Greenwood, T. C. Gibb, "Mössbauer Spectroscopy", (Chapman and Hall, London, 1971).

- [20] P. V. Evans, J. Worth, A. Bosland, S. C. Flood, "Proc. 4<sup>th</sup> Decennial International Conf. on Solidification Processing", Sheffield (1997) 531.
- [21] M. W. Meridith, A. L. Greer, P. V. Evans, "Proc. 4<sup>th</sup> Decennial International Conf. on Solidification Processing", Sheffield (1997) 541.
- [22] C. Janot, P. Delcroix, *Acta Metall.*, **24** (1976) 197.
- [23] S. Nagy, A. Vertes, Z. Homonnay, L. Murgas, *Acta Met.*, **35** (1987) 735.
- [24] S. D. Forder, J. S. Brooks, A. Reeder, P. V. Evans, *Hyp. Int.*, **116** (1998) 209.
- [25] N. N. Greenwood, T. C. Gibb, "Mössbauer Spectroscopy", (Chapman and Hall, London, 1971).
- [26] R. Ingalls, *Phys. Rev. A*, **133**(3) (1964) 787.
- [27] Cotton, Wilkinson, Gaus, "Basic Inorganic Chemistry", (Wiley, UK, 1987)
- [28] G. M. Bancroft, "Mössbauer Spectroscopy", (McGraw Hill, London, 1971).
- [29] J. S. Brooks, G. L. Williams, D. W. Allen, *Phys. Chem. Glasses*, **33**(5) (1992) 171.
- [30] M. M. Stupel, M. Ron, B. Z. Weiss, *J. Appl. Phys.*, **47**(1) (1976) 6.
- [31] R. M. K. Young, T. W. Clyne, *Scripta Met.*, **15** (1981) 1211.
- [32] E. H. Hollingsworth, G. R. Frank, R. E. Willet, *Trans. Met. Soc. AIME*, **224** (1962) 188.
- [33] K. L. Walford, *Acta Cryst.*, **18** (1965) 287.
- [34] Y. Wang, H. Jones, P. V. Evans, "Proc. 4<sup>th</sup> Decennial International Conf. on Solidification Processing", Sheffield (1997) 568.
- [35] J. C. E. Harmer, "Organo-Iron Compounds on Clays and Pillared Clays", PhD Thesis, Sheffield Hallam University, 1998.
- [36] E. Kuzmann, A. Vertes, A. Griger, V. Stefaniay, *Hyp. Int.*, **92** (1994) 943.
- [37] P. J. Schurer, B. Koopmans, F. Van Der Woude, *Sol. Stat. Comm.*, **59** (1986) 619.
- [38] I. Mikki, H. Kousage, K. Nagahama, *J. Inst. L. Met.*, **25** (1975) 1.
- [39] P. Skjerpe, *Acta Cryst.*, **B44** (1988) 480.
- [40] S. Nagy, Z. Homonnay, A. Vertes, L. Murgas, *Acta Met.*, **35** (1987) 741.
- [41] M. Cooper, *Acta Cryst.*, **23** (1967) 1106.
- [42] M. Cooper, K. Robinson, *Acta Cryst.*, **20** (1966) 614.

- [43] R. N. Corby, P. J. Black, *Acta Cryst.*, **B33** (1977) 3468.
- [44] A. D. I. Nicols, *Acta Cryst.*, **6** (1953) 285.
- [45] L. F. Mondolfo, "*Aluminum Alloys: Structure and Properties*", (Butterworths, London, 1976).
- [46] G. V. Raynor, *J. Inst. Met.*, *Met. Abstracts*, **11** (1934-1965) 397.
- [47] R. Petrucci, "*General Chemistry*", (Macmillan, London, 1985).
- [48] M. Warmuzck, A. Gazad, *J. Anal. At. Spectrom.*, **14** (1999) 535.
- [49] H. Cama, J. Worth, P. V. Evans, A. Bosland, J. M. Brown, "*Proc. 4<sup>th</sup> Decennial International Conf. on Solidification Processing*", Sheffield (1997) 555.
- [50] J. Zou, A. E. Carlsson, *Phys. Rev. Letts.*, **70(24)** (1993) 3748.
- [51] S. Nagy, A. Vertes, Z. Homonnay, L. Murgas, *Acta Met.*, **35** (1987) 735.
- [52] R. S. Preston, *Met. Trans. A*, **3**(1972) 1831.
- [53] A. Vertes, S. Nagy, M. Zaki-Awad, J. Laker, E. Kovacs-Cselenyi, G. Groma, *Scripta Met.*, **16** (1982) 145.
- [54] S. Nasu, U. Gonser, R. S. Preston, *J. de Phys.*, **C1** (1980) 385.
- [55] C. M. Chittaranjan, V. Kumar, B. Viswanathan, K. P. Gopinathan, *Sol. Stat. Comm.*, **79** (1991) 69.
- [56] L. Murgas, Z. Homonnay, S. Nagy, A. Vertes, *Met Trans. A*, **19** (1988) 259.
- [57] A. Vertes, Cs. Szeles, S. Nagy, K. Suveg, Z. Homonnay, L. Murgas, *Hyp. Int.*, **66** (1991) 191.
- [58] P. V. Evans, J. Worth, A. Bosland, S. C. Flood, "*Proc. 4<sup>th</sup> Decennial International Conf. on Solidification Processing*", Sheffield (1997) 531.
- [59] Program Source Code

## CHAPTER 5

### DC-CAST INGOT SAMPLES

#### 5.1 ALLOY PREPARATION

The alloy used in this study was prepared from super purity aluminium, containing 0.3% Fe and 0.1% Si, and was cast using a laboratory Direct Chill (DC) arrangement, a general description of the process is shown in Chapter 1.2.1.1. The parent alloy was cast at a casting speed of  $70 \text{ mm min}^{-1}$ . Two thin slices were sectioned from the central region of the alloy, samples *A* and *B*, using a diamond wheel and ground on silicon carbide abrasive paper to obtain a finish of 600 grit. These were then isothermally heat treated at  $500^\circ\text{C}$  for four hours and then water quenched. The two samples were cut in half; one half was trimmed to fit into the cryogenic systems to obtain Mössbauer spectra from the aluminium intermetallic compounds within the matrix. The butanol extraction method [1] was performed on the remaining sections, and Mössbauer absorbers were prepared using the same method as described earlier, see Chapter 4.1.3.

##### 5.1.1 PROCEDURE FOR THE DE-CONVOLUTION OF THE MÖSSBAUER SPECTRA FOR SAMPLE *A* AND *B*

The Mössbauer experiments were performed at 150 K and 250 K, and the resultant spectra were de-convoluted using the following procedure to determine the intermetallic compound combination present within sample *A* and *B*. Initially the spectra were de-convoluted using a combination of fixed hyperfine parameter values for the selected aluminium intermetallic compounds. These parameters were obtained from the appropriate temperatures during the variable temperature Mössbauer studies of the individual extracted compounds, see Chapter 4. The absorption areas were free to vary, and the best initial de-convolution procedure was determined by the lowest  $\chi^2$

value. Allowing each of the hyperfine parameters to vary independently then refined this de-convolution procedure, and the change in the  $\chi^2$  value was recorded.

### 5.1.2 SAMPLE A

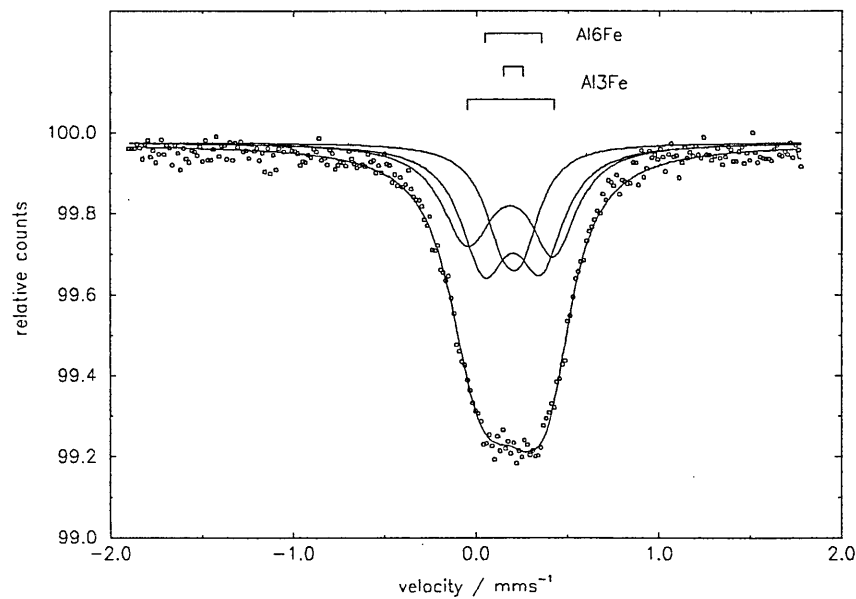


Fig 5.1 The spectrum of alloy sample *A* (insitu) obtained at 150 K

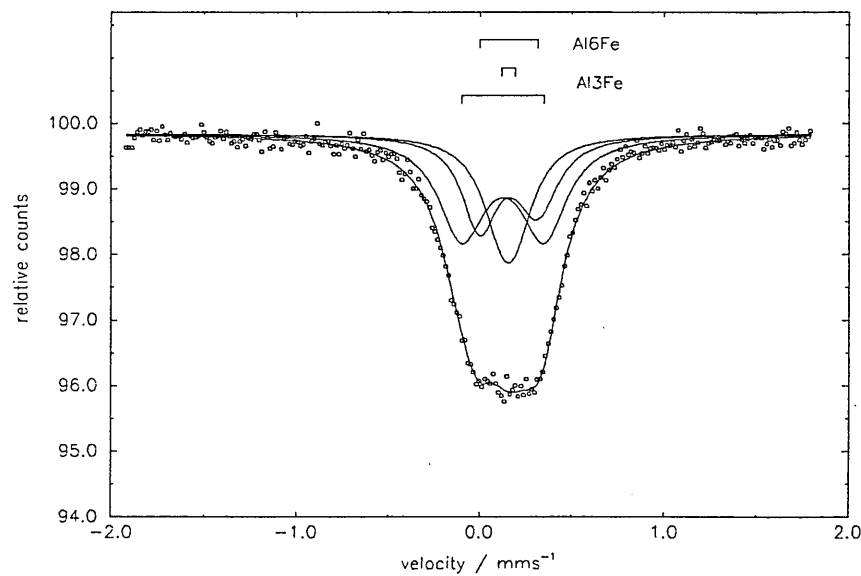


Fig 5.1 The spectrum of alloy sample *A* (insitu) obtained at 250 K

Phase Combination	Starting Parameters (Fixed)			$\chi^2$	Final Parameters (Freed)			$\chi^2$
	$\delta$	$\Delta/2$	$\Gamma/2$		$\delta$	$\Delta/2$	$\Gamma/2$	
Al <sub>3</sub> Fe	0.27	0.21	0.15, 0.15	1.097	0.29	0.22	0.17, 0.15	0.500
	0.28	0.06	0.15, 0.15		0.29	0.05	0.13, 0.12	
Al <sub>6</sub> Fe	0.30	0.14	0.15, 0.15		0.30	0.15	0.15, 0.15	
Al <sub>3</sub> Fe	0.27	0.21	0.15, 0.15	No Fit				
	0.28	0.06	0.15, 0.15					
Al <sub>m</sub> Fe	0.23	0.16	0.22, 0.22					
Al <sub>3</sub> Fe	0.27	0.21	0.15, 0.15	1.723				
	0.28	0.06	0.15, 0.15					
Al <sub>x</sub> Fe	0.24	0.15	0.20, 0.17					
Al <sub>3</sub> Fe $\alpha_c$ -AlFeSi	0.27	0.21	0.15, 0.15	No Fit				
	0.28	0.06	0.15, 0.15					
	0.34	0.11	0.18, 0.18					
	0.26	0.19	0.18, 0.18					
Al <sub>6</sub> Fe	0.30	0.14	0.15, 0.15	1.196				
Al <sub>m</sub> Fe	0.23	0.16	0.22, 0.22					
Al <sub>6</sub> Fe	0.30	0.14	0.15, 0.15	1.130				
	0.24	0.15	0.20, 0.17					
Al <sub>6</sub> Fe $\alpha_c$ -AlFeSi	0.30	0.14	0.15, 0.15	No Fit				
	0.34	0.11	0.18, 0.18					
	0.26	0.19	0.18, 0.18					
Al <sub>m</sub> Fe $\alpha_c$ -AlFeSi	0.23	0.16	0.22, 0.22	No Fit				
	0.34	0.11	0.18, 0.18					
	0.26	0.19	0.18, 0.18					
Al <sub>m</sub> Fe	0.23	0.16	0.22, 0.22	No Fit				
	0.24	0.15	0.20, 0.17					
Al <sub>x</sub> Fe $\alpha_c$ -AlFeSi	0.24	0.15	0.20, 0.17	No Fit				
	0.34	0.11	0.18, 0.18					
	0.26	0.19	0.18, 0.18					

Table 5.1 Parameters used to test different possible phase de-convolution procedures for alloy sample *A* (insitu) at 150 K. All parameters are measured in mm s<sup>-1</sup>, and  $\delta$  is given relative to  $\alpha$ -Fe.

Phase Combination	Starting Parameters (Fixed)			$\chi^2$	Final Parameters (Freed)			$\chi^2$
	$\delta$	$\Delta/2$	$\Gamma/2$		$\delta$	$\Delta/2$	$\Gamma/2$	
Al <sub>3</sub> Fe	0.22	0.20	0.16, 0.14	4.606	0.24	0.22	0.16, 0.16	2.582
	0.22	0.06	0.14, 0.14		0.25	0.04	0.13, 0.13	
Al <sub>6</sub> Fe	0.25	0.15	0.15, 0.14		0.27	0.16	0.12, 0.14	
Al <sub>3</sub> Fe	0.22	0.20	0.16, 0.14	No Fit				
	0.22	0.06	0.14, 0.14					
Al <sub>m</sub> Fe	0.20	0.16	0.22, 0.22					
Al <sub>3</sub> Fe	0.22	0.20	0.16, 0.14	No Fit				
	0.22	0.06	0.14, 0.14					
Al <sub>x</sub> Fe	0.21	0.16	0.22, 0.19					
Al <sub>3</sub> Fe  $\alpha_c$ -AlFeSi	0.22	0.20	0.16, 0.14	No Fit				
	0.22	0.06	0.14, 0.14					
	0.31	0.11	0.19, 0.19					
	0.22	0.19	0.19, 0.19					
Al <sub>6</sub> Fe	0.25	0.15	0.15, 0.14	6.228				
Al <sub>m</sub> Fe	0.20	0.16	0.22, 0.22					
Al <sub>6</sub> Fe	0.25	0.15	0.15, 0.14	5.763				
	0.21	0.16	0.22, 0.19					
Al <sub>6</sub> Fe  $\alpha_c$ -AlFeSi	0.25	0.15	0.15, 0.14	No Fit				
	0.31	0.11	0.19, 0.19					
	0.22	0.19	0.19, 0.19					
Al <sub>m</sub> Fe  $\alpha_c$ -AlFeSi	0.20	0.16	0.22, 0.22	No Fit				
	0.31	0.11	0.19, 0.19					
	0.22	0.19	0.19, 0.19					
Al <sub>m</sub> Fe	0.20	0.16	0.22, 0.22	No Fit				
	0.21	0.15	0.22, 0.19					
Al <sub>x</sub> Fe  $\alpha_c$ -AlFeSi	0.21	0.15	0.22, 0.19	No Fit				
	0.31	0.11	0.19, 0.19					
	0.22	0.19	0.19, 0.19					

Table 5.2 Parameters used to test different possible phase de-convolution procedures for alloy sample A (insitu) at 250 K. All parameters are measured in mm s<sup>-1</sup>, and  $\delta$  is given relative to  $\alpha$ -Fe.

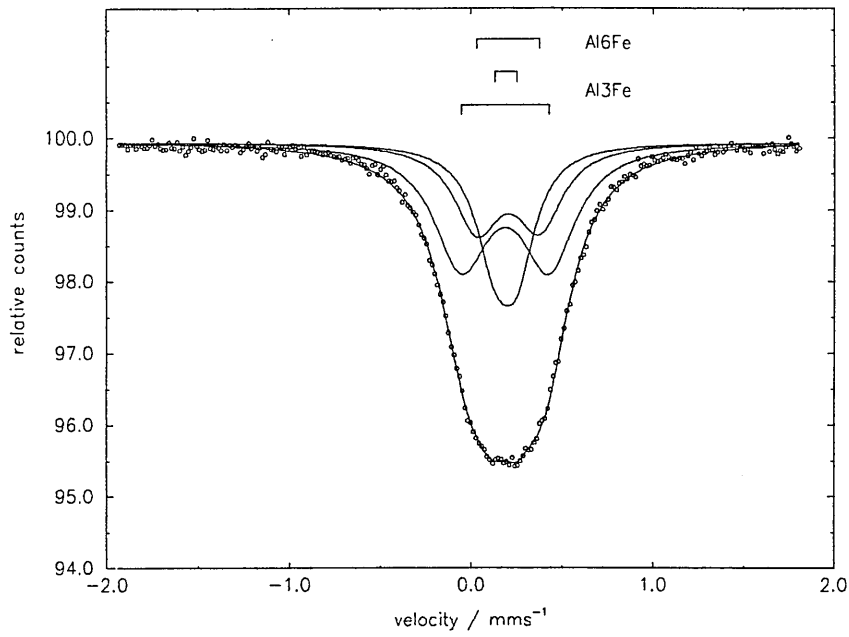


Fig 5.3 The spectrum of alloy sample *A* (extracted) obtained at 150 K

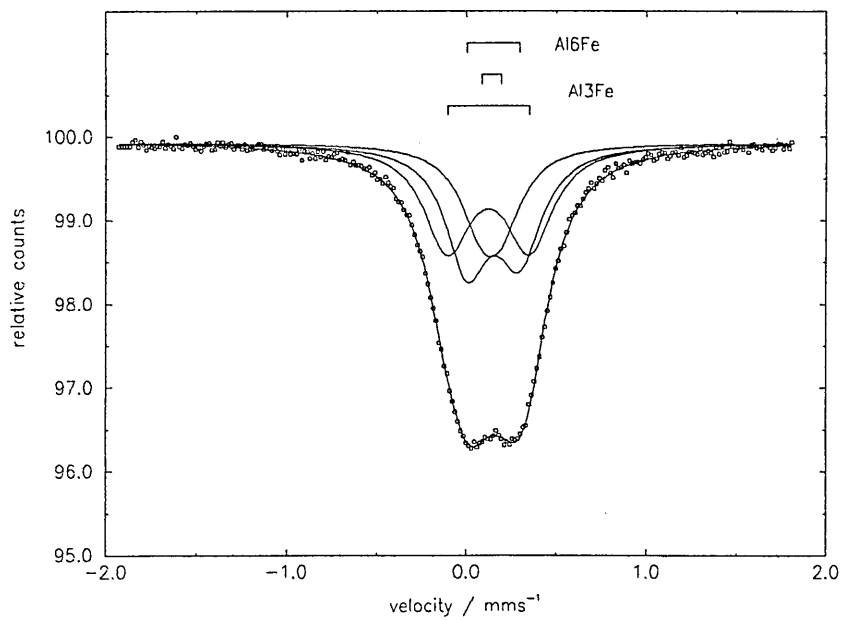


Fig 5.4 The spectrum of alloy sample *A* (extracted) obtained at 250 K

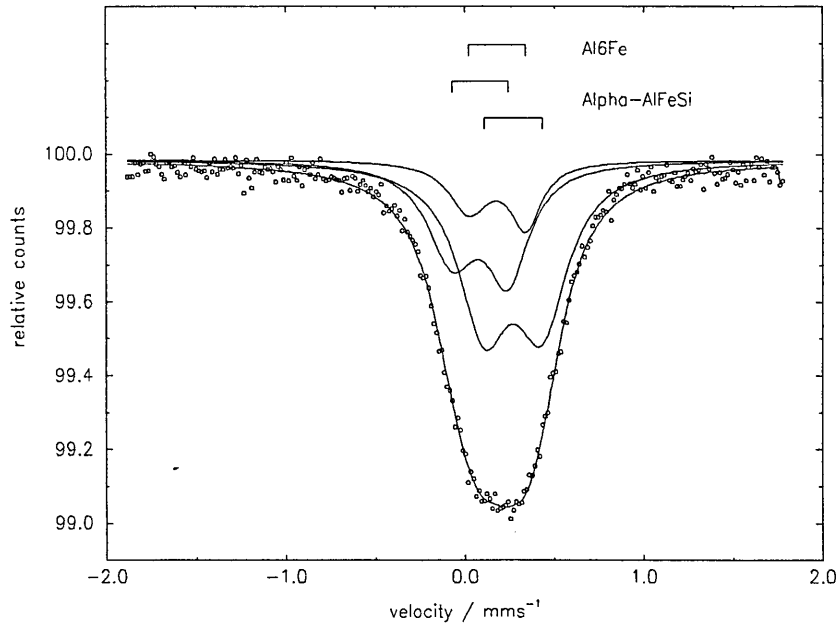
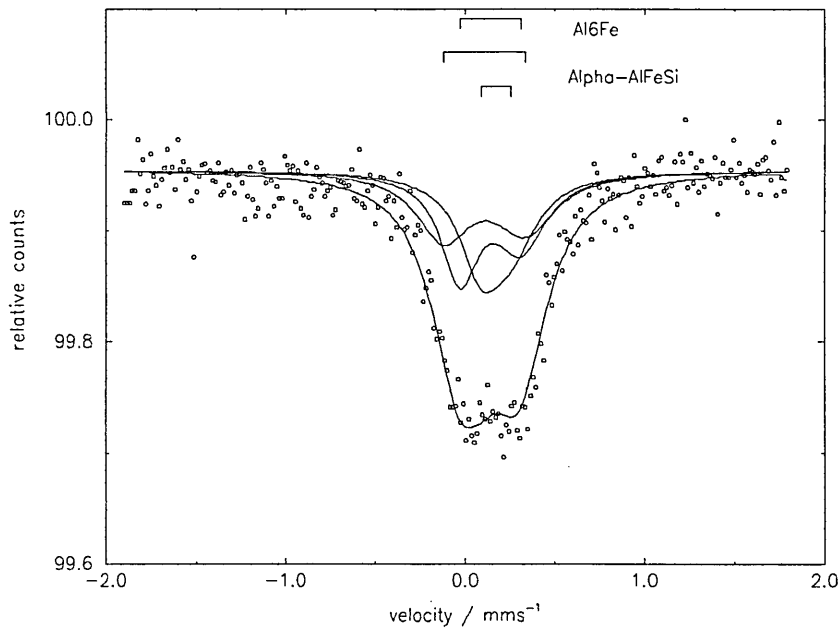
Phase Combination	Starting Parameters (Fixed)			$\chi^2$	Final Parameters (Freed)			$\chi^2$
	$\delta$	$\Delta/2$	$\Gamma/2$		$\delta$	$\Delta/2$	$\Gamma/2$	
Al <sub>3</sub> Fe	0.27	0.21	0.15, 0.15	5.039	0.29	0.24	0.17, 0.17	0.569
	0.28	0.06	0.15, 0.15		0.30	0.06	0.13, 0.12	
Al <sub>6</sub> Fe	0.30	0.14	0.15, 0.15		0.31	0.16	0.15, 0.16	
Al <sub>3</sub> Fe	0.27	0.21	0.15, 0.15	7.666				
	0.28	0.06	0.15, 0.15					
Al <sub>m</sub> Fe	0.23	0.16	0.22, 0.22					
Al <sub>3</sub> Fe	0.27	0.21	0.15, 0.15	7.561				
	0.28	0.06	0.15, 0.15					
Al <sub>x</sub> Fe	0.24	0.15	0.20, 0.17					
Al <sub>3</sub> Fe   α <sub>c</sub> -AlFeSi	0.27	0.21	0.15, 0.15	No Fit				
	0.28	0.06	0.15, 0.15					
	0.34	0.11	0.18, 0.18					
	0.26	0.19	0.18, 0.18					
Al <sub>6</sub> Fe	0.30	0.14	0.15, 0.15	5.865				
Al <sub>m</sub> Fe	0.23	0.16	0.22, 0.22					
Al <sub>6</sub> Fe	0.30	0.14	0.15, 0.15	5.828				
	0.24	0.15	0.20, 0.17					
Al <sub>6</sub> Fe  α <sub>c</sub> -AlFeSi	0.30	0.14	0.15, 0.15	No Fit				
	0.34	0.11	0.18, 0.18					
	0.26	0.19	0.18, 0.18					
Al <sub>m</sub> Fe	0.23	0.16	0.22, 0.22	No Fit				
α <sub>c</sub> -AlFeSi	0.34	0.11	0.18, 0.18					
	0.26	0.19	0.18, 0.18					
Al <sub>m</sub> Fe	0.23	0.16	0.22, 0.22	No Fit				
Al <sub>x</sub> Fe	0.24	0.15	0.20, 0.17					
Al <sub>x</sub> Fe	0.24	0.15	0.20, 0.17	No Fit				
α <sub>c</sub> -AlFeSi	0.34	0.11	0.18, 0.18					
	0.26	0.19	0.18, 0.18					

Table 5.3 Parameters used to test different possible phase de-convolution procedures for alloy sample *A* (extracted) at 150 K. All parameters are measured in mm s<sup>-1</sup>, and  $\delta$  is given relative to  $\alpha$ -Fe.

Phase Combination	Starting Parameters (Fixed)			$\chi^2$	Final Parameters (Freed)			$\chi^2$
	$\delta$	$\Delta/2$	$\Gamma/2$		$\delta$	$\Delta/2$	$\Gamma/2$	
Al <sub>3</sub> Fe	0.22	0.20	0.16, 0.14	1.555	0.23	0.23	0.16, 0.16	0.436
	0.22	0.06	0.14, 0.14		0.25	0.05	0.14, 0.14	
Al <sub>6</sub> Fe	0.25	0.15	0.15, 0.14		0.26	0.15	0.14, 0.15	
Al <sub>3</sub> Fe	0.22	0.20	0.16, 0.14	No Fit				
	0.22	0.06	0.14, 0.14					
Al <sub>m</sub> Fe	0.20	0.16	0.22, 0.22					
Al <sub>3</sub> Fe	0.22	0.20	0.16, 0.14	2.480				
	0.22	0.06	0.14, 0.14					
Al <sub>x</sub> Fe	0.21	0.16	0.22, 0.19					
Al <sub>3</sub> Fe  $\alpha_c$ -AlFeSi	0.22	0.20	0.16, 0.14	No Fit				
	0.22	0.06	0.14, 0.14					
	0.31	0.11	0.19, 0.19					
	0.22	0.19	0.19, 0.19					
Al <sub>6</sub> Fe	0.25	0.15	0.15, 0.14	2.239				
Al <sub>m</sub> Fe	0.20	0.16	0.22, 0.22					
Al <sub>6</sub> Fe	0.25	0.15	0.15, 0.14	2.061				
	0.21	0.16	0.22, 0.19					
Al <sub>6</sub> Fe  $\alpha_c$ -AlFeSi	0.25	0.15	0.15, 0.14	No Fit				
	0.31	0.11	0.19, 0.19					
	0.22	0.19	0.19, 0.19					
Al <sub>m</sub> Fe  $\alpha_c$ -AlFeSi	0.20	0.16	0.22, 0.22	No Fit				
	0.31	0.11	0.19, 0.19					
	0.22	0.19	0.19, 0.19					
Al <sub>m</sub> Fe	0.20	0.16	0.22, 0.22	No Fit				
	0.21	0.15	0.22, 0.19					
Al <sub>x</sub> Fe  $\alpha_c$ -AlFeSi	0.21	0.15	0.22, 0.19	No Fit				
	0.31	0.11	0.19, 0.19					
	0.22	0.19	0.19, 0.19					

Table 5.4 Parameters used to test different possible phase de-convolution procedures for alloy sample A (extracted) at 250 K. All parameters are measured in mm s<sup>-1</sup>, and  $\delta$  is given relative to  $\alpha$ -Fe.

## 5.1.3 SAMPLE B

Fig 5.5 The spectrum of alloy sample *B* (insitu) obtained at 150 KFig 5.6 The spectrum of alloy sample *B* (insitu) obtained at 250 K

Phase Combination	Starting Parameters (Fixed)			$\chi^2$	Final Parameters (Freed)			$\chi^2$
	$\delta$	$\Delta/2$	$\Gamma/2$		$\delta$	$\Delta/2$	$\Gamma/2$	
Al <sub>3</sub> Fe	0.27	0.21	0.15, 0.15	1.857				
	0.28	0.06	0.15, 0.15					
Al <sub>6</sub> Fe	0.30	0.14	0.15, 0.15					
Al <sub>3</sub> Fe	0.27	0.21	0.15, 0.15	No Fit				
	0.28	0.06	0.15, 0.15					
Al <sub>m</sub> Fe	0.23	0.16	0.22, 0.22					
Al <sub>3</sub> Fe	0.27	0.21	0.15, 0.15	2.519				
	0.28	0.06	0.15, 0.15					
Al <sub>x</sub> Fe	0.24	0.15	0.20, 0.17					
Al <sub>3</sub> Fe  $\alpha_c$ -AlFeSi	0.27	0.21	0.15, 0.15	1.883				
	0.28	0.06	0.15, 0.15					
	0.34	0.11	0.18, 0.18					
	0.26	0.19	0.18, 0.18					
Al <sub>6</sub> Fe	0.30	0.14	0.15, 0.15	1.796				
Al <sub>m</sub> Fe	0.23	0.16	0.22, 0.22					
Al <sub>6</sub> Fe	0.30	0.14	0.15, 0.15	1.892				
	0.24	0.15	0.20, 0.17					
Al <sub>6</sub> Fe  $\alpha_c$ -AlFeSi	0.30	0.14	0.15, 0.15	0.904	0.29	0.16	0.14, 0.13	0.552
	0.34	0.11	0.18, 0.18		0.36	0.14	0.17, 0.17	
	0.26	0.19	0.18, 0.18		0.24	0.17	0.17, 0.14	
Al <sub>m</sub> Fe	0.23	0.16	0.22, 0.22	No Fit				
$\alpha_c$ -AlFeSi	0.34	0.11	0.18, 0.18					
	0.26	0.19	0.18, 0.18					
Al <sub>m</sub> Fe	0.23	0.16	0.22, 0.22	No Fit				
Al <sub>x</sub> Fe	0.24	0.15	0.20, 0.17					
Al <sub>x</sub> Fe	0.24	0.15	0.20, 0.17	No Fit				
$\alpha_c$ -AlFeSi	0.34	0.11	0.18, 0.18					
	0.26	0.19	0.18, 0.18					

Table 5.5 Parameters used to test different possible phase de-convolution procedures for alloy sample *B* (insitu) at 150 K. All parameters are measured in mm s<sup>-1</sup>, and  $\delta$  is given relative to  $\alpha$ -Fe.

Phase Combination	Starting Parameters (Fixed)			$\chi^2$	Final Parameters (Freed)			$\chi^2$
	$\delta$	$\Delta/2$	$\Gamma/2$		$\delta$	$\Delta/2$	$\Gamma/2$	
Al <sub>3</sub> Fe	0.22	0.20	0.16, 0.14	0.441				
	0.22	0.06	0.14, 0.14					
Al <sub>6</sub> Fe	0.25	0.15	0.15, 0.14					
Al <sub>3</sub> Fe	0.22	0.20	0.16, 0.14	No Fit				
	0.22	0.06	0.14, 0.14					
Al <sub>m</sub> Fe	0.20	0.16	0.22, 0.22					
Al <sub>3</sub> Fe	0.22	0.20	0.16, 0.14	No Fit				
	0.22	0.06	0.14, 0.14					
Al <sub>x</sub> Fe	0.21	0.16	0.22, 0.19					
Al <sub>3</sub> Fe  $\alpha_c$ -AlFeSi	0.22	0.20	0.16, 0.14	0.434				
	0.22	0.06	0.14, 0.14					
	0.31	0.11	0.19, 0.19					
	0.22	0.19	0.19, 0.19					
Al <sub>6</sub> Fe	0.25	0.15	0.15, 0.14	0.425				
Al <sub>m</sub> Fe	0.20	0.16	0.22, 0.22					
Al <sub>6</sub> Fe	0.25	0.15	0.15, 0.14	0.424				
	0.21	0.16	0.22, 0.19					
Al <sub>6</sub> Fe $\alpha_c$ -AlFeSi	0.25	0.15	0.15, 0.14	0.412	0.25	0.17	0.12, 0.17	0.426
	0.31	0.11	0.19, 0.19		0.28	0.10	0.14, 0.18	
	0.22	0.19	0.19, 0.19		0.22	0.22	0.18, 0.18	
Al <sub>m</sub> Fe	0.20	0.16	0.22, 0.22	No Fit				
$\alpha_c$ -AlFeSi	0.31	0.11	0.19, 0.19					
	0.22	0.19	0.19, 0.19					
Al <sub>m</sub> Fe	0.20	0.16	0.22, 0.22	No Fit				
Al <sub>x</sub> Fe	0.21	0.15	0.22, 0.19					
Al <sub>x</sub> Fe $\alpha_c$ -AlFeSi	0.21	0.15	0.22, 0.19	No Fit				
	0.31	0.11	0.19, 0.19					
	0.22	0.19	0.19, 0.19					

Table 5.6 Parameters used to test different possible phase de-convolution procedures for alloy sample B (insitu) at 250 K. All parameters are measured in mm s<sup>-1</sup>, and  $\delta$  is given relative to  $\alpha$ -Fe.

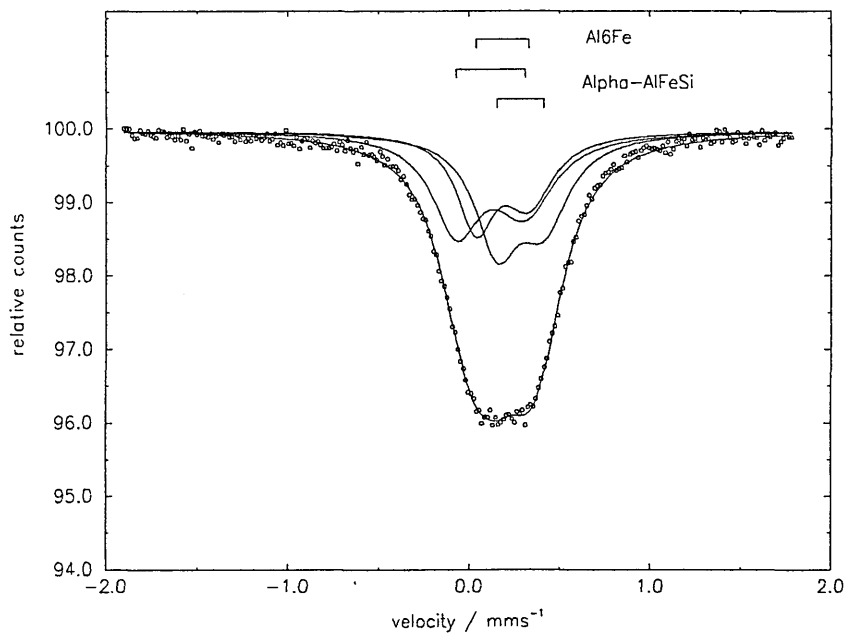


Fig 5.7 The spectrum of alloy sample *B* (extracted) obtained at 150 K

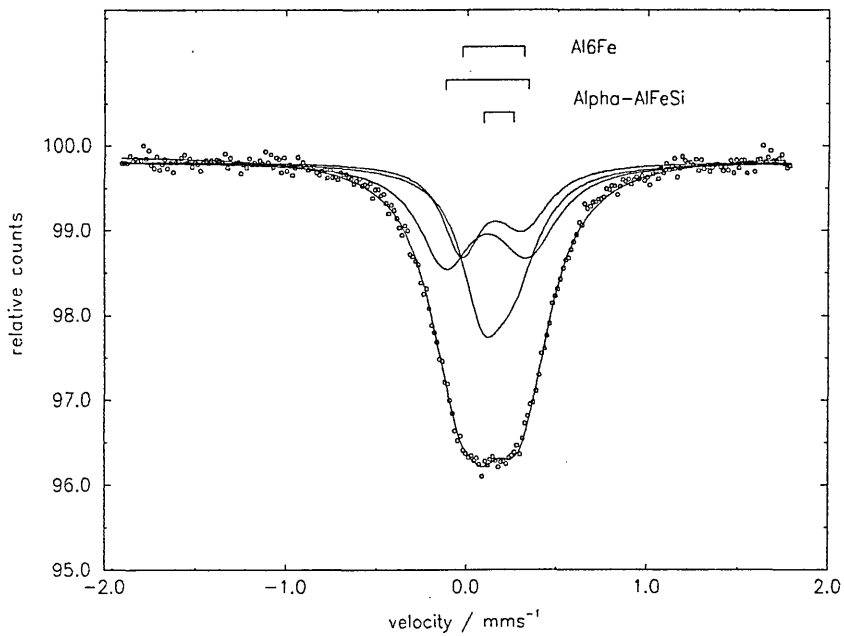


Fig 5.8 The spectrum of alloy sample *B* (extracted) obtained at 250 K

Phase Combination	Starting Parameters (Fixed)			$\chi^2$	Final Parameters (Freed)			$\chi^2$
	$\delta$	$\Delta/2$	$\Gamma/2$		$\delta$	$\Delta/2$	$\Gamma/2$	
Al <sub>3</sub> Fe	0.27	0.21	0.15, 0.15	2.878				
	0.28	0.06	0.15, 0.15					
Al <sub>6</sub> Fe	0.30	0.14	0.15, 0.15					
Al <sub>3</sub> Fe	0.27	0.21	0.15, 0.15	4.386				
	0.28	0.06	0.15, 0.15					
Al <sub>m</sub> Fe	0.23	0.16	0.22, 0.22					
Al <sub>3</sub> Fe	0.27	0.21	0.15, 0.15	4.338				
	0.28	0.06	0.15, 0.15					
Al <sub>x</sub> Fe	0.24	0.15	0.20, 0.17					
Al <sub>3</sub> Fe  $\alpha_c$ -AlFeSi	0.27	0.21	0.15, 0.15	1.739				
	0.28	0.06	0.15, 0.15					
	0.34	0.11	0.18, 0.18					
	0.26	0.19	0.18, 0.18					
Al <sub>6</sub> Fe	0.30	0.14	0.15, 0.15	2.635				
Al <sub>m</sub> Fe	0.23	0.16	0.22, 0.22					
Al <sub>6</sub> Fe	0.30	0.14	0.15, 0.15	3.007				
	0.24	0.15	0.20, 0.17					
Al <sub>6</sub> Fe $\alpha_c$ -AlFeSi	0.30	0.14	0.15, 0.15	1.563	0.29	0.15	0.13, 0.16	0.645
	0.34	0.11	0.18, 0.18		0.37	0.13	0.14, 0.18	
	0.26	0.19	0.18, 0.18		0.24	0.19	0.14, 0.16	
Al <sub>m</sub> Fe	0.23	0.16	0.22, 0.22	1.668				
$\alpha_c$ -AlFeSi	0.34	0.11	0.18, 0.18					
	0.26	0.19	0.18, 0.18					
Al <sub>m</sub> Fe	0.23	0.16	0.22, 0.22	No Fit				
Al <sub>x</sub> Fe	0.24	0.15	0.20, 0.17					
Al <sub>x</sub> Fe $\alpha_c$ -AlFeSi	0.24	0.15	0.20, 0.17	1.677				
	0.34	0.11	0.18, 0.18					
	0.26	0.19	0.18, 0.18					

Table 5.7 Parameters used to test different possible phase de-convolution procedures for alloy sample *B* (extracted) at 150 K. All parameters are measured in mm s<sup>-1</sup>, and  $\delta$  is given relative to  $\alpha$ -Fe.

Phase Combination	Starting Parameters (Fixed)			$\chi^2$	Final Parameters (Freed)			$\chi^2$
	$\delta$	$\Delta/2$	$\Gamma/2$		$\delta$	$\Delta/2$	$\Gamma/2$	
Al <sub>3</sub> Fe	0.22	0.20	0.16, 0.14	1.542				
	0.22	0.06	0.14, 0.14					
Al <sub>6</sub> Fe	0.25	0.15	0.15, 0.14					
Al <sub>3</sub> Fe	0.22	0.20	0.16, 0.14	1.709				
	0.22	0.06	0.14, 0.14					
Al <sub>m</sub> Fe	0.20	0.16	0.22, 0.22					
Al <sub>3</sub> Fe	0.22	0.20	0.16, 0.14	1.506				
	0.22	0.06	0.14, 0.14					
Al <sub>x</sub> Fe	0.21	0.16	0.22, 0.19					
Al <sub>3</sub> Fe  $\alpha_c$ -AlFeSi	0.22	0.20	0.16, 0.14	1.123				
	0.22	0.06	0.14, 0.14					
	0.31	0.11	0.19, 0.19					
	0.22	0.19	0.19, 0.19					
Al <sub>6</sub> Fe	0.25	0.15	0.15, 0.14	1.821				
Al <sub>m</sub> Fe	0.20	0.16	0.22, 0.22					
Al <sub>6</sub> Fe	0.25	0.15	0.15, 0.14	1.523				
	0.21	0.16	0.22, 0.19					
Al <sub>6</sub> Fe $\alpha_c$ -AlFeSi	0.25	0.15	0.15, 0.14	1.030	0.26	0.17	0.13, 0.17	0.588
	0.31	0.11	0.19, 0.19		0.29	0.10	0.14, 0.18	
	0.22	0.19	0.19, 0.19		0.22	0.22	0.18, 0.20	
Al <sub>m</sub> Fe	0.20	0.16	0.22, 0.22	1.083				
$\alpha_c$ -AlFeSi	0.31	0.11	0.19, 0.19					
	0.22	0.19	0.19, 0.19					
Al <sub>m</sub> Fe	0.20	0.16	0.22, 0.22	No Fit				
Al <sub>x</sub> Fe	0.21	0.15	0.22, 0.19					
Al <sub>x</sub> Fe $\alpha_c$ -AlFeSi	0.21	0.15	0.22, 0.19	1.074				
	0.31	0.11	0.19, 0.19					
	0.22	0.19	0.19, 0.19					

Table 5.8 Parameters used to test different possible phase de-convolution procedures for alloy sample *B* (extracted) at 250 K. All parameters are measured in mm s<sup>-1</sup>, and  $\delta$  is given relative to  $\alpha$ -Fe.

#### 5.1.4 RELATIVE PROPORTION OF THE INTERMETALLIC COMPOUNDS WITHIN SAMPLE *A* AND *B*

The relative proportions of the aluminium intermetallic compounds that were present within alloy samples *A* and *B* were calculated from the relative spectral absorption area, and the relative molecular mass of the intermetallic compound under study. The process will be described with reference to a general intermetallic phase combination  $\text{Al}_6\text{Fe}$  and  $\text{Al}_3\text{Fe}$ , which was found present within alloy sample *A*.

The relative mass density of the intermetallic compound  $\text{Al}_6\text{Fe}$  present within alloy sample *A* was determined by the following expression:

$$\rho_{\text{Al}_6\text{Fe}}^{\text{Rel}} = \frac{(U_{\text{Al}_6\text{Fe}} \cdot \text{RMM}_{\text{Al}_6\text{Fe}})}{(U_{\text{Al}_6\text{Fe}} \cdot \text{RMM}_{\text{Al}_6\text{Fe}}) + (U_{\text{Al}_3\text{Fe}} \cdot \text{RMM}_{\text{Al}_3\text{Fe}})} \quad \text{Equation 5.1}$$

where  $U_{\text{Al}_6\text{Fe}}$  = Relative mass present of  $\text{Al}_6\text{Fe}$  expressed in percent terms

$\text{RMM}_{\text{Al}_6\text{Fe}}$  = Relative molecular mass of the intermetallic compound  $\text{Al}_6\text{Fe}$

$U_{\text{Al}_3\text{Fe}}$  = Relative mass present of  $\text{Al}_3\text{Fe}$  expressed in percent terms

$\text{RMM}_{\text{Al}_3\text{Fe}}$  = Relative molecular mass of the intermetallic compound  $\text{Al}_3\text{Fe}$

A similar expression was derived for calculating the relative mass density of the intermetallic compound  $\text{Al}_3\text{Fe}$  present within alloy sample *A*, Equation 5.2.

$$\rho_{\text{Al}_3\text{Fe}}^{\text{Rel}} = \frac{(U_{\text{Al}_3\text{Fe}} \cdot \text{RMM}_{\text{Al}_3\text{Fe}})}{(U_{\text{Al}_6\text{Fe}} \cdot \text{RMM}_{\text{Al}_6\text{Fe}}) + (U_{\text{Al}_3\text{Fe}} \cdot \text{RMM}_{\text{Al}_3\text{Fe}})} \quad \text{Equation 5.2}$$

However, it has been shown that the absorption spectral area is related to the recoil free fraction,  $f$ , by the numerical solution of the Debye equation, see Chapter 2.5.3.1. That implies that the calculated relative mass density for each intermetallic compound

must be corrected for by  $f$ , at the appropriate temperature, for the relative proportions,  $X$ , to be determined.

The relative proportions of the intermetallic compounds present within alloy sample  $A$  were calculated by Equation 5.3 and 5.4.

$$X_{Al_6Fe} = \frac{\rho_{Al_6Fe}^{Rel}}{f_{Al_6Fe}^x} \quad \text{Equation 5.3}$$

where  $f_{Al_6Fe}^x$  = The  $f$ -factor for  $Al_6Fe$ ,  $x$  equals the  $f$ -factor calculated for the temperatures of 150 K or 250 K from the LNAT program

$$X_{Al_3Fe} = \frac{\rho_{Al_3Fe}^{Rel}}{f_{Al_3Fe}^x} \quad \text{Equation 5.4}$$

where  $f_{Al_3Fe}^x$  = The  $f$ -factor for  $Al_3Fe$ ,  $x$  equals the  $f$ -factor calculated for the temperatures of 150 K or 250 K from the LNAT program

The calculated relative intermetallic compound ratios for each of the alloy samples  $A$  and  $B$  are shown in Table 5.9.

The alloy sample  $A$  was shown to contain the aluminium intermetallic compound combination  $Al_3Fe + Al_6Fe$ , which was present in a relative proportion of  $50:50 \pm 5\%$ . Sample  $B$  was shown to have to aluminium intermetallic compound combination  $Al_6Fe + \alpha_c\text{-AlFeSi}$  in a relative proportion of  $30:70 \pm 5\%$ . The calculated results for the aluminium intermetallic compound combination for the insitu sample of alloy  $B$  have been ignored, due to very poor signal to noise ratio of the spectra. This would have produced inaccurate spectral absorption areas in the de-convolution procedure. This could be attributed to the low Fe content within the alloy sample, and the low activity of the  $^{57}\text{Co}$  source at the time of the Mössbauer experiments being performed.

Alloy Sample	Temp.	Compound Combination	Compound Environment	Relative Proportion
<i>A</i>	150 K	Al <sub>3</sub> Fe + Al <sub>6</sub> Fe	Insitu	53.00%, 47.00%
	250 K	Al <sub>3</sub> Fe + Al <sub>6</sub> Fe	Insitu	49.19%, 50.81%
	150 K	Al <sub>3</sub> Fe + Al <sub>6</sub> Fe	Extracted	47.98%, 52.02%
	250 K	Al <sub>3</sub> Fe + Al <sub>6</sub> Fe	Extracted	53.32%, 46.68%
<i>B</i>	150 K	Al <sub>6</sub> Fe + $\alpha_c$ -AlFeSi	Insitu	16.71%, 83.29%
	250 K	Al <sub>6</sub> Fe + $\alpha_c$ -AlFeSi	Insitu	40.40%, 59.60%
	150 K	Al <sub>6</sub> Fe + $\alpha_c$ -AlFeSi	Extracted	31.54%, 68.46%
	250 K	Al <sub>6</sub> Fe + $\alpha_c$ -AlFeSi	Extracted	27.27%, 72.30%

Table 5.9 Relative phase proportions within the alloy samples *A* and *B*.

It was impossible to speculate as to what local solidification rates were experienced by the alloy samples *A* and *B*, and consequently the positions of the alloy samples from the parent alloy ingot surface during the casting process. This was due to the alloy samples being isothermally heat treated at 500°C for four hours and then water quenched, which would have the effect of increasing the amount of the more thermodynamically stable compounds or promoting a phase change within the sample. This has the affect of distorting the actual cast intermetallic compound combinations, and relative proportions, within the samples.

However, the purpose of this program of Mössbauer experiments was not to predict the positions of alloy samples taken from the parent ingot, but as a tool to identify and quantify the aluminium intermetallic compound combination. This has been achieved, as all the results were verified by XRD measurements performed at Alcan International upon the extracted forms of alloy samples *A* and *B*.

This method must be used speculatively as some aluminium intermetallic compounds show very similar hyperfine parameters, mainly  $Al_mFe$  and  $Al_xFe$ . It would, therefore, inherently be very difficult to accurately de-convolute the Mössbauer spectrum accordingly.

## 5.2 INITIAL SURFACE STUDIES APPLIED TO ALLOY SAMPLE *B* (CEMS, SEM, EDS)

Another alloy sample of *B* was prepared, from the same parent DC-cast ingot, with a surface area of approximately 9 cm<sup>2</sup> and 4 mm in thickness. Initially, the surface was mechanically polished, using conventional techniques, and the CEMS, SEM and EDS surface studies were then performed. The same surface was electro-etched in KI solution for 10 minutes, and a further 5 minutes, with an applied voltage of 30 V. Then the same surface studies were repeated. This particular etching process was chosen as it removes the aluminium matrix, and thus leaves the aluminium intermetallic compounds standing proud of the surface.

### 5.2.1 THE APPLICATION OF CEMS TO THE Al-Fe SYSTEM

Historically, the application of the CEMS (Conversion Electron Mössbauer spectroscopy) technique has mainly been used to study two important areas of scientific interests, Fe/Al multi-layers and ion implantation studies, and these areas will be discussed briefly. However, when reviewing the literature there appears to be no reference made to any CEMS study on DC-cast alloys. This was not surprising when considering the inherently low concentration and the distribution of Fe within the ingot, as it would make the experimental data collection difficult.

#### 5.2.1.1 Fe/Al MULTI-LAYERS

There has been a great deal of interest in artificially layered structures for their use as new magnetic materials. The fundamental magnetic, electronic, and optical properties of these structures are quite different from their bulk properties, and it has been shown that these properties are greatly influenced by the interfaces of the multi-layers [2, 3, 4]. Chowdhury *et al* [5] attempted to define the interface structure of Fe/Al multi-layers, as they have the potential to be used as a thin-film magnetic head for recording media. These structures have been shown to possess excellent soft magnetic properties

[6, 7, 8], which are a prerequisite for such a use. Chowdhury *et al* [5] prepared four multi-layer samples (19 Å Fe/5 Å Al, 11 Å Fe/11 Å Al, 21 Å Fe/11 Å Al, 60 Å Fe/11 Å Al), and de-convoluted the resultant Mössbauer spectra with seven magnetic hyperfine interactions. The Mössbauer parameters and calculated hyperfine fields were consistent with the following structures being present within the interface: *bcc* Fe, Fe<sub>3</sub>Al, random alloy Fe<sub>55</sub>Al<sub>45</sub> with *bcc* symmetry, Fe-Al alloy having a Fe site with four Al as nearest neighbours, Fe-Al alloy with six Al as nearest neighbours, aluminium rich Fe-Al alloy having an Fe site with eight Al nearest neighbours in an *fcc* symmetry, and an aluminium rich Fe-Al alloy having an Fe site with eleven Al nearest neighbours in an *fcc* symmetry. The only difference in the resultant spectra of the different multi-layer structures were the relative intensity of each of the components. However, there was no evidence that any of the known aluminium rich intermetallic compounds played any role in the overall structure of the multi-layers studied.

Gratton *et al* [9] applied the technique of ion-beam mixing to Al-Fe multi-layers, which induces a high degree of inhomogeneity, to study the structural evolution of the amorphous Al-Fe intermetallic phase by annealing. The multi-layers were prepared by sequential deposition of Al ( $\approx 50$  nm), <sup>57</sup>Fe ( $\approx 10$  nm), Al ( $\approx 40$  nm) layers upon Si/SiO<sub>2</sub> substrates. The CEM spectrum of the as-deposited sample was de-convoluted as a magnetic hyperfine interaction, which was typical of metallic  $\alpha$ -Fe. However, when the Al-Fe multi-layers were mixed with 100 keV krypton ions the resultant CEM spectrum was found to be attributed to the amorphous Al<sub>86</sub>Fe<sub>14</sub> intermetallic compound. The annealing process followed the structural transformation of the amorphous Al<sub>86</sub>Fe<sub>14</sub>  $\rightarrow$  icosahedrally co-ordinated quasi-crystalline Al<sub>86</sub>Fe<sub>14</sub>  $\rightarrow$  crystalline metastable Al<sub>6</sub>Fe compound.

### 5.2.1.2 ION IMPLANTATION STUDIES

A comprehensive investigation was performed by Reuther [10] on the implantation of aluminium ions onto iron substrates. The aluminium ions were implanted with different doses ( $5 \times 10^{16}$  -  $5 \times 10^{17}$  cm<sup>-2</sup>) at energies of 50, 100, and 200 keV, and the resulting

interactions were studied by CEMS. At the impact energies 50 keV and 200 keV the resultant CEM spectra, regardless of the ion dose, could only be de-convoluted with two magnetic hyperfine interactions, which were attributed to *bcc* Fe and the non-stoichiometric compound Fe<sub>3</sub>Al. However, at the impact energy of 100 keV a singlet appeared in the de-convoluted spectra at the higher aluminium dose rate, which was attributed to the formation of the FeAl compound. This was in conjunction with the two common magnetic hyperfine interactions, shown earlier. These features are similar to that of some of the features within Fe/Al multi-layer systems [5]. The effect of annealing the alloy samples had the effect of reducing the hyperfine field distributions, and the presence of the singlet was removed for the sample that had undergone the aluminium ion impact of 100 keV.

The implantation of aluminium ions into iron was shown to lead to the formation of a highly disordered region, which contains mainly two magnetic components. However, a non-magnetic component was created at higher aluminium ion dosage. Again, there was no evidence of any aluminium intermetallic compounds being formed in this study, or similar investigations [11, 12].

Hu *et al* [13] induced the formation of Al-Fe intermetallic compounds by the <sup>57</sup>Fe implantation into an aluminium foil, which was the opposite approach to that used by Reuther [10]. The <sup>57</sup>Fe were implanted at dose rates of  $1 \times 10^{16}$  -  $5 \times 10^{16}$  cm<sup>-2</sup>, and the intermetallic compounds that were formed were Al<sub>6</sub>Fe and Al<sub>5</sub>Fe<sub>2</sub> [14, 15, 16]. After the implantation of Al ions, at a dose rate of  $1 \times 10^{16}$  -  $5 \times 10^{16}$  cm<sup>-2</sup>, the formation of a third quadrupole interaction was observed when the resultant Mössbauer spectrum was de-convoluted, which was enhanced as the dose rate was increased. This third component was attributed to the formation of large iron clusters, which Hu *et al* [13] speculated was the first stage in the formation of *bcc* Fe. This was confirmed when the sample that was subjected to the highest <sup>57</sup>Fe dose rate was annealed. As the annealing temperature was increased the appearance of the quadrupole interaction attributed to the presence of large iron clusters was observed, and as the temperature was increased

further this component underwent a phase transformation and a magnetic hyperfine interaction was observed with a hyperfine field consistent with *bcc* Fe.

It has been shown that the CEMS study of aluminium intermetallic compounds have only been performed by the  $^{57}\text{Fe}$  ion implantation onto an aluminium foil [13, 17, 18, 19], and there are no reported CEMS studies on commercial DC-cast aluminium ingots. This could be due to the very low iron concentration present within the ingots, which would make the accumulation of a representative CEMS spectrum difficult without  $^{57}\text{Fe}$  enrichment.

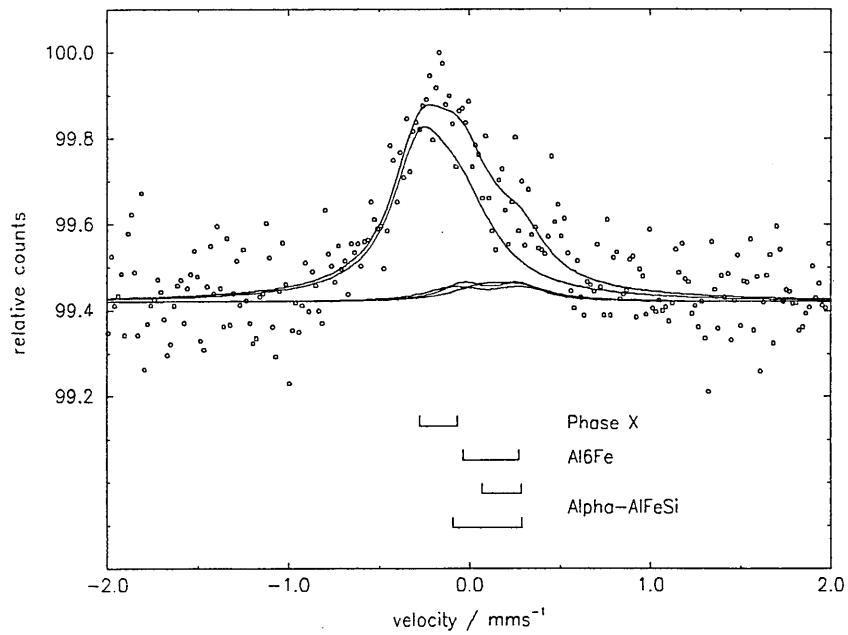
5.2.2 CEMS STUDY OF ALLOY SAMPLE *B*

Fig 5.9 CEMS spectrum of the unetched surface of alloy *B* at room temperature

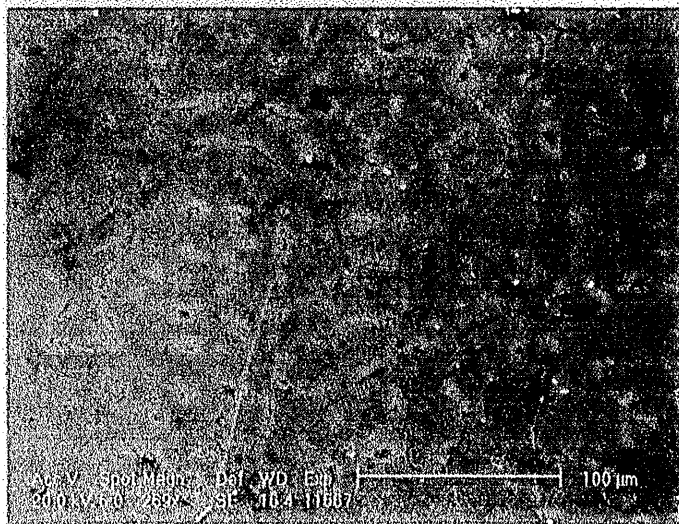


Fig 5.10 SEM image of the unetched surface of alloy *B*

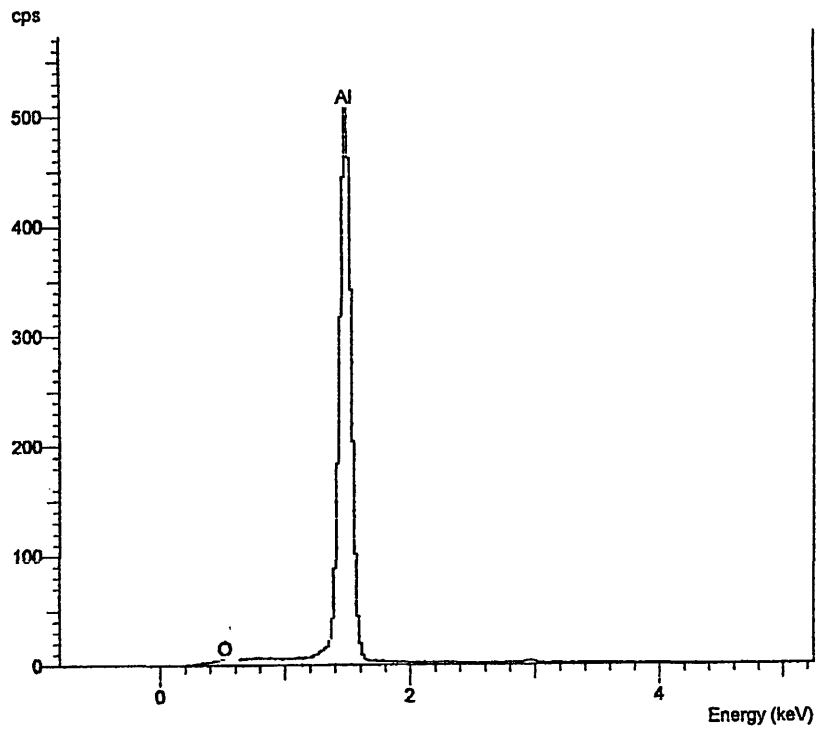


Fig 5.11 Representative EDS spectrum taken from the centre of a grain

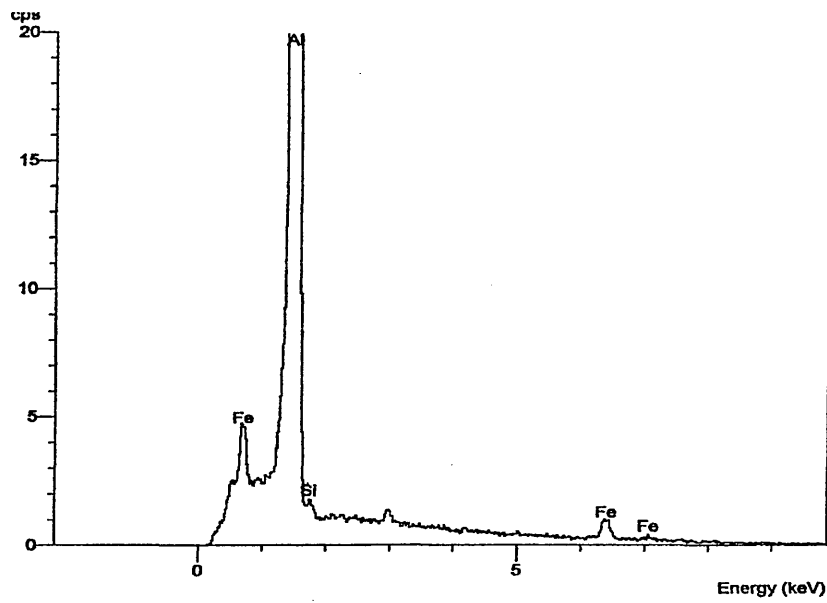


Fig 5.12 Representative EDS spectrum taken from the grain boundary

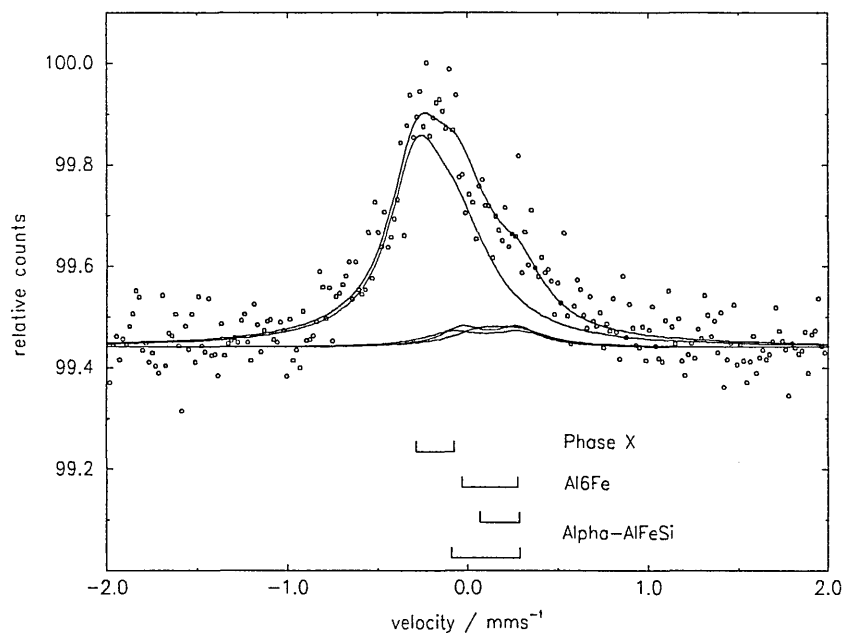


Fig 5.13 CEMS spectrum of the 10 minute KI-electro etch surface of alloy *B* at room temperature

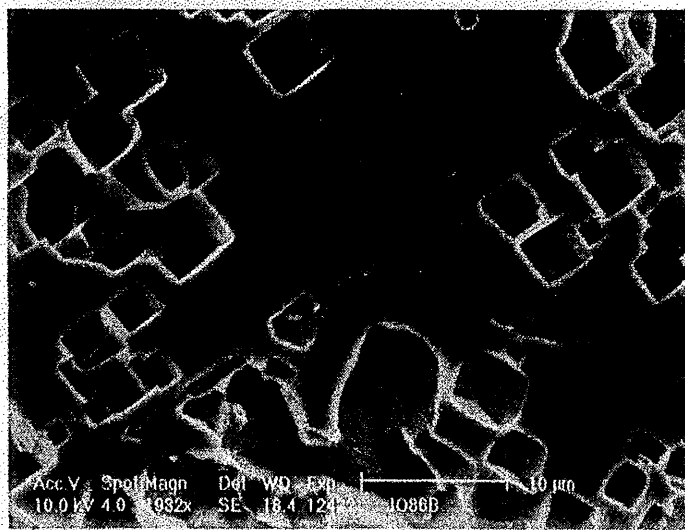


Fig 5.14 SEM image of the 10 minute KI-electro etch surface of alloy *B*

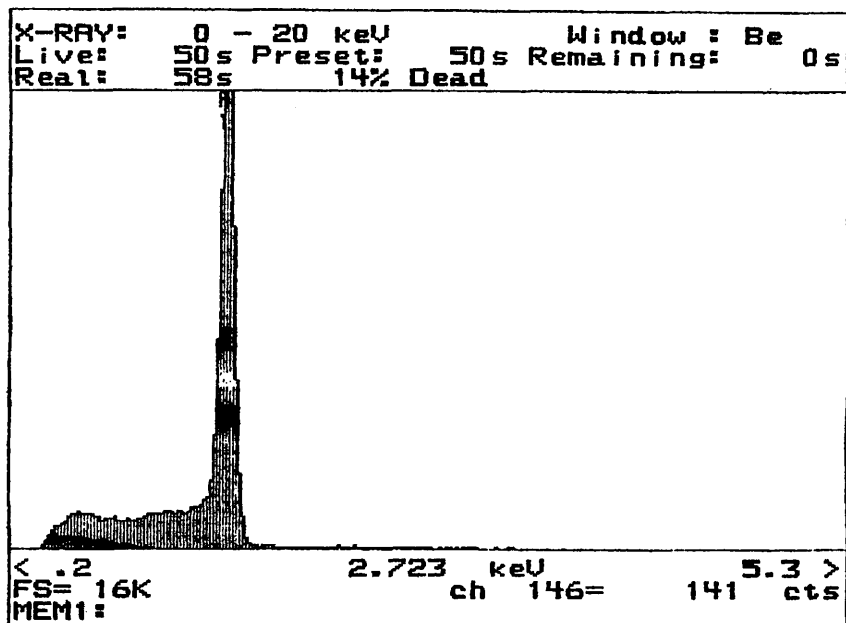


Fig 5.15 Representative EDS spectrum taken from the unetched region of the sample *B* after being exposed to a 10 minute KI electro-etch

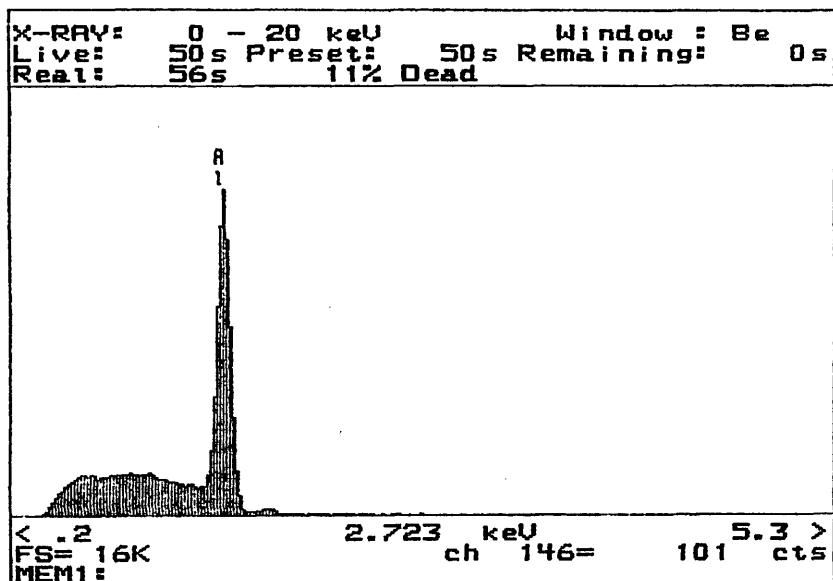


Fig 5.16 Representative EDS spectrum taken from the centre of an etch pit from sample *B* after being exposed to a 10 minute KI electro-etch

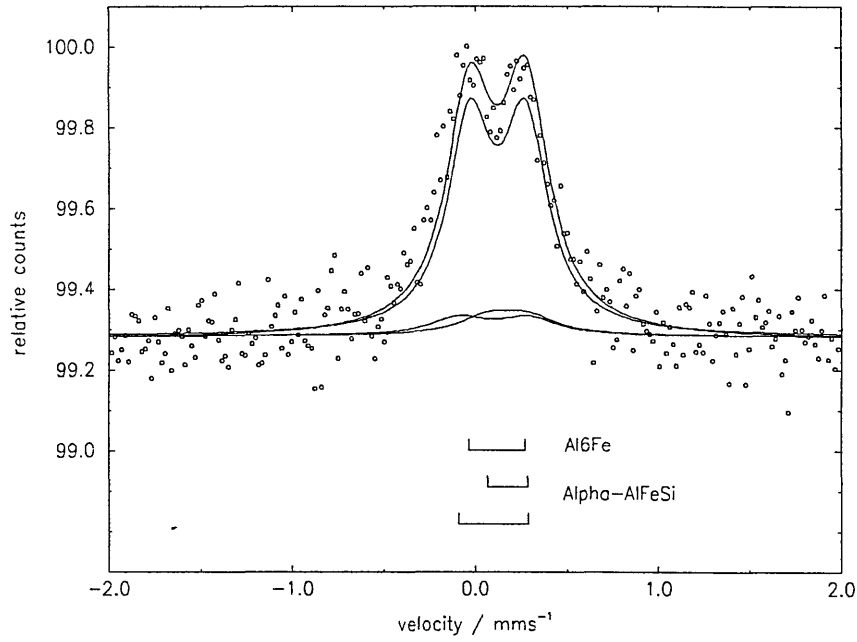


Fig 5.17 CEMS spectrum of the 15 minute KI-electro etch surface of alloy *B* at room temperature

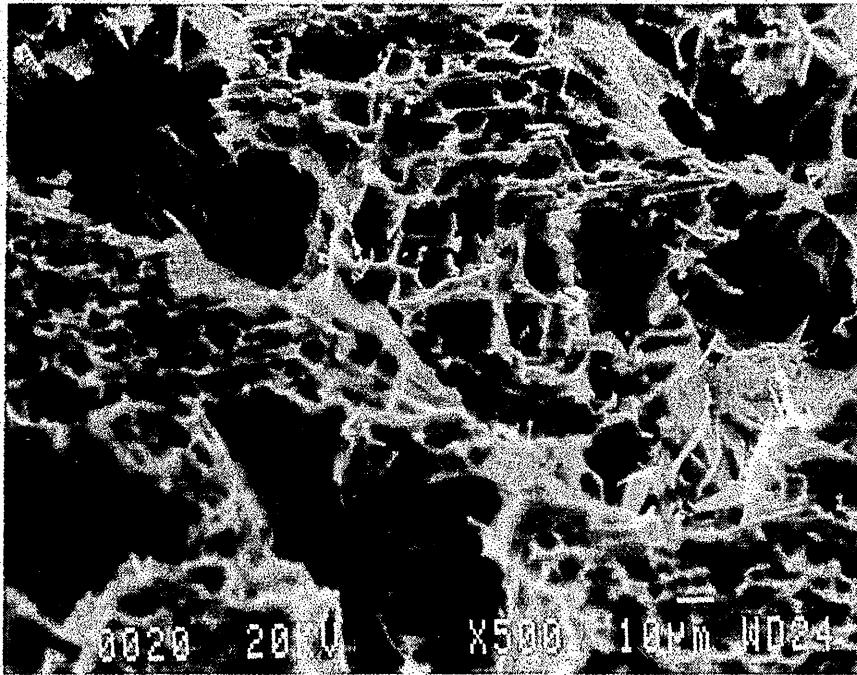


Fig 5.18 SEM image of the 15 minute KI-electro etch surface of alloy *B*

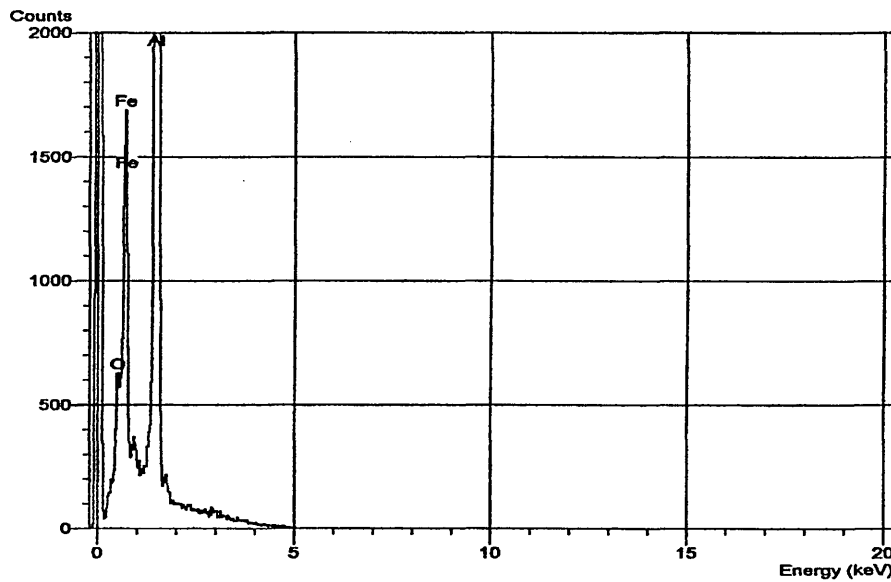


Fig 5.19 Representative EDS spectrum taken from a exposed intermetallic particle from sample *B* after being exposed to a 15 minute KI electro-etch

#### 5.2.2.1 ANALYSIS OF THE CEMS SPECTRA OF ALLOY SAMPLE *B*

The SEM micrograph of the surface of the unetched alloy sample *B* is shown in Fig 5.10. The first main feature that was interpreted from that image was that the grains of the solid alloy are approximately 80  $\mu\text{m}$  in diameter, and a different type of surface morphology was evident along these grain boundaries. Taking EDS measurements from the centre of the grains shows that only aluminium was present, see Fig 5.11. However, repeating the same measurements from the different surface morphology along the alloy grain boundaries, see Fig 5.12, aluminium, iron, and trace amounts of silicon were present. This was consistent with the known solidification mechanisms that exist for an aluminium rich Al-Fe-Si alloys, see Chapter 1.2.1.1. The Fe and Si elements form intermetallic compounds from the final part of the aluminium to solidify, and this occurs between the dendrite arms of the alloy. This was due to the very low solid solubility of these elements in aluminium.

The CEMS technique was then applied to the surface of the alloy sample *B*. The maximum probe depth of the conversion electrons has been quoted at approximately 300 nm [10]. However, Williamson *et al* [20] has calculated that approximately 50% of conversion electrons come from the first 50 nm and 75% come from the first 100 nm. These figures were calculated for aluminium ions implanted onto a steel substrate, and for this study they shall only be quoted as a gross approximation.

The corrosive resistant oxide film that forms from freshly cast aluminium exposed to air has been shown to be approximately 2.5 nm in depth [21]. The film growth stabilises at a typical thickness of 30-40 nm, but the film continues to grow at a rapidly reduced rate [21]. However, annealing can accelerate the growth rate. Therefore, the CEMS technique would only realistically analyse the surface properties of the iron containing compounds from the first 60 nm of the alloy, beneath the oxide layer.

The Mössbauer spectrum that was produced by using the CEMS technique was shown in Fig 5.9. Initially, the resultant Mössbauer spectrum was de-convoluted according to the room temperature parameters for the intermetallic compound combination that was obtained by using the transmission arrangement,  $\alpha_c$ -AlFeSi and Al<sub>6</sub>Fe. However, the  $\chi^2$  value that was obtained was very high, and this resulted in a further component being added to the de-convolution procedure, compound *X*. The final Mössbauer parameters that were obtained for this procedure are shown in Table 5.10. It should be noted that the signal to noise ratio for this experiment was very low, only 0.54163, and that all of the reported Mössbauer parameters should be treated with a degree of caution.

Compound	$\delta$ , mm s <sup>-1</sup>	$\Delta/2$ , mm s <sup>-1</sup>	$\Gamma/2$ (l), mm s <sup>-1</sup>	$\Gamma/2$ (r), mm s <sup>-1</sup>	Rel. Area, %	$\chi^2$
Unknown, X	-0.06	0.11	0.18	0.24	76	0.472
$\alpha_c$ -AlFeSi	0.28	0.10	0.19	0.19	8	
	0.18	0.19	0.19	0.19	8	
Al <sub>6</sub> Fe	0.23	0.15	0.15	0.15	8	

Errors:  $\delta = \pm 0.02$  mm s<sup>-1</sup>,  $\Delta/2 = \pm 0.02$  mm s<sup>-1</sup>,  $\Gamma/2 = \pm 0.02$  mm s<sup>-1</sup>,

Isomer shifts relative to  $\alpha$ -iron.

Table 5.10 Final Mössbauer parameters obtained for the CEMS technique applied to the unetched surface of alloy sample *B*

The process of electro-etching using KI solution was used upon the surface of alloy sample *B*. This technique was a proven process used commonly at Alcan International for the preferential removal of the oxide layer and aluminium matrix, and thus leaving the aluminium intermetallic compounds standing proud of the surface. Initially, the alloy sample *B* was placed in the KI solution and etched for 10 minutes using an applied voltage of 30 V.

The resultant effect upon the surface was illustrated by the SEM micrograph, Fig 5.18. The etching process had started and was shown by the presence of deep etch pits on the surface, which are characteristic of the etchant reacting along defects present within the surface. However, the process was not complete as the intermetallic compounds were still embedded in the grain boundaries of the alloy. This was reinforced by a schematic EDS analysis of the surface, which showed that no iron was exposed within the etch pits or on the unetched regions, see Fig 5.15 and 5.16. The resultant de-convoluted Mössbauer parameters from the room temperature analysis are shown in Table 5.11.

Compound	$\delta$ , mm s <sup>-1</sup>	$\Delta/2$ , mm s <sup>-1</sup>	$\Gamma/2$ (l), mm s <sup>-1</sup>	$\Gamma/2$ (r), mm s <sup>-1</sup>	Rel. Area, %	$\chi^2$
Unknown, X	-0.07	0.11	0.18	0.25	76	0.601
$\alpha_c$ -AlFeSi	0.28	0.10	0.19	0.19	8	
	0.18	0.19	0.19	0.19	8	
Al <sub>6</sub> Fe	0.23	0.15	0.15	0.15	8	

Errors:  $\delta = \pm 0.02$  mm s<sup>-1</sup>,  $\Delta/2 = \pm 0.02$  mm s<sup>-1</sup>,  $\Gamma/2 = \pm 0.02$  mm s<sup>-1</sup>,

Isomer shifts relative to  $\alpha$ -iron.

Table 5.10 Final Mössbauer parameters obtained for the CEMS technique applied to the 10 minute KI electro-etched surface of alloy sample *B*

The de-convolution procedure was used as the one applied to the unetched surface, and no appreciable change in any of the Mössbauer parameters was observed.

However, the signal to noise ratio was improved, 0.95417, which would indicate that the etching process had partially removed the oxide film. This improvement was not that significant, and the resultant Mössbauer parameters should still be treated with a degree of caution.

The etching procedure was repeated for a further 5 minutes, and a dramatic change was evident in the surface morphology, see Fig 5.18 for the SEM micrograph. The aluminium intermetallic compounds can be clearly seen standing proud of the surface of the alloy, and thus made the CEM spectrum easier to analyse. This was confirmed by EDS analysis taken from the exposed particles, which showed a relatively high iron content being present, see Fig 5.19. The resultant Mössbauer spectrum had changed considerably. The de-convoluted component attributed to the unknown compound *X* was removed, thus indicating that this particular compound was present within the oxide layer. The spectrum was then de-convoluted according to the room temperature

Mössbauer parameters of the aluminium intermetallic compounds  $\alpha_c$ -AlFeSi and Al<sub>6</sub>Fe, see Table 5.11 for the Mössbauer parameters. It should be noted that the signal to noise ratio was 0.98502, which was very similar to that observed for 10 minute KI electro-etched. This would imply that the 10 minute KI electro-etch removed the vast majority of the oxide layer, which inhibited the progress of the conversion electrons to the detector.

Compound	$\delta$ , mm s <sup>-1</sup>	$\Delta/2$ , mm s <sup>-1</sup>	$\Gamma/2$ (l), mm s <sup>-1</sup>	$\Gamma/2$ (r), mm s <sup>-1</sup>	Rel. Area, %	$\chi^2$
$\alpha_c$ -AlFeSi	0.28	0.10	0.19	0.19	9	0.642
	0.18	0.19	0.19	0.19	9	
Al <sub>6</sub> Fe	0.23	0.15	0.15	0.15	82	

Errors:  $\delta = \pm 0.02$  mm s<sup>-1</sup>,  $\Delta/2 = \pm 0.02$  mm s<sup>-1</sup>,  $\Gamma/2 = \pm 0.02$  mm s<sup>-1</sup>,  
Isomer shifts relative to  $\alpha$ -iron.

Table 5.11 Final Mössbauer parameters obtained for the CEMS technique applied to the 15 minute KI electro-etched surface of alloy sample *B*

The resultant CEM spectrum from the 15 minute KI electro-etch was de-convoluted to contain three quadrupole interactions, which were representative of the two intermetallic compounds  $\alpha_c$ -AlFeSi and Al<sub>6</sub>Fe. The calculated relative proportions of the two compounds were  $85 \pm 5$  % Al<sub>6</sub>Fe and  $15 \pm 5$  %  $\alpha_c$ -AlFeSi. This was different to the relative proportions obtained from transmission Mössbauer experiments performed upon the extracted aluminium intermetallic compounds, which produced a relative proportion of  $30 \pm 5$  % Al<sub>6</sub>Fe and  $70 \pm 5$  %  $\alpha_c$ -AlFeSi.

This reversal in the calculated relative proportions attributed to each of the aluminium intermetallic compounds was unexpected. During the solidification of the parent alloy the aluminium intermetallic compounds are formed as discrete particles between the

dendrite arms of the solid. Therefore, the KI electro-etching of the surface of alloy sample *B* must have had the effect of preferentially removing the  $\alpha_c$ -AlFeSi particles. This could be explained by the different particle morphology of the two aluminium intermetallic compounds [22].

The unexpected presence of the unknown compound *X* was initially an enigma. This particular component of the surface of the alloy sample *B* was de-convoluted, in this study, as an asymmetrical quadrupole interaction, with very broad line-widths. These broad line-widths were indicative of this particular compound being amorphous, which can be further explained by the Jahn-Teller effect. However, this component of the Mössbauer spectrum could equally have been de-convoluted as a very broad Lorentzian line, and this was due to the very poor signal to noise ratio making accurate de-convolution of the Mössbauer spectrum inherently difficult. Therefore, it was logical to say that the only accurate Mössbauer hyperfine parameter that could have been used for the identification of the unknown compound *X* was the isomer shift. The isomer shift for this compound was slightly negative, the actual value being  $-0.06 \pm 0.02 \text{ mm s}^{-1}$ , and it did not correspond to any of the known aluminium intermetallic compounds or Fe substituted  $\text{Al}_2\text{O}_3$  variations [23, 24, 25, 26, 27, 28, 29, 30]. However, the isomer shift, and the very general characteristics of this particular component of the Mössbauer spectrum, matched those of very fine super-paramagnetic grains,  $\delta = -0.04 \pm 0.02 \text{ mm s}^{-1}$  (relative to  $\alpha$ -iron). These were observed during the artificial creation of aluminium intermetallic compounds using  $^{57}\text{Fe}$  implantation on aluminium foil substrates [13, 14].

These findings are consistent with those found by Shimizu *et al* [31] when investigating the oxide layer  $\text{Al}_6\text{Fe}$  interface. The interface was studied using Energy-Filtering TEM, and an iron enriched region was found to exist between this region. The region was found to be heavily disordered and approximately 1 nm in width, but the occasional presence of ordered domains was observed. There was also no evidence of the formation of iron clusters within this region. The formation of this region was explained due to selective oxidation of aluminium within the intermetallic immediately

beneath the oxide layer. Since the surface of the intermetallic particles, in this study, was found to consist of predominately  $Al_6Fe$  it would be logical to assume that this selective oxidation took place.

### 5.3 SAXPS AND SAAES

The surface of the alloy sample *B* was analysed using Small Area Auger Electron Spectroscopy (SAAES) and Small Area X-ray Photoelectron Spectroscopy (SAXPS). The incident X-ray beam was focused down to approximately 60  $\mu\text{m}$  in diameter, which was achieved by an array of magnetic lenses. The region of the unetched surface that was investigated by these two techniques was chosen to provide the maximum iron content, i.e. a junction of grain boundaries. However, the region of the KI electro-etched surface did not need any careful selection. This was due to the etching process leaving a fairly uniform distribution of iron above the ingot sample surface.

#### 5.3.1 FUNDAMENTALS OF THE AUGER PROCESS

When an atom is excited with incident radiation the removal of an electron from one of the inner electron energy levels may occur, and a relaxation process is needed to leave the atom in an energetically lower state. This relaxation process can be achieved by two different mechanisms. One method is by X-ray fluorescence, and is favoured for elements with high *Z* values, and will not be discussed any further. The other method involves the relaxation of the atom by the emission of an Auger electron. Basically, the Auger emission process involves the de-excitation of an electron from a higher energy level to occupy the vacant electron state in the lower energy level. The remaining energy is then emitted from the atom by the ejection of an electron from one of the higher energy levels, which are closer to the Fermi level. The Auger process is shown schematically in Fig 5.19 for a KLL transition. A more detailed description and analysis of this process is given elsewhere [32, 33].

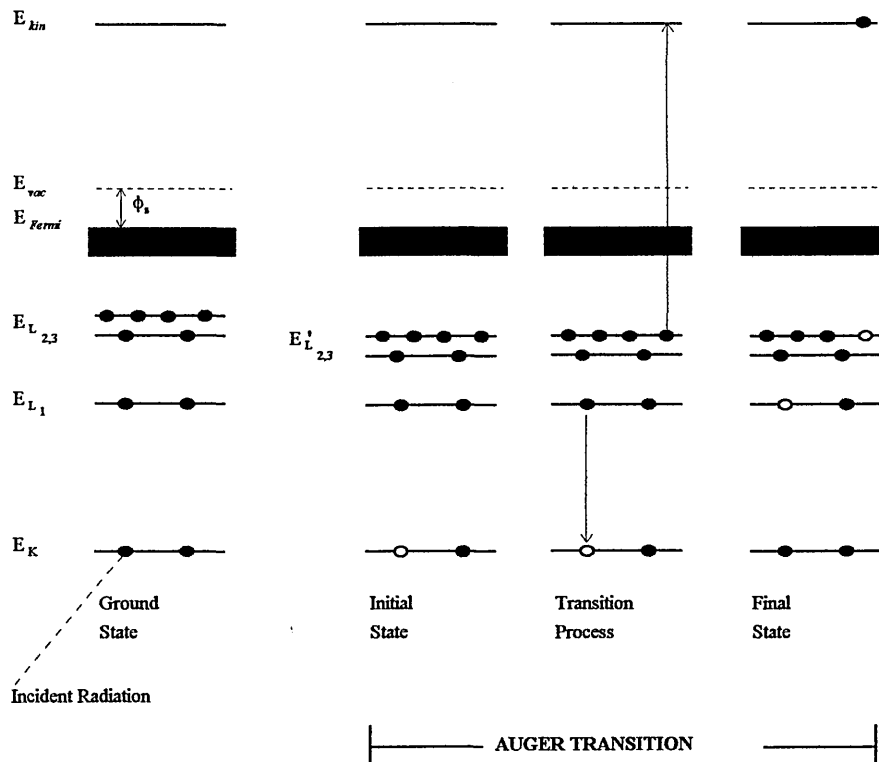


Fig 5.19 Schematic representation of the KLL Auger process. The atom in the ground state is excited either by electron impact or photons. The vacant electron in the core energy level leads to a contraction in the outer energy levels, and is denoted by  $E'_{L_{2,3}}$ . The K vacancy is filled by an L electron in the transition process and the excess energy is transferred to another L electron, which is then ejected from the atom. The final state is a doubly ionised atom [33].

### 5.3.1.1 THE AUGER TRANSITIONS

The standard X-ray nomenclature is used when describing the possible transitions when an atom undergoes the Auger process. This type of nomenclature describes the interactions between the orbital angular momentum,  $l$ , (which take the values 0,1,2,3 etc. due to the quantized nature of the orbital paths of the electron), and the spin momentum,  $s$ , (which take either of the values  $\pm\frac{1}{2}$  due to the Pauli exclusion principle) of the electron. The interaction between these two momenta is a simple vector summation, and is termed as the total electronic angular momentum of the electron.

However, the vector summation can be carried performed in two different ways, which are termed as j-j coupling and L-S (Russell-Saunders) coupling respectively [32].

#### 5.3.1.1.1 j-j COUPLING

The total electronic angular momentum,  $j$ , of a single isolated electron is obtained by summing vectorially the individual spin momenta and the orbital angular momenta.

This characteristic quantum number is calculated by the following expression:

$$j = l + s \qquad \text{Equation 5.5}$$

The total atomic angular momentum,  $J$ , for the whole atom can then be calculated from the summation for all the electrons orbiting around the nucleus, see Equation 5.6.

This type of description is termed j-j coupling.

$$J = \sum l \qquad \text{Equation 5.6}$$

However, j-j coupling only accurately describes the electronic interaction in elements with high atomic numbers, typically where  $Z > \approx 75$ , but the nomenclature generated by the technique is used for Auger transitions for all parts of the periodic table. This can lead to inadequate descriptions of the final state of the atom.

The nomenclature based upon the j-j coupling scheme is based upon the historical X-ray notation and the electronic quantum numbers,  $l$  and  $j$ , which obeys some very simple rules. The nomenclature is summarised in Table 5.12. The X-ray notation is almost always used for describing the Auger process, so that, for example, in j-j coupling there would be six predicted KLL transitions, i.e.  $KL_1L_1$ ,  $KL_1L_2$ ,  $KL_1L_3$ ,  $KL_2L_2$ ,  $KL_2L_3$ , and  $KL_3L_3$ .

$n$	$l$	$j$	X-ray Suffix	X-ray Level	Spectroscopic Level
1	0	1/2	1	K	1s <sub>1/2</sub>
2	0	1/2	1	L <sub>1</sub>	2s <sub>1/2</sub>
2	1	1/2	2	L <sub>2</sub>	2p <sub>1/2</sub>
2	1	3/2	3	L <sub>3</sub>	2p <sub>3/2</sub>
3	0	1/2	1	M <sub>1</sub>	3s <sub>1/2</sub>
3	1	1/2	2	M <sub>2</sub>	3p <sub>1/2</sub>
3	1	3/2	3	M <sub>3</sub>	3p <sub>3/2</sub>
3	2	3/2	4	M <sub>4</sub>	3d <sub>3/2</sub>
3	2	5/2	5	M <sub>5</sub>	3d <sub>5/2</sub>

Table 5.12 X-ray and spectroscopic notation shown for the first three principal quantum numbers [32]

#### 5.3.1.1.2 L-S COUPLING

The other method for performing the vectorial summation is first to sum all the individual electronic angular momenta and then all the individual electronic spin momenta. These two momenta are then characterised by two quantum numbers, the total atomic orbital angular momentum quantum number,  $L$ , and the total atomic spin quantum number,  $S$ . The coupling of the two total momenta can then be defined to yield the total atomic angular momentum,  $J$ , by the following expression:

$$J = \sum l + \sum s = |L \pm S| \quad \text{Equation 5.7}$$

The L-S coupling method has been found to apply to elements of low atomic number, typically where  $Z < \approx 20$ . In this scheme the nomenclature is that of terms of symbols in the form of  $^{(2S+1)}L$ , which describes the electron distribution in the final state. The states where  $L = 0, 1, 2, 3$  etc., are given the notation S, P, D, F, etc. This method also predicts six possible transitions in the KLL series, which are listed in Table 5.13.

However, the  $^3P$  transition is forbidden, as the conservation of parity must be upheld [33].

Transition	Configuration	$L$	$S$	Term
$KL_1L_1$	$2s^02p^6$	0	0	$^1S$
$KL_1L_{2,3}$	$2s^12p^5$	1	0	$^1P$
		1	1	$^3P$
$KL_{2,3}L_{2,3}$	$2s^22p^4$	0	0	$^1S$
		1	1	$^3P$
		2	0	$^1D$

Table 5.13 Notation used for L-S coupling for the KLL series

The L-S classification and notation have mainly been used for the recording of high energy resolution Auger spectra in order to provide experimental data for the comparison with theoretical models, and is not generally used.

### 5.3.1.1.3 INTERMEDIATE COUPLING

The intermediate coupling scheme exists for regions of the Periodic Table where neither j-j coupling nor L-S coupling adequately describes the final energy state configuration. In intermediate coupling each L-S term is split into multiplets of different  $J$  values, and the term symbols are now in the form  $(^{2S+1})L_J$ . This coupling method predicts ten possible final energy states in the KLL transition series, which are illustrated in Table 5.14.

However, it is customary to use a mixed notation when quoting the final energy states, so the KLL series, in approximate order of increasing energy, would be:  $KL_1L_1$  ( $^1S_0$ ),  $KL_1L_2$  ( $^1P_1$ ),  $KL_1L_2$  ( $^3P_0$ ),  $KL_2L_2$  ( $^1S_0$ ),  $KL_1L_3$  ( $^3P_1$ ),  $KL_1L_3$  ( $^3P_2$ ),  $KL_2L_3$  ( $^2D_1$ ),  $KL_2L_3$  ( $^3P_1$ ),  $KL_3L_3$  ( $^3P_0$ ),  $KL_3L_3$  ( $^3P_2$ ). The transition  $KL_2L_3$  ( $^3P_1$ ) is also forbidden, due to the conservation parity, so only nine states are allowed.

Transition	Configuration	L-S Term	<i>L</i>	<i>S</i>	<i>J</i>	IC Term
KL <sub>1</sub> L <sub>1</sub>	2s <sup>0</sup> 2p <sup>6</sup>	<sup>1</sup> S	0	0	0	<sup>1</sup> S <sub>0</sub>
		<sup>1</sup> P	1	0	1	<sup>1</sup> P <sub>1</sub>
KL <sub>1</sub> L <sub>2,3</sub>	2s <sup>1</sup> 2p <sup>5</sup>		1	1	0	<sup>3</sup> P <sub>0</sub>
		<sup>3</sup> P	1	1	1	<sup>3</sup> P <sub>1</sub>
			1	1	2	<sup>3</sup> P <sub>2</sub>
		<sup>1</sup> S	0	0	0	<sup>1</sup> S <sub>0</sub>
KL <sub>2,3</sub> L <sub>2,3</sub>	2s <sup>2</sup> 2p <sup>4</sup>		1	1	0	<sup>3</sup> P <sub>0</sub>
		<sup>3</sup> P	1	1	1	<sup>3</sup> P <sub>1</sub>
			1	1	2	<sup>3</sup> P <sub>2</sub>
		<sup>1</sup> D	2	0	2	<sup>1</sup> D <sub>2</sub>

Table 5.14 Notation used for intermediate coupling for the KLL series

### 5.3.1.2 DEPTH RESOLUTION OF THE AES PROCESS

The surface sensitivity of the AES technique is mainly due to the limited travelling distance of the emitted Auger electrons in a solid, which is a consequence of their high inelastic scattering cross section. The escape depth from a solid for Auger electrons with energies 10-2000 eV have been calculated to lie typically between 5-50 Å. This is termed the inelastic mean free path of the electrons. This by definition is the average distance an emitted electron will travel, with a given energy, between successive collisions. This implies that the emitted Auger electrons travel along straight lines between their point of origin in the sample and the detector, since the elastic scattering factor is insignificant.

The inelastic mean free path of the electrons in a solid exhibit the behaviour of a “Universal Curve”, and an empirical model was first proposed by Seah *et al* [34] to

calculate these values for an element, inorganic compound, and an organic compound.

These are shown in Equations 5.8, 5.9, and 5.10.

$$\text{Element: } \lambda_M = \frac{538}{E^2} a + 0.41 a^{3/2} E^{1/2} \quad [\text{nm}] \quad \text{Equation 5.8}$$

$$\text{Inorganic compound: } \lambda_M = \frac{2170}{E^2} a + 0.72 a^{3/2} E^{1/2} \quad [\text{nm}] \quad \text{Equation 5.9}$$

$$\text{Organic Compound: } \lambda_M = \frac{49}{E^2} a + 0.11 E^{1/2} \quad [\text{mg m}^{-2}] \quad \text{Equation 5.10}$$

where  $\lambda_M$  = Inelastic mean free path, measured in monolayers.

$E$  = The emitted Auger electron energy, measured in eV.

$a$  = Mean atomic diameter, measured in nanometers.

The mean atomic diameter is calculated from the following expression:

$$a = \left[ \frac{M}{1000 \cdot \rho \cdot N_A} \right]^{1/3} \quad \text{Equation 5.11}$$

where  $M$  = Relative Molecular Mass.

$\rho$  = Bulk density, measured in  $\text{kg m}^{-3}$ .

$N_A$  = Avogadro constant, measured in  $\text{mol}^{-1}$ .

Using the above approach it can be seen that the calculated inelastic mean free path for aluminium and oxygen is approximately 23 and 15 monolayers respectively (assuming that the most intense Auger lines are used), and highlights the extreme surface sensitivity of the particular analytical technique. There exist other, more complicated, empirical models to calculate this value [35, 36], which are discussed in more detail elsewhere [33].

### 5.3.2 FUNDAMENTALS OF THE X-RAY PHOTOELECTRON SPECTROSCOPY

The interaction of an incident X-ray photon with a solid sample leads to the ejection of photoelectrons, as shown in Fig 5.20.

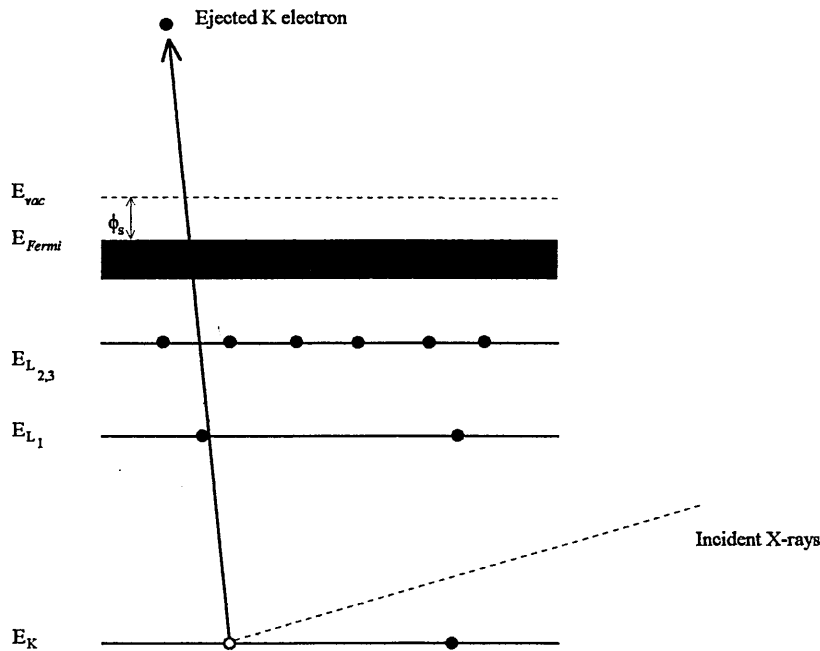


Fig 5.20 Schematic representation of the photo-emission process [33]

The diagram Fig 5.20 illustrates the X-ray photon interacting with an electron in the K shell, which causes the emission of a 1s photoelectron. An electron from a higher energy level, which can lead to either X-ray fluorescence or the de-excitation process of Auger emission fills the resulting vacancy. The determination of the kinetic energy of the outgoing electron is the principle of the experimental X-ray Photoelectron Spectroscopy.

The kinetic energy of the ejected photoelectron is related to the electron binding energy,  $E_B$ , which is the parameter that defines both the element and atomic level from which it emanated, and other instrumental terms in the following manner:

$$E_K = h\nu - E_B - E_R - \phi - \delta E \quad \text{Equation 5.12}$$

The term  $E_R$  is defined as the recoil energy, which has been shown to be fundamental in the experimental observation of the Mössbauer effect, but it is generally ignored for this technique due to its very small value, typically 0.1 - 0.01 eV. As the photon energy of the X-rays,  $h\nu$ , and the spectrometer work function,  $\phi$ , which is determined experimentally, are known the calculation of the electron binding energy is a simple matter. The final term  $\delta E$  only comes into play when investigating insulators with this particular technique, as it reflects the electrostatic charging of the specimen.

The nomenclature used when interpreting a XP spectrum is based entirely upon which orbital the emitted photoelectron was generated from, and is shown in Table 5.12.

### 5.3.2.1 DEPTH RESOLUTION OF THE XPS PROCESS

The emission of a photoelectron,  $I_d$ , as a function of depth,  $d$ , is predicted by the following Beer-Lambert equation [33]:

$$I_d = I_\infty \cdot \exp\left(-\frac{d}{\lambda} \cdot \sin \theta\right) \quad \text{Equation 5.13}$$

where  $I_\infty$  = Intensity from an infinitely thick, clean substrate

$\theta$  = Electron take off angle relative to the sample surface

The equation 5.13 implies an exponential decay of the electron signal as a function of depth, and although the XPS analysis depth is taken as  $3\lambda$  the analysis is heavily biased towards the surface layers. Approximately 65% of the total signal originates from the outer  $1\lambda$  of the surface of the sample [33].

In this study the incident X-rays were generated from the Mg( $K_{\alpha}$ ) line, which had an energy of 1.253 keV. That implied that the majority of the signal was generated from approximately the first 0.98 nm of the sample surface.

## 5.3.3 SAAES AND SAXPS SPECTRA

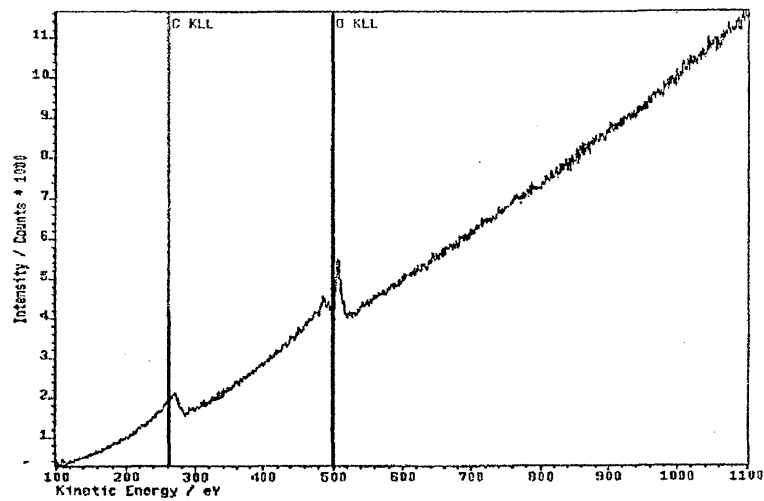


Fig 5.20 A representative SAAES spectrum obtained from the unetched surface prior to  $\text{Ar}^+$  cleaning

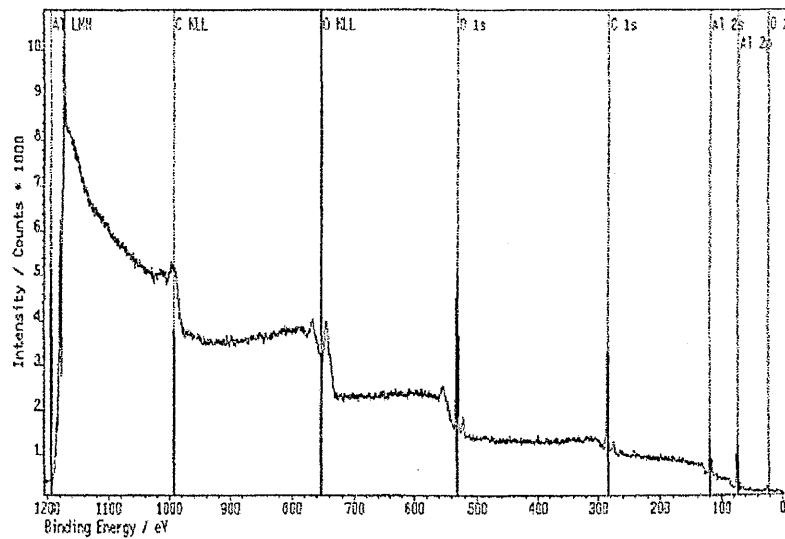


Fig 5.21 A representative SAXPS spectrum obtained from the unetched surface prior to  $\text{Ar}^+$  cleaning

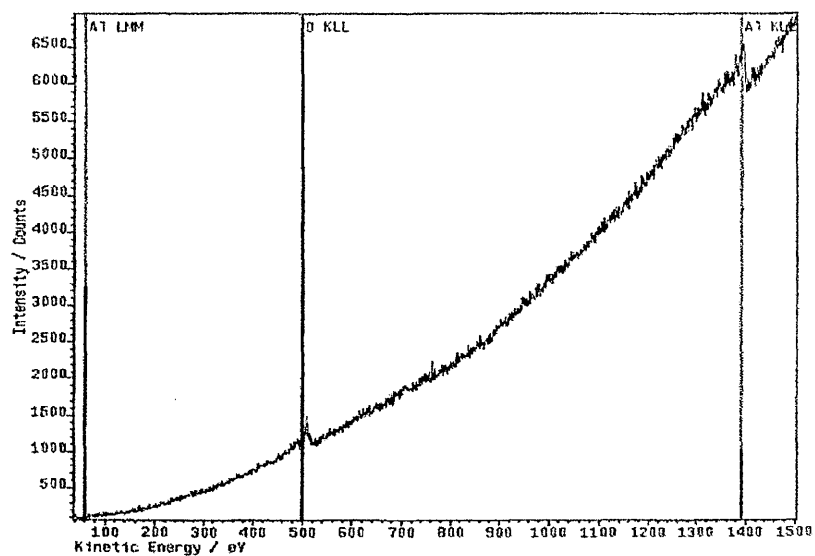


Fig 5.22 A representative SAAES spectrum obtained from the unetched surface after  $\text{Ar}^+$  cleaning

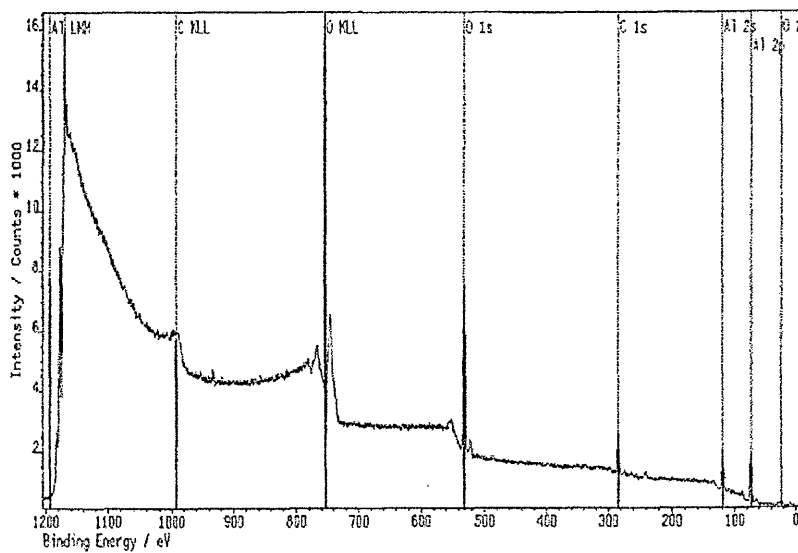


Fig 5.23 A representative SAXPS spectrum obtained from the unetched surface after  $\text{Ar}^+$  cleaning

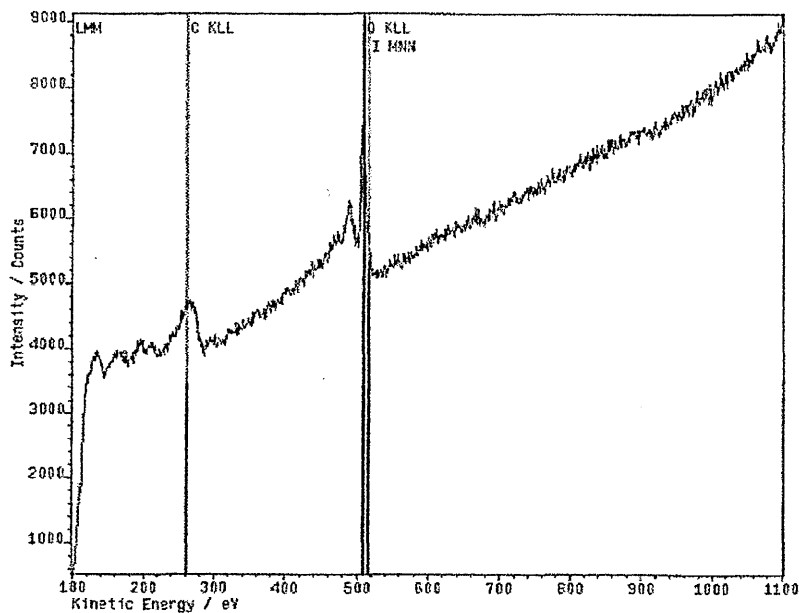
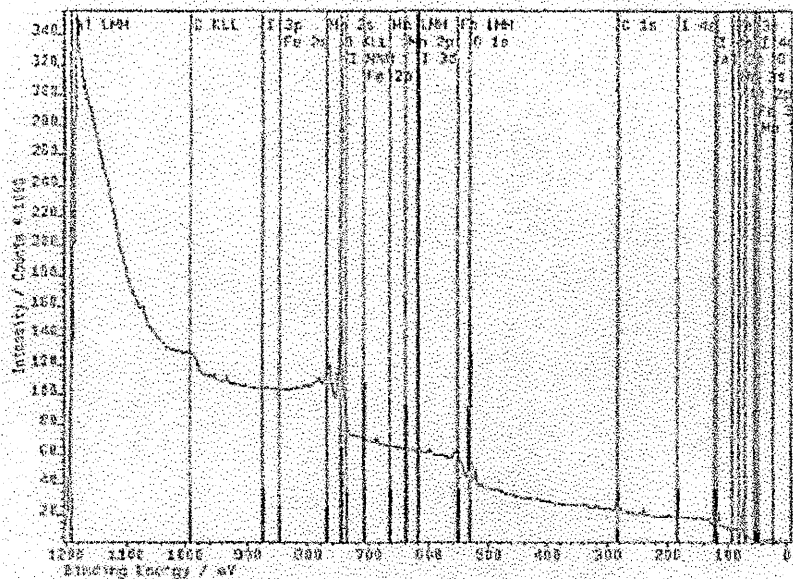


Fig 5.24 A representative SAAES spectrum obtained after the surface exposed to a 15 minute KI electro-etch prior to  $\text{Ar}^+$  cleaning



*Note: The author apologises for the quality of this image, as it was due to the original quality of the image being poor. However, all the necessary information can still be drawn from this image.*

Fig 5.25 A representative SAXPS spectrum obtained after the surface exposed to a 15 minute KI electro-etch prior to  $\text{Ar}^+$  cleaning



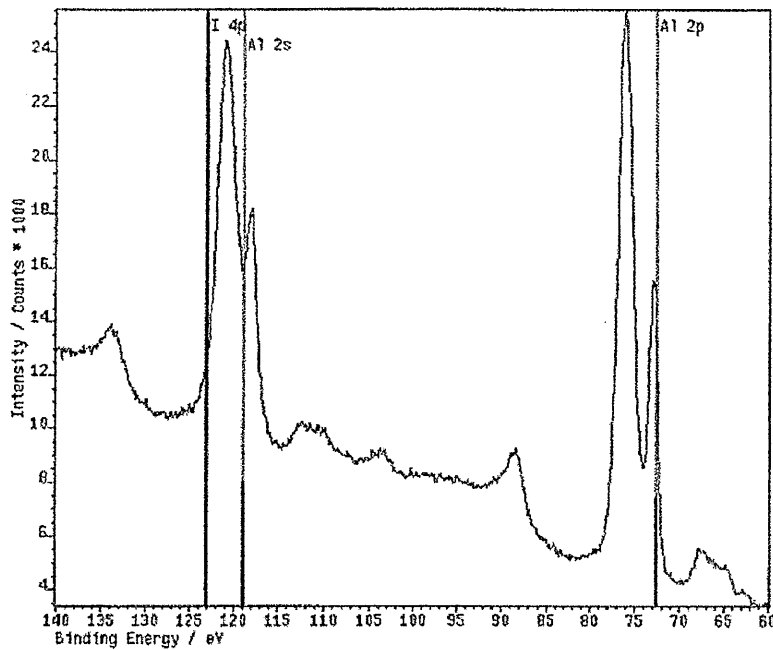


Fig 5.28 An enhanced view of the 60-140 binding energy range for the representative SAXPS spectra obtained after the surface exposed to a 15 minute KI electro-etch after Ar<sup>+</sup> cleaning

### 5.3.3.1 INTERPRETATION OF THE SAAES AND SAXPS SPECTRA FROM THE UNETCHED SURFACE

The un-differentiated SAAES spectrum obtained from the unetched surface of alloy sample *B*, prior to any Ar<sup>+</sup> cleaning, showed two main features, which corresponded to the elements carbon (C KLL) and oxygen (O KLL), see Fig 5.20. The corresponding SAXPS spectrum taken from the same surface region showed that the elements carbon (C KLL, C 1s), oxygen (O KLL, O 1s, O 2s, O 2p), and aluminium (Al LMM, Al 2s, Al 2p) were present, see Fig 5.21.

After  $\text{Ar}^+$  cleaning, for approximately 10 minutes at an accelerating voltage of 5 kV, the un-differentiated SAAES spectrum had changed. The presence of carbon had been removed from the surface, and aluminium (Al KLL, Al LMM) was now detected along with oxygen (O KLL), when using this technique, see Fig 5.23. However, the only change in the corresponding SAXPS spectrum was the decreased intensity of the carbon (C KLL, C 1s) peaks.

Therefore, a hypothesis can be drawn from these spectra regarding the surface structure of the unetched alloy sample *B*. Initially, approximately the first 50 Å surface of the alloy sample consisted of a uniform very thin layer of carbon. This carbon layer was due to natural contamination, and below lay an oxygen rich region. The  $\text{Ar}^+$  cleaning process, which was timed to remove only the carbon layer, confirmed this. The Auger process then detected the presence of aluminium.

The realistic inherent sampling depth of the XPS technique has been shown to be approximately 100 nm. Therefore, this technique probed the region of the surface, which was beneath the carbon and oxygen rich layers. There was a noticeable splitting of the aluminium and oxygen photoelectron peaks, which corresponded to the compound  $\text{Al}_2\text{O}_3$  being present [32]. This splitting was independent of surface cleaning. There was only a slight change in the spectral features after  $\text{Ar}^+$  cleaning, which was the decrease in the relative intensity of the carbon peaks. This would imply that carbon had diffused into the oxide layer to a depth of greater than 50 Å. However, no iron was present in any of the SAAES and SAXPS spectra, which would seem to indicate that the oxide layer was greater than 100 nm in thickness above the aluminium intermetallic compounds distributed along the grain boundaries.

### 5.3.3.2 INTERPRETATION OF THE SAAES AND SAXPS SPECTRA FROM THE KI ELECTRO-ETCHED SURFACE

The un-differentiated SAAES spectrum obtained from the 15 minute KI electro-etched surface of alloy sample *B*, prior to any Ar<sup>+</sup> cleaning, showed three main features, which corresponded to the elements carbon (C KLL), oxygen (O KLL), and iodine (I MNN), see Fig 5.24. The corresponding SAXPS spectrum taken from the same surface region showed that the elements carbon (C KLL, C 1s), oxygen (O KLL, O 1s, O 2s, O 2p), iodine (I MNN, I 3p, I 3d, I 4s, I 4p, I 4d) aluminium (Al LMM, Al 2s, Al 2p), iron (Fe LMM, Fe 2s, Fe 2p, Fe 3s, Fe 3p) and manganese (Mn LMM, Mn 2s, Mn 2p, Mn 3s, Mn 3p) were present, see Fig 5.25.

After Ar<sup>+</sup> cleaning, for approximately 10 minutes at an accelerating voltage of 5 kV, the un-differentiated SAAES spectrum had changed. The presence of carbon and iodine had been removed from the surface, and aluminium (Al KLL, Al LMM) was now detected along with oxygen (O KLL), when using this technique, see Fig 5.26. However, the corresponding SAXPS spectrum detected the presence of carbon (C KLL, C 1s), oxygen (O KLL, O 1s, O 2s, O 2p), aluminium (Al LMM, Al 2s, Al 2p), iron (Fe LMM, Fe 2s, Fe 2p, Fe 3s, Fe 3p) and manganese (Mn LMM, Mn 2s, Mn 2p, Mn 3s, Mn 3p), see Fig 5.27.

The surface of the alloy sample *B* after the KI electro-etching consisted of carbon, oxygen, and iodine in the first 50 Å. The presence of carbon and oxygen was expected, due to reasons described earlier. However, the existence of iodine would have been present as a by product of the electro-etching process. The corresponding XPS spectrum from the same region detected the same elements as the unetched surface, but the presence of metallic iron was now detected. This was not surprising as the electro-etching process had removed the thick oxide layer, and thus left the intermetallic compounds standing proud of the surface. Therefore, the freshly grown oxide layer over these intermetallic compounds would only be a few nanometers in thickness [21] making the detection of this element easy by using the XPS technique.

The existence of metallic manganese could have two explanations. The first is that the element was present as an impurity in the etching chemicals, or as an impurity in the original casting composition of the parent ingot.

After the surface was cleaned using  $\text{Ar}^+$  the change there was a considerable change in the SAAES and SAXPS spectra taken from the same surface region of the alloy sample *B*. There was no evidence of iodine being present in either spectra, which would indicate that the iodine was only present in the outermost regions of the surface and was totally removed in the cleaning process. There was also only a trace level of carbon left in the SAXPS spectrum, which seems to indicate that the carbon had diffused into the intermetallic compounds and the surface of the unetched regions. The cleaning process made no appreciable change in the relative intensity of manganese, which would seem to indicate that this element was a trace impurity in the original casting composition of the parent ingot.

The Fig 5.28 illustrates the splitting in the Al 2p peak, which corresponded to the presence of pure aluminium and  $\text{Al}_2\text{O}_3$  that was evident in all the SAXPS spectra. Also, the peak shift in the iodine 4p peak was shown, and by the comparison to the database that was used in the fitting of the spectra, to be  $\text{KIO}_4^-$ .

## 5.4 CONCLUSIONS

The parent alloy used in this investigation was made from super-purity aluminium, with the addition of 0.3% Fe, and 0.1% Si. The composition was consistent with a 1xxx series alloy. The parent alloy was cast using a laboratory Direct Chill (DC) arrangement, and two thin slices were sectioned from the central region of the alloy, samples *A* and *B*.

Transmission Mössbauer spectroscopy was then performed at two temperatures, 150 K and 250 K. The resultant Mössbauer spectra were then de-convoluted using combinations of fixed hyperfine parameters for selected aluminium intermetallic compounds, which were obtained from the variable temperature studies of the individual aluminium intermetallic compounds.

The relative proportion of the aluminium intermetallic compounds that were present within alloy samples *A* and *B* were calculated from the relative spectral absorption area, and the relative molecular mass of the intermetallic compound under study. The results of the aluminium intermetallic compound combination, within alloy samples *A* and *B*, and their relative proportions are shown in Table 5.15.

Alloy Sample	Intermetallic Combination	Relative Proportions
A	$\text{Al}_3\text{Fe} + \text{Al}_6\text{Fe}$	50:50 $\pm$ 5 %
B	$\text{Al}_6\text{Fe} + \alpha\text{-AlFeSi}$	30:70 $\pm$ 5 %

Table 5.15 The aluminium intermetallic compound combination, and their relative proportions, obtained by using transmission Mössbauer spectroscopy on alloy samples *A* and *B*.

It was impossible to speculate as to what local solidification rates were experienced by the alloy samples *A* and *B*. This was due to the alloy samples being isothermally heat treated and then water quenched. This would have the effect of increasing the amount of the more thermodynamically stable metastable intermetallic compounds, or promoting a phase change within the region of the parent alloy of interest. This would distort the actual cast intermetallic compound combinations, and relative proportions, within the samples.

However, the main purpose of this particular type of investigation was not to predict the positions of alloy samples taken from the parent ingot, but as a tool to identify and quantify the aluminium intermetallic combination. This has been achieved by using the Mössbauer technique, which complements the existing processes available to the research team at Alcan International.

This method must be used speculatively as it has been shown that some aluminium intermetallic compounds show very similar hyperfine parameters and lattice dynamics, mainly  $\text{Al}_m\text{Fe}$  and  $\text{Al}_x\text{Fe}$ . It would, therefore, inherently be very difficult to accurately de-convolute the Mössbauer spectrum from an alloy sample containing these intermetallic compounds accordingly, so further testing using the Mössbauer technique applied to this system would be required.

Another alloy sample of *B* was prepared, from the same parent DC-cast ingot, and various surface analysis techniques were applied to the ingot alloy sample. SEM indicated that the grains within the alloy were approximately 80  $\mu\text{m}$  in diameter, and a different type of surface morphology was evident along these grain boundaries. The EDS measurements taken from the centre of a grain indicated that only aluminium was present. However, EDS measurements taken from the grain boundary showed that aluminium, iron, and silicon were present. This was consistent with the known solidification mechanisms that occur for aluminium rich Al-Fe-Si alloys, see Chapter 1.2.1.1.

The CEMS technique was then applied to the surface of the alloy sample *B*. The deconvolution of the spectrum showed the presence of another dominant iron containing compound, which was not present in the transmission spectra, along with the known aluminium intermetallic compounds. The section of the spectrum that was attributed to the unknown dominant iron containing compound was de-convoluted as a quadrupole interaction with the following parameters:  $\delta = -0.06 \text{ mm s}^{-1}$  (relative to  $\alpha$ -iron),  $\Delta/2 = 0.11 \text{ mm s}^{-1}$ ,  $\Gamma(l) = 0.18 \text{ mm s}^{-1}$ ,  $\Gamma(r) = 0.24 \text{ mm s}^{-1}$ , and a relative absorption area =  $76 \pm 5 \%$ . Interpreting the Mössbauer parameters for this compound indicated that it was highly amorphous and distorted, but the physical characteristics of this compound were uncertain. The spectrum had a low signal to noise ratio, which was due to the low iron content of the alloy and the iron distribution within the alloy sample, and the resulting Mössbauer parameters were used with some caution. Therefore, the only accurate hyperfine parameter that was used for the identification of the unknown compound was the isomer shift. The isomer shift did not correspond to any of the known aluminium intermetallic compounds or Fe substituted  $\text{Al}_2\text{O}_3$  variations. However, the isomer shift, and the very general characteristics of this particular component of the Mössbauer spectrum, matched those of very fine super-paramagnetic grains,  $\delta = -0.04 \pm 0.02 \text{ mm s}^{-1}$  (relative to  $\alpha$ -iron) [13,14].

SAAES and SAXPS were performed on regions of the alloy sample surface where the iron content was the highest, i.e. a node of several grain boundaries. SAAES measurements, taken prior to  $\text{Ar}^+$  cleaning, showed that only carbon, an impurity of the polishing process, and oxygen were present within approximately the first 50 Å of the surface. This would seem to imply that there existed a uniform carbon layer and an oxygen rich layer on the outermost regions of the alloy surface. The corresponding SAXPS spectrum, taken from the same region of the surface, showed that aluminium was detected along with carbon and oxygen. The aluminium and oxygen peaks in the SAXPS spectra showed splitting, which was consistent with the presence of  $\text{Al}_2\text{O}_3$  along with the pure elements. After  $\text{Ar}^+$  cleaning carbon was removed from the SAAES spectrum, and aluminium was now detected. The only change in the corresponding SAXPS spectrum was the decrease in intensity of the carbon peak,

which would indicate that a small amount of carbon had diffused into the oxide layer during the polishing process.

Iron or silicon was not present in either SAAES spectra, which was not surprising since corrosive resistant oxide film that forms from freshly cast aluminium exposed to air has been shown to be approximately 2.5 nm in depth [21], and are too thick for the Auger electrons to be emitted from the alloy. Iron was also not present in either SAXPS spectra. This was not surprising since the depth sensitivity of the SAXPS and SAAES techniques were comparable. However, 75% of the CEMS spectrum was accumulated from the first 100 nm [20] of the surface. Therefore, the CEMS technique probes a deeper section of the surface region of the sample, when compared to SAAES and SAXPS, and thus iron was present in all the CEM spectra. A schematic representation of the surface of the alloy sample *B* is shown in Fig 5.29.

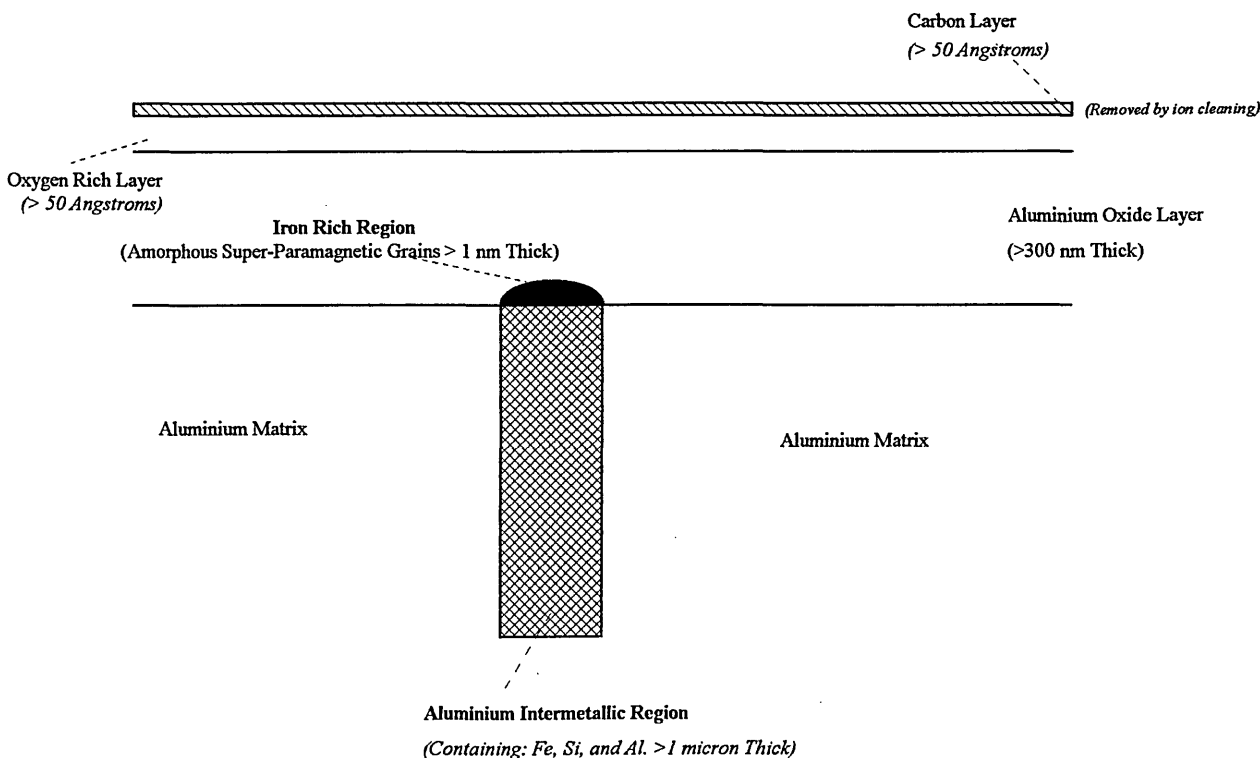


Fig 5.29 Schematic representation of the surface of alloy sample *B* prior to KI electro-etching

The surface of the alloy sample *B* was electro-etched in KI solution at 30 V for 10 minutes, and then a further 5 minutes. This etching process was done by the research team at Alcan International. This was devised to etch the oxide layer and the aluminium matrix and thus leaving the aluminium intermetallic compounds standing proud of the surface.

The CEMS spectrum obtained from the surface after the 10 minute KI electro-etch was no different to the Mössbauer spectrum obtained from the unetched surface. However, the signal to noise ratio had improved. This was due to the etching process having removed a significant amount of the oxide layer but being incomplete, as the intermetallic compounds were still imbedded within the grain boundaries of the alloy sample. This was illustrated by the corresponding SEM micrograph. Which showed the presence of etch pits that were characteristic of the etchant reacting with the surface along defects.

However, when the etching was continued for a further 5 minutes the surface morphology of the alloy sample had changed dramatically. The aluminium intermetallic compounds were left standing proud of the surface, which was illustrated by the SEM micrograph and the EDS measurements. The resultant CEM spectrum had also changed dramatically. The component attributed to the unknown compound had been removed, and thus indicated that it had been an iron rich region between the intermetallic compounds and the oxide layer. The remaining components of the spectrum were de-convoluted according to the known aluminium intermetallic compounds that were present,  $\text{Al}_6\text{Fe}$  and  $\alpha_c\text{-AlFeSi}$ . The calculated relative proportions of the two intermetallic compounds were  $85 \pm 5\%$   $\text{Al}_6\text{Fe}$  and  $15 \pm 5\%$   $\alpha_c\text{-AlFeSi}$ . This was contrary to the transmission Mössbauer experiments performed upon the extracted aluminium intermetallic compounds, which produced a relative proportion of  $30 \pm 5\%$   $\text{Al}_6\text{Fe}$  and  $70 \pm 5\%$   $\alpha_c\text{-AlFeSi}$ .

The different particle morphology of the two aluminium intermetallic compounds meant that preferential etching effect occurred, when attempting to expose the

intermetallic compounds from the aluminium matrix using the KI electro-etch process. This caused a reversal in the calculated relative proportions attributed to each of the aluminium intermetallic compounds.

These findings are consistent with those found by Shimizu *et al* [31] when investigating the oxide layer Al<sub>6</sub>Fe interface. An iron rich region was found to exist along the interface, which was found to be heavily disordered and approximately 1 nm in width. The formation of this region was explained due to selective oxidation of aluminium within the intermetallic immediately beneath the oxide layer. Since the surface of the intermetallic particles, in this study, was found to consist of predominately Al<sub>6</sub>Fe it would be logical to assume that this selective oxidation took place.

The SAAES spectrum of the surface of the alloy sample *B* was found to consist of carbon and iodine, which were induced impurities from the polishing and etching processes, along with oxygen. The corresponding SAXPS spectrum showed the same elements being present as the unetched surface, along with iodine, iron, and manganese. The iodine peak shift indicated that KIO<sub>4</sub><sup>-</sup> was present, whereas iron and manganese existed in their metallic form.

After the surface of the alloy sample was Ar<sup>+</sup> cleaned the corresponding SAAES spectrum was similar to that of the unetched SAAES spectrum, after cleaning. This indicated that a fresh Al<sub>2</sub>O<sub>3</sub> oxide layer had grown over the exposed aluminium intermetallic compounds. However, the SAXPS spectrum indicated that all of the iodine had been removed during the cleaning process, and only the carbon peak had been reduced in its intensity.

## 5.5 FUTURE WORK

1. The method of aluminium intermetallic compound identification, and calculation of their relative proportions, should be performed on other DC-cast alloy samples. Identifying aluminium intermetallic compounds with similar hyperfine parameters should initially test this method. If this method proves to be successful then it could be applied to alloy samples containing more than two aluminium intermetallic compounds. Eventually the technique could be refined to investigate the complex surface region of the parent ingot.
2. There is a considerable amount of scientific work needed on the identification of the unknown compound that was found in the CEMS spectrum of the unetched surface of the alloy sample *B*.
3. The signal to noise ratio of the CEMS spectrum could be improved in several ways: <sup>57</sup>Fe enrichment of the parent alloy, increased initial activity of the <sup>57</sup>Co source, collimation of the radiation directed upon the grain boundaries, and low temperature CEMS studies. The low temperature CEMS studies would allow confirmation of whether compound *X* is super-paramagnetic or not. Each of these, or a combination, would improve the signal to noise ratio significantly, and thus more representative hyperfine parameters could be obtained for the unknown compound.
4. The thickness of the Al<sub>2</sub>O<sub>3</sub> layer above the grain boundaries could be determined by a variety of methods. The non-destructive depth selective CEMS and CXMS (Conversion X-ray Mössbauer Spectroscopy) could be applied to this type of system, which would accurately determine the oxide thickness when coupled with the appropriate calculations. Also the destructive techniques, such as: depth profiling by SAXPS, depth profiling by SAAES, SIMS, and GDOES could be applied. However, due to the destructive nature these techniques would make further analysis of the surface by other techniques difficult.

## REFERENCES

- [1] C. J. Simensen, P. Fartum, A. Andersen, *Fresenius Z. Anal. Chem.*, **319** (1984) 286.
- [2] Z. S. Shan, S. Nafis, J. Woolham, S. H. Liou, D. J. Sellmyer, *J. Appl. Phys.*, **73** (1993) 6347.
- [3] C. D. England, W. R. Bennet, C. M. Falco, *J. Appl. Phys.*, **64** (1988) 5757.
- [4] C. H. Lee, H. He, F. J. Lamelas, W. Vavra, C. Uher, R. Clarke, *Phys. Rev.*, **B42** (1990) 1066.
- [5] A. R. Chowdhury, A. E. Freitag, *J. Appl. Phys.*, **79** (1996) 6303.
- [6] T. Hamaguchi, H. Aida, S. Nakagawa, M. Naoe, *J. Appl. Phys.*, **73** (1993) 6444.
- [7] M. Nagakubo, T. Yamamoto, M. Naoe, *J. Appl. Phys.*, **63** (1988) 5751.
- [8] T. Haeiwa, H. Negoro, M. Matsumoto, *J. Appl. Phys.*, **69** (1991) 5346.
- [9] L. M. Gratton, A. Miotello, C. Tosello, D. C. Kothari, G. Principi, A. Tomasi, *Nucl. Inst. Meths. Phys. Res.*, **B59/60** (1991) 541.
- [10] H. Reuter, *Nucl. Inst. Meths. Phys. Res.*, **B53** (1991) 167.
- [11] H. Reuter, *Hyp. Inter.*, **56** (1990) 1637.
- [12] H. Reuter, *Nucl. Inst. Meths. Phys. Res.*, **B30** (1988) 61.
- [13] W. X. Hu, G. L. Zhang, W. H. Liu, F. Xu, Y. G. Li, *Nucl. Inst. Meths. Phys. Res.*, **B72** (1992) 387.
- [14] M. A. Z. Vasconcellos, S. R. Teixeira, P. H. Dionisio, W. H. Schreiner, I. J. R. Baumvol, *Nucl. Inst. Meths. Phys. Res.*, **A280** (1989) 557.
- [15] C. A. Stickels, R. J. Bush, *Metall. Trans.*, **2** (1971) 2031.
- [16] S. Nasu, U. Gonser, R. S. Preston, *J. Phys. Colloq. C1*, **41** (1980) 385.
- [17] B. D. Sawicka, M. Drwiega, J. A. Sawicka, J. Stanek, *Hyp. Inter.*, **5** (1978) 147.
- [18] E. Verbiest, H. Pattyn, *Phys. Rev.*, **B25** (1982) 5097.
- [19] H. de Waard, G. L. Zhang, *Hyp. Inter.*, **56** (1990) 1569.
- [20] D. L. Williamson, F. M. Kutas, D. F. Fobare, M. S. Misra, *J. Appl. Phys.*, **60** (1986) 1493.
- [21] I. J. Polmear, "*Light Alloys - Metallurgy of the Light Metals*", (Chapman and Hall, London, 1989).

- [22] Y. Wang, H. Jones, P. V. Evans, "Proc. 4<sup>th</sup> Decennial International Conf. on Solidification Processing", Sheffield (1997) 568.
- [23] N. N. Greenwood, T. C. Gibb, "Mössbauer Spectroscopy", (Chapman and Hall, London, 1971).
- [24] C. A. Stickels, R. H. Bush, *Met. Trans. A*, **2** (1971) 2031.
- [25] C. M. Chittaranjan, V. Kumar, B. Viswanathan, K. P. Gopinathan, *Sol. Stat. Comm.*, **79** (1991) 69.
- [26] A. Vertes, S. Nagy, M. Zaki-Awad, J. Laker, E. Kovacs-Cselenyi, G. Groma, *Scripta Met.*, **16** (1982) 145.
- [27] E. Kuzmann, A. Vertes, A. Griger, V. Stefaniay, *Hyp. Int.*, **92** (1994) 943.
- [28] P. J. Schurer, B. Koopmans, F. Van Der Woude, *Sol. Stat. Comm.*, **59** (1986) 619.
- [29] S. Nagy, Z. Homonnay, A. Vertes, L. Murgas, *Acta Met.*, **35** (1987) 741.
- [30] S. Nasu, U. Gonser, R. S. Preston, *J. de Phys.*, **C1** (1980) 385.
- [31] K. Shimizu, G. M. Brown, H. Habazaki, K. Kobayahsi, P. Skeldon, G. E. Thompson, G. C. Wood, "Proc. 6<sup>th</sup> International Conf. on Aluminium Alloys, Vol. 3", (1998) 1565.
- [32] D. Brigg, M. P. Seah, "Practical Surface Analysis Volume 1: X-Ray Photoelectron Spectroscopy", (Wiley, London, 1983).
- [33] J. M. Walls, R. Smith, "Surface Science Techniques", (Alden, Oxford, 1994).
- [34] M. P. Seah, W. A. Dench, *Surface Interface Anal.*, **1** (1979) 2.
- [35] S. Tanuma, C. J. Powell, D. R. Penn, *Surface Interface Anal.*, **11** (1988) 577.
- [36] J. Szajman, J. Liesegang, J. G. Jenkin, R. C. G. Leckey, *J. Electron Spectrosc., Rel. Phenom.*, **23** (1981) 97.

## CHAPTER 6

### GENERAL CONCLUSIONS

#### 6.1 VARIABLE TEMPERATURE MÖSSBAUER SPECTROSCOPY

The most common aluminium intermetallic compounds that form during commercial DC casting of the 1xxx series alloys have been investigated using  $^{57}\text{Fe}$  variable temperature Mössbauer spectroscopy. The compounds were the equilibrium Al-Fe compound,  $\text{Al}_3\text{Fe}$ , the metastable Al-Fe compounds,  $\text{Al}_m\text{Fe}$ ,  $\text{Al}_x\text{Fe}$ , and the metastable Al-Fe-Si compound,  $\alpha_c\text{-AlFeSi}$ . Also the equilibrium intermetallic compound  $\text{Al}_6(\text{Fe,Mn})$  has been analysed using the same techniques, which can be considered as being a Fe substituted form of the equilibrium Al-Mn intermetallic compound,  $\text{Al}_6\text{Mn}$ .

Model alloys were prepared using a Bridgman furnace, which enabled the solidification rate of the alloy to be accurately determined, and the growth velocity could be tuned to promote the formation of an individual intermetallic compound between the dendrite arms of the host alloy matrix. The intermetallic compounds were then extracted from the aluminium matrix using the butanol extraction method, and the XRD traces of the individual intermetallic compounds were compared to a database prepared in-house at Alcan International.

The Mössbauer spectra for each of the aluminium intermetallic compounds studied were de-convoluted according to the crystallographic structure. When studying the crystallographic structure of each of the aluminium intermetallics it was found that the Fe site resided in the centre of a polyhedron with aluminium atoms at the vertices. The only changes in the different types of polyhedra were the co-ordination number, from 9-10 in some cases, and slight variations in the Al-Fe bond lengths.

The  $\theta_D$  values, when calculated by the normalised spectral area method, produces a variety of different values of each of the intermetallic compounds studied, see Table 6.1.

Intermetallic	Calculated $\theta_D$ , K	Calculated $f_{291}$
Al <sub>3</sub> Fe	452 Fe(1)-Fe(5)	0.81 Fe(1)-Fe(5)
	434 Fe(1)-Fe(4)	0.80 Fe(1)-Fe(4)
	488 Fe(5)	0.84 Fe(5)
Al <sub>x</sub> Fe	360	0.73
Al <sub>m</sub> Fe	358	0.72
$\alpha_c$ -AlFeSi	311 Fe(1)-Fe(2)	0.66 Fe(1)-Fe(2)
	297 Fe(1)	0.63 Fe(1)
	329 Fe(2)	0.68 Fe(2)
Al <sub>6</sub> (Fe,Mn)	352	0.71

Errors:  $\theta_D = \pm 5$  K,  $f_{291} = \pm 0.02$ .

Table 6.1 Comparison of the calculated  $\theta_D$  and  $f_{291}$  for the various aluminium intermetallic compounds studied

On closer investigation it appears that the factor that determines the  $\theta_D$  value was the Al-Fe shortest bond, which was a common feature of all the known Fe centred Al polyhedra. However, it appears that as the shortest Al-Fe bond length increases the Al-Fe bonds of the remaining atoms play a more significant role in determining the  $\theta_D$  value.

The quadrupole interaction did not vary with temperature for all the aluminium intermetallic compounds studied. This indicates that the oxidation state of the iron nucleus could either be Fe(II) or Fe(III), but by taking the value of the isomer shift into

account a speculative assessment can be made regarding the oxidation state as being Fe(II).

Predominant asymmetry was observed within the spectra of  $Al_xFe$ , and to a lesser degree,  $Al_3Fe$ . This was attributed to a combination of physical characteristics: preferred growth directions, and the presence of internal mechanical stress fields. However, it was not possible to speculate which was the major contributing factor, but due to the uni-directional solidification mechanism of the Bridgman furnace it would appear that preferred growth direction would be the most probable cause.

Line broadening was observed within all the Mössbauer spectra. This would indicate that a distribution of Fe environments exist within the different unit cells. The different aluminium intermetallic compounds have internal defects, which would contribute to the observed line broadening, and thus the distribution of Fe sites.

## 6.2 DC-CAST ALLOYS

The parent alloy had a composition that was consistent with a 1xxx series alloy. Two thin slices were sectioned from the central region of the alloy, samples *A* and *B*. Transmission Mössbauer spectroscopy was then performed on absorbers prepared from alloy, with the intermetallic compounds embedded within the matrix, and extracted specimens.

Mössbauer spectroscopy has been used successfully as a tool to identify and quantify the aluminium intermetallic combination. However, this method must be used speculatively as it has been shown that some aluminium intermetallic compounds show very similar hyperfine parameters and lattice dynamics.

Alloy Sample	Intermetallic Combination	Relative Proportions, %
A	$\text{Al}_3\text{Fe} + \text{Al}_6\text{Fe}$	$50:50 \pm 5$
B	$\text{Al}_6\text{Fe} + \alpha_c\text{-AlFeSi}$	$30:70 \pm 5$

Table 5.15 The aluminium intermetallic compound combination, and their relative proportions, obtained by using transmission Mössbauer spectroscopy on alloy samples *A* and *B*.

Another alloy sample of *B* was prepared, from the same parent DC-cast ingot. Initially, the surface was mechanically polished, which was done by using conventional techniques. SEM and EDS measurements indicated that the iron and silicon was distributed along the grain boundaries of the alloy. This was consistent with the known solidification mechanisms that occur for aluminium rich Al-Fe-Si alloys.

The CEMS technique was then applied to the surface of the alloy sample *B*. The deconvolution of the spectrum showed the presence of another dominant iron containing compound, which was not present in the transmission spectra, along with the known aluminium intermetallic compounds.

Interpreting the Mössbauer parameters for this compound indicated that it was highly amorphous, but the physical characteristics of this compound were uncertain. The spectrum had a low signal to noise ratio, which was due to the low iron content of the alloy and the iron distribution within the alloy sample.

The isomer shift of the compound did not correspond to any of the known aluminium intermetallic compounds or Fe substituted  $\text{Al}_2\text{O}_3$  variations. However, the isomer shift, and the very general characteristics of this particular component of the Mössbauer spectrum, matched those of very fine super-paramagnetic iron grains.

SAAES and SAXPS were performed on regions of the alloy sample surface where the iron content was the highest, i.e. a node of several grain boundaries. These techniques indicated that the oxide layer had grown across the grain boundaries, after the impurity carbon had been  $\text{Ar}^+$  cleaned off. Iron or silicon was not present in the SAAES spectra, which was not surprising since escape depth of the Auger electrons is limited.

However, iron was also not present in the SAXPS spectra. This was not surprising since the depth sensitivity of the SAXPS and SAAES techniques were comparable.

The surface of the alloy sample *B* was electro-etched in KI solution. This process was devised to etch the oxide layer and the aluminium matrix, and thus leaving the aluminium intermetallic compounds standing proud of the surface.

When the etching process was performed for 15 minutes the surface morphology of the alloy sample had changed dramatically. The resultant CEMS spectrum had also changed dramatically. The component attributed to the unknown compound had been removed, and thus indicated that it had been an iron rich region between the intermetallic compounds and the oxide layer. The remaining components of the spectrum were de-convoluted according to the known aluminium intermetallic compounds that were present,  $\text{Al}_6\text{Fe}$  and  $\alpha_c\text{-AlFeSi}$ . The calculated relative proportions of the two intermetallic compounds were  $85 \pm 5\%$   $\text{Al}_6\text{Fe}$  and  $15 \pm 5\%$   $\alpha_c\text{-AlFeSi}$ . This was contrary to the transmission Mössbauer experiments performed upon the extracted aluminium intermetallic compounds, which produced a relative proportion of  $30 \pm 5\%$   $\text{Al}_6\text{Fe}$  and  $70 \pm 5\%$   $\alpha_c\text{-AlFeSi}$ . This reversal in the calculated relative proportions can be explained by the different aluminium intermetallic compound morphology.

Since the surface of the intermetallic particles, in this study, was found to consist of predominately  $\text{Al}_6\text{Fe}$  selective oxidation took place, which was responsible for the formation of amorphous super-paramagnetic grains of  $\alpha$ -iron.

The SAAES spectra of the surface of the alloy sample *B* indicated that a fresh  $\text{Al}_2\text{O}_3$  oxide layer had grown over the exposed aluminium intermetallic compounds.

However, the SAXPS spectra indicated iron and manganese existed in their metallic forms.

## CHAPTER 7

## POSTGRADUATE STUDY

## 7.1 COURSES AND CONFERENCES

Date	Course / Conference	Location	Duration
1995 - 1998 <sup>1</sup>	Materials Research Institute seminars	Sheffield Hallam University	1 hour weekly
1995	Royal Society of Chemistry, Mössbauer Discussion Group	Nottingham University	2 days
1995	Phase Transitions and Monte- Carlo Methods in Material Modelling	Sheffield Hallam University	8 × 2 hour
1995	Mössbauer Spectroscopy course	Sheffield Hallam University	12 × 2 hour
1996	Electron Microscopy and X-ray Techniques, part 1	Sheffield Hallam University	8 × 2 hour
1996	Electron Microscopy and X-ray Techniques, part 2	Sheffield Hallam University	8 × 2 hour
1996 <sup>1</sup>	Royal Society of Chemistry, Mössbauer Discussion Group	Nottingham University	2 days
1997 <sup>2</sup>	Materials Research Institute Open Day	Sheffield Hallam University	1 day
1997	4 <sup>th</sup> Decennial International Conference on Solidification Processing	Sheffield University	4 days
1997 <sup>3</sup>	Royal Society of Chemistry, Mössbauer Discussion Group	Nottingham University	2 days
1998 <sup>4</sup>	Royal Society of Chemistry, Mössbauer Discussion Group	Nottingham University	2 days

1. A paper titled "*Variable Temperature  $^{57}\text{Fe}$  Mössbauer Spectroscopy Studies of Various Al-Fe Intermetallic Compounds which Form in Commercially Pure Al Alloys*", was presented at this meeting.
2. A paper titled " *$^{57}\text{Fe}$  Mössbauer Spectroscopy Studies of Direct Chill Cast Commercially Pure Al Alloys*", was presented at this meeting by both poster and oral methods.
3. A paper titled " *$^{57}\text{Fe}$  Mössbauer Spectroscopy Studies of Direct Chill Cast Commercially Pure Al Alloys*", was presented at this meeting.
4. A paper titled "*The Characterisation of Aluminium Intermetallic Phases Within Industrially Cast Aluminium*", was presented at this meeting.

## 7.2 PUBLICATIONS

S. D. Forder, J. S. Brooks, A. Reeder, and P. V. Evans, *Hyperfine Interactions* **116** (1998) 209-214.

S. D. Forder, J. S. Brooks, A. Reeder, and P. V. Evans, *Scripta Mat.*, 40(1) (1999) 45-48

A. Reeder, S. D. Forder, J. S. Brooks, and P. V. Evans, *Hyperfine Interactions* submitted 1999.

## LIST OF ABBREVAITIONS

AES – Auger Electron Spectroscopy  
ASEM – Analytical Scanning Electron Microscope  
CEM – Conversion Electron Mössbauer  
CEMS – Conversion Electron Mössbauer Spectroscopy  
CXMS – Conversion X-ray Mössbauer Spectroscopy  
DC – Direct Chill  
EDS – Energy Dispersive Spectroscopy  
EXAFS – Extended X-ray Absorption Fine Spectra  
GDOES – Glow Discharge Optical Emission Spectroscopy  
SAAES – Small Area Auger Electron Spectroscopy  
SAXPS – Small Area X-ray Photoelectron Spectroscopy  
“SIBUT” – Aluminium Intermetallic Extraction Method  
SIMS – Secondary Ion Mass Spectroscopy  
SEM – Scanning Electron Microscopy  
TEM – Transmission Electron Microscopy  
WDS – Wavelength Dispersive Spectroscopy  
XPS – X-ray Photoelectron Microscopy  
XRD – X-ray Diffraction

# The characterization of the iron content of industrially cast aluminium

S.D. Forder<sup>a</sup>, J.S. Brooks<sup>a</sup>, A. Reeder<sup>a</sup> and P.V. Evans<sup>b</sup>

<sup>a</sup> *Materials Research Institute, Sheffield Hallam University, Sheffield S1 1WB, UK*

<sup>b</sup> *Alcan International Limited, Banbury Laboratory, Southam Road, Banbury OX16 7SP, UK*

Received 4 May 1998

Pure intermetallic phases  $\text{Al}_{13}\text{Fe}_4$ ,  $\text{Al}_6\text{Fe}$ ,  $\text{Al}_m\text{Fe}$  and  $\text{Al}_x\text{Fe}$  have been extracted from Bridgman grown model aluminium–iron binary alloys by dissolving the aluminium matrix in butanol. Each phase has a distinct Mössbauer spectrum and variable temperature  $^{57}\text{Fe}$  Mössbauer studies have enabled the Debye temperature  $\theta_D$  of each phase to be determined. Hence, the variation of the recoil-free fraction  $f$  with temperature is determined for each phase. From this information it is possible to measure the proportion of each phase, either when the phases are extracted or in situ in aluminium. The results obtained can be used in the characterisation of industrially cast aluminium.

## 1. Introduction

A widely used technique for casting industrial aluminium alloy ingots is direct-chill (D.C.) casting. For commercial purity alloys, which contain small amounts of iron and silicon, intermetallic phases are formed inter-dendritically from the final liquid to solidify, and comprise typically 1% of the microstructure. During the casting the solidification rate varies substantially with position in the ingot [1] so various phases can form, ranging from the equilibrium phase  $\text{Al}_{13}\text{Fe}_4$ , to increasingly metastable phases, such as  $\text{Al}_6\text{Fe}$ ,  $\text{Al}_x\text{Fe}$  and  $\text{Al}_m\text{Fe}$  or  $\alpha\text{-AlFeSi}$ , as the solidification rate increases. The ease of processing and final gauge properties can be influenced by the phase or phases that actually form.

$^{57}\text{Fe}$  Mössbauer spectroscopy provides a suitable technique to identify the different phases present in an alloy, since each phase has a characteristic spectrum. Several authors [2–4] have reported Mössbauer data on Al–Fe phases in aluminium. In this work the phases of interest have been extracted from super-purity based, Bridgman grown model aluminium–iron binary alloys by dissolving the aluminium matrix in butanol [5]. This provides the pure phase and thus increases the proportion of iron giving an improved signal to noise ratio for Mössbauer spectroscopy.

Using phases extracted in this way, variable temperature  $^{57}\text{Fe}$  Mössbauer studies have been carried out on  $\text{Al}_{13}\text{Fe}_4$ ,  $\text{Al}_m\text{Fe}$ ,  $\text{Al}_x\text{Fe}$  and  $\text{Al}_6\text{Fe}$ . The variation with temperature of the absorption area was obtained. This enabled the Debye temperature  $\theta_D$

of each phase to be determined. It was then possible, using the correct recoil-free fraction for each phase, to determine the proportion of  $\text{Al}_{13}\text{Fe}_4$  and  $\text{Al}_6\text{Fe}$  in an extracted sample containing both phases, and in the as cast rod of the aluminium containing both phases in situ.

## 2. Experimental

A binary Al-0.5 wt.% Fe alloy was prepared from 99.999 wt% aluminium, and equivalent purity Al-Fe master alloy, and cast to appropriate dimensions to be melted in a Bridgman furnace [6]. After equilibration, each sample was withdrawn from the furnace at a velocity appropriate for the solidification of each of the phases  $\text{Al}_{13}\text{Fe}_4$ ,  $\text{Al}_6\text{Fe}$  and  $\text{Al}_x\text{Fe}$ .  $\text{Al}_m\text{Fe}$  was prepared from an alloy also containing 0.1 wt.% Si. Butanol dissolution [5] was used to extract the phases from samples cut from the central portion of the resolidified samples. This technique has been described in detail previously, and it has been shown that the identity of the phases is confirmed by XRD [6].

Each extracted crystalline phase was ground and mixed with iron-free graphite powder to form an absorber disc with a Mössbauer thickness  $t < 1.0$  [7].  $^{57}\text{Fe}$  Mössbauer measurements were made using a constant-acceleration spectrometer with a 25 mCi  $^{57}\text{Co}$  source in a rhodium matrix. At room temperature the source had a full width at half-height,  $\Gamma$ , of  $0.22 \text{ mm s}^{-1}$  and a recoil-free fraction  $f$  of 0.75. This gave a single emission line with an isomer shift  $\delta$  of  $0.106 \text{ mm s}^{-1}$  with respect to an  $\alpha$ -iron sextet. All spectra in this paper are relative to rhodium. The data were fitted with Lorentzian functions by a nonlinear least-squares fitting program. The detection and low temperature systems have been described previously [6].

Variable temperature studies were carried out on the individual phases between 15–300 K. Then an absorber was prepared containing phases that had been extracted by butanol dissolution from a section of Bridgman sample, grown under conditions promoting the formation of a mixture of binary phases. Mössbauer spectra were obtained at 80 K and 250 K. Finally, Mössbauer spectra were obtained for the same mixture of phases in situ in the Bridgman sample at 100 K and 250 K.

## 3. Results and discussion

Each phase can be seen to have a distinct Mössbauer spectrum, figure 1. The spectra have been fitted with consideration of the crystal structure of each phase [8–11] as shown in table 1. It should be noted that  $\text{Al}_{13}\text{Fe}_4$  has been fitted considering the five iron sites that exist within the structure. In four sites the iron atoms have very similar asymmetric environments and are fitted as the doublet with the larger quadrupole splitting. The fifth iron atom is in a different more symmetric environment, and the corresponding doublet has a smaller quadrupole splitting. This agrees with the fitting regime of Chittaranjan [11] and is more satisfactory than a fit of three single lines adopted by some authors [12].

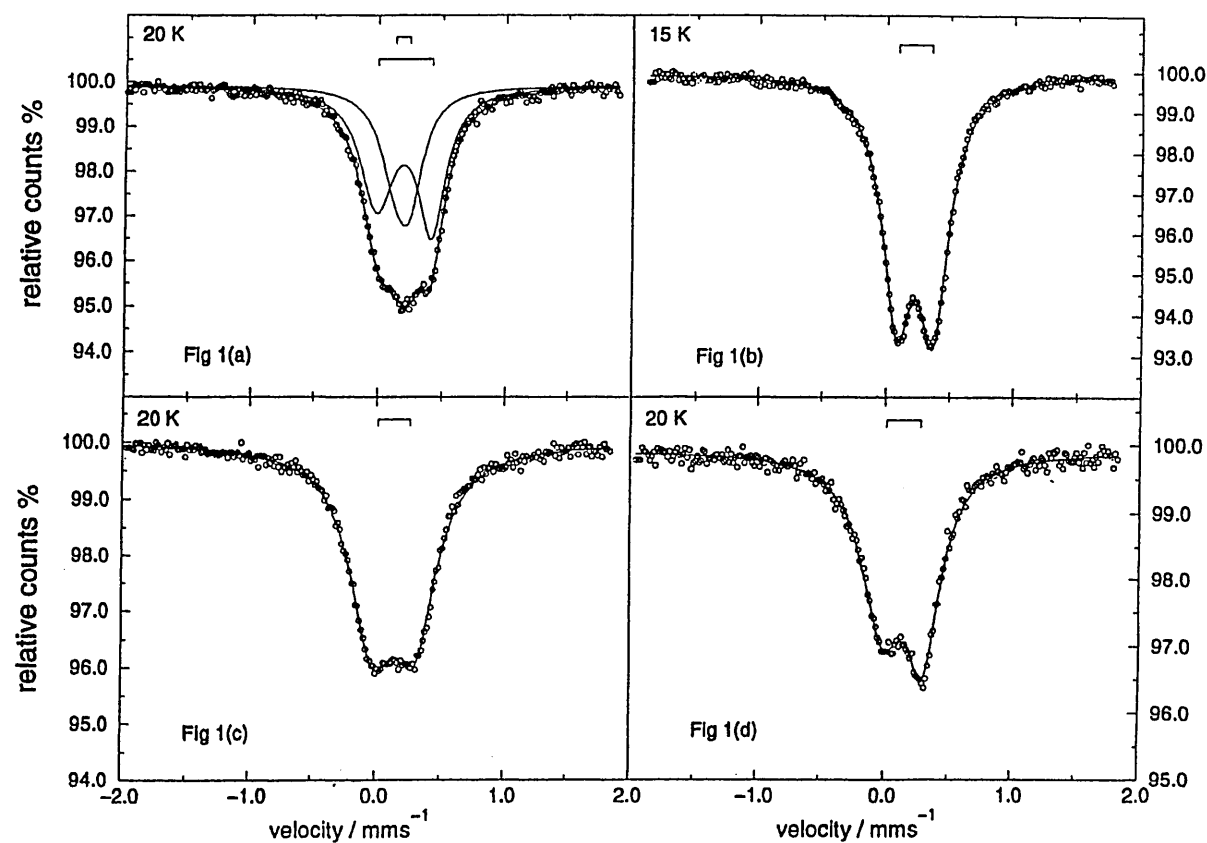


Figure 1.  $^{57}\text{Fe}$  Mössbauer spectra of (a)  $\text{Al}_{13}\text{Fe}_4$ ; (b)  $\text{Al}_6\text{Fe}$ ; (c)  $\text{Al}_m\text{Fe}$ ; and (d)  $\text{Al}_x\text{Fe}$ .

Table 1

The Debye temperature, recoil-free fraction and crystal structure for Al-Fe intermetallic phases.

Phase	Debye temperature $\theta_D$ (K)	Recoil-free fraction $f_{291}$ ( $\pm 0.01$ )	Crystal structure
$\text{Al}_{13}\text{Fe}_4$	$419 \pm 5$	0.79	monoclinic [11]
$\text{Al}_m\text{Fe}$	$373 \pm 4$	0.74	body-centred tetragonal [8]
$\text{Al}_x\text{Fe}$	$347 \pm 3$	0.71	monoclinic [9]
$\text{Al}_6\text{Fe}$	$327 \pm 5$	0.68	orthorhombic [10]

Variable temperature Mössbauer studies allow the vibration properties of the Mössbauer atom to be studied and enable the determination of the Debye temperature  $\theta_D$  and the recoil-free fraction  $f$ . These parameters reflect how tightly the  $^{57}\text{Fe}$  Mössbauer atom is held in the structure. A variable-temperature absorption area fitting routine, based on a monatomic cubic lattice, uses a nonlinear least squares routine used upon a modified version of the Levenburg-Marquardt algorithm [13] to obtain best fit of the theoretical function to a set of experimental data values for area and temperature [14]. For thin Mössbauer absorbers ( $t < 1$ ), the absorption line area  $A(T)$  is proportional to the recoil-free fraction [7].

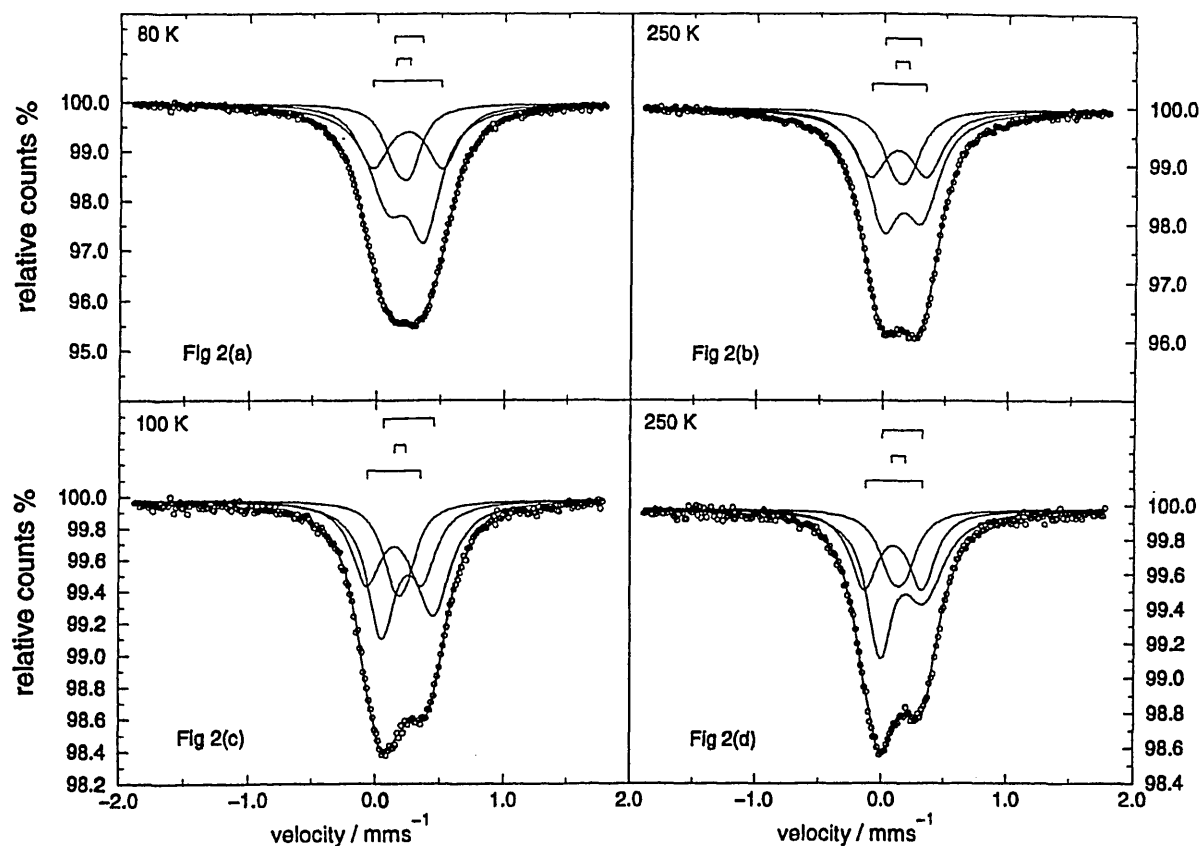


Figure 2.  $^{57}\text{Fe}$  Mössbauer spectra of extracted  $\text{Al}_{13}\text{Fe}_4$  and  $\text{Al}_6\text{Fe}$  at (a) 80 K and (b) 250 K, and the same phases in situ in aluminium at (c) 100 K and (d) 250 K.

The variation of the absorption area with temperature was analysed according to the Debye model. The values for  $\theta_D$  and  $f$  at 291 K, obtained using software that uses the full Debye integral, are presented in table 1.

To demonstrate the benefit of the variable temperature studies, in this work it has been possible to calculate the relative amount of each phase, both in the extracted phases and in situ. At any particular temperature  $T$ , the absorption area  $A(T)$  and the recoilless fraction  $f(T)$  for each phase are known. Therefore the amount of Fe-57,  $X_A$  in phase  $A$ , can be obtained from the relationship  $A(T) \propto X_A f_A(T)$ . Then the relative proportions of the phases can be obtained from  $X_A = A/f_A$  and  $X_B = B/f_B$  giving the ratio  $X_A/(X_A + X_B)$ .

The fitted spectra of data obtained at 80 K and 250 K for phases extracted from a Bridgman sample grown under conditions promoting the formation of a mixture of  $\text{Al}_{13}\text{Fe}_4$  and  $\text{Al}_6\text{Fe}$  are plotted in figures 2(a) and (b). The appropriate isomer shift and quadrupole splitting values for each phase at each temperature were used and then the area fraction arising from each phase was adjusted until the best fit was obtained. Then, using the known recoil-free fraction for each phase at each temperature, the proportion of each phase was calculated, shown in table 2. This ratio represents the relative proportion of Fe-57 in each phase. Further calculation, taking the chemical formulae of the phases into account, gives the relative mass densities of each phase

Table 2  
Relative proportions of Al<sub>13</sub>Fe<sub>4</sub> to Al<sub>6</sub>Fe for extracted phases and phases in situ.

Absorber	Temperature (K)	Ratio ( $\pm 0.05$ ) $X_A/(X_A + X_B)$	Relative mass densities Al <sub>13</sub> Fe <sub>4</sub> to Al <sub>6</sub> Fe
Extracted phases,	80	0.46	45 : 55
Al <sub>13</sub> Fe <sub>4</sub> + Al <sub>6</sub> Fe	250	0.46	45 : 55
Al <sub>13</sub> Fe <sub>4</sub> + Al <sub>6</sub> Fe in situ	100	0.50	40 : 60
	250	0.46	45 : 55

in the sample, table 2. Figures 2(c) and (d) show the fitted spectra of data obtained at 100 K and 250 K for the intermetallic phases in situ in the Bridgman sample. The same procedure was used to determine the relative mass densities of the phases in this sample and the results are presented in table 2. The results are consistent, with the same proportion of each phase being detected in the extracted phases and in situ in the aluminium. The asymmetry of the Al<sub>6</sub>Fe doublet is due to texture within the ingot [6]. It has not been possible to resolve the contribution to the spectra due to Al(Fe) solid solution because of the low solubility limit of 0.04 wt.%. This would give rise to a singlet with an isomer shift of 0.31 mm s<sup>-1</sup>.

#### 4. Conclusions

- (1) The results demonstrate that Mössbauer spectroscopy can be used to identify the different intermetallic phases formed in aluminium alloys during D.C. casting.
- (2) Variable temperature studies enable the Debye temperature  $\theta_D$  to be determined for each phase and hence the variation of the recoil-free fraction with temperature. This enables the relative proportion of each phase to be determined.

#### Acknowledgement

The authors acknowledge the financial support of Alcan International.

#### References

- [1] S. Nagy, L. Murgas, Z. Homonnay and A. Vertes, *Materials Science Forum* 13/14 (1987) 313.
- [2] S. Nasu, U. Gonser and R.S. Preston, *J. Phys. C* 1.41 (1980) 385.
- [3] R.S. Preston and R. Gerlach, *Phys. Rev. B* 3(5) (1971) 1519.
- [4] C.A. Stickels and R.H. Bush, *Met. Trans.* 2 (1971) 2031.
- [5] C.J. Simensen, P. Fartum and A. Andersen, *Fresenius Z. Anal. Chem.* 319(3) (1984) 286.
- [6] S.D. Forder, J.S. Brooks and P.V. Evans, *Scripta Mat.* 35(10) (1996) 1167.
- [7] J.M. Williams and J.S. Brooks, *Nucl. Instrum. Methods* 128 (1975) 363.
- [8] P. Skjerpe, *Acta Cryst. B* 44 (1980) 480.
- [9] R.M.K. Young and T.W. Clyne, *Scripta Mat.* 15 (1981) 1211.
- [10] L.K. Walford, *Acta Cryst.* 18 (1965) 287.

- [11] C.M. Chittaranjan, V. Kurmar, B. Viswanathan and K.P. Gopinathan, *Solid State Comm.* 79(1) (1991) 69.
- [12] L. Murgas, Z. Homonnay, S. Nagy and A. Vertes, *Metallurgical Trans. A* 19 (1988) 259.
- [13] J.J. More, in: *Lecture Notes in Mathematics* 630 (Springer, New York, 1978) p. 105.
- [14] J.S. Brooks, G.L. Williams and D.W. Allen, *Physics Chem. Glasses* 33(5) (1992) 171.



## <sup>57</sup>Fe MÖSSBAUER SPECTROSCOPY OF INTERMETALLIC PHASES IN D.C. CAST ALUMINIUM

S.D. Forder<sup>1</sup>, J.S. Brooks<sup>1</sup>, A. Reeder<sup>1</sup> and P.V. Evans<sup>2</sup>

<sup>1</sup>Materials Research Institute, Sheffield Hallam University, Sheffield S1 1WB, UK

<sup>2</sup>Alcan International Limited, Banbury Laboratory, Southam Road, Banbury, OX16 7SP, UK

(Received July 7, 1998)

(Accepted in revised form September 16, 1998)

### Introduction

Direct-chill (D.C.) casting is a widely used technique for casting industrial aluminium alloy ingots. Commercial purity alloys contain small amounts of iron and silicon. During casting, intermetallic phases are formed inter-dendritically from the final liquid to solidify. Since the solidification rate varies substantially with position in the ingot [1] various phases can form, ranging from the equilibrium phase  $\text{Al}_{13}\text{Fe}_4$ , to increasingly metastable phases, such as  $\text{Al}_6\text{Fe}$ ,  $\text{Al}_x\text{Fe}$ ,  $\text{Al}_m\text{Fe}$  or  $\alpha\text{-AlFeSi}$ , as the solidification rate increases. The binary phases likely to form under different solidification rates are summarised in Table 1. The phases formed may influence the ease of processing and the final gauge properties of the material.

<sup>57</sup>Fe Mössbauer spectroscopy has been used previously to identify the intermetallic phases in situ in aluminium from Bridgman grown model alloys [5]. Also variable temperature studies have been carried out [6] on the phases extracted from the alloys by butanol dissolution [7]. The work reported in this paper demonstrates how the Mössbauer data obtained from the previous studies can now be used to identify and quantify the proportion of different phases formed in ingots prepared by direct-chill casting and subsequent heat treatments.

### Experimental

The alloy studied was based on super-purity aluminium, with additions of 0.3% Fe, 0.1% Si and the samples (A and B) were taken from a section of an ingot which had been laboratory D.C. cast at a casting speed of 70 mm/min. These were then heat treated isothermally at 500°C for four hours and water quenched. Thin slices were sectioned from the samples using a diamond wheel and ground on silicon carbide abrasive paper to obtain a finish of 600 grit. Mössbauer spectroscopy was performed on two such slices, data being obtained for each slice at 150 K and 250 K, giving the Mössbauer spectra of the phases in situ. The phases were extracted from the two samples (A and B) by butanol dissolution [7] and Mössbauer spectroscopy was performed on the extracted phases. The Mössbauer spectrometer and the detection and low temperature systems have been described previously [5,6].

TABLE 1  
The Binary Al-Fe Phases That May Form at Different Solidification Rates.

Intermetallic phase	Solidification rate, K/s	Author
Al <sub>m</sub> Fe/Al <sub>9</sub> Fe <sub>2</sub>	More than 10	[2] [3]
Al <sub>6</sub> Fe	1-10	[4]
Al <sub>x</sub> Fe	0.5-5	[2]
Al <sub>13</sub> Fe <sub>4</sub>	Less than 1	[2] [3]

### Results

XRD results for the extracted phases indicate that sample A contains two different binary phases, whereas sample B contained a ternary and a binary phase. The Mössbauer spectra were fitted using the following procedure to determine which combinations of phases are present in the samples. Initially the spectra were fitted using fixed values of the parameters obtained at the appropriate temperatures during variable temperature Mössbauer studies of the individual extracted phases [6]. The fit for each individual phase is appropriate for the crystal structure of the phase. The absorption area due to each phase was free to vary, and the best initial fit of the Mössbauer spectrum obtained at 250K for the phases extracted from Sample A is indicated by the lowest  $\chi^2$ , Table 2.

Comparison of the fits suggests that sample A contains Al<sub>13</sub>Fe<sub>4</sub> and Al<sub>6</sub>Fe. This broadly agrees with the XRD results on extracted phases, which showed strong reflections characteristic of both Al<sub>13</sub>Fe<sub>4</sub> and Al<sub>6</sub>Fe [8]. The fits were then refined by allowing the value of each of the parameters  $\delta$ ,  $\Delta/2$  and  $\Gamma/2$  to vary independently until the lowest possible  $\chi^2$  was obtained, Table 2.

TABLE 2  
Mössbauer Parameters at 250 K Used to Test Different Possible Combinations of Binary Phases in the Phases Extracted from Sample A.  $\infty$  Indicates That No Meaningful Fit Was Obtained.  $\delta$  is Relative to  $\alpha$ -iron at 293 K.

Combination of Phases	Fixed Starting Parameters			$\chi^2$	Released Final parameters			$\chi^2$
	$\delta$ mm/s	$\Delta/2$ mm/s	$\Gamma/2$ mm/s		$\delta$ mm/s $\pm 0.02$	$\Delta/2$ mm/s $\pm 0.02$	$\Gamma/2$ mm/s $\pm 0.02$	
Al <sub>13</sub> Fe <sub>4</sub>	0.22	0.22	0.16, 0.13	1.383	0.23	0.23	0.16, 0.16	0.436
	0.23	0.01	0.14, 0.16		0.25	0.01	0.15, 0.18	
Al <sub>6</sub> Fe	0.25	0.15	0.15, 0.14		0.26	0.15	0.14, 0.15	
Al <sub>13</sub> Fe <sub>4</sub>	0.22	0.22	0.16, 0.13	$\infty$				
	0.23	0.01	0.14, 0.16					
Al <sub>m</sub> Fe	0.12	0.16	0.22, 0.22					
Al <sub>13</sub> Fe <sub>4</sub>	0.22	0.22	0.16, 0.13	3.529	0.25	0.23	0.18, 0.15	0.442
	0.23	0.01	0.14, 0.16		0.24	0.01	0.11, 0.13	
Al <sub>x</sub> Fe	0.22	0.15	0.22, 0.20		0.23	0.16	0.14, 0.14	
Al <sub>6</sub> Fe	0.25	0.15	0.15, 0.14	2.222	0.29	0.15	0.16, 0.16	0.497
Al <sub>m</sub> Fe	0.12	0.16	0.22, 0.22		0.01	0.16	0.16, 0.16	
Al <sub>6</sub> Fe	0.25	0.15	0.15, 0.14	2.084	0.29	0.15	0.15, 0.16	0.459
Al <sub>x</sub> Fe	0.22	0.15	0.22, 0.20		0.01	0.15	0.16, 0.15	
Al <sub>m</sub> Fe	0.12	0.16	0.22, 0.22	$\infty$				
Al <sub>x</sub> Fe	0.22	0.15	0.22, 0.20					

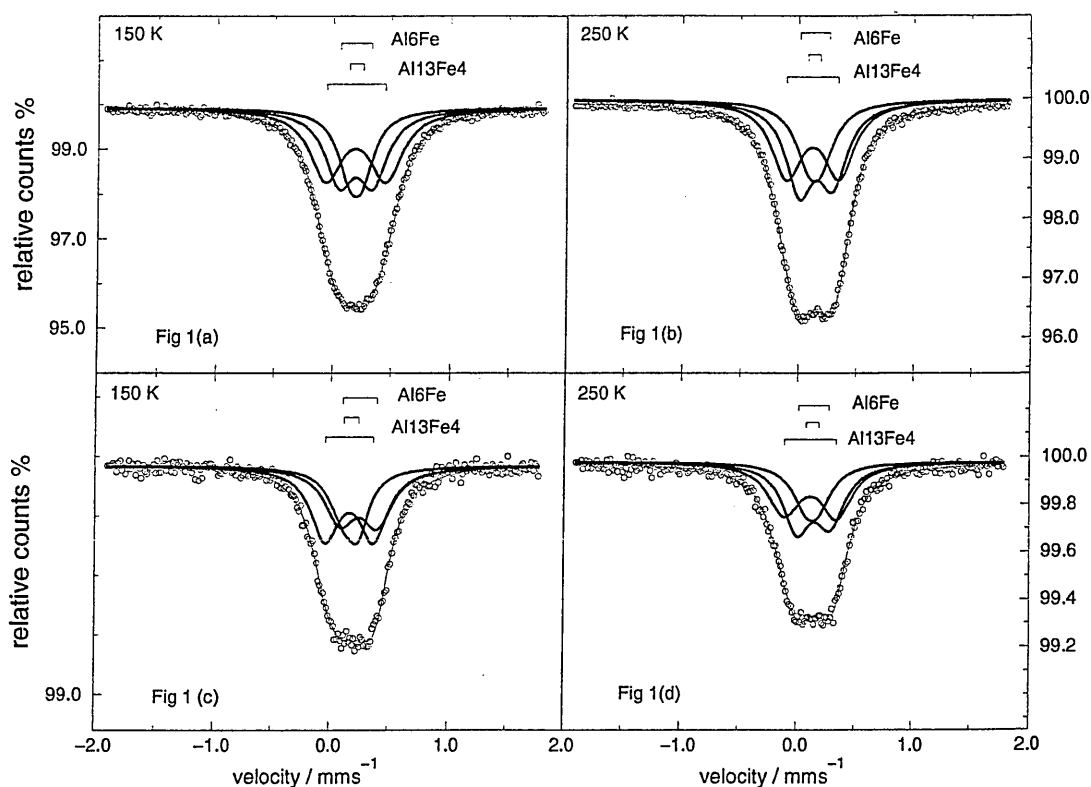


Figure 1.  $^{57}\text{Fe}$  Mössbauer spectra of extracted phases recorded at (a) 150 K and (b) 250 K, and the same phases in situ at (c) 150 K and (d) 250 K.

It can be seen that the adjustment required to obtain the final parameters lies within the normal experimental fitting error of  $\pm .02 \text{ mm s}^{-1}$ , for only the  $\text{Al}_{13}\text{Fe}_4$  and  $\text{Al}_6\text{Fe}$  combination. The final parameters achieved for other combinations of phases have required a greater modification of some of the parameter values so that the final values are no longer representative of the phases being tested.

The same procedure was used for all four sets of data. The final fits for the data for the sample containing the phases in situ were derived by the fitting routine starting with the parameters for the combination of extracted phases [6], and thus preventing unrealistic linewidths and relative areas from being generated by the fitting program.

Figure 1 shows the best fits for the extracted phases and the phases in situ in aluminium for Sample A. Mössbauer spectra were obtained for each sample at 100 K and 250 K. These experiments provide a check of the analysis used. If the fitting procedure is correct, then the quantitative information derived from the spectra should agree for the extracted phases and phases in situ.

Using the absorption areas for the extracted phases and the phases in situ with the appropriate recoil free fraction [6], the ratio of the relative mass densities of the phases in Sample A is estimated to be 53  $\text{Al}_{13}\text{Fe}_4$ : 47  $\text{Al}_6\text{Fe}$  ( $\pm 5\%$ ). The results for the four sets of data are given in Table 3. The results of the experiments are consistent as expected.

Equivalent experiments were carried out on sample B with the same fitting procedure used as for sample A. The results indicate that sample B contains  $\alpha\text{-AlFeSi}$  and  $\text{Al}_6\text{Fe}$ , again in agreement with the XRD measurement. Continuing with the same analysis to determine the relative mass densities of the phases extracted from sample B, it was found that B contained 70:30 ( $\pm 5\%$ )  $\alpha\text{-AlFeSi}$ :  $\text{Al}_6\text{Fe}$ . Due to the low iron concentration the statistical quality of the Mössbauer data was poor for the sample B with the phases in situ, and although  $\alpha\text{-AlFeSi}$  and  $\text{Al}_6\text{Fe}$  gave the best fit, the data did not allow a determination of the relative proportion of the phases in situ.

TABLE 3  
Relative Mass Densities of the  $Al_{13}Fe_4$  and  $Al_6Fe$  for the Extracted Phases and Phases In Situ.

Absorber	Temperature/K	Relative Mass Densities, $Al_{13}Fe_4$ : $Al_6Fe$
Extracted phases	150	52:48
$Al_{13}Fe_4$ and $Al_6Fe$	250	53:47
Phases in situ in aluminium	150	54:46
$Al_{13}Fe_4$ and $Al_6Fe$	250	54:46

A comparison of the results for the two samples A and B shows that different combinations of intermetallic phases have formed in samples taken from a D.C. cast aluminium ingot and then heat treated. The phases formed are sensitive to the composition of the alloy and the local conditions during solidification and subsequent heat treatments.

### Conclusion

It is possible to use  $^{57}Fe$  Mössbauer Spectroscopy to identify the intermetallic phases and to estimate the relative proportion of phases within D.C. cast aluminium ingots.

### Acknowledgment

The authors acknowledge the financial support of Alcan International.

### References

1. S. Nagy, L. Murgas, Z. Homonnay, and A. Vertes, *Mater. Sci. Forum.* 13/14, 313 (1987).
2. R. M. K. Young and T. W. Clyne, *Scripta Metall.* 15, 1211 (1981).
3. I. Mikki, H. Kousage, and K. Nagahama, *J. Jpn. Inst. L. Met.* 25, 1 (1975).
4. P. Skjerpe, *Acta Cryst.* B44, 480 (1988).
5. S. D. Forder, J. S. Brooks, and P. V. Evans, *Scripta Mater.* 35, 1167 (1996).
6. S. D. Forder, J. S. Brooks, A. Reeder, and P. V. Evans, in *ISIAME '96, Hyperfine Interactions*, in press (1998).
7. C. J. Simensen, P. Fartnum, and A. Andersen, *Fresenius Z. Anal. Chem.* 319, 286 (1984).
8. P. V. Evans, J. Worth, A. Bosland, and S. C. Flood, in *Proceedings of the 4th Decennial International Conference on Solidification Processing*, pp. 531–535 (1997).

# The characterisation of iron-containing intermetallic phases within industrially cast aluminium

S.D. Forder<sup>a</sup>, A. Reeder<sup>a</sup>, J.S. Brooks<sup>b</sup>, M. Rignall<sup>a</sup> and P.V. Evans<sup>c</sup>

<sup>a</sup> *Materials Research Institute, Sheffield Hallam University, Sheffield S1 1WB, UK*

<sup>b</sup> *University of Wolverhampton, Wulfruna Street, Wolverhampton WV5 7DQ, UK*

<sup>c</sup> *Alcan International Limited, Banbury Laboratory, Southam Road, Banbury OX16 7SP, UK*

<sup>57</sup>Fe conversion electron Mössbauer spectroscopy has been used to investigate the intermetallic phases near the surface of a D.C. cast aluminium ingot. The CEMS data is used with SAAES (selected area Auger electron spectroscopy) and SAXPS (selected area X-ray photoelectron spectroscopy) data to propose a model of the surface region above the grain boundaries.

## 1. Introduction

Previous studies have shown that Mössbauer spectroscopy can be used to identify the intermetallic phases that form within aluminium [1,2]. The phases that form are dependent on the alloy composition and the solidification rate which can vary across the ingot. A higher solidification rate near the surface tends to promote the formation of metastable phases. The phases that form influence the properties of the material. Variable temperature Mössbauer studies have determined the Debye temperature  $\theta_D$  of different phases. This permits the relative proportion of different phases to be determined within a section of an ingot [1,2].

Transmission Mössbauer spectroscopy has been used to identify the intermetallic phases extracted from a section of a direct chill (D.C.) cast ingot. The phases were extracted by butanol dissolution [3], and the relative phase proportion was determined [2]. The study has been extended by using conversion electron Mössbauer spectroscopy CEMS to investigate the phase ratio within the first 60 nm of the surface of a sample taken from the same region of the ingot. These results are complemented by SAAES (selected area Auger electron spectroscopy) and SAXPS (selected area X-ray photoelectron spectroscopy).

## 2. Experimental procedure

The alloy studied was based on super-purity aluminium, with additions of 0.3% Fe and 0.1% Si. The sample was taken from a section of an ingot that had been laboratory D.C. cast at a casting speed of 70 mm/min. The sample was then heated isothermally

at 500°C for four hours and water quenched [2]. Thin slices were sectioned from the sample using a diamond wheel and ground on silicon carbide paper to obtain a finish of 600 grit.  $^{57}\text{Fe}$  Mössbauer measurements were made using a constant-acceleration spectrometer with a 25 mCi  $^{57}\text{Co}$  source in a rhodium matrix. At room temperature the source had a full width at half-height,  $\Gamma$ , of  $0.22 \text{ mm s}^{-1}$  and a recoil-free fraction  $f$  of 0.75. This gave a single emission line with an isomer shift  $\delta$  of  $0.106 \text{ mm s}^{-1}$  with respect to an  $\alpha$ -iron sextet. The Mössbauer spectra and data presented in this paper are relative to rhodium, and were fitted by a least squares Lorentzian fitting routine using a Silicon Graphics Indy workstation.

The detection and low temperature systems used for the transmission Mössbauer measurements on the phases extracted from the sample have been described previously [4]. The CEMS detector was a single anode wire, gas-flow proportional counter with He/5% CH<sub>4</sub> [5]. A CEMS spectrum was obtained of the sample surface. Then the surface of the sample was given a 15 min, 30 V KI electro-etch and a CEMS spectrum was obtained of the etched surface.

A Kratos Axis 165 spectrometer was used with an Mg(K $_{\alpha}$  1253 eV) X-ray source with an energy resolution of 0.9 eV. A standard electron gun was fitted to the instrument which operated between 10 and 15 keV, with an Oxford Instruments Energy Dispersive X-ray (EDX) analysis system. EDXA was carried out to identify surface regions of high Fe content. The electron beam was locked in the same area and AES was carried out. Finally this area was flooded with a 60  $\mu\text{m}$  diameter beam of X-rays to obtain the XPS data. Some surface cleaning of the samples was required, and this was performed in situ within the spectrometer using a standard Ar<sup>+</sup> gun operating at 5 keV.

### 3. Results and discussion

Transmission Mössbauer spectra were recorded of the phases extracted from the sample at 150 K and 250 K. Combinations of different phases were used in the fitting program until the best fit was achieved for a mixture of Al<sub>6</sub>Fe and cubic  $\alpha$ -AlFeSi [2]. The parameters are given in table 1. The identification agreed with XRD on the extracted phases. The as-cast sample contained only Al<sub>6</sub>Fe and the heat treatment has resulted in a partial phase transformation to a mixture of Al<sub>6</sub>Fe and  $\alpha$ -AlFeSi,

Table 1

Analysis using transmission Mössbauer spectroscopy of phases extracted from the aluminium ingot.

Phase combination	Mössbauer parameters, relative to rhodium, at 295 K ( $\pm 0.02 \text{ mm s}^{-1}$ )			Relative areas at 150 K	Relative areas at 250 K	Phase ratio at 150 K	Phase ratio at 250 K	Mean phase ratio
	$\delta$	$\Delta E_Q$	$\Gamma$					
$\alpha$ -AlFeSi	0.10	0.38	0.38	73	76	68	72	(70 $\pm$ 5)%
	0.18	0.22	0.38					
Al <sub>6</sub> Fe	0.12	0.30	0.29	27	24	32	28	(30 $\pm$ 5)%

which are both metastable phases in alloys of this composition [6]. Previously variable temperature Mössbauer spectroscopy had been used on extracted samples of the individual phases to obtain the values of the Debye temperature  $\theta_D$  ( $\text{Al}_6\text{Fe} = 327$  K,  $\alpha\text{-AlFeSi} = 312$  K [7]). The appropriate recoil-free fractions were used to determine the relative proportion of the phases extracted from the sample from the ingot being studied, see table 1.

Figure 1(a) shows the CEMS spectrum of the unetched surface. The  $\text{Al}_6\text{Fe}$  and  $\alpha\text{-AlFeSi}$  are still evident in the same relative proportion, see table 2, as seen in the phases extracted from the bulk. However, the spectrum is dominated by a large unresolved doublet indicating the presence of a phase X that has formed at the interface between the intermetallic particle and the aluminium oxide layer. The Mössbauer parameters of phase X (fitted as an asymmetric doublet,  $\delta = -0.17$  mm/s,  $\Delta E_Q = 0.22$  mm/s,  $\Gamma = 0.36, 0.48$  mm/s) do not correspond to those published for Al-Fe intermetallics, and do not agree with other known iron compounds. The heat treatment of the sample in air results in general oxidation of the surface and a specific reaction product X, which must be localised above the iron-rich intermetallic particles. Shimizu et al. [8] have used energy-filtering transmission electron microscopy to study the growth of porous anodic films on aluminium alloys containing  $\text{Al}_6\text{Fe}$  and  $\text{Al}_3\text{Fe}$  intermetallics. They report that the anodic oxide for-

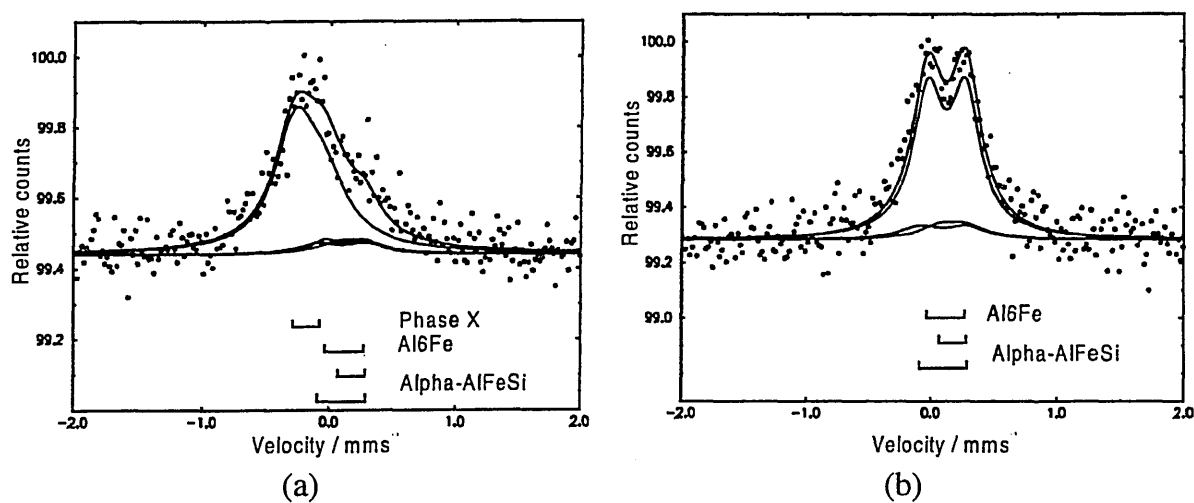


Figure 1. CEMS spectrum of (a) unetched surface and (b) etched surface.

Table 2  
Analysis of the surface of the aluminium ingot using CEMS.

Phase combination	Relative areas $\pm 5\%$	
	sample unetched	sample etched
$\alpha\text{-AlFeSi}$	17	18
$\text{Al}_6\text{Fe}$	8	82
Phase X	75	0

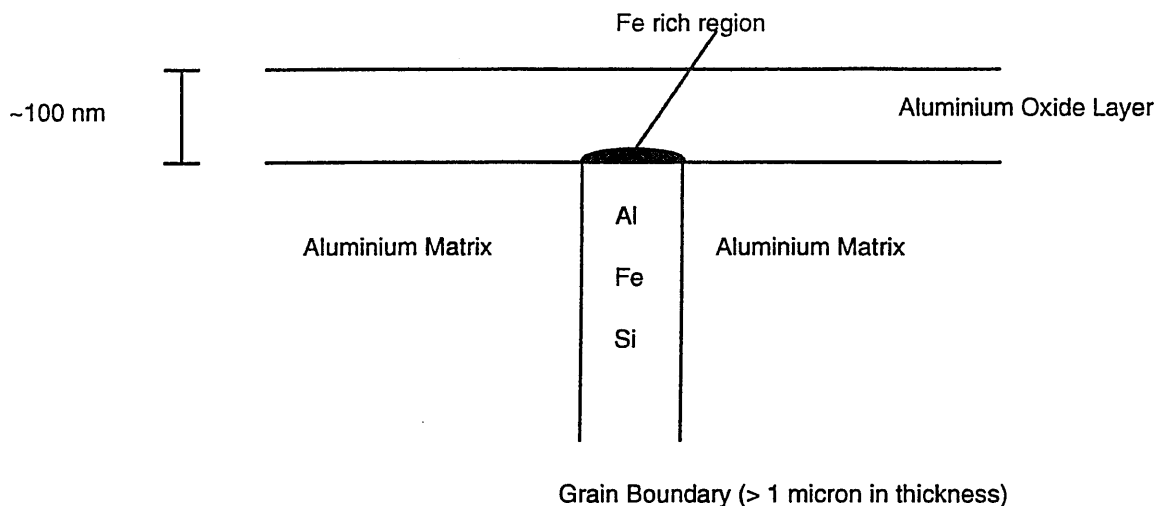


Figure 2. Proposed schematic model of the surface region above a grain boundary.

mation on the intermetallic phase involves initial and selective oxidation of aluminium and interfacial enrichment of iron, with the composition of this enriched layer being represented approximately by  $\text{Al}_{80}\text{Fe}_{20}$ . However, the Mössbauer parameters observed for phase X are not consistent with  $\text{Al}_{80}\text{Fe}_{20}$  which could be expected to have a more positive isomer shift. It may be possible that very fine superparamagnetic grains of iron have formed at the interface. These grains would give rise to a Mössbauer resonance at the isomer shift observed. A CEMS spectrum of such grains has been reported [9] when  $^{57}\text{Fe}$  was implanted in Al foils and then annealed.

EDXA confirmed the presence of Al, Fe and O in the inter-dendritic regions. When SAAES and SAXPS were performed in this region on the unetched sample the spectra show evidence of aluminium and oxygen above the grain boundary, with no Fe detected by these techniques. The peak shifts indicate that the oxide  $\text{Al}_2\text{O}_3$  is present. A proposed model of the region based on the SAAES, SAXPS and CEMS results is shown in figure 2.

Following the KI etch, used to leave the intermetallics exposed at the grain boundaries, the SAAES still shows only aluminium and oxygen, but the SAXPS spectrum now reveals Fe at the grain boundary, figure 3. The KI etching process also leads to the possibility of the formation of phases containing potassium and iodine. The surface of the sample was  $\text{Ar}^+$  ion etched to remove the presence of carbon and products of the KI etch. Figure 1(b) shows the CEMS spectrum of the surface following the KI etch and shows that phase X has been completely removed, leaving only evidence of  $\text{Al}_6\text{Fe}$  and  $\alpha\text{-AlFeSi}$ . However the relative proportion of the phases detected after etching are very different to those detected in the bulk and pre-etch phase ratios, table 2. It is hypothesised that this could be due to preferential etching of the  $\alpha\text{-AlFeSi}$  phase, or the preferential loss of this phase during etching due to its blocky morphology compared to the acicular morphology of the  $\text{Al}_6\text{Fe}$  phase.

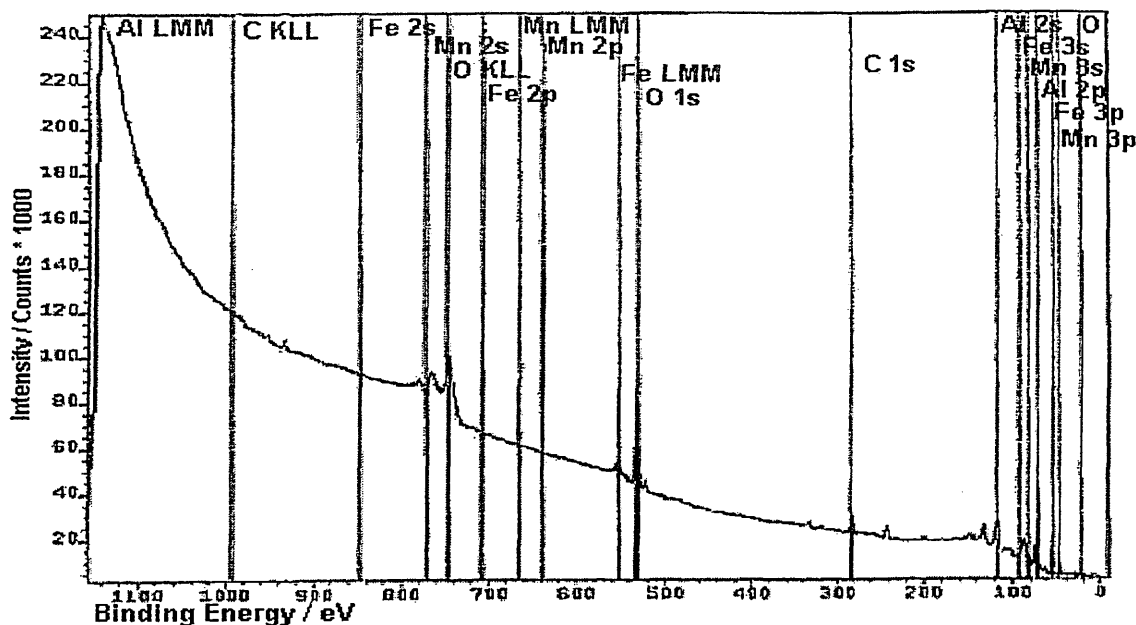


Figure 3. SAXPS spectra of grain boundary region after a KI etch and Ar<sup>+</sup> cleaning.

#### 4. Conclusion

This study has used the complementary techniques of SAAES, SAXPS and CEMS to investigate the oxidation reaction occurring above the iron-containing intermetallic phases which occur in the inter-dendritic region of a D.C. cast dilute aluminium alloy. The CEMS gives evidence of the formation of a phase at the interface between the oxide and the underlying intermetallic particles, figure 2. The identity of this phase has not yet been determined. The proposed model agrees with results obtained from energy-filtering transmission electron microscopy [8], where the formation of an oxide film on intermetallic phases was found to be accompanied by the rejection of Fe and the consequent formation of an Fe-enriched layer at the oxide interface. However, the Mössbauer parameters of this phase suggest that super-paramagnetic iron grains may have formed at the interface.

#### References

- [1] S.D. Forder, J.S. Brooks, A. Reeder and P.V. Evans, *Hyp. Interact.* 116 (1998) 209.
- [2] S.D. Forder, J.S. Brooks, A. Reeder and P.V. Evans, *Scripta Mat.* 40(1) (1999) 45.
- [3] C.J. Simensen, P. Fartum and A. Andersen, *Fresenius Z. Anal. Chem.* 319(3) (1984) 286.
- [4] S.D. Forder, J.S. Brooks and P.V. Evans, *Scripta Mat.* 35(10) (1996) 1167.
- [5] J.S. Brooks and S.C. Thorpe, *Hyp. Interact.* 47 (1989) 159.
- [6] S. Nagy, Z. Homonnay, A. Vertes and L. Murgas, *Acta Metall.* 35(3) (1987) 741.
- [7] A. Reeder, Ph.D. thesis, in preparation, Sheffield Hallam University (1999).
- [8] K. Shimizu, G.M. Brown, H. Habazaki, K. Kobayashi, P. Skeldon, G.E. Thompson and G.C. Wood, in: *Proc. of ICAA-6 on Aluminium Alloys*, Vol. 3 (1998) p. 1565.
- [9] W.X. Hu, G.L. Zhang, W.H. Liu, F.Xu and Y.G. Li, *Nucl. Instrum. Methods B* 72 (1992) 387.